Non-Orthogonal Multiple Access for 6G: Performance Analysis With Stochastic Geometry

Chao Zhang

Doctor of Philosophy

School of Electronic Engineering and Computer Science

Queen Mary University of London

December 12, 2023

Statement of Originality

I, Chao Zhang, confirm that the research included within this thesis is my own work or that where it has been carried out in collaboration with, or supported by others, that this is duly acknowledged below and my contribution indicated. Previously published material is also acknowledged below.

I attest that I have exercised reasonable care to ensure that the work is original, and does not to the best of my knowledge break any UK law, infringe any third partys copyright or other Intellectual Property Right, or contain any confidential material.

I accept that Queen Mary University of London has the right to use plagiarism detection software to check the electronic version of the thesis.

I confirm that this thesis has not been previously submitted for the award of a degree by this or any other university.

Signature: Chao Zhang

Date: December 12, 2023

Details of collaboration and publications:

1. **C. Zhang**, Y. Liu and Z. Ding, "Semi-Grant-Free NOMA: A Stochastic Geometry Model," *IEEE Trans. Wireless Commun.*, vol. 21, no. 2, pp. 1197-1213, Feb. 2022. Appear in Chapter 3.

2. **C. Zhang**, Y. Liu, W. Yi, Z. Qin and Z. Ding, "Semi-Grant-Free NOMA: Ergodic Rates Analysis with Random Deployed Users," *IEEE Wireless Commun. Lett.*, vol. 10, no. 4, pp. 692-695, Apr. 2021. Appear in Chapter 3.

3. **C. Zhang**, W. Yi and Y. Liu, "Reconfigurable Intelligent Surfaces Aided Multi-Cell NOMA Networks: A Stochastic Geometry Model," *IEEE Trans. Commun.*, vol. 70, no. 2, pp. 951-966, Feb. 2022.

4. **C. Zhang**, Y. Liu and Z. Ding, "Semi-Grant-Free NOMA: A Stochastic Geometry Model," *IEEE Trans. Wireless Commun.*, vol. 21, no. 2, pp. 1197-1213, Feb. 2022. Appear in Chapter 4.

5. **C. Zhang**, W. Yi, Y. Liu, Z. Ding and L. Song, "STAR-IOS Aided NOMA Networks: Channel Model Approximation and Performance Analysis," *IEEE Tran. Wireless Commun.*, vol. 21, no. 9, pp. 6861-6876, Sep. 2022. Appear in Chapter 5.

6. **C. Zhang**, W. Yi, Y. Liu and L. Hanzo, "Semi-Integrated-Sensing-and-Communication (Semi-ISaC): From OMA to NOMA", *IEEE Trans. Commun.*, vol. 71, no. 4, pp. 1878-1893, Apr. 2023. Appear in Chapter 6.

Acknowledgements

I would like to express my heartfelt appreciation to Dr. Yuanwei Liu, my supervisor during my Ph.D. studies. Dr. Yuanwei has been an incredible support throughout my research journey, offering his time and expertise in discussing ideas, providing timely and meticulous feedback, and encouraging me when I encountered obstacles. I believe that with his help, anyone aspiring to make significant contributions and pursuing a better career path would succeed. The days during these years cannot be easily summarized in a few sentences; hence, I want to sincerely convey hope for the STAR group, including Dr. Yuanwei, team members from the past to the future, and other related colleagues, to continuously progress.

I am also grateful to my second supervisor, Yue Chen, and independent assessor, Michael Chai, for their invaluable suggestions and discussions over the four years of my study. They are exceptionally kind individuals. I would also like to acknowledge the friendly and welcoming environment at Queen Mary University of London and extend my gratitude to my colleagues and staff members. Special thanks go to Dr. Wenqiang Yi for his patient assistance and detailed guidance.

I want to express my deepest gratitude to my family and friends for their unwavering support. My mother and father have been there for me emotionally and financially, and I couldn't have completed this monumental task without them. I am also grateful to my friends in the department who engaged in spirited discussions with me. Thank you all.

Having experienced three years of the Coronavirus pandemic, receiving both kindness and discrimination, tasting enough happiness and sorrows, bidding goodbye to the past and embracing the newborn, I believe I should thank this world, including myself, for helping me gradually find the meaning of my life: I would keep my way to spreading kindness. Hopefully, I could achieve my life goal:

"Music for Therapy and Technologies for Service."

Instead of a researcher, I prefer to be an artist, enjoying the beauty of matter, the sounds of nature, and the art of the universe. Instead of achieving great self-contribution, living with interesting phenomena and encountering unique people is more attractive. Whether I stay in academia or not, I would be a protector, safeguarding the followers, the new generation, the hope, the nature, and the "small amount of people". I would protect their uniqueness, which defines who they are. Every rose has its beauty, so let them freely bloom, whether they are roses or not. I was in the rain, so I would build a shelter for the followers, flowers, and whatever.

Abstract

Driven by an immense escalation of the wireless capacity requirements, ranging from conventional mobile services to machine-type devices and virtual reality, Sixth-Generation (6G) wireless networks are facing arduous challenges in enhancing massive connectivity with high reliability while low latency. As one of the promising solutions, non-orthogonal multiple access (NOMA), compared to orthogonal multiple access (OMA), allows multiple users to share the same time or frequency resource while being allocated at the transmitter with different codes or power levels and split at the receiver exploiting successive interference cancellation (SIC) techniques. Additionally, the emerging technologies of Fifth-Generation (5G) and 6G communications have excellent compatibility with NOMA, which further meets the requirements of massive connectivity, low latency, and multi-functional communication. In particular, NOMA-aided grant-free (GF) transmission balances the tradeoff between high quality-of-service (QoS) and low latency; reconfigurable intelligent surfaces (RISs) flexibly adjust the SIC detecting orders in NOMA networks as a new degree of freedom; and NOMA facilitates integrated sensing and communication (ISaC) networks achieve simultaneously coexistence of wireless connection and sensing functions in the same resource blocks. With the above potentials, this thesis focuses on NOMA networks with promising technologies from protocol designs to 6G massive connectivity scenarios, such as 6G massive machine-type communication (mMTC) connectivity, 6G full coverage connectivity, and 6G multi-functional connectivity for ultra-high frequency communications. As for the main mathematical tools, this thesis exploits stochastic geometry models to facilitate the performance evaluation and to derive performance metrics as insights, including diversity gains, high signal-to-noise ratio, etc. Finally, the contributions are highlighted in the conclusion to achieve massive connectivity.

Table of Contents

List of Figures

List of Tables

List of Abbreviations

2-D	Two-Dimensional
5G	Fifth-Generation
6G	Sixth-Generation
AWGN	Additive White Gaussian Noise
BE	Bandwidth Efficiency
BPCU	Bit Per Cell Use
BS	Base Station
CDF	Cumulative Distribution Function
CRLB	Cramér-Rao Lower Bound
CoMP	Coordinated Multi-Point Transmission
CSI	Channel State Information
DoF	Degree of Freedom
EM	Electromagnetic
ES	Energy Splitting
FD	Frequency-Division
GB	Grant-Based
GF	Grant-Free
HPPP	Homogeneous Poisson Point Process
IoT	Internet of Things
ISaC	Integrated Sensing and Communication
LoS	Line of Sight
MA	Multiple Access

MCP	Matérn Cluster Process
mMTC	Massive Machine-Type Communications
MIMO	Multiple-Input-Multiple-Output
MISO	Multiple-Input-Single-Output
MS	Mode Switching
mm-wave	Millimeter-Wave
NLoS	Non-Line-of-Sight
NOMA	Non-Orthogonal Multiple Access
OMA	Orthogonal Multiple Access
OP	Outage Probability
PCP	Poisson Cluster Process
PDF	Probability Density Function
PGFL	Probability Generating Functional
PPP	Poisson Point Process
QoS	Quality of Service
REIR	Radar Estimation Information Rate
RIS	Reconfigurable Intelligent Surfaces
Semi-ISaC	Semi-Integrated Sensing and Communication
Semi-GF	Semi-Grant-Free
SIC	Successive Interference Cancellation
SINR	Signal-to-Interference-and-Noise Ratio
SISO	Single-Input-Single-Output
SNR	Signal-to-Noise Ratio
SRE	Smart Radio Environments
STAR-IOSs	Simultaneous Transmitting and Reflecting Intelligent Omini-Surface
TS	Time Switching
UAV	Unmanned Aerial Vehicle

Chapter 1

Introduction

1.1 Background and Motivations

Since the Fifth-Generation (5G) wireless communication systems are commercially exploited [1], the investigation of the Sixth-Generation (6G) wireless communication systems has been focusing on new requirements, one of which points to massive connectivity due to the tremendous improvement of mobile applications and devices [2]. With a prediction that even 10 million connections per square kilometer or more may be evolved in 6G systems, it is doubtless envisioned that a massive number of connections will be required to be served for diverse services, including traditional wireless communications, massive machine-type communications (mMTC), sensing, etc. As one of the conventional solutions of massive connectivity (MA), non-orthogonal multiple access (NOMA) assigned multiple users in the time and frequency resource with different codes or power levels and split them by the successive interference cancellation (SIC) technique. With excellent compatibility, it has emerged as a promising contender for 6G systems, offering several key advantages. With the aid of its extra degree of freedom (DoF), such as power domain and code domain, NOMA enables high spectrum efficiency and improves system throughput by allowing multiple users evolved in one resource block. Additionally, these DoFs have the advantage of solving collisions of users in the same resource block due to failed authorization via handshakes or even without authorization. Moreover, thanks

to the development of the SIC technique, NOMA can be easily integrated to achieve new application scenarios with an easy-understanding and low-complexity design, such as mMTC, internet of things (IoT), sensing, and even the combination of different functions.

From 5G to 6G, NOMA demonstrates significant capability alongside various emerging technologies to meet the requirement of massive connectivity in 6G systems. This thesis utilizes these advantages to explore protocol designs and performance enhancements. Collaborating with different technologies, NOMA exhibits high potential in enhancing the connectivity of diverse 6G communication networks. 1)Due to the surge of wireless communication devices in 6G mMTC networks, NOMA-aided GF transmission remains a promising solution for achieving massive connectivity with high reliability and low latency. 2) Thanks to investigations into meta-materials, reconfigurable intelligent surfaces (RIS) have been proven to adjust SIC decoding orders [3], providing a new degree of freedom. By exploiting well-designed SIC orders and power allocation, spectrum efficiency could be significantly increased. Additionally, through the use of RISs, previously blocked users are reintegrated into the entire system, resulting in enhanced connections. 3) With the bandwidth of wireless communication reaching millimeter-wave levels since the advent of 5G, it is an inevitable challenge that wireless communication and sensing channels are overlapped. For integrated sensing and communication (ISaC), NOMA presents a solution to achieve multi-functional connectivity, enabling both wireless communication and sensing functions within the same resource block. The following subsections further outline the three requirements: 6G mMTC connectivity, 6G full coverage connectivity, and 6G multi-functional connectivity.

1.1.1 6G mMTC Connectivity

A huge proliferation of devices or services, i.e., 1) mobile devices such as sensors, machines and robots and 2) mobile services such as mobile online videos and mobile pay, is predicted as a trend of mMTC networks [4, 5],

which leads to an explosive growth of mobile broadband traffic [6, 7]. To meet the ultra reliable and low latency communication raised by the 5G requirements, GF transmission has been exploited for multiple access. To define the GF transmission, it can be regarded as a promising paradigm that eliminates uplink scheduling requests and dynamic scheduling grants in traditional grant-based (GB) transmission schemes [8]. The primary synchronization signal and secondary synchronization signal are replaced by broadcasting fast uplink grants to change the downlink synchronization process [9]. Moreover, several handshakes to transmit random access preambles and connection requests are avoided, thus achieving low-latency transmission [10]. To sum up, GF transmission enables users to transmit messages without permission from BSs whenever they want.

However, it is obvious that GF transmission without the authorization of BSs is more unstable than the conventional GB transmission since frequent collisions lead to multi-user detection issues, which is the most significant challenge of GF transmission strategies [11, 12]. Various attempts have been proposed to solve this collision issue of GF transmission. Recent research concludes that NOMA emerges as a promising solution for the coexistence of high connectivity, low latency, and few collisions [13, 14]. With the aid of the code-domain or power-domain multiplexing and SIC technologies [15], NOMA allows multiple devices to share the same resource blocks with few errors [1, 16]. As a result, although users with GF transmission may still collide frequently in the same time slots, their messages could be successfully decoded through varying power levels or codebooks [17–19]. Although NOMA-aided GF transmission meets machine-type devices, wireless transmitters via GB transmission cannot be ignored. Hence, a semi-grant-free (Semi-GF) transmission concept is proposed, which allows a portion of GF users join in a dedicated channel for GB transmission. By designing proper protocols for choosing GF and GB users, NOMA-aided Semi-GF transmission can achieve dual-functional massive connectivity in 6G mMTC systems.

1.1.2 6G Full Coverage Connectivity

Although NOMA-aided Semi-GF transmission provides great connectivity in 6G mMTC systems, it cannot avoid the influence of channel environments [20, 21]. If the users are blocked severely, these users may face failures at decoding their information due to low received power and severe interference, which may generally happen at the cell-edged users in NOMA systems. Since designing protocols may not deal with the environmental problem, this thesis then moves to the investigation of RISs in NOMA systems [22, 23].

Emerged as a promising technique in 6G communication networks, RISs, a type of meta-material, have the ability of enhancing the channel quality [22–26]. RISs are made of two-dimensional-equivalent reconfigurable meta-materials consisting of scattering particles or meta-atoms [27, 28]. Based on physical properties of this material, RISs are able to absorb incident waves or modify the reflected wavefronts by adjusting the angle of reflection and electric field strength [29–32]. By utilizing RIS-aided line of sight (LoS) propagation, one significant benefit is that RISs can improve the channel condition for users who are obstructed by high buildings and experiencing inevitable outage situations [23]. After covering the blind points by RISs, the channel quality and connectivity is enhanced.

Before harnessing RISs into NOMA networks, one of the main open research challenges is to investigate the path loss models of RIS reflecting channels. Recent research has studied two path loss models: one is correlated to the sum of incidence and reflection distances, and the other is correlated to the product of these distances [27]. Both models are correct but are suitable for different application scenarios. The "sum of distances" model is suitable for short-distance communications such as indoor scenarios, while the "product of distances" model is suitable for long-distance communications such as outdoor scenarios. To reduce path loss and interference, RISs are placed near the served NOMA user. This spatial grouping property can be depicted by a tractable stochastic geometry model called the Poisson cluster process (PCP), which provides a theoretical framework for investigating the

average performance of RIS-aided NOMA networks [33–36].

After ensuring the channel models of RISs and mimicking the spatial grouping properties, RISs can be exploited to address several implementation challenges associated with NOMA networks [22, 23]. For instance, cell-edged users typically have unsatisfactory performance, and NOMA techniques may even further degrade their performance due to the additional interference. To enhance the channel quality between the cell-edged users and their target BSs, exploiting RISs is a promising solution. Moreover, RISs can provide flexible decoding orders based on the quality of service (QoS). In uplink NOMA networks, for example, RISs can adjust the active number or passive beamforming patterns of RIS elements to improve the channel quality of the far user. This enables the far user to have better channel quality than the near user and take over the SIC process, thereby improving its performance. The NOMA technique also achieves enhanced connectivity in networks by providing a degree of freedom in the power domain. By integrating NOMA techniques and RISs, massive throughput requirements can be further met, making RIS-aided NOMA networks promising for 6G and beyond.

Despite their extraordinary benefits, conventional RISs have opaque substrates that may block signals to users behind them, resulting in poor performance for the blocked users. To overcome this limitation, the recent development of meta-surfaces, namely simultaneously transmitting and reflecting intelligent omini-surfaces (STAR-IOSs), allows signals to pass through substrates via refraction [37–41], thus providing highly flexible full-space smart radio environments (SREs) [42,43]. Unlike conventional RISs with half-space SREs, STAR-IOSs enable independent reflection and refraction beamforming, offering high flexibility for STAR-IOS serving areas [44,45]. As a result, STAR-IOSs bring the 360° coverage of SREs into reality. Therefore, investigating the effectiveness of STAR-IOSs in 6G networks is significantly important [31, 46].

Recent works propose three STAR-IOS protocols, namely the energy

splitting (ES) protocol, the mode switching (MS) protocol, and the time switching (TS) protocol, to enhance the full-space coverage of SREs. The TS protocol leverages all STAR-IOS elements in different time blocks to separate reflecting and transmitting links, while the ES and MS protocols provide the flexibility of SIC orders for a NOMA-aided transmission scheme [31, 42]. Specifically, the ES protocol allocates energy among reflecting and transmitting links, whereas the MS protocol activates different numbers of STAR-IOS elements for reflecting and transmitting links. Consequently, the ES and MS protocols enable us to artificially differentiate the channel quality of the reflecting and transmitting links through different ES coefficients or active numbers of STAR-IOS elements, respectively. By controlling the channel quality, the STAR-IOSs can adjust the SIC order for satisfying various constraints, such as enabling the user with high priority to obtain high channel gain and ensuring a successful SIC process when a reflecting user and a transmitting user are paired in one NOMA cluster. Therefore, the STAR-IOSs distinguish the SREs of NOMA users and efficiently expand the applications of NOMA in 6G [47, 48]. Therefore, it is highly valuable to investigate the evaluation of STAR-IOSs in NOMA systems to achieve 360° full coverage.

1.1.3 6G Multi-Functional Connectivity

Given the incessant escalation of wireless tele-traffic, the impending spectrum-crunch can only be circumvented by the migration to millimeter-wave (mm-wave) carriers. However, since radar sensing technologies also rely on mm-wave carriers, the bandwidth of sensing and wireless communication might become overlapped [49–51]. Indeed, it is possible to economize by sophisticated bandwidth-sharing in 6G wireless communications with the aid of ISaC [52].

ISaC faces challenges in exploiting the entire spectrum due to various applications occupying different bandwidths. For instance, the L-band (1-2 GHz) is used for long-range air traffic control and surveillance. The S-band

(2-4 GHz) is used for terminal air traffic control, moderate-range surveillance, and long-range weather observation. The C-band (4-8 GHz) is used for long-range tracking, weapon location, and weather observation. The mm-waves are used for high-resolution mapping, satellite altimetry, vehicular radars, and police radars [53]. Therefore, it is more practical to allocate a portion of the bandwidth for ISaC while leaving the rest for wireless communications or radar detection. Specifically, semi-integrated sensing and communication (Semi-ISaC), defined from conventional ISaC scenarios, is a more promising solution for 6G networks.

In the context of Semi-ISaC, NOMA presents a more promising solution compared to orthogonal multiple access (OMA), as the SIC concept aligns well with the ISaC scenarios. There are multiple advantages to utilizing NOMA in Semi-ISaC networks. One significant advantage is the increased bandwidth efficiency (BE) of each resource block, as NOMA enables multiple users to join in the same resource block. Furthermore, due to the maturity of the SIC scheme, fundamental analysis can effectively leverage NOMA in Semi-ISaC networks. In addition, with the use of NOMA, BSs can accurately control the transmit powers of communication users and the transmit power for radar detection, thus avoiding the need for predicted radar echoes, which may enhance the accuracy of computing radar information [54]. Additionally, utilizing NOMA provides a new degree of freedom for Semi-ISaC networks

1.2 Contributions

Motivated by the advantages and challenges aforementioned, the thesis investigates the NOMA networks with several emerging technologies in 6G wireless communication systems. The content spans several chapters, including Chapter 3 to Chapter 6. By exploiting the stochastic geometry models that are introduced in Chapter 2, the average system performance is evaluated and the spatial effect is well considered. The specific contributions of this dissertation are summarized and listed in the following:

1. In Chapter 3, semi-GF NOMA networks are investigated to reduce collision situations and enhanced connectivity for 6G mMTC systems. With the open-loop protocol as the benchmark, a novel dynamic protocol is proposed to select GF users into the dedicated channels of GB transmission. By considering the random deployment of GF and GB users, the outage performance and the ergodic rate are evaluated with insights, such as diversity gains and high signal-to-noise ratio (SNR) slopes, respectively.

2. When considering full coverage to further improve connectivity, a RIS-assisted NOMA network is considered in Chapter 4 where the LoS links are blocked. As for the stochastic geometry models, the PCP model is invoked to capture the spatial effects of NOMA users. This chapter provides the path loss models of the reflecting links of linear RISs, which are correlated with the product of distances to conform with long-distance regions. With the channel models, the coverage probability and ergodic rate are derived as the performance metrics.

3. In Chapter 5, the investigation of RISs is migrated to STAR-IOSs to cover the blind areas generated/obscured by conventional RISs. With randomly deployed users in a circle area, a STAR-IOS-aided NOMA network is investigated to achieve 360° full connectivity. This chapter provides three tractable channel models for RISs (including STAR-IOSs), such as the M-fold convolution (MFC) model, the central limit (CL) model, and the curve fitting (CF) model. By exploiting the CF model, the system performance of the STAR-IOS-aided NOMA network is investigated, while the diversity gains are derived by exploiting the MFC model under ES, TS, and MS modes.

4. To meet the requirement of 6G connectivity with sensing functions, a novel concept is proposed in Chapter 6, namely Semi-ISaC. As for Semi-ISaC, a portion of the bandwidth is exclusively used for either wireless communication or radar detection, while the rest is for ISaC

transmission. A migration from OMA Semi-ISaC to NOMA Semi-ISaC is presented. As for wireless communication, the outage probability (OP) and ergodic rate are the considered metrics. As for radar detection, a new metric, namely ergodic radar estimation information rate (REIR) is proposed. Based on the new concept and the metrics, the performance of the OMA case is first evaluated, followed by that of the NOMA case.

1.2.1 Author's Submitted Papers

Journal papers

1. **C. Zhang**, W. Yi, Y. Liu and Z, Ma, "NOMA for Multi-Cell RIS Networks: A Stochastic Geometry Model," submitted to *IEEE Trans. Wireless Commun.*, under review.

2. **C. Zhang**, W. Yi, Y. Liu and L. Hanzo, "Semi-Integrated-Sensing-and-Communication (Semi-ISaC): From OMA to NOMA", *IEEE Trans. Commun.*, vol. 71, no. 4, pp. 1878-1893, Apr. 2023. (This paper has been included in Chapter 6.)

3. **C. Zhang**, W. Yi, Y. Liu, Z. Ding and L. Song, "STAR-IOS Aided NOMA Networks: Channel Model Approximation and Performance Analysis," *IEEE Tran. Wireless Commun.*, vol. 21, no. 9, pp. 6861-6876, Sep. 2022. (This paper has been included in Chapter 5.)

4. **C. Zhang**, W. Yi and Y. Liu, "Reconfigurable Intelligent Surfaces Aided Multi-Cell NOMA Networks: A Stochastic Geometry Model," *IEEE Trans. Commun.*, vol. 70, no. 2, pp. 951-966, Feb. 2022. (This paper has been included in Chapter 4.)

5. **C. Zhang**, Y. Liu and Z. Ding, "Semi-Grant-Free NOMA: A Stochastic Geometry Model," *IEEE Trans. Wireless Commun.*, vol. 21, no. 2, pp. 1197-1213, Feb. 2022. (This paper has been included in Chapter 3.)

6. **C. Zhang**, Y. Liu, W. Yi, Z. Qin and Z. Ding, "Semi-Grant-Free NOMA: Ergodic Rates Analysis with Random Deployed Users," *IEEE Wireless Commun. Lett.*, vol. 10, no. 4, pp. 692-695, Apr. 2021. (This paper has been included in Chapter 3.)

7. Z. Liu, X. Yue, **C. Zhang**, Y. Liu, Y. Yao, Y. Wang and Z. Ding, "Performance Analysis of Reconfigurable Intelligent Surface Assisted Two-Way NOMA Networks," *IEEE Trans. Veh. Technol.*, vol. 71, no. 12, pp. 13091-13104, Dec. 2022.

8. B. Zhao, **C. Zhang**, W. Yi and Y. Liu, "Ergodic Rate Analysis of STAR-RIS Aided NOMA Systems," *IEEE Commun. Lett.*, vol. 26, no. 10, pp. 2297-2301, Oct. 2022.

Conference papers

1. **C. Zhang**, W. Yi and Y. Liu, "Semi-Integrated-Sensing-and-Communication (Semi-ISaC) Networks Assisted by NOMA," in *Proc. IEEE Int. Commun. Conf. (ICC'22)*, Seoul, South Korea, May 2022.

2. **C. Zhang**, W. Yi, K. Han,Y. Liu, Z. Ding, and M. Renzo, "Simultaneously Transmitting And Reflecting RIS Aided NOMA With Randomly Deployed Users", in *Proc. IEEE Global Commun. Conf. (GLOBECOM'21)*, Madrid, Spain, Dec. 2021.

3. **C. Zhang**, W. Yi,Y. Liu, and Q. Wang, "Multi-cell NOMA: Coherent Reconfigurable Intelligent Surfaces Model With Stochastic Geometry", in *Proc. IEEE Int. Commun. Conf. (ICC'21)*, Jun. 2021.

4. **C. Zhang**, W. Yi,Y. Liu, Z. Qin, and K. K. Chai, "Downlink Analysis for Reconfigurable Intelligent Surfaces Aided NOMA Networks", in *Proc. IEEE Global Commun. Conf. (GLOBECOM'20)*, Taibei, China, Dec. 2020.

5. **C. Zhang**, Y. Liu, Z. Qin and K. K. Chai, "Semi-Grant-Free Uplink

NOMA with Contention Control: A Stochastic Geometry Model", in *Proc. IEEE Int. Commun. Conf. (ICC'20)*, Jun. 2020.

1.3 Dissertation Organization

The structure of this thesis consists of several chapters. Chapter 2 presents some essential concepts of stochastic geometry models, such as the Poisson point process (PPP) and PCP. Chapter 3 examines the performance of the NOMA-aided Semi-GF network under different protocols. In Chapter 4, we analyze the performance of the linear-RIS-assisted NOMA networks in scenarios without LoS links. Furthermore, Chapter 5 explores the STAR-IOS-aided NOMA network to provide complete coverage. Moreover, Chapter 6 proposes a new Semi-ISaC network and describes the transformation from OMA Semi-ISaC networks to NOMA Semi-ISaC networks. Finally, Chapter 7 summarizes this thesis and outlines the potential research directions for future work.

Chapter 2

Fundamental Concepts and Literature Review

In this chapter, the basic concept of NOMA is introduced, followed by presenting mathematical preliminaries to introduce the foundations of stochastic geometry. Then, the literature review of the NOMA networks with emerging technologies is presented.

2.1 NOMA Concept

Before exploiting the potential of NOMA, the theoretical concepts of the system's performance gain are first brought into our focus. The fundamental concept of NOMA is to support multiple users in non-orthogonal channels, including the power domain, code domain, space domain, etc. Indeed, the NOMA concept could be briefly explained as a special case of downlink broadcasting. With the aid of superposition coding (SC) technique, the channel capacity gain has been evaluated for a realistically imperfect discrete memoryless broadcast channel [55], which has inspired the search for Gaussian channel capacity [56]. Exploiting the NOMA basis, several researchers started to investigate the potential performance enhancement in the way of theoretical evaluation, such that the authors of [57, 58] have found a new evaluation criterion to quantify the performance gain of NOMA over OMA by comparing TDMA and NOMA in terms of their capacity region. Additionally, the investigation of NOMA networks could be further

refined in terms of downlink NOMA and uplink NOMA [59–63], respectively, since the power allocation and SIC processes of downlink/uplink NOMA are generally different. Hence, in the following sections, this thesis provides the basic concept and key differences of the downlink and uplink NOMA, respectively

2.1.1 Key Technologies of NOMA

Recall that NOMA revolutionizes wireless communication by enabling multiple users to share the same time and frequency resources through different DoFs, including but not limited to power domain, code domain, space domain, and other NOMA patterns [2].

As for the power domain NOMA, with different power allocation algorithms based on power domain NOMA, the transmitter assigns different power levels to users, and the signals are decoded based on signal strengths at the receiver sides by SIC technique [64]. Users with weaker channel conditions receive higher power levels, allowing simultaneous transmissions at different power levels and decoding at the receiver based on signal strengths.

Code domain multiplexing, such as sparse code multiple access (SCMA) [65] and multi-user shared access (MUSA) [66], is similar to CDMA or multi-carrier CDMA, where different users are assigned different codes. Signals are then multiplexed over the same time-frequency resources. The difference is that code domain multiplexing can achieve certain spreading gain and shaping gain at the cost of increased signal bandwidth [67].

Regarding the space domain, it leverages multiple antennas at the transmitters and receivers to serve multiple users simultaneously using spatial multiplexing techniques. Currently, it is more generally noted as multiple-input-multi-output (MIMO) [68, 69] or massive MIMO [70] instead of space domain NOMA, although it still aligns with the general concept of NOMA.

Additionally, there are some other types of NOMA techniques presented. Pattern-division multiple access (PDMA) maximizes diversity and minimizes overlaps among multiple users' non-orthogonal patterns at the trans-

mitter, then chooses appropriate multiplexing techniques for signal decoding at the receiver, such as code domain, spatial domain, or a combination of both [71]. Furthermore, rate splitting multiple access (RSMA) exploits the commonality of rate-splitting (RS) principles. RS involves splitting a user message (e.g., information bits) into two or multiple parts, allowing flexible decoding at one or multiple receivers. Each receiver retrieves each part to reconstruct the original message [72].

Among the aforementioned NOMA technologies, performance analysis often emphasizes power domain NOMA since the power allocation process is easily expressed in the SNR expressions. Consequently, performance metrics, including outage probability or average system rates based on the Shannon capacity, can be evaluated. As for the other NOMA technologies, such as code domain, space domain, etc., different code designs and precoding algorithms pose challenges for performance evaluation. Tractable derivations may not be easily obtained, resulting in limited insights for these domains. To conduct a more targeted investigation, this thesis focuses on enhancing massive connectivity by exploiting the power domain NOMA. Compared to conventional MA technologies, new DoFs are provided by NOMA techniques to allow multiple users to occupy the same resource block. Since NOMA fits the feasibility of current techniques, it is considered an add-on technique to improve connectivity.

2.1.2 Downlink NOMA Transmission

Recall that this thesis mainly focuses on power domain NOMA. The basic concept of the power domain NOMA employs two techniques, including SC at the transmitters and SIC at the receivers.

- SC: The fundamental concept of SC is designed that it is capable of encoding a message for a user associated with poor channel conditions at a low rate and then superimposing the signal of a user having better channel conditions on it.

- SIC: The basic concept of SIC is to improve spectrum efficiency with the aid of efficient interference management. The procedures of SIC are summarized as follows. The strongest signal, which is the least interference-contaminated signal, is first detected. The strongest user then reencodes and remodulates its signal. In the following, the regenerated signal is subtracted from the composite signal, followed by the detection of the second strongest signal, until all users have been detected.

To clearly introduce the NOMA technique, a two-user downlink case is defined here as an example, where the channel coefficients of the user m and user n are expressed as h_m and h_n with $|h_m|^2 < |h_n|^2$. With the above two technologies in the downlink NOMA transmission, the BS utilizes the SC technique to transmit a composite of signals with different power levels, while users employ SIC techniques to cancel interference. The main processes are listed in the following:

- Resource Allocation: Instead of assigning different resources exclusively to each user, the BS multiplexes the signals of the NOMA users in the same resource blocks with different power levels. The BS allocates power allocation coefficients to the NOMA users. For the user with a better channel gain than the others, it receives a smaller power allocation coefficient to balance the received power and to obtain enhanced achievable rates. As for the example, the user m is allocated a large coefficient and the user n has a small one.

- SIC Process: The users receive the integrated signals. The strong user exploits SIC to remove the interference of the weak user's signal and then detects its own signal. The weak user directly detects its own signal with a larger power allocation coefficient. Based on the example of the user m and user n with the relationship of $|h_m|^2 < |h_n|^2$, the user m directly detects its signal, and the user n undergoes the SIC process, followed by its signal detection.

2.1.3 Uplink NOMA Transmission

In uplink NOMA transmission, several users send the uplink signals to the BS by exploiting the same time and frequency resources. The BS employs the SIC technique to split all users' messages. Compared to the downlink NOMA, several key distinctions of the uplink NOMA transmission are outlined below:

- Resource Allocation: Unlike the resource allocation in downlink NOMA transmission, the transmit power of users can be the same in uplink NOMA, while the difference in power levels relies on different users' channel conditions. At the BS side, the received power of users with significantly different channel conditions can be considered as users with different power levels. Hence, the SIC process carries on.

- SIC Process: The SIC process between the downlink and uplink NOMA transmission is also different. The BS undergoes the SIC process. After the BS receives the integrated signals of the NOMA users (and other necessary process such as synchronization), the BS first detects the signal of the user with strong channel condition. After the strong user's detection, the BS exploits SIC to regenerate and subtract the strong user's signal. In the end, the BS could detect the rest signal of the weak user. By considering the example to explain, the BS firstly detects the signal of the user n, followed by the user m.

2.1.4 Comparison Between OMA and NOMA

The SNR expressions for OMA and NOMA are to be presented in the following to illustrate the relationship of the two techniques. As for the OMA case, the frequency and time resource allocation coefficient is defined as $\frac{1}{2}$. As for the NOMA case, the power allocation coefficients are denoted as α_m and α_n for the user m and the user n, respectively. Recall that the channel conditions of users have the relationship of $|h_m|^2 < |h_n|^2$. With the transmit SNR at the BS and the NOMA users sides, denoted as ρ, the SNR

expressions at the receivers are expressed as

- The OMA case:

$$\gamma_m^{OMA} = \frac{1}{2}\log_2\left(1+\rho|h_m|^2\right) \tag{2.1}$$

and

$$\gamma_n^{OMA} = \frac{1}{2}\log_2\left(1+\rho|h_n|^2\right), \tag{2.2}$$

- The downlink NOMA case:

$$\gamma_m^{NOMA,d} = \log_2\left(1+\frac{\rho\alpha_m|h_m|^2}{1+\rho\alpha_n|h_n|^2}\right) \tag{2.3}$$

and

$$\gamma_n^{NOMA,d} = \log_2\left(1+\rho\alpha_n|h_n|^2\right), \tag{2.4}$$

- The uplink NOMA case:

$$\gamma_n^{NOMA,u} = \log_2\left(1+\frac{\rho|h_n|^2}{1+\rho|h_m|^2}\right) \tag{2.5}$$

and

$$\gamma_m^{NOMA,u} = \log_2\left(1+\rho|h_m|^2\right). \tag{2.6}$$

where γ_m^{OMA} and γ_n^{OMA} are the SNR for the OMA case. Coefficients $\gamma_m^{NOMA,d}$ and $\gamma_n^{NOMA,d}$ are the SINR and SNR for the downlnk NOMA transmission, respectively. Additionally, coefficients $\gamma_n^{NOMA,u}$ and $\gamma_m^{NOMA,u}$ are the SINR and SNR for the uplink NOMA case.

2.2 Mathematical Preliminaries

This section presents the basis concepts of the main mathematical tools, stochastic geometry models, that this thesis utilized. The chapter 4 and 5 frequently utilize the following concepts and lemmas to derive the performance metrics. To make it clearly to understand, this chapter contains the foundamental basis of stochastic geometry models.

A point process is a measure space-based countable random collection of points, which restrict to point processes on the Euclidean space, denoted as $\mathbb{R}^d$. Generally, in wireless communication system models, the parameter d is often considered as 2 for simplicity to represent the vertical view of cells. Hence, the exploited point processes in this thesis mimic the two-dimensional (2-D) spatial locations of nodes, such as BSs, users, access points, etc. Denote a point process as Φ, an instance of the point process Φ as ϕ, and the number of points for the point process in a set $A \in \mathbb{R}^2$ as $\Phi(\mathbb{R})$. With the presentation above, the definition of a 2-D point process is defined as follows.

Definition 1. Point Process: Let $\mathfrak{N}$ as the space of all 2-D vectors with elements in $\mathbb{R}^2$. A point process Φ is a measurable map, that is, a random variable taking values in the space $\mathfrak{N}$.

Note that any bounded set contains a finite number of points and a point pattern is called simple if $\phi_k \neq \phi_l$ with $k \neq l$. As the ordering of the points is usually irrelevant, the instance ϕ is sometimes regarded as a collection of points.

2.2.1 Random Measures of Point Processes

The notion of void probability is presented before the random measures are introduced to characterize the equivalent character of two point processes.

Definition 2. Void Probability: Over all bounded sets $A \in \mathbb{R}^2$, the void probability of a point process, denoted as Φ, is defined as $\mathbb{P}\{\Phi(A) = 0\}$.

Definition 3. Equivalence: If two simple point processes have the same void probability distributions through all bounded sets A, they are referred to as equivalent point processes.

The density (intensity) measure is then characterized, which is frequently exploited in the derivations of stationary point processes, such as the PPP and the PCP, introduced in the following subsection. Note that the density measure could be a constant or a function, depending on whether the point process is stationary or not. As for stationarity, it is defined that $\Phi = \{x_m\}$ is a stationary point process if $\Phi = \{x_m + x\}$ has the same distribution as Φ for every $x \in \mathbb{R}^2$. Hence, we have the density measure of a stationary point process Φ as follows.

Definition 4. Density (Intensity) Measure: For every $A \in \mathbb{R}^2$, the density of Φ is defined as

$$\lambda = \frac{[\Phi(A)]}{|A|}. \tag{2.7}$$

2.2.2 Examples of Point Processes

In this subsection, the mostly-utilized point processes are introduced, including the PPP and the PCP. Additionally, several functions of point processes are also derived to evaluate the sums over point processes and products over point processes.

2.2.2.1 Definition of PPP

A stationary (homogeneous) point process Φ with the density λ is a PPP when it satisfies the following two conditions: 1) The number of points in any bounded set $A \in \mathbb{R}^2$ follows a Poisson distribution with the constant mean value, denoted as $\lambda|A|$; 2) The number of points in disjoint sets are

independent. Hence, the probability of numbers is presented as

$$\mathbb{P}\{\Phi(A) = k\} = \frac{(\lambda|A|)^k}{k!} \exp(-\lambda|A|), \tag{2.8}$$

and the points are uniformly distributed in the area A as the points have a constant density. This definition is exploited in Chapter 4.

2.2.2.2 Definition of PCP

The PCP could be referred to as the combination of two PPPs, including parent points and daughter points. To generate the parent points, a PPP Φ_p is exploited with the density λ_p in a large area $A_p \in \mathbb{R}^2$. Then, the daughter points are further deployed based on another PPP Φ_d with the density λ_d in a small area $A_d \in \mathbb{R}^2$, whose centers are the parent points. Note that generally the area A_d is smaller than A_p. Since the two PPPs are independent, the parent points and daughter points are uniformly distributed in the targeted areas. Hence, the cumulative distribution function (CDF) of the distance of the nearest point could be utilized to evaluate the performance of all nodes because of the stationarity. Hence, the CDF and the probability density function (PDF) of D, denoted as F_D and f_D, are respectively derived as

$$F_D(r) = \Pr\{\mathrm{D} \geq \mathrm{r}\} = \exp\left(-\lambda_\mathrm{t}\pi \mathrm{r}^2\right) \tag{2.9}$$

and

$$f_D(r) = 2\lambda_t \pi r \exp\left(-\lambda_t \pi r^2\right). \tag{2.10}$$

which is proved by

$$\begin{aligned} F_D(r) &= \Pr\{\mathrm{D} \geq \mathrm{r}\} = \Pr\{\mathrm{B}(\mathrm{o}, \mathrm{r}) \in \emptyset\} \\ &= \Pr\{\Phi(\mathrm{B}(\mathrm{o}, \mathrm{r})) = 0\} = \exp\left(-\lambda_\mathrm{t} |\mathrm{B}(\mathrm{o}, \mathrm{r})|\right) \\ &= \exp\left(-\lambda_t \pi r^2\right), \end{aligned} \tag{2.11}$$

where $t \in \{p, d\}$ represents parent points and daughter points, respectively. The $B(o, r)$ is the bounded area (disc) with the origin o and the radius r. This definition is exploited in Chapter 5.

Additionally, the Campbell Theorem and the Probability Generating Functional (PGFL) is frequently exploited in this thesis. Hence, the following two lemmas first introduces the Campbell Theorem and the PGFL, respectively.

As for the sums over point processes, the Campbell Theorem is exploited. The definition of the Campbell Theorem is introduced as follows.

Lemma 1. Let a PPP Φ be with the density λ and the mapping $f(x) : \mathbb{R}^2 \to \mathbb{R}^+$. The Campbell Theorem is then presented as

$$\mathbb{E}\left[\sum_{x\in\Phi} f(x)\right] = \lambda \int_{\mathbb{R}^2} f(x)dx. \tag{2.12}$$

As for the products over point processes, The PGFL is utilized. The following lemma presents the definition of the PGFL.

Lemma 2. Let a PPP Φ be with the density λ and the mapping $f(x) : \mathbb{R}^2 \to [0, 1]$. The definition of PGFL is expressed as

$$\mathbb{E}\left[\prod_{x\in\Phi} f(x)\right] = \exp\left(-\lambda \int_{\mathbb{R}^2} (1 - f(x))dx\right). \tag{2.13}$$

2.3 Literature review

This section introduces the literature review of related topics, including stochastic geometry methods, GF transmission, RIS and STAR-IOS systems, and ISaC systems.

2.3.1 Related Works for Stochastic Geometry Methods

As a powerful mathematical tool to capture the spatial randomness of wireless networks, stochastic geometry has been widely utilized for analyzing the performance of various networks [73]. For clarification, the stochastic models and distance distributions are evaluated such as homogeneous Poisson point process (HPPP) and Poisson cluster processes (PCP) for cellular networks [33, 74, 75]. With the aid of stochastic geometry methods, some initial NOMA contributions have been investigated [21, 76–81]. More particularly, a massive GF NOMA network [76] and a cache-enabled heterogeneous network [77] were recognized as finite uniformly random networks, thereby being investigated by HPPP. For scenarios with nodes in randomly distributed clusters, PCP is universally invoked to model the spatial distributions of clustered nodes, such as coordinated multi-point transmission (CoMP) systems [78], unmanned aerial vehicle (UAV) networks [79, 80] and clustered mm-wave networks [21]. Moreover, the locations of users were arranged into discs and rings in [81] to simplify the spatial distributions.

As stochastic geometry methods are mathematical models, these methods are able to be exploited in different networks if the system model designs are proper. Currently, the performance analysis with stochastic geometry models has been well evaluated for the 5G wireless communication systems and now it is time to move forward to investigate 6G communications. Hence, this thesis focuses on the 6G wireless communication networks with the aid of stochastic geometry models to evaluate the average performance of an entire system.

2.3.2 Related Works for GF Transmission

Because of the properties of GF transmission schemes such as low latency, high connectivity and high collision probability, we exploit the NOMA technique to achieve high reliability for users without bringing additional signalling overhead. Extensive research contributions have explored the potential performance enhancement brought by the uplink NOMA scheme

as benchmarks. Several survey papers such as [82] and [83] introduce the elemental definitions in NOMA systems. Typical models of multiple access (MA) designs in uplink NOMA were analyzed [84–86]. Modelling and analysis of conventional uplink NOMA were further evaluated by exploiting various aspects such as user pairing theory [87], power allocation [88] and energy harvesting designs [89, 90]. In terms of GF NOMA networks, code-domain multiplexing is universally considered on multi-user detection designs [91, 92], while the research contributions on power domain GF NOMA designs are still in their infancy.

Compared to the state-of-the-art research, this thesis highlights the performance analysis on a Semi-GF system, which allows the conventional GF and GB transmission to appear at the same time. By designing the Semi-GF protocols, the bandwidth resource is well exploited to accommodate more users than the conventional GF transmission or GB transmission solely. In Chapter 3, the Semi-GF transmission protocol is proposed and the performance is evaluated.

2.3.3 Related Works for RIS Networks

Recent research contributions have evaluated RIS-aided networks in several aspects. For information-theoretic fundamentals of RIS-aided networks, different channel models including propagation and path loss modelling have been proposed [3, 23, 27, 28, 93, 94]. Additionally, various specific pass loss models are provided by [23, 28, 93]. More specifically, the channel models for linear materials have been proposed and investigated by [3, 27] and other works focus on RIS models with antenna elements [23, 28, 93, 94]. Based on the channel models, contributions to different applications are summarized in the following. One breakthrough for RISs is the passive beamforming design [95–99], which is the main focus of RIS-aided systems. Several aspects of technologies have provided theoretical basics for performance analysis, including passive beamforming [99], information transfer [97], modulation [100], and resource allocation [98]. Additionally, research papers

focusing on RIS applications in different scenarios have indicated the benefit that RISs have high compatibility, such as RISs combined with machine learning methods [101, 102], RIS-aided mmWave networks [103, 104], and RIS-aided IoT networks [105].

As in most cases, scholars focus on the main property of the RIS that RISs can enhance the channel gain of the users. When considering this property in NOMA networks, it brings a new degree of freedom for creating power differences in NOMA. In general, NOMA exploits power allocation (downlink) or considers users with different channel conditions (uplink) to create different power levels. With the aid of RISs, we can change the channel condition by exploiting RISs or not, to adjust which user undergoes the SIC process. Hence, based on the investigation of this thesis, the flexible adjustment of SIC orders is possible, which is mainly presented in Chapter 4.

2.3.4 Related Works for STAR-IOS networks

As a brand-new topic, only a few works have been investigated for the STAR-IOS-aided NOMA systems. The recent research focuses on the optimal beamforming designs of STAR-IOS networks based on power consumption minimization [42], phase shift optimization [106], sum-rate maximization [107], and sum coverage range maximization [108]. Additionally, a joint design for STAR-IOS enhanced CoMP NOMA systems is proposed by [109]. As the STAR-IOSs improve the flexibility for downlink NOMA systems [31], physical layer performance analysis is needed to derive valuable insights for finding out more optimization problems. However, obtaining tractable channel models is the main challenge for performance analysis of STAR-IOS-aided networks. Additionally, theoretical performance analysis for STAR-IOS-aided NOMA systems is still in its infancy. The Chapter 5 of this thesis covers the performance analysis of STAR-IOS.

2.3.5 Related Works for ISaC

The fundamental designs of ISaC networks are investigated in [110–113], including spectrum sharing methods [110, 111], waveform designs [112], and resource allocation algorithms [113]. The hottest topic in ISaC networks is the investigation of MIMO ISaC networks, including their MIMO-aided transceiver designs [114–118], interference exploitation or interference removal [119–121], and the subject of multi-user MIMO ISaC networks [122]. But again, the performance analysis of NOMA-based ISaC is still in its infancy. Since the MIMO and NOMA techniques use different domains for MA, their comparison, combination, and cooperation under the concept of MIMO ISaC networks is warranted. Additionally, several authors investigated the average performance of ISaC systems relying on the SIC scheme [54, 123], demonstrating the feasibility of NOMA in Semi-ISaC networks. Hence, there is ample inspiration to pave the way for the evolution of Semi-ISaC networks from OMA to NOMA, investigated in Chapter 6.

The next chapter (Chapter 3) will start from the Semi-GF transmission, followed by the performance analysis for the RIS-aided NOMA network in Chapter 4, STAR-IOS-aided NOMA network in Chapter 5, and the Semi-ISaC network in Chapter 6. A conclusion in Chapter 7 highlights the innovation and contribution of this thesis.

Chapter 3

Semi-GF NOMA Networks

This chapter uplink semi-GF NOMA networks where the GF and GB users are combined in orthogonal channels, which are employed into the same resource blocks. Since the distances for the GB and GF users are not predetermined, there are two potential scenarios: 1) the GF users are located as near users while the GB users as cell-edge users, denoted as *Scenario I* and 2) the GB users are situated in the center areas while the GF users are determined as far users, denoted as *Scenario II*. Based on the mentioned scenarios, the primary contributions are summarized as:

- A novel *dynamic protocol* is proposed to determine whether the GF users join the channels occupied by the GB users. Compared to the open-loop protocol, the channel quality thresholds of the dynamic protocol are more accurate. Hence, the unexpected interference from the GF users is reduced. The latency of the conventional GF, GB and Semi-GF protocols is evaluated, followed by the discussion of the signalling overhead.

- *As for Scenario I*: The analytical expressions of OP for the GF and GB users under two protocols are derived. Furthermore, diversity orders for the GF and GB users are calculated in terms of the asymptotic analysis of Semi-GF NOMA networks. Analytical results reveal that two protocols, including the open-loop protocol and the dynamic protocol, have the same diversity gains.

- *As for Scenario II*: The analytical and asymptotic expressions of OP are derived when the SIC orders turn out the contrary compared with Scenario I. The diversity gains for the GF and GB users are also evaluated. Analytical results illustrate that the diversity orders are determined by the SIC orders that: 1) the value equals one for near users and 2) zero for far users.

- Simulation results demonstrate that the dynamic protocol outperforms the open-loop protocol on the outage performance.

3.1 Network model

The following section delves into the Semi-GF NOMA system, spatial distributions, protocol designs, randomly deployed user statistics, and signal models.

3.1.1 Spatial Distributions

The spatial distribution of this Semi-GF NOMA system is illustrated as Fig. 3.1. Considered that the BS is fixed at the center of the disc, this system model is simplified into two types of spatial distributions. 1) In *Scenario I*, GB users (denoted as GB_j, as the near users) randomly locate in a disc with the radium as R_1 m. Far GF users (denoted as GF_i) have the chance to use the channels occupied by the GB users[1], which are deployed in a ring with radius R_1 m and R_2 m (assuming $R_2 > R_1$). Near GF users are not allowed to use the dedicated channels to maintain the performance of GB users. 2) In *Scenario II*, the GB users are far users deployed in the ring with radius R_1 m and R_2 m. Only near GF users distributed in the disc with radium R_1 m have chance to join the occupied channels.[2] Based on the latency tolerance of GB users, these two scenarios meet the requirements of

[1]Among the far GF users, only the ones that meet Semi-GF protocols join the occupied channels.

[2]The ring model is a simplified model to divide users into two categories, near and far users. Delay-sensitive and delay-tolerant GB users will be treated as different scenarios.

two types of GB users. In scenario I for the delay-sensitive GB users, GB users avoid doing SIC procedure to reduce the latency of GB users. Thus, near GB users and far GF users will be chosen as NOMA clusters, thereby GB users acquire low latency. In scenario II for the delay-tolerant GB users, GB users are with SIC procedures to further reduce the latency of GF users. Hence, far GB users and near GF users are selected into the same resource blocks.

On random deployment, the location distributions of the GF and GB users are modeled as two HPPPs Φ_{GF} and Φ_{GB} with densities $\lambda_{\Phi_{GF}}$ and $\lambda_{\Phi_{GB}}$, respectively. Thus, the number of the GF and GB users obey the Poisson distribution, which is expressed as $\Pr(N_G = k) = \left(\mu_G^k/k!\right)\exp(-\mu_G)$, where $G \in \{GF, GB\}$, μ_G denotes the mean measures for the GF and GB users, including $\mu_G = \pi R_1^2 \lambda_{\Phi_G}$ for the near users and $\mu_G = \pi\left(R_2^2 - R_1^2\right)\lambda_{\Phi_G}$ for the far users. Additionally, define the distances from the BS to the GF users and the GB users as $d_{GF,i}$ and $d_{GB,j}$, respectively. Hence, the PDF of distances can be derived as $f_{d_{G,k}^{near}}(x) = 2x \Big/ R_1^2$ and $f_{d_{G,k}^{far}}(x) = 2x \Big/ (R_2^2 - R_1^2)$, where $k \in \{i, j\}$ representing for GF or GB users.

3.1.2 Protocol Designs

Note that this chapter focuses on Semi-GF transmission enabling GB and GF users sharing the same resource blocks. The protocol designs are focusing on the Semi-GF transmission instead of GF transmission sorely. Fig. 3.2 compares the handshakes among the traditional GB and GF transmission schemes and two Semi-GF protocols. Several assumptions exploited for the Semi-GF protocol designs are listed in the following:

- The channel state information (CSI) of the connected GB users is known by BSs. Since in Semi-GF scenarios, the GB users have been connected into the channels. Hence, CSI is obtained from the handshakes between BSs and GB users. It is also considered that the GB users' CSI can be broadcasted to all GF users with no errors to simplify this model.

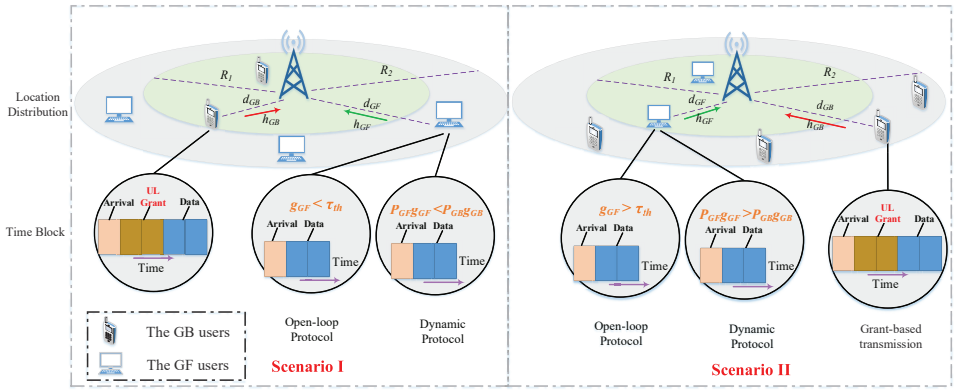

Figure 3.1: An illustration of uplink NOMA networks for conventional GB transmission, the open-loop protocol, and the dynamic protocol. Parameters are defined: R_1 and R_2 are the radii of the discs, d_{GB} and d_{GF} are the distance between the BS to the GB user or the GF user, h_{GB} and h_{GF} are the small-scale fading for the GB and GF channel, g_{GB} and g_{GF} are the channel effect including small-scale fading and path loss for the GB and GF channel, P_{GB} and P_{GF} are the transmit power for the GB and GF user, and τ_{th} is the threshold for the open-loop protocol.

- All GF users know their own CSI before data transmission begins. Since the GB users' CSI should be broadcasted prior to data transmission, GF users obtain their CSI via the downlink broadcasting.
- Different power levels are allocated to GF users. Thus, the GF users can be decoded during the collision situations by power-domain NOMA techniques.

Thus, detailed description of traditional GF, GB and Semi-GF transmission schemes are presented in the following.

3.1.2.1 The Conventional GB and GF Transmissions

The process of conventional GB transmission scheme is indicated as follows. 1) Synchronization is achieved by two handshakes, which transmit the primary synchronization signal and secondary synchronization signal to obtain the cell identity and frame timing. 2) The random access preambles, such as Zadoff-Chu code, are uploaded by GB users to identify the occupied chan-

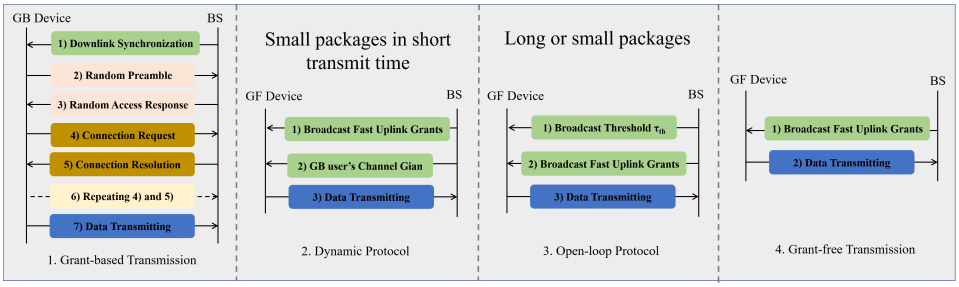

Figure 3.2: Handshakes for conventional GB transmission, conventional GF transmission, the open-loop protocol, and the dynamic protocol.

nels. If no collision scenarios, the GB user occupies a certain channel and send connection request. Otherwise, users would experience a contention access period to solve the collision, such as randomly waiting for a time period and retrying the channels. 3) After experienced a contention access period with at least a pair of handshakes and obtaining BS's permission, data transmissions begin. Based on the GB transmission scheme, uplink grants can reduce the collision situations, whereas it culminates long latency.

As for the GF transmission, BSs broadcast the fast uplink grants once used for the entire cell, which contains channel messages and other data that GF users need. After that, all the GF users would transmit messages at any time on their own initiative. Hence, latency is highly reduced, while users face high collision probability.

3.1.2.2 Open Loop Protocol

Compared to the conventional GF transmission scheme, fewer collisions and higher spectrum efficiency is required. Thus, Semi-GF NOMA networks are considered where GB and GF users share the same spectrum resources. Denote the combined channel gains of GF users as $g_{GF,i} = |h_{GF,i}|^2 (d_{GF,i})^{-\alpha}$, where $|h_{GF,i}|^2$ is small-scale fading, $(d_{GF.i})^{-\alpha}$ is path loss with distance $d_{GF,i}$ and path loss exponent α, and i is the number of GF users. Based on [124, 125], the design of the open-loop protocol is described as several steps. 1) The fast uplink grants and the channel quality threshold τ_{th} are

broadcasted after a GB user occupies a channel. Denote the transmit power of GF and GB users as P_{GF} and P_{GB}. The channel quality threshold of the open-loop protocol is $\tau_{th} = \mathbb{E}\left[P_{GB}P_{GF}^{-1}|h_{GB,j}|^2(d_{GB,j})^{-\alpha}\right]$, where $\mathbb{E}[\cdot]$ is the mean value, $|h_{GB,j}|^2$ is the small-scale fading of GB users, $d_{GB,j}$ is the distance of the GB users. 2) Compare the channel gains of the GF users and τ_{th}. 3) Select GF users into the channels occupied by the GB users. For far GB users, the condition of selecting GF users is $g_{GF,i} > \tau_{th}$; For near GB users, the condition is $g_{GF,i} < \tau_{th}$.

3.1.2.3 The Dynamic Protocol

A dynamic protocol is proposed to define more accurate values of channel quality thresholds in stochastic geometry models compared to the open-loop protocol. Define the combined channel gain of the GB users as $g_{GB,j} = |h_{GB,j}|^2(d_{GB.j})^{-\alpha}$. Compared to the open-loop protocol, the key difference of the dynamic protocol is that the BS sends instantaneous channel quality thresholds, denoted as $P_{GB}g_{GB,j}$, instead of a fixed average threshold. For far GB users, the constraint of selecting GF users is $P_{GF}g_{GF,i} > P_{GB}g_{GB,j}$, while the constraint for near GB users is $P_{GF}g_{GF,i} < P_{GB}g_{GB,j}$. Other steps are the same as the open-loop protocol. The practical scenario of the dynamic protocol is that GF users send small packets within a short transmit time, thereby the small-scale fading can be considered as a fixed value. Thus, the instantaneous CSI is exploited as the threshold. Hence, the selection of the dynamic protocol is more accurate than the open-loop protocol.

3.1.2.4 Comparison Between Signalling Overhead and Latency

Both conventional GF and Semi-GF transmission schemes have lower signalling overhead compared to traditional GB transmission, as the time-consuming handshakes have been significantly reduced. Although Semi-GF transmission schemes have a larger signalling overhead compared to GF transmission schemes due to the transmission of channel quality threshold-

s, they still outperform GB transmission. In terms of signalling overhead rank, it is predicted that latency will be ranked in descending order as GB transmission, Semi-GF transmission, and GF transmission.

3.1.3 Signal Model

The channels of both GF and GB users are modeled as Rayleigh fading channels. Noted that the Rayleigh fading is used for the case where the transmitted signal encounters multiple scattering objects, which means that there is no dominant line-of-sight path between the transmitter and receiver. Hence, this model could mimic the practical scenarios with scattering such as urban environments. SNR expressions are expressed in two scenarios based on SIC orders. In this treatise, a scenario is considered in which a GF user accesses a channel that is already occupied by a GB user. The derivations can be extended to scenarios where more GF users are allocated in the same channel. It is worth noting that pass loss has a more stable and dominant effect than instantaneous small-scale fading [126]. As a result, users who are closer to the channel always have better channel gains with the first SIC order than those who are farther away.

3.1.3.1 Scenario I

The GB users are deployed within the disc as near users while the GF users are located in the ring as far users. Thus, the signals of GB users are decoded first. With the fixed access thresholds τ_{th} for the open-loop protocol or flexible thresholds $P_{GB}g_{GB,j}$ for the dynamic protocol, the SNR of GB users can be expressed as:

$$\gamma_{GB,j}^{I} = \frac{P_{GB}|h_{GB,j}|^2 \left(d_{GB,j}\right)^{-\alpha}}{P_{GF}|h_{GF,i}|^2 \left(d_{GF,i}\right)^{-\alpha} + \sigma^2}, \tag{3.1}$$

where P_{GB} and P_{GF} are the transmit powers of GB and GF devices, $h_{GF,i}$ and $h_{GB,j}$ are the channel gains for i^{th} GF and j^{th} GB users, respectively, σ^2 means variance of AWGN, and α is the path loss exponent.

After the SIC process, the SNR of GF users can be written as:

$$\gamma_{GF,i}^{I} = \frac{P_{GF}|h_{GF,i}|^2(d_{GF,i})^{-\alpha}}{\sigma^2}. \tag{3.2}$$

3.1.3.2 Scenario II

In Scenario II, the GF users are located in the disc as near users with first decoding orders. The SNR expressions of GF and GB users are derived respectively as:

$$\gamma_{GF,i}^{II} = \frac{P_{GF}|h_{GF,i}|^2(d_{GF,i})^{-\alpha}}{P_{GB}|h_{GB,j}|^2(d_{GB,j})^{-\alpha} + \sigma^2} \tag{3.3}$$

and

$$\gamma_{GB,j}^{II} = \frac{P_{GB}|h_{GB,j}|^2(d_{GB,j})^{-\alpha}}{\sigma^2}. \tag{3.4}$$

Additionally, the following notation includes the transmit SNR of users as $\rho_{GB} = P_{GB}/\sigma^2$ and $\rho_{GF} = P_{GF}/\sigma^2$, the combined channel gains as $g_{GF,i} = |h_{GF,i}|^2(d_{GF,i})^{-\alpha}$ for the i^{th} GF user and $g_{GB,j} = |h_{GB,j}|^2(d_{GB,j})^{-\alpha}$ for the j^{th} GB user used.

3.1.4 New Statistics

The channel gains with small-scale and large-scale fading are denoted as $g_{G,k}$ with $G \in \{GF, GB\}$ and $k \in \{i, j\}$. **Lemma 3** presents derivations of the PDFs of $g_{G,k}$. **Corollary 1** and **Corollary 2** derive two types of expressions for CDFs of $g_{G,k}$.

Lemma 3. Conditioned on $G \in \{GF, GB\}$ and $k \in \{i, j\}$ to express a general scenario for the j^{th} GB and the i^{th} GF users, the combined channel gain including large-scale and small-scale fadings is denoted as $g_{G,k}$, whose PDFs for both near and far users can be derived as:

$$f_{g_{G,k}}^{near}(x) = \frac{b_{1,1}^{G}}{x^{b_3}}\gamma\left(b_3, b_{2,1}^{G}x\right) \tag{3.5}$$

and

$$f_{g_{G,k}}^{far}(x) = \frac{b_{1,2}^{G}}{x^{b_3}}\left[\gamma\left(b_3, b_{2,2}^{G}x\right) - \gamma\left(b_3, b_{2,1}^{G}x\right)\right], \tag{3.6}$$

where $\gamma(\cdot,\cdot)$ means lower incomplete gamma function, λ_G is the mean of Rayleigh distribution with $G = GB$ for the GB users and $G = GF$ for the GF users, $b_{1,1}^{G} = 2(\lambda_G)^{\frac{2}{\alpha}}\Big/\alpha R_1^2$, $b_{1,2}^{G} = 2(\lambda_G)^{\frac{2}{\alpha}}\Big/\left[\alpha\left(R_2^2 - R_1^2\right)\right]$, $b_{2,1}^{G} = R_1^{\alpha}/\lambda_G$, $b_{2,2}^{G} = R_2^{\alpha}/\lambda_G$, and $b_3 = \frac{2}{\alpha} + 1$.

Proof. Near users and far users are deployed into the disc or the ring. Based on the PDFs of $d_{G,k}$, the PDFs of $d_{G,k}^{\alpha}$ can be derived as $f_{\left(d_{GB,i}^{near}\right)^{\alpha}}(x) = 2x^{\frac{2}{\alpha}-1}\Big/\left(\alpha R_1^2\right)$ and $f_{\left(d_{GB,i}^{far}\right)^{\alpha}}(x) = 2x^{\frac{2}{\alpha}-1}\Big/\left[\alpha\left(R_2^2 - R_1^2\right)\right]$. Under Rayleigh fading channels, the PDFs of $g_{G,k}$ can be derived as:

$$f_{g_{G,k}}^{near}(x) = \int_0^{R_1^{\alpha}} y f_{|h_{G,k}|^2}(xy)\, f_{\left(d_{G,k}^{near}\right)^{\alpha}}(y)\, dy \tag{3.7}$$

and

$$f_{g_{G,k}}^{far}(x) = \int_{R_1^{\alpha}}^{R_2^{\alpha}} y f_{|h_{G,k}|^2}(xy)\, f_{\left(d_{G,k}^{far}\right)^{\alpha}}(y)\, dy, \tag{3.8}$$

which can be derived by substituting the PDFs of the Exponential distribution and $d_{G,k}^{\alpha}$ to obtain (3.5) and (3.6). □

Corollary 1. Based on the PDF of $g_{G,k}$ in **Lemma 3**, expressions of the the CDFs of $g_{G,k}$ can be derived by utilizing hypergeometric functions as:

$$F_{g_{G,k}}^{near}(x) = \frac{b_{1,1}^{G}\left(b_{2,1}^{G}\right)^{b_3}}{b_3} x_2F_2\left(b_3, 1; b_3+1, 2; -b_{2,1}^{G}x\right) \tag{3.9}$$

and

$$\begin{aligned} F_{g_{G,k}}^{far}(x) =& \frac{b_{1,2}^{G}\left(b_{2,2}^{G}\right)^{b_3}}{b_3} x_2F_2\left(b_3, 1; b_3+1, 2; -b_{2,2}^{G}x\right) \\ &- \frac{b_{1,2}^{G}\left(b_{2,1}^{G}\right)^{b_3}}{b_3} x_2F_2\left(b_3, 1; b_3+1, 2; -b_{2,1}^{G}x\right), \end{aligned} \tag{3.10}$$

where ${}_pF_q(\cdot)$ is the hypergeometric function.

Proof. In terms of the expressions of Eq.[2.10.2.2] in [127], the CDFs can be derived via the PDFs in **Lemma 3**. □

Corollary 2. Invoked by the lower incomplete gamma functions and the CDF of the Exponential distribution, the CDF expressions of $g_{G,k}$ can be equivalently derived as:

$$F_{g_{G,k}}^{near}(x) = 1 - \frac{2}{\alpha R_1^2}\left(\frac{\lambda_G}{x}\right)^{b_3-1} \gamma\left(b_3 - 1, b_{2,1}^G x\right) \tag{3.11}$$

and

$$F_{g_{G,k}}^{far}(x) = 1 - \frac{2}{\alpha\left(R_2^2 - R_1^2\right)}\left(\frac{\lambda_G}{x}\right)^{b_3-1} \times \left[\gamma\left(b_3 - 1, b_{2,2}^G x\right) - \gamma\left(b_3 - 1, b_{2,1}^G x\right)\right]. \tag{3.12}$$

Proof. The CDFs of $g_{G,k}$ can be expressed as $F_{g_{G,k}}^{near}(x) = \Pr\left\{|h_{G,k}|^2 < \left(d_{G,k}^{near}\right)^{\alpha} x\right\}$ for the near users and $F_{g_{G,k}}^{far}(x) = \Pr\left\{|h_{G,k}|^2 < \left(d_{G,k}^{far}\right)^{\alpha} x\right\}$ for the far users. Thus, the CDF expressions can be derived as (3.11) and (3.12). □

3.2 Outage Performance in Scenario I

Recall that the Scenario I is for GB users that are delay-sensitive users with messages such as voice calls or emergency health-care status. As the delay-sensitive GB users should avoid the SIC procedure to achieve low latency, GF users with lower channel gains compared to the connected GB user are selected into the occupied channels. This section expresses the exact expressions of OP via **Theorem 1** to **Theorem 4**, followed by several corollaries to derive the closed-form expressions.

3.2.1 Analytical OP Under the Dynamic Protocol in Scenario I

The channel capacities of the GB and GF users are given by $C_{GB_j} = \log_2\left(1+\gamma^I_{GB,j}\right) = \log_2\left(1+\frac{\rho_{GB}g_{GB,j}}{\rho_{GF}g_{GF,i}+1}\right)$ and $C_{GF_j} = \log_2\left(1+\gamma^I_{GF,i}\right) = \log_2\left(1+\rho_{GF}g_{GF,i}\right)$. Conditioned on $P_{GF}g_{GF,i} < P_{GB}g_{GB,j}$ in Scenario I, the OP expressions of the GF and the GB users are expressed as:

$$\mathbb{P}^{GB,I}_{out,p_2} = \Pr\left\{\frac{\rho_{GB}g_{GB,j}}{\rho_{GF}g_{GF,i}+1} < \gamma^{GB}_{th}, g_{GF,i} < \frac{P_{GB}}{P_{GF}}g_{GB,j}\right\} \tag{3.13}$$

and

$$\mathbb{P}^{GF,I}_{out,p_2} = \mathbb{P}^{GB,I}_{out,p_2} + \underbrace{\Pr\left\{\frac{\rho_{GB}g_{GB,j}}{\rho_{GF}g_{GF,i}+1} > \gamma^{GB}_{th},\ g_{GF,i} < \frac{\gamma^{GF}_{th}}{\rho_{GF}}, g_{GF,i} < \frac{P_{GB}g_{GB,j}}{P_{GF}}\right\}}_{Q_1}. \tag{3.14}$$

Theorem 1. With the constraint of $P_{GF}g_{GF,i} < P_{GB}g_{GB,j}$ in Scenario I, the OP of the GB users varies into two situations with various derivations: *a)* the received power of the signal is higher than interference and noise, denoted as $\gamma^{GB}_{th} > 1$ and *b)* the signal strength is lower than interference and noise, denoted as $\gamma^{GB}_{th} \leq 1$. Based on two situations, the OP of the GB users can be derived as:

$$\begin{aligned}\mathbb{P}^{GB,I}_{out,p_2} = &\int_0^{\infty} F^{near}_{g_{GB,j}}\left(\frac{\gamma^{GB}_{th}\rho_{GF}x+\gamma^{GB}_{th}}{\rho_{GB}}\right) f^{far}_{g_{GF,i}}(x)\,dx \\ &- \int_0^{\infty} F^{near}_{g_{GB,j}}\left(\frac{\rho_{GF}}{\rho_{GB}}x\right) f^{far}_{g_{GF,i}}(x)\,dx, \quad \left(\gamma^{GB}_{th} > 1\right)\end{aligned} \tag{3.15}$$

and

$$\begin{aligned}\mathbb{P}^{GB,I}_{out,p_2} = &\int_0^{\sigma_1} F^{near}_{g_{GB,j}}\left(\frac{\gamma^{GB}_{th}\rho_{GF}x+\gamma^{GB}_{th}}{\rho_{GB}}\right) f^{far}_{g_{GF,i}}(x)\,dx \\ &- \int_0^{\sigma_1} F^{near}_{g_{GB,j}}\left(\frac{\rho_{GF}}{\rho_{GB}}x\right) f^{far}_{g_{GF,i}}(x)\,dx, \quad \left(\gamma^{GB}_{th} \leq 1\right),\end{aligned} \tag{3.16}$$

where $\sigma_1 = \frac{\gamma_{th}^{GB}}{\rho_{GF}\left(1-\gamma_{th}^{GB}\right)}$. **Corollary 3** and **Corollary 4** can express the closed-form expressions in the two situations.

Corollary 3. Assume that the GF users experience satisfying channel conditions with high transmit SNR ($\rho_{GF} \gg 1$) since the transmit power is always higher than the noise strength. Conditioned on $\gamma_{th}^{GB} > 1$, the exact closed-from expression of the OP for GB users can be derived as:

$$\begin{aligned}\mathbb{P}_{out,p_2}^{GB,I} =& C_1\left[U\left(\frac{b_{2,1}^{GB}\rho_{GF}}{\rho_{GB}}, b_{2,2}^{GF}\right) - U\left(\frac{b_{2,1}^{GB}\rho_{GF}}{\rho_{GB}}, b_{2,1}^{GF}\right)\right] \\ &- C_1\sum_{n=0}^{\infty}\sum_{t=0}^{n}\binom{n}{r}\left(\frac{-\gamma_{th}^{GB}\rho_{GF}}{\rho_{GB}}\right)^n \frac{\left(b_{2,1}^{GB}\right)^{\frac{2}{\alpha}+n}}{n!\left(\frac{2}{\alpha}+n\right)} \\ &\times \frac{\Gamma\left(n-t-\frac{2}{\alpha}\right)\left[\left(b_{2,1}^{GF}\right)^{\frac{2}{\alpha}+t-n} - \left(b_{2,2}^{GF}\right)^{\frac{2}{\alpha}+t-n}\right]}{\rho_{GF}^t\left(n-t-\frac{2}{\alpha}\right)},\end{aligned} \tag{3.17}$$

where $C_1 = 2\lambda_{GB}^{\frac{2}{\alpha}} b_{1,2}^{GF} \Big/ \left(\alpha R_1^2\right)$, $\binom{n}{r} = n!/[t!\,(n-t)!]$, $\theta_2 = \frac{\Gamma(2-b_3)\Gamma(b_3-1)}{2(1-b_3)t^{2(1-b_3)}}$, $U\left(a,t\right) = {}_3F_2\left(1, b_3, 2-b_3; b_3+1, 3-b_3; \frac{-t}{a}\right)\theta_1 - \theta_2$, $\theta_1 = \frac{-t^{b_3}\Gamma(1)}{b_3(2-b_3)a^{2-b_3}}$, and $\Gamma(\cdot)$ is gamma function.

Proof. Substituting (3.6) and (3.11) into the OP expressions, $\mathbb{P}_{out,p_2}^{GB,I}$ can be rewritten as:

$$\begin{aligned}\mathbb{P}_{out,p_2}^{GB,I} =& \underbrace{\int_0^{\infty} \frac{2b_{1,2}^{GF}\gamma\left(b_3-1, b_{2,1}^{GB}x\right)}{\alpha R_1^2 x^{b_3}\left(\frac{\lambda_{GB}}{x}\right)^{1-b_3}}\left[\gamma\left(b_3, b_{2,2}^{GF}x\right) - \gamma\left(b_3, b_{2,1}^{GF}x\right)\right]dx}_{I_1} \\ &- \underbrace{\int_0^{\infty} \frac{2}{\alpha R_1^2}\left(\frac{\rho_{GB}\lambda_{GB}}{\gamma_{th}^{GB}\rho_{GF}x + \gamma_{th}^{GB}}\right)^{b_3-1}\gamma\left[b_3-1, \frac{\left(\rho_{GF}x+1\right)\gamma_{th}^{GB}b_{2,1}^{GB}}{\rho_{GB}}\right]}_{I_2} \\ &\times \underbrace{\frac{b_{1,2}^{GF}}{x^{b_3}}\left[\gamma\left(b_3, b_{2,2}^{GF}x\right) - \gamma\left(b_3, b_{2,1}^{GF}x\right)\right]dx}_{I_2}.\end{aligned} \tag{3.18}$$

Based on Eq.[2.10.6.2] in [127] to derive I_1, the expressions can be sim-

plified as:

$$I_1 = C_1 \int_0^{\infty} x^{2(1-b_3)-1} \gamma\left(b_3 - 1, \frac{b_{2,1}^{GB}\rho_{GF}}{\rho_{GB}} x\right) \times \left[\gamma\left(b_3, b_{2,2}^{GF} x\right) - \gamma\left(b_3, b_{2,1}^{GF} x\right)\right] dx. \tag{3.19}$$

Based on (3.38), binomial expansions, and Eq. [2.10.2.1] in [127], I_2 is derived as:

$$I_2 = C_1 \sum_{n=0}^{\infty}\sum_{t=0}^{n} \binom{n}{r} \left(\frac{-\gamma_{th}^{GB}\rho_{GF}}{\rho_{GB}}\right)^n \frac{\left(b_{2,1}^{GB}\right)^{\frac{2}{\alpha}+n}}{n!\left(\frac{2}{\alpha}+n\right)} \times \frac{\Gamma\left(n-t-\frac{2}{\alpha}\right)\left[\left(b_{2,1}^{GF}\right)^{\frac{2}{\alpha}+t-n} - \left(b_{2,2}^{GF}\right)^{\frac{2}{\alpha}+t-n}\right]}{\rho_{GF}^{t}\left(n-t-\frac{2}{\alpha}\right)}. \tag{3.20}$$

Substituting (3.19) and (3.20) into (3.18), the corollary is proved. □

Corollary 4. Conditioned on $\omega_s = \frac{\pi}{N}$ and $x_s = \cos\left(\frac{2s-1}{2S}\pi\right)$, the Chebyshev-Gauss quadrature as a numerical analytical method with limited upper and lower limits is approximated as $\int_a^b f(x)dx = \sum_{s=1}^{S} \frac{(b-a)\omega_s}{2[1-t_s^2(x_s,a,b)]^{-\frac{1}{2}}} f\left[t_s(x_s,a,b)\right]$, where $t_s(x_s,a,b) = (x_s+1)\frac{b-a}{2} + a$. When $\gamma_{th}^{GB} \leq 1$ as the second situation, the OP expressions of the GB users can be derived as:

$$\mathbb{P}_{out,p_2}^{GB,I} = \underbrace{\int_0^{\sigma_1} F_{g_{GB,j}}^{near}\left(\frac{\gamma_{th}^{GB}\rho_{GF}x + \gamma_{th}^{GB}}{\rho_{GB}}\right) f_{g_{GF,i}}^{far}(x)\, dx}_{I_3} - \underbrace{\int_0^{\sigma_1} F_{g_{GB,j}}^{near}\left(\frac{\rho_{GF}}{\rho_{GB}}x\right) f_{g_{GF,i}}^{far}(x)\, dx}_{I_4}, \tag{3.21}$$

where closed-from expressions of I_3 and I_4 can be derived as:

$$I_3 = F_{g_{GF,i}}^{far}(\sigma_1) - \sum_{s=1}^{S} \gamma\left[\frac{2}{\alpha}, \frac{\gamma_{th}^{GB} b_{2,1}^{GB}\left(\rho_{GF}\iota_{s,1}+1\right)}{\rho_{GB}}\right] \times \Lambda_1(\sigma_1, \iota_{s,1})\left[\gamma\left(b_3, b_{2,2}^{GF}\iota_{s,1}\right) - \gamma\left(b_3, b_{2,1}^{GF}\iota_{s,1}\right)\right] \tag{3.22}$$

and

$$I_4 = F_{g_{GF,i}}^{far}(\sigma_1) - \sum_{s=1}^{S} \Lambda_2(\sigma_1, \iota_{s,1}) \gamma\left(b_3 - 1, b_{2,1}^{G} \iota_{s,1}\right) \times \left[\gamma\left(b_3, b_{2,2}^{GF} \iota_{s,1}\right) - \gamma\left(b_3, b_{2,1}^{GF} \iota_{s,1}\right)\right], \tag{3.23}$$

where $\Lambda_2(a,x) = \frac{C_1}{2} a \omega_s x^{1-2b_3} \left(1-x^2\right)^{\frac{1}{2}} \rho_{GB}^{b_3-1} \rho_{GF}^{1-b_3}$, $\Lambda_1(a,x) = \frac{C_1}{2} a \omega_s x^{-b_3} \times \left(1-x^2\right)^{\frac{1}{2}} \rho_{GB}^{b_3-1} \left[\gamma_{th}^{GB}\left(\rho_{GF} x + 1\right)\right]^{\frac{-2}{\alpha}}$, and $\iota_{s,1} = t_s(x_s, 0, \sigma_1)$.

Proof. Based on (3.6), (3.9), (3.11), and the Chabyshev-gauss quadrature, the final expression is derived. Similar derivations are ignored due to limited contents. □

Theorem 2. Note that $\mathbb{P}_{out,p_2}^{GB,I}$ is given as **Theorem 1** and Q_1 is given in (3.14). The integration Q_1 can be derived by different derivations under two situations: *a)* $\gamma_{th}^{GB} > \gamma_{th}^{GF}/\left(1+\gamma_{th}^{GF}\right)$ and *b)* $\gamma_{th}^{GB} \leq \gamma_{th}^{GF}/\left(1+\gamma_{th}^{GF}\right)$. Thus, The OP of the GF users under the dynamic protocol in Scenario I can be expressed as:

$$\mathbb{P}_{out,p_2}^{GF,I} = Q_1 + \mathbb{P}_{out,p_2}^{GB,I}, \tag{3.24}$$

where closed-from expressions are derived by substituting $\mathbb{P}_{out,p_2}^{GB,I}$ in **Theorem 1** and Q_1 in the following corollaries as **Corollary 5**, **Corollary 6**, and **Corollary 7**.

Corollary 5. Note that the first situation as $\gamma_{th}^{GB} > \gamma_{th}^{GF}/\left(1+\gamma_{th}^{GF}\right)$ is considered. For the first case, with the aid of the lower incomplete gamma functions and binomial expansions, the closed-from expressions of Q_1 can be derived as:

$$Q_1 = C_1 \sum_{n=0}^{\infty} \sum_{t=0}^{n} \binom{n}{r} \left(\frac{-\gamma_{th}^{GB} \rho_{GF}}{\rho_{GB}}\right)^n \frac{\left(b_{2,1}^{GB}\right)^{\frac{2}{\alpha}+n}}{n!\left(\frac{2}{\alpha}+n\right)\rho_{GF}^{t}} \times \left[M\left(\sigma_2, q, b_3, b_{2,2}^{GF}\right) - M\left(\sigma_2, q, b_3, b_{2,1}^{GF}\right)\right], \tag{3.25}$$

where $\sigma_2 = \gamma_{th}^{GF}/\rho_{GF}$, $q = n - t - \frac{2}{\alpha}$ and $M(t, \alpha, \beta, \delta)$ is defined as:

$$\begin{aligned} M(t, \alpha, \beta, \delta) &= \int_0^t x^{\alpha-1} \gamma(\beta, \delta x)\, dx \\ &= \frac{t^{\alpha+\beta}}{\delta^{-\beta}\beta} B(1, \alpha+\beta)\, {}_2F_2(\beta, \alpha+\beta; \beta+1, \alpha+\beta+1; -t\delta). \end{aligned} \tag{3.26}$$

Proof. Proved by utilizing $\gamma(a, b) = \sum_{n=0}^{\infty} \frac{(-1)^n b^{a+n}}{n!(a+n)}$, binary series expansions, and Eq. [2.10.2.2] in [127]. □

Corollary 6. Note that $\gamma_{th}^{GB} > \gamma_{th}^{GF}/\left(1 + \gamma_{th}^{GF}\right)$ is considered. The Chebyshev-Gauss quadrature is invoked to calculate the closed-form expressions of the OP for GF users, thereby the approximated expressions of Q_1 can be presented as:

$$\begin{aligned} \mathrm{Q}_1 = \sum_{s=1}^{S} \Lambda_1(\sigma_2, \iota_{s,2}) \gamma \left[b_3 - 1, \frac{b_{2,1}^{GB} \gamma_{th}^{GB} (\rho_{GF} \iota_{s,2} + 1)}{\rho_{GB}} \right] \\ \times \left[\gamma\left(b_3, b_{2,2}^{GF} \iota_{s,2}\right) - \gamma\left(b_3, b_{2,1}^{GF} \iota_{s,2}\right) \right], \end{aligned} \tag{3.27}$$

where $\iota_{s,2} = t_s(x_s, 0, \sigma_2)$.

Corollary 7. Conditioned on the second situation, denoted as $\gamma_{th}^{GB} \leq \gamma_{th}^{GF}/\left(1 + \gamma_{th}^{GF}\right)$, the closed-from expressions of Q_1 can be derived as:

$$\begin{aligned} Q_1 = \sum_{s=1}^{S} \gamma \left(b_3 - 1, b_{2,1}^{GB} \frac{\gamma_{th}^{GB} \rho_{GF} \iota_{s,1} + \gamma_{th}^{GB}}{\rho_{GB}} \right) \\ \times \Lambda_1(\sigma_1, \iota_{s,1}) \left[\gamma\left(b_3, b_{2,2}^{GF} \iota_{s,1}\right) - \gamma\left(b_3, b_{2,1}^{GF} \iota_{s,1}\right) \right] \\ + \Lambda_2[(\sigma_2 - \sigma_1), \iota_{s,12}] \gamma \left(b_3 - 1, \frac{b_{2,1}^{GB} \rho_{GF}}{\rho_{GB}} \iota_{s,12} \right) \\ \times \left[\gamma\left(b_3, b_{2,2}^{GF} \iota_{s,12}\right) - \gamma\left(b_3, b_{2,1}^{GF} \iota_{s,12}\right) \right], \end{aligned} \tag{3.28}$$

where $\iota_{s,12} = t_s(x_s, \sigma_1, \sigma_2)$.

3.2.2 Analytical OP Under the Open-loop Protocol in Scenario I

Instead of exploiting the instantaneous CSI in the dynamic protocol, the open-loop protocol broadcasts an average channel quality threshold. With the selection protocol as $g_{GF,i} < \tau_{th}$, the OP of GB and GF users can be expressed as:

$$P_{out,p_1}^{GB,I} = \Pr\left\{\frac{\rho_{GB} g_{GB,j}}{\rho_{GF} g_{GF,i} + 1} < \gamma_{th}^{GB}, g_{GF,i} < \tau_{th}\right\} \tag{3.29}$$

and

$$\mathbb{P}_{out,p_1}^{GF,I} = \mathbb{P}_{out,p_1}^{GB,I} + \underbrace{\Pr\left\{\frac{\rho_{GB} g_{GB,j}}{\rho_{GF} g_{GF,i} + 1} > \gamma_{th}^{GB}, g_{GF,i} < \min\left(\frac{\gamma_{th}^{GF}}{\rho_{GF}}, \tau_{th}\right)\right\}}_{Q_2}. \tag{3.30}$$

Theorem 3. Under the condition of $g_{GF} < \tau_{th}$, the OP expression for GB users can be expressed as:

$$P_{out,p_1}^{GB,I} = \int_0^{\tau_{th}} F_{g_{GB,j}}^{near}\left(\frac{\gamma_{th}^{GB}\rho_{GF}x + \gamma_{th}^{GB}}{\rho_{GB}}\right) f_{g_{GF,i}}^{far}(x)\, dx, \tag{3.31}$$

where the closed-form expressions are derived by **Corollary 8** and **Corollary 9**.

Corollary 8. Based on the two types of the CDF expressions of $g_{G,k}$, two types of closed-form expressions by the Chebyshev-Gauss quadrature can be derived as:

$$\begin{aligned}\mathbb{P}_{out,p_1}^{GB,I} =& \sum_{s=1}^{S} \frac{\tau_{th} b_{1,1}^{GB} b_{1,2}^{GF} \left(b_{2,1}^{GB}\right)^{b_3} \omega_s}{2(1 - t_s^2(x_s, 0, \tau_{th}))^{-\frac{1}{2}} b_3 x^{b_3 - 1}} \\ & \times {}_2F_2\left[b_3, 1; b_3 + 1, 2; b_{2,1}^{GB}\gamma_{th}^{GB}\left(\frac{\rho_{GF} t_s(x_s, 0, \tau_{th}) + 1}{-\rho_{GB}}\right)\right] \\ & \times \left\{\gamma\left[b_3, b_{2,2}^{GF} t_s(x_s, 0, \tau_{th})\right] - \gamma\left[b_3, b_{2,1}^{GF} t_s(x_s, 0, \tau_{th})\right]\right\}\end{aligned} \tag{3.32}$$

and

$$\begin{aligned}\mathbb{P}_{out,p_1}^{GB,I} =& \sum_{s=1}^{S} \frac{\tau_{th}\omega_s \left[1-t_s^2\left(x_s,0,\tau_{th}\right)\right]^{\frac{1}{2}} b_{1,2}^{GF}}{2[t_s\left(x_s,0,\tau_{th}\right)]^{b_3}} \\ &\times \left\{\gamma\left[b_3, b_{2,2}^{GF} t_s\left(x_s,0,\tau_{th}\right)\right] - \gamma\left[b_3, b_{2,1}^{GF} t_s\left(x_s,0,\tau_{th}\right)\right]\right\} \\ &\times \left[1-\Xi_s \gamma\left(\frac{2}{\alpha}, \frac{\left(\rho_{GF} t_s\left(x_s,0,\tau_{th}\right)+1\right)\gamma_{th}^{GB} R_1^{\alpha}}{\rho_{GB}\lambda_{GB}}\right)\right], \end{aligned} \tag{3.33}$$

where $\Xi_s = \frac{2}{\alpha R_1^2 \gamma_{th}^{GB}} \left(\frac{\rho_{GB}\lambda_{GB}}{\rho_{GF} t_s(x_s,0,\tau_{th})+1}\right)^{\frac{2}{\alpha}}$.

Proof. Substituting (3.6), (3.9) and (3.11) into (3.31), the derivations can be obtained by utilizing the Chebyshev-Gauss quadrature. □

Corollary 9. Assume that all the GF users fit the condition of selection, which means $g_{GF} \ll \tau_{th}$. Then, the approximated expressions of OP when $\tau_{th} \to \infty$ are derived as:

$$\begin{aligned}\mathbb{P}_{out,p_1}^{GB,I} =& F_{g_{GB,j}}^{near}\left(\tau_{th}\right) - \frac{2b_{1,2}^{GF}}{\alpha R_1^2}\left(\frac{\rho_{GB}\lambda_{GB}}{\gamma_{th}^{GB}\rho_{GF}}\right)^{\frac{2}{\alpha}} \\ &\times \left[U\left(\frac{\gamma_{th}^{GB}\rho_{GF}R_1^{\alpha}}{\rho_{GB}\lambda_{GB}}, b_{2,2}^{GF}\right) - U\left(\frac{\gamma_{th}^{GB}\rho_{GF}R_1^{\alpha}}{\rho_{GB}\lambda_{GB}}, b_{2,1}^{GF}\right)\right], \end{aligned} \tag{3.34}$$

where $U\left(a,t\right)$ is defined in **Corollary 3**.

Proof. Conditioned on $\tau_{th} \to \infty$ and based on (3.6) and (3.11), (3.31) can be derived by substituting Eq.[2.10.6.2] in [127]. □

Remark 1. *The condition ($\tau_{th} \to \infty$) means that the channel quality of the GB user is the best among itself and other GF users. The following step is to further simplify the OP in* ***Corollary 9*** *as $\mathbb{P}_{out,p_1}^{GB,I} = 1 - \mathrm{C}$, where* C *is constant. Thus, the equation reveals that the OP has a lower limit when all the GF users has been selected to join the occupied channel.*

Then, the outage performance of the GF users is investigated. Based on the **Theorem 4**, the exact and approximated closed-form expressions are derived in **Corollary 10** and **Corollary 11**.

Theorem 4. Note that the GF users are decoded at the last decoding orders in Scenario I. Thus, two outage situations are involved: *a)* the messages of the GB users cannot be detected so that the SIC procedure is not successful and *b)* the BS can detect the messages of the GB users but cannot detect those of the GF users. Based on **Theorem 3**, the first situation has been analyzed by deriving Q_2 as:

$$Q_2 = \int_0^{\min\left(\frac{\gamma_{th}^{GF}}{\rho_{GF}}, \tau_{th}\right)} \left[1 - F_{g_{GB,j}}^{near}\left(\frac{\gamma_{th}^{GB}\rho_{GF}x + \gamma_{th}^{GB}}{\rho_{GB}}\right)\right] f_{g_{GF,i}}^{far}(x)\, dx, \quad (3.35)$$

where **Corollary 10** and **Corollary 11** can provide two closed-from expressions. Thus, based on **Theorem 3** and **Theorem 4**, the final OP of GF users in Scenario I can be derived as $\mathbb{P}_{out,p_1}^{GF,I} = Q_2 + P_{out,p_1}^{GB,I}$.

Corollary 10. Based on the Chebyshev-Gauss quadrature, the closed-form expressions of Q_2 can be derived as:

$$\begin{aligned} Q_2 = &\sum_{s=1}^{S} \frac{\omega_s \min\left(\frac{\gamma_{th}^{GF}}{\rho_{GF}}, \tau_{th}\right) \left(\rho_{GB}\lambda_{GB}\right)^{b_3-1}}{\alpha R_1^2 (1-{\iota_{s,0}}^2)^{-\frac{1}{2}} \left(\gamma_{th}^{GB}\rho_{GF}x + \gamma_{th}^{GB}\right)^{b_3-1}} \\ &\times \frac{b_{1,2}^{GF}}{{\iota_{s,0}}^{b_3}} \gamma\left[b_3 - 1, \frac{b_{2,1}^{GB}\gamma_{th}^{GB}\left(\rho_{GF}\iota_{s,0} + 1\right)}{\rho_{GB}}\right] \\ &\times \left[\gamma\left(b_3, b_{2,2}^{GF}\iota_{s,0}\right) - \gamma\left(b_3, b_{2,1}^{GF}\iota_{s,0}\right)\right], \end{aligned} \quad (3.36)$$

where $\iota_{s,0}{=}t_s\left(x_s, 0, \sigma_0\right)$ and $\sigma_0 = \min\left(\frac{\gamma_{th}^{GF}}{\rho_{GF}}, \tau_{th}\right)$.

Proof. See **Corollary 8**. □

Corollary 11. Based on the expansions of lower incomplete gamma functions as $\gamma(a,b) = \sum_{n=0}^{\infty} \frac{(-1)^n b^{a+n}}{n!(a+n)}$, the closed-form expressions of Q_2 can be equally derived as:

$$\begin{aligned} Q_2 = &C_1 \sum_{n=0}^{\infty}\sum_{t=0}^{n} \binom{n}{r} \left(\frac{-\gamma_{th}^{GB}\rho_{GF}}{\rho_{GB}}\right)^n \frac{\left(b_{2,1}^{GB}\right)^{\frac{2}{\alpha}+n}}{n!\left(\frac{2}{\alpha}+n\right)\rho_{GF}^t} \\ &\times \left\{M\left[\sigma_0, q, b_3, b_{2,2}^{GF}\right] - M\left[\sigma_0, q, b_3, b_{2,1}^{GF}\right]\right\}. \end{aligned} \quad (3.37)$$

Proof. See **Corollary 5**. □

3.2.3 Asymptotic OP Under the Dynamic Protocol in Scenario I

Diversity orders as intuitive indicators present performance changing with variables such as transmit SNR $\rho_G = P_G/\sigma^2$ and $G \in \{GF, GB\}$. The asymptotic analysis follows the assumption with $\rho_{GB} \to \infty$ and a fixed ρ_{GF}. Based on the expansions of lower incomplete gamma functions, the asymptotic expressions are derived by remaining the first two items, denoted as:

$$\gamma(a,b) = \sum_{n=0}^{\infty} \frac{(-1)^n b^{a+n}}{n!\,(a+n)} = \frac{b^a}{a} - \frac{b^{a+1}}{a+1}. \tag{3.38}$$

In the following, the asymptotic OP expressions of the GB and the GF users under the dynamic protocol are derived as **Corollary 12** and **Corollary 13**.

Corollary 12. Based on **Theorem 1**, two situations as $\gamma_{th}^{GB} > 1$ and $\gamma_{th}^{GB} \leq 1$ are involved in this corollary. Under two situations, the expressions for the GB users can be derived in terms of asymptotic OP.

Conditioned on $\gamma_{th}^{GB} > 1$, the asymptotic OP can be derived as:

$$\begin{aligned}\mathbb{P}_{out,p_2}^{GB,I,\infty} =& C_1 \left(\frac{\rho_{GB}}{\rho_{GF}}\right)^{b_3-1} \left[U\left(\frac{b_{2,1}^{GB}\rho_{GF}}{\rho_{GB}}, b_{2,2}^{GF}\right)\right. \\ & \left. - U\left(\frac{b_{2,1}^{GB}\rho_{GF}}{\rho_{GB}}, b_{2,1}^{GF}\right)\right] - 1 + \mathbb{P}_{out,p_1}^{GB,I,\infty}(\infty),\end{aligned} \tag{3.39}$$

where $P_{out,p_1}^{GB,I,\infty}(\infty)$ is as (3.46) in **Proposition 1**.

Conditioned on $\gamma_{th}^{GB} \leq 1$, the asymptotic OP can be calculated as:

$$\mathbb{P}_{out,p_2}^{GB,I,\infty} = \mathbb{P}_{out,p_1}^{GB,I,\infty}(\sigma_1) - I_5, \tag{3.40}$$

where $P_{out,p_1}^{GB,I,\infty}(\cdot)$ is expressed by (3.44) and I_5 is as:

$$I_5 = F_{g_{GF}}^{far}(\sigma_1) - \sum_{s=1}^{S} \Lambda_2(\sigma_1, \iota_{s,1}) \gamma\left(b_3 - 1, b_{2,1}^{GB} \frac{\rho_{GF}}{\rho_{GB}} \iota_{s,1}\right) \times \left[\gamma\left(b_3, b_{2,2}^{GF} \iota_{s,1}\right) - \gamma\left(b_3, b_{2,1}^{GF} \iota_{s,1}\right)\right]. \tag{3.41}$$

Proof. When $\gamma_{th}^{GB} > 1$, substituting (3.5), (3.9) and (3.38) into the GB users' OP expressions, the asymptotic expressions are obtained by utilizing Eq. [2.10.6.2] in [127]. When $\gamma_{th}^{GB} \leq 1$, the derivations in **Proposition 1** and the Chebyshev-Gauss quadrature are invoked to achieve the final expressions. □

Corollary 13. Two outage situations are considered, including: *a)* $\gamma_{th}^{GB} > \gamma_{th}^{GF}/\left(1+\gamma_{th}^{GF}\right)$ or *b)* $\gamma_{th}^{GB} \leq \gamma_{th}^{GF}/\left(1+\gamma_{th}^{GF}\right)$. Thus, using the asymptotic expressions of the lower incomplete gamma function, the asymptotic OP of the GF users can be derived.

In terms of $\gamma_{th}^{GB} > \gamma_{th}^{GF}/\left(1+\gamma_{th}^{GF}\right)$, the asymptotic expressions can be derived as:

$$\mathbb{P}_{out,p_2}^{GF,I,\infty} = F_{g_{GF}}^{far}(\sigma_2) - \mathbb{P}_{out,p_1}^{GB,I,\infty}(\sigma_2) + \mathbb{P}_{out,p_2}^{GB,I}. \tag{3.42}$$

In term of $\gamma_{th}^{GB} \leq \gamma_{th}^{GF}/\left(1+\gamma_{th}^{GF}\right)$, the asymptotic expressions are derived as:

$$\begin{aligned}\mathbb{P}_{out,p_2}^{GF,I,\infty} =& F_{g_{GF}}^{far}(\sigma_1) - \mathbb{P}_{out,p_1}^{GB,I,\infty}(\sigma_1) + \mathbb{P}_{out,p_2}^{GB,I} \\ &+ \Lambda_2\left[(\sigma_2 - \sigma_1), \iota_{s,12}\right] \gamma\left(b_3 - 1, \frac{b_{2,1}^{GB} \rho_{GF}}{\rho_{GB}} \iota_{s,12}\right) \\ &\times \left[\gamma\left(b_3, b_{2,2}^{GF} \iota_{s,12}\right) - \gamma\left(b_3, b_{2,1}^{GF} \iota_{s,12}\right)\right].\end{aligned} \tag{3.43}$$

Proof. Based on the derivations of (3.10), (3.39), (3.40), and (3.46), the asymptotic expressions of OP for the GF users can be derived. □

3.2.4 Asymptotic OP Under the Open-loop Protocol in Scenario I

Under the conditions as $g_{GF} < \tau_{th}$ and $P_{GB} \to \infty$, diversity orders of Scenario I are analyzed as **Corollary 14** and **Corollary 15** to evaluate the outage performance in high SNR region.

Corollary 14. Conditioned that only the transmit powers of the GB users are ultra-high, denoted as $P_{GB} \to \infty$, whereas the transmit power of the GF users P_{GF} are fixed, the high SNR expressions of the GB users are obtained. Thus, in Scenario I under the open-loop protocol, the asymptotic expressions of OP for the GB users can be derived as:

$$\begin{aligned}\mathbb{P}_{out,p_1}^{GB,I,\infty}(\tau_{th}) =& \Upsilon \left[\rho_{GF} b_{1,2}^{GF} M\left(\tau_{th}, 2-b_3, b_3, b_{2,2}^{GF}\right)\right. \\ & \left. -\rho_{GF} b_{1,2}^{GF} M\left(\tau_{th}, 2-b_3, b_3, b_{2,1}^{GF}\right) + F_{g_{GF}}^{far}\left(\tau_{th}\right)\right], \end{aligned} \tag{3.44}$$

where $\Upsilon = \frac{2\left(b_{2,1}^{GB}\right)^{\frac{2}{\alpha}+1} \lambda_{GB}{}^{\frac{2}{\alpha}} \gamma_{th}^{GB}}{(\alpha+2) R_1^2 \rho_{GB}}$.

Proof. Substituting (3.38) into the expressions of OP of the GB users under the open-loop protocol, it can be derived as:

$$\mathbb{P}_{out,p_1}^{GB,I,\infty}(\tau_{th}) = \int_0^{\tau_{th}} \left[\Upsilon\left(\rho_{GF} x + 1\right)\right] f_{g_{GF}}^{far}(x) dx. \tag{3.45}$$

Utilizing Eq. [2.10.2.2] in [127], the final closed-form expressions can be obtained. □

Remark 2. *The asymptotic expressions of GB users are negatively correlated to the transmit SNR ρ_{GB}, denoted as $\mathbb{P}_{out,p_1}^{GB,I,\infty}(\tau_{th}) \sim \frac{1}{\rho_{GB}}$.*

Proposition 1. One special case is described that all the GF users can access into the GB channels when $g_{GF} \ll \tau_{th}$. Thus, it is assumed as $\tau_{th} \to \infty$ to derive the approximated expressions of OP for the GB users as:

$$\mathbb{P}_{out,p_1}^{GB,I,\infty}(\infty) = \Upsilon \left\{ \frac{\rho_{GF} b_{1,2}^{GF} \Gamma(2)}{(2-b_3)} \left[\left(b_{2,1}^{GF}\right)^{b_3-2} - \left(b_{2,2}^{GF}\right)^{b_3-2}\right] + 1 \right\}. \tag{3.46}$$

Proof. Based on **Corollary 14** and Eq. [2.10.2.2] in [127], this proposition can be proved. □

Remark 3. *In terms of* $\tau_{th} \to \infty$, $\mathbb{P}_{out,p_1}^{GB,I,\infty}(\infty)$ *has a lower limit since* $\mathbb{P}_{out,p_1}^{GB,I,\infty}(\infty)$ *is in connection with* τ_{th}.

Corollary 15. Note that same assumptions in **Corollary 14** are utilized in this corollary. Thus, the asymptotic expressions of OP for the GF users can be derived as:

$$\mathbb{P}_{out,p_1}^{GF,I,\infty} = F_{g_{GF}}^{far}\left[\min\left(\sigma_2, \tau_{th}\right)\right] - \mathbb{P}_{out,p_1}^{GB,I,\infty}\left[\min\left(\sigma_2, \tau_{th}\right)\right] + \mathbb{P}_{out,p_1}^{GB,I,\infty}(\tau_{th}), \tag{3.47}$$

where the final expressions can be obtained by substituting (3.10) *and* (3.44).

Proof. Substituting the expansions of lower incomplete gamma function into the expressions of OP for the GF users, one can be achieved as:

$$\mathbb{P}_{out,p_1}^{GF,I,\infty} = \int_0^{\min(\sigma_2,\tau_{th})} \left[1 - \Upsilon\left(\rho_{GF}x + 1\right)\right] f_{g_{GF}}^{far}(x)dx + \mathbb{P}_{out,p_1}^{GB,I,\infty}(\tau_{th}). \tag{3.48}$$

Based on the derivations in **Corollary 14** and change the upper limits from τ_{th} to $\min\left(\sigma_2, \tau_{th}\right)$, the asymptotic expressions can be derived as (3.47). □

Remark 4. *The expressions of diversity orders for the GB users can be presented as:*

$$d_{GB} = -\lim_{\rho_{GB}\to\infty} \frac{\log \mathbb{P}_{out,p_a}^{GB,I,\infty}(\rho_{GB})}{\log \rho_{GB}} = 1, \tag{3.49}$$

where $\mathbb{P}_{out,p_a}^{GB,I,\infty}$ *is the asymptotic OP in Scenario I with* $a \in \{1, 2\}$ *as different protocols and* ρ_{GB} *means the transmit SNR of the GB users.*

Remark 5. *The expressions of diversity orders for the GF user are derived as:*

$$d_{GF} = -\lim_{\rho_{GF}\to\infty} \frac{\log \mathbb{P}_{out,p_a}^{GF,I,\infty}(\rho_{GF})}{\log \rho_{GF}} = 0, \tag{3.50}$$

where $\mathbb{P}_{out,p_a}^{GF,I,\infty}$ *is the asymptotic OP and* ρ_{GF} *means the transmit SNR for the GF users.*

Remark 6. *The outage performance of GB users has a linear relationship with transit SNR* ρ_{GB} *in the high SNR region, while the outage performance of GF users has lower limits.*

3.3 Outage Performance in Scenario II

In Scenario II, the GB users are delay-tolerant users. To further reduce the latency of GF users, GB users will accomplish the SIC procedure. Based on the two protocols, the exact expressions of OP are derived as **Theorem 5** to **Theorem 8** and several corollaries.

3.3.1 Analytical OP Under the Dynamic Protocol in Scenario II

Under Scenario II, the OP with the dynamic protocol can be expressed as:

$$\mathbb{P}_{out,p_2}^{GF,II} = \Pr\left\{\frac{\rho_{GF} g_{GF,i}}{\rho_{GB} g_{GB,j} + 1} < \gamma_{th}^{GF}, g_{GF,i} > \frac{P_{GB}}{P_{GF}} g_{GB,j}\right\} \tag{3.51}$$

and

$$\begin{aligned}\mathbb{P}_{out,p_2}^{GB,II} =& P_{out,p_2}^{GF,II} + \Pr\left\{\frac{\rho_{GF} g_{GF,i}}{\rho_{GB} g_{GB,j} + 1} > \gamma_{th}^{GF},\right. \\ & \left. g_{GB,i} < \frac{\gamma_{th}^{GB}}{\rho_{GB}}, g_{GF,i} > \frac{P_{GB} g_{GB,j}}{P_{GF}}\right\}.\end{aligned} \tag{3.52}$$

Theorem 5. Conditioned on $\gamma_{th}^{GB} < 1$ and $\gamma_{th}^{GB} \geq 1$, the derivations can be derived by various expressions.

a) With $\gamma_{th}^{GB} \geq 1$, the expressions of OP for the GF users can be obtained as:

$$\mathbb{P}_{out,p_2}^{GF,II} = \underbrace{\int_0^{\infty} F_{g_{GF}}^{near}\left(\frac{\gamma_{th}^{GF}\rho_{GB}}{\rho_{GF}}x + \frac{\gamma_{th}^{GF}}{\rho_{GF}}\right) f_{g_{GB}}^{far}(x)\,dx}_{I_5} - \underbrace{\int_0^{\infty} F_{g_{GF}}^{near}\left(\frac{\rho_{GB}}{\rho_{GF}}x\right) f_{g_{GB}}^{far}(x)\,dx}_{I_6}. \tag{3.53}$$

b) With $\gamma_{th}^{GB} < 1$, the expressions of OP for the GF users are rewritten as:

$$\mathbb{P}_{out,p_2}^{GF,II} = \int_0^{\sigma_3} F_{g_{GF}}^{near}\left(\frac{\gamma_{th}^{GF}\rho_{GB}}{\rho_{GF}}x + \frac{\gamma_{th}^{GF}}{\rho_{GF}}\right) f_{g_{GB}}^{far}(x)\,dx - \int_0^{\sigma_3} F_{g_{GF}}^{near}\left(\frac{\rho_{GB}}{\rho_{GF}}x\right) f_{g_{GB}}^{far}(x)\,dx, \tag{3.54}$$

where $\sigma_3 = \gamma_{th}^{GF} \big/ \left(\rho_{GF} - \rho_{GB}\gamma_{th}^{GF}\right)$ and the closed-form expressions are given in **Corollary 16**.

Corollary 16. Conditioned on $\rho_{GF} \to \infty$ and $\gamma_{th}^{GB} \geq 1$, which means the GF users have satisfying channel conditions, the approximated expression of I_5 and the accurate derivation of I_6 are derived as:

$$I_5 = 1 - C_2(\rho_{GB}\sigma_2)^{1-b_3} U\left(b_{2,1}^{GF}\rho_{GB}\sigma_2, b_{2,2}^{GB}\right) - C_2(\rho_{GB}\sigma_2)^{1-b_3} U\left(b_{2,1}^{GF}\rho_{GB}\sigma_2, b_{2,1}^{GB}\right) \tag{3.55}$$

and

$$I_6 = 1 - C_2\left(\frac{\rho_{GB}}{\rho_{GF}}\right)^{1-b_3} U\left(\frac{b_{2,1}^{GF}\rho_{GB}}{\rho_{GF}}, b_{2,2}^{GB}\right) - C_2\left(\frac{\rho_{GB}}{\rho_{GF}}\right)^{1-b_3} U\left(\frac{b_{2,1}^{GF}\rho_{GB}}{\rho_{GF}}, b_{2,1}^{GB}\right), \tag{3.56}$$

where $C_2 = 2b_{1,2}^{GB}\lambda_{\mathrm{GF}}^{b_3-1} \big/ \left(\alpha R_1^2\right)$. Substituting the expressions of I_5 and I_6, the closed-form expressions of OP for the GF users can be obtained.

Conditioned on $\gamma_{th}^{GB} < 1$, based on the Chebyshev-Gauss quadrature, the OP for the GF users can be figured out as:

$$\begin{aligned}\mathbb{P}_{out,p_2}^{GF,II} =& \sum_{s=1}^{S} \Lambda_3\left(\sigma_3, \iota_{s,3}\right) \gamma\left(b_3 - 1, b_{2,1}^{GF} \frac{\rho_{GB}}{\rho_{GF}} \iota_{s,3}\right) \\ & \times \left[\gamma\left(b_3, b_{2,2}^{GB} \iota_{s,3}\right) - \gamma\left(b_3, b_{2,1}^{GB} \iota_{s,3}\right)\right] \\ & - \Lambda_3\left(\sigma_3, \iota_{s,3}\right) \gamma\left[b_3 - 1, b_{2,1}^{GF} \sigma_2\left(\rho_{GB} \iota_{s,3} + 1\right)\right] \\ & \times \left[\gamma\left(b_3, b_{2,2}^{GB} \iota_{s,3}\right) - \gamma\left(b_3, b_{2,1}^{GB} \iota_{s,3}\right)\right], \end{aligned} \tag{3.57}$$

where $\Lambda_3\left(a, x\right) = \frac{C_2}{2} a \omega_s x^{1-2b_3} \left(1 - x^2\right)^{\frac{1}{2}} \rho_{GF}^{b_3 - 1} \rho_{GB}^{1-b_3}$ and $\iota_{s,3} = t_s\left(x_s, 0, \sigma_3\right)$

Theorem 6. The closed-form OP expressions of the GB users are derived under two situations as *a)* $\gamma_{th}^{GF} > \gamma_{th}^{GB} / \left(\gamma_{th}^{GB} + 1\right)$ and *b)* $\gamma_{th}^{GF} \leq \gamma_{th}^{GB} / \left(\gamma_{th}^{GB} + 1\right)$.

a) With $\gamma_{th}^{GF} > \gamma_{th}^{GB} / \left(\gamma_{th}^{GB} + 1\right)$, the OP expressions are derived as:

$$\begin{aligned}\mathbb{P}_{out,p_2}^{GB,II} =& \sum_{s=1}^{S} \Lambda_4\left(\sigma_3, \iota_{s,3}\right) \gamma\left[b_3 - 1, b_{2,1}^{GF} \sigma_2\left(\rho_{GB} \iota_{s,3} + 1\right)\right] \\ & \times \left[\gamma\left(b_3, b_{2,2}^{GB} \iota_{s,3}\right) - \gamma\left(b_3, b_{2,1}^{GB} \iota_{s,3}\right)\right] + P_{out,p_2}^{GF,II}. \end{aligned} \tag{3.58}$$

*b)*With $\gamma_{th}^{GF} \leq \gamma_{th}^{GB} / \left(\gamma_{th}^{GB} + 1\right)$, the closed-form expressions are obtained as:

$$\begin{aligned}\mathbb{P}_{out,p_2}^{GB,II} =& \sum_{s=1}^{S} \Lambda_4\left(\sigma_3, \iota_{s,3}\right) \gamma\left[b_3 - 1, b_{2,1}^{GF} \sigma_2\left(\rho_{GB} \iota_{s,3} + 1\right)\right] \\ & \times \left[\gamma\left(b_3, b_{2,2}^{GB} \iota_{s,3}\right) - \gamma\left(b_3, b_{2,1}^{GB} \iota_{s,3}\right)\right] \\ & + \Lambda_3\left[\left(\sigma_3 - \sigma_4\right), \iota_{s,34}\right] \gamma\left(b_3 - 1, b_{2,1}^{GF} \sigma_2 \iota_{s,34}\right) \\ & \times \left[\gamma\left(b_3, b_{2,2}^{GB} \iota_{s,34}\right) - \gamma\left(b_3, b_{2,1}^{GB} \iota_{s,34}\right)\right] + P_{out,p_2}^{GF,II}, \end{aligned} \tag{3.59}$$

where $\sigma_4 = \gamma_{th}^{GB} / \rho_{GB}$, $\iota_{s,34} = t_s\left(x_s, \sigma_3, \sigma_4\right)$ and $\Lambda_4(a, x) = \frac{C_2}{2} x^{-b_3} \omega_s a \times \left(1 - x^2\right)^{\frac{1}{2}} \left(\gamma_{th}^{GF}\right)^{1-b_3} \rho_{GF}^{b_3 - 1} \left(\rho_{GB} x + 1\right)^{1-b_3}$.

3.3.2 Analytical OP Under the Open-loop Protocol in Scenario II

Under Scenario II, the OP with the open-loop protocol can be expressed as:

$$\mathbb{P}_{out,p_1}^{GF,II} = \Pr\left\{\frac{\rho_{GF} g_{GF,i}}{\rho_{GB} g_{GB,j}+1} < \gamma_{th}^{GF}, g_{GF,i} > \tau_{th}\right\} \tag{3.60}$$

and

$$\mathbb{P}_{out,p_1}^{GB,II} = P_{out,p_1}^{GF,II} + \Pr\left\{\frac{\rho_{GF} g_{GF,i}}{\rho_{GB} g_{GB,j}+1} > \gamma_{th}^{GF},\ g_{GB,i} < \frac{\gamma_{th}^{GB}}{\rho_{GB}}, g_{GF,i} > \tau_{th}\right\}. \tag{3.61}$$

Theorem 7. Under the open-loop protocol, the OP expressions of the GF users vary from *a)* $\rho_{GF} \geq \gamma_{th}^{GF}/\tau_{th}$ and *b)* $\rho_{GF} < \gamma_{th}^{GF}/\tau_{th}$. *Thus, for* $\rho_{GF} \geq \gamma_{th}^{GF}/\tau_{th}$*, the OP expressions of the GF users can be derived as:*

$$\begin{aligned}\mathbb{P}_{out,p_1}^{GF,II} = &\int_{\sigma_5^{-1}}^{\infty} F_{g_{GF}}^{near}\left(\frac{\rho_{GB}\gamma_{th}^{GF}}{\rho_{GF}}x + \frac{\gamma_{th}^{GF}}{\rho_{GF}}\right) f_{g_{GB}}^{far}(x)\,dx \\ &- \int_{\sigma_5^{-1}}^{\infty} F_{g_{GF}}^{near}(\tau_{th})\, f_{g_{GB}}^{far}(x)\,dx,\end{aligned} \tag{3.62}$$

and when $\rho_{GF} < \gamma_{th}^{GF}/\tau_{th}$, the OP expressions for the GF users are derived as:

$$\begin{aligned}\mathbb{P}_{out,p_1}^{GF,II} = &\int_{0}^{\infty} F_{g_{GF}}^{near}\left(\frac{\rho_{GB}\gamma_{th}^{GF}}{\rho_{GF}}x + \frac{\gamma_{th}^{GF}}{\rho_{GF}}\right) f_{g_{GB}}^{far}(x)\,dx \\ &- \int_{0}^{\infty} F_{g_{GF}}^{near}(\tau_{th})\, f_{g_{GB}}^{far}(x)\,dx,\end{aligned} \tag{3.63}$$

where $\sigma_5 = \gamma_{th}^{GF}\rho_{GB}/\left(\rho_{GF}\tau_{th} - \gamma_{th}^{GF}\right)$. **Corollary 17** and **Corollary 18** show the closed-form expressions of OP.

Corollary 17. Two situations are presented by two conditions, denoted as $\tau_{th} \to 0$ and $\rho_{GF} \to \infty$, which means the special case that: *a)* all the GF users can join the channels occupied by the GB users and *b)* the GF users experience good channel conditions. Conditioned on $\rho_{GF} < \gamma_{th}^{GF}/\tau_{th}$, the

OP of the GF users can be approximated as:

$$\mathbb{P}_{out,p_1}^{GF,II} = 1 - F_{g_{GF}}^{near}(\tau_{th}) - C_2\left(\frac{\rho_{GF}}{\rho_{GB}\gamma_{th}^{GF}}\right)^{b_3-1} \times \left[U\left(\frac{b_{2,1}^{GF}\rho_{GB}\gamma_{th}^{GF}}{\rho_{GF}}, b_{2,2}^{GB}\right) - U\left(\frac{b_{2,1}^{GF}\rho_{GB}\gamma_{th}^{GF}}{\rho_{GF}}, b_{2,1}^{GB}\right)\right]. \quad (3.64)$$

Proof. Based on ***Lemma 3*** *and* ***Corollary 9****, this corollary is proved.* □

Corollary 18. Conditioned on $\rho_{GF} \geq \gamma_{th}^{GF}/\tau_{th}$, the closed-form expressions of OP of the GF users are derived as:

$$\mathbb{P}_{out,p_1}^{GF,II} = \sum_{s=1}^{S}\left\{\vartheta_1\gamma\left(b_3-1, b_{2,1}^{GF}\tau_{th}\right) - \vartheta_2\gamma\left[b_3-1, b_{2,1}^{GF}\gamma_{th}^{GF}\left(\frac{\rho_{GB}+\iota_{s,5}}{\rho_{GF}\iota_{s,5}}\right)\right]\right\} \times \left[\gamma\left(b_3, \frac{b_{2,2}^{GB}}{\iota_{s,5}}\right) - \gamma\left(b_3, \frac{b_{2,1}^{GB}}{\iota_{s,5}}\right)\right], \quad (3.65)$$

where $\iota_{s,5} = t_s(x_s, 0, \sigma_5)$, $\vartheta_1 = \tau_{th}^{1-b_3}\Lambda_5(\sigma_5, \iota_{s,5})$, $\vartheta_2 = (\rho_{GF}\iota_{s,5})^{b_3-1}\iota_{s,5} \times\left(\rho_{GB}\gamma_{th}^{GF}+\gamma_{th}^{GF}\right)^{1-b_3}\Lambda_5(\sigma_5, \iota_{s,5})$, and $\Lambda_5(a,x) = \frac{C_2}{2}a^{-1}\omega_s x^{b_3-2}\left(1-x^2\right)^{\frac{1}{2}}$.

Theorem 8. After the SIC procedure, the OP expressions of the GB users can be written as $\mathbb{P}_{out,p_1}^{GB,II} = Q_3 + \mathbb{P}_{out,p_1}^{GF,II}$, where Q_3 can be expressed as $Q_3 = \Pr\left\{g_{GF,i} > \frac{\rho_{GB}\gamma_{th}^{GF}}{\rho_{GF}}g_{GB,j} + \frac{\gamma_{th}^{GF}}{\rho_{GF}}, g_{GB} < \frac{\gamma_{th}^{GB}}{\rho_{GB}}, g_{GF} > \tau_{th}\right\}$. Based on **Theorem 7** and **Corollary 19**, the closed-form OP expressions for the GB users under the open-loop protocol in Scenario II are achieved.

Corollary 19. With various range of the transmit SNR of the GF users, i.e., $\rho_{GF} \leq \gamma_{th}^{GF}/\tau_{th}$, $\gamma_{th}^{GF}/\tau_{th} < \rho_{GF} < \gamma_{th}^{GF}\left(1+\gamma_{th}^{GB}\right)/\tau_{th}$, and $\rho_{GF} \geq \gamma_{th}^{GF}\left(1+\gamma_{th}^{GB}\right)/\tau_{th}$, different derivations of OP for Q_3 are calculated.

a) With $\rho_{GF} \leq \gamma_{th}^{GF}/\tau_{th}$, Q_3 can be derived as:

$$Q_3 = \sum_{s=1}^{S}\Lambda_4(\sigma_2, \iota_{s,2})\gamma\left[b_3-1, \frac{b_{2,1}^{GF}\gamma_{th}^{GF}}{\rho_{GF}}\left(\rho_{GB}\iota_{s,2}+1\right)\right] \times\left[\gamma\left(b_3, b_{2,2}^{GB}\iota_{s,2}\right) - \gamma\left(b_3, b_{2,1}^{GB}\iota_{s,2}\right)\right]. \quad (3.66)$$

b) With $\gamma_{th}^{GF}/\tau_{th} < \rho_{GF} < \gamma_{th}^{GF}\left(1+\gamma_{th}^{GB}\right)/\tau_{th}$, the expressions of Q_3 can be derived as:

$$\begin{aligned} Q_3 =& F_{g_{GB}}^{far}\left(\sigma_5^{-1}\right)\left[1-F_{g_{GF}}^{near}\left(\tau_{th}\right)\right]+\sum_{s=1}^{S}\Lambda_4(\varepsilon,\iota_{s,52}) \\ &\times\gamma\left[b_3-1,b_{2,1}^{GF}\sigma_2\left(\rho_{GB}\iota_{s,52}+1\right)\right] \\ &\times\left[\gamma\left(b_3,b_{2,2}^{GB}\iota_{s,52}\right)-\gamma\left(b_3,b_{2,1}^{GB}\iota_{s,52}\right)\right], \end{aligned} \tag{3.67}$$

where $\iota_{s,52}=t_s\left(x_s,\sigma_5^{-1},\sigma_2\right)$, $\varepsilon=\left(\gamma_{th}^{GF}\sigma_5-\rho_{GF}\right)/\left(\rho_{GF}\sigma_5\right)$.

c) With $\rho_{GF}\geq\gamma_{th}^{GF}\left(1+\gamma_{th}^{GB}\right)/\tau_{th}$, the expressions of Q_3 are derived as:

$$Q_3=F_{g_{GB}}^{far}\left(\frac{\gamma_{th}^{GF}}{\rho_{GF}}\right)\left[1-F_{g_{GF}}^{near}\left(\tau_{th}\right)\right]. \tag{3.68}$$

3.3.3 Asymptotic OP Under the Dynamic Protocol in Scenario II

It is assumed that $P_{GF}\to\infty$ and a fixed P_{GB} are presented to achieve the asymptotic expressions in Scenario II under the dynamic protocol as **Corollary 20** and **Corollary 21**.

Corollary 20. Since $P_{GF}\to\infty$ means $\rho_{GF}\to\infty$, the asymptotic OP expressions of the GF users under the dynamic protocol can be derived in the following two situations as:

a) With $\gamma_{th}^{GB}>1$,

$$\mathbb{P}_{out,p_2}^{GF,II,\infty}=I_5^{\infty}-I_6, \tag{3.69}$$

where $C_3=2R_1^{\alpha}/\left[\left(\alpha+2\right)\lambda_{GF}\right]$ and I_5^{∞} can be expressed as:

$$\begin{aligned} I_5^{\infty} =& C_3\sigma_2 b_{1,2}^{GB}\frac{\rho_{GB}\Gamma\left(2\right)}{2-b_3}\left[\left(b_{2,1}^{GB}\right)^{b_3-2}-\left(b_{2,2}^{GB}\right)^{b_3-2}\right] \\ &+C_3\sigma_2 b_{1,2}^{GB}\frac{\Gamma\left(1\right)}{1-b_3}\left[\left(b_{2,1}^{GB}\right)^{b_3-1}-\left(b_{2,2}^{GB}\right)^{b_3-1}\right], \end{aligned} \tag{3.70}$$

b) and with $\gamma_{th}^{GB} \leq 1$,

$$\begin{aligned}\mathbb{P}_{out,p_2}^{GF,II,\infty} =& - F_{g_{GB}}^{far}\left(\sigma_3\right) + \sum_{s=1}^{S}\left[\frac{C_4}{\iota_{s,3}^{b_3}}\left(\rho_{GB}\iota_{s,3}+1\right) + \frac{C_2}{\iota_{s,3}^{2b_3-1}}\right. \\ & \left.\times\left(\frac{\rho_{GF}}{\rho_{GB}}\right)^{b_3-1}\gamma\left(b_3-1, b_{2,1}^{GF}\frac{\rho_{GB}}{\rho_{GF}}x\right)\right] \\ & \times\left[\gamma\left(b_3, b_{2,2}^{GB}\iota_{s,3}\right) - \gamma\left(b_3, b_{2,1}^{GB}\iota_{s,3}\right)\right], \end{aligned} \tag{3.71}$$

where $C_4 = C_3\sigma_2 b_{1,2}^{GB}$.

Corollary 21. In Scenario II with the dynamic protocol, under the condition that $P_{GF} \to \infty$, the asymptotic expressions of OP for the GF users are derived as the following two situations:

a) With $\gamma_{th}^{GF} > \gamma_{th}^{GB}/\left(\gamma_{th}^{GB}+1\right)$,

$$\mathbb{P}_{out,p_2}^{GB,II,\infty} = Q_4\left(\sigma_4\right) + \mathbb{P}_{out,p_2}^{GF,II,\infty}, \tag{3.72}$$

b) and with $\gamma_{th}^{GF} < \gamma_{th}^{GB}/\left(\gamma_{th}^{GB}+1\right)$,

$$\begin{aligned}\mathbb{P}_{out,p_2}^{GB,II,\infty} =& \mathbb{P}_{out,p_2}^{GF,II,\infty} + Q_4\left(\sigma_3\right) + F_{g_{GB}}^{far}\left(\sigma_4\right) - F_{g_{GB}}^{far}\left(\sigma_3\right) \\ & - \frac{C_4}{\rho_{GF}}\left[M\left(\sigma_4, 2-b_3, b_3, b_{2,2}^{GB}\right) - M\left(\sigma_4, 2-b_3, b_3, b_{2,1}^{GB}\right)\right. \\ & \left. - M\left(\sigma_3, 2-b_3, b_3, b_{2,2}^{GB}\right) + M\left(\sigma_3, 2-b_3, b_3, b_{2,1}^{GB}\right)\right], \end{aligned} \tag{3.73}$$

where $Q_4\left(x\right)$ is defined as:

$$\begin{aligned} Q_4\left(x\right) =& F_{g_{GB}}^{far}\left(x\right) - C_4\rho_{GB} \\ & \times\left[M\left(x, 2-b_3, b_3, b_{2,2}^{GB}\right) - M\left(x, 2-b_3, b_3, b_{2,1}^{GB}\right)\right] \\ & + C_4\left[M\left(x, 1-b_3, b_3, b_{2,2}^{GB}\right) - M\left(x, 1-b_3, b_3, b_{2,1}^{GB}\right)\right]. \end{aligned} \tag{3.74}$$

3.3.4 Asymptotic OP Under the Open-loop Protocol in Scenario II

The asymptotic expressions under the open-loop protocol are derived as **Corollary 22** and **Corollary 23**.

Corollary 22. Based on $P_{GF} \to \infty$ and (3.38), the asymptotic derivations for the GF users are derived.

a) Conditioned on $\rho_{GF} < \gamma_{th}^{GF}/\tau_{th}$, the asymptotic OP of the GF users can be derived as:

$$\mathbb{P}_{out,p_1}^{GF,II,\infty} = I_5^{\infty} - F_{g_{GF}}^{near}\left(\tau_{th}\right). \tag{3.75}$$

b) Conditioned on $\rho_{GF} > \gamma_{th}^{GF}/\tau_{th}$, the asymptotic OP expressions are expressed as:

$$\begin{aligned}\mathbb{P}_{out,p_1}^{GF,II,\infty} =& \sum_{s=1}^{S} \Xi_{s,2}\left[C_3\sigma_2\left(\frac{\rho_{GB}}{\iota_{s,5}}+1\right) - F_{g_{GF}}^{near}\left(\tau_{th}\right)\right] \\ &\times\left[\gamma\left(b_3, b_{2,2}^{GB}\iota_{s,5}^{-1}\right) - \gamma\left(b_3, b_{2,1}^{GB}\iota_{s,5}^{-1}\right)\right],\end{aligned} \tag{3.76}$$

where $\Xi_{s,2} = \frac{1}{2}b_{1,2}^{GB}\sigma_5\omega_s\iota_{s,5}^{b_3-2}\left(1-\iota_{s,5}^2\right)^{\frac{1}{2}}$.

Corollary 23. Utilizing the same assumption in **Corollary 22**, the asymptotic OP expressions of the GB users can be derived under the following three conditions.

a) As for $\rho_{GF} < \gamma_{th}^{GF}/\tau_{th}$, $\mathbb{P}_{out,p_1}^{GB,II,\infty}$ can be derived as:

$$\mathbb{P}_{out,p_1}^{GB,II,\infty} = Q_4\left(\sigma_2\right) + \mathbb{P}_{out,p_1}^{GF,II,\infty}. \tag{3.77}$$

b) As for $\gamma_{th}^{GF}/\tau_{th} < \rho_{GF} < \gamma_{th}^{GF}\left(1+\gamma_{th}^{GB}\right)/\tau_{th}$, the asymptotic expressions of OP can be calculated as:

$$\begin{aligned}\mathbb{P}_{out,p_1}^{GB,II,\infty} =& F_{g_{GB}}^{far}\left(\sigma_5^{-1}\right)\left[1 - F_{g_{GF}}^{near}\left(\tau_{th}\right)\right] + Q_4\left(\sigma_2\right) \\ &- Q_4\left(\sigma_5^{-1}\right) + \mathbb{P}_{out,p_1}^{GF,II,\infty}.\end{aligned} \tag{3.78}$$

c) As for $\rho_{GF} \geq \gamma_{th}^{GF}\left(1+\gamma_{th}^{GB}\right)/\tau_{th}$, the asymptotic expressions are derived as:

$$\mathbb{P}_{out,p_1}^{GB,II,\infty} = \Theta\left[1 - F_{g_{GF}}^{near}\left(\tau_{th}\right)\right] + \mathbb{P}_{out,p_1}^{GF,II,\infty}, \tag{3.79}$$

where $\Theta = 2\sigma_2\left(R_2^{2+\alpha} - R_1^{2+\alpha}\right)/\left[(2+\alpha)\left(R_2^2 - R_1^2\right)\lambda_{GB}\right]$.

Remark 7. *Note that different protocols, including the open-loop protocol and the dynamic protocol, have equivalent diversity gains. Compared to diversity orders in Scenario I and Scenario II, one conclusion can be obtained that constant diversity gains are obtained as 1) one for the near users and 2) zero for the far users.*

3.4 Ergodic Rates

Ergodic rates indicate the average achievable rate, with the definition of $\mathbb{E}\left[R_G\right] = \mathbb{E}\left[\log_2\left(1+\gamma_G\right)\right]$, where $\mathbb{E}[\cdot]$ is calculating the expectation with $G \in \{GF, GB\}$. Thus, the high ergodic rate achieves superior performance. Under the dynamic protocol, the ergodic rates of the GB and GF users are expressed as:

$$\mathbb{E}\left[R_{GB}\right] = \int_0^\infty \frac{\mathbb{P}_c^{GB}\left(\gamma_{GB}^{th}\right)}{1+\gamma_{GB}^{th}} d\gamma_{GB}^{th} \tag{3.80}$$

and

$$\mathbb{E}\left[R_{GF}\right] = \int_0^\infty \frac{\mathbb{P}_c^{GF}\left(\gamma_{GF}^{th}\right)}{1+\gamma_{GF}^{th}} d\gamma_{GF}^{th}, \tag{3.81}$$

where γ_{GB}^{th} and γ_{GF}^{th} are the outage thresholds of users, $g_{GF} = P_{GF}|h_{GF}|^2 d_{GF}^{-\alpha}$, $g_{GB} = P_{GB}|h_{GB}|^2 d_{GB}^{-\alpha}$. Recall that $\mathbb{P}_c^{GB}$ and $\mathbb{P}_c^{GF}$ are the coverage probability of users, which are expressed as:

$$\mathbb{P}_c^{GB} = \Pr\left\{\gamma_{GB} > \gamma_{GB}^{th}, g_{GF} < g_{GB}\right\} \tag{3.82}$$

and

$$\mathbb{P}_c^{GF} = \Pr\left\{\gamma_{GB} > \gamma_{GB}^{th}, \gamma_{GF} > \gamma_{GF}^{th}, g_{GF} < g_{GB}\right\}. \tag{3.83}$$

3.4.1 Exact Analysis on Ergodic Rates

In this subsection, the exact closed-form expressions of ergodic rates are derived for the GF and GB users, shown as **Theorem 9** and **Theorem 10**, respectively.

3.4.1.1 Ergodic Rates for the GB Users

Bases on the definition of Ergodic rates in (3.80), recalled as $\mathrm{E}[R_{GB}] = \int_0^\infty \frac{P_c^{GB}(\gamma_{GB}^{th})}{1+\gamma_{GB}^{th}} d\gamma_{GB}^{th}$, this integral has the range of γ_{GB}^{th} from zero to infinity. However, the derivations of this integral in different intervals $[0, 1]$ and $[1, \infty]$ are different. Hence, before deriving the final expressions of ergodic rates for the GB users with $\gamma_{GB}^{th} \in [0, \infty]$, two derivation parts are analyzed as **Lemma 4** with $\gamma_{GB}^{th} \in [1, \infty]$ and **Lemma 5** with $\gamma_{GB}^{th} \in [0, 1]$ since the derivations are different. For the first case, signals can be decoded as the signal strength is stronger than the interference strength. For the second case, although the signal strength is weaker than that of interference, error correction coding can be used to help the decoding.

Lemma 4. Conditioned on $\gamma_{GB}^{th} \in [1, \infty]$, the closed-form expressions of ergodic rates for the GB users are derived as:

$$\begin{aligned}\mathbb{E}[R_{GB}]_1 = 2R_L^{\alpha-1} \sum_{n=1}^{N}\sum_{m=1}^{M} & \frac{\omega_n\sqrt{1+\varepsilon_n^2}\omega_m\sqrt{1+\varepsilon_m^2}}{(\varepsilon_m+1)^2\left(1+\frac{1}{\alpha}\right)\Theta_1} \\ & \times \frac{\exp\left(-\Theta_2\Omega_1^\alpha(\varepsilon_n)\,\Omega_2(\varepsilon_m)\right)}{\Omega_1^{\alpha-1}(\varepsilon_n)\left(\Omega_2(\varepsilon_m)+\Omega_2^2(\varepsilon_m)\right)} \\ & \times {}_2F_1\left(1, \frac{2+\alpha}{\alpha}; 2+\frac{2}{\alpha}; -\frac{R_L^\alpha\Omega_1^{-\alpha}(\varepsilon_n)}{\Theta_1\Omega_2(\varepsilon_m)}\right),\end{aligned} \tag{3.84}$$

where ${}_2F_1(\cdot)$ is the hypergeometric function in [127], $\Omega_1(x) = \frac{R_L}{2}(x+1)$, $\Omega_2(x) = \frac{2}{x+1}$, $\varepsilon_n = \cos\left(\frac{2n-1}{2N}\pi\right)$, $\varepsilon_m = \cos\left(\frac{2m-1}{2M}\pi\right)$, $\omega_n = \pi/N$, $\omega_i = \pi/M$,

M and N is the coefficients of the Chebyshev-Gauss quadrature, $\Theta_1 = \frac{\lambda_{GF}P_{GF}}{\lambda_{GB}P_{GB}}$, and $\Theta_2 = \frac{\sigma^2}{\lambda_{GB}P_{GB}}$.

Proof. See Appendix A.1. □

Lemma 5. Note that messages can be decoded via error correction coding with redundant information when $\gamma_{GB}^{th} \in [0,1]$ for the GB user. Thus, the closed-form expressions of ergodic rates can be derived as:

$$\mathbb{E}\left[R_{GB}\right]_2 = \mathrm{I}_3 + \mathrm{I}_4, \tag{3.85}$$

where I_3 and I_4 is the first and second items in (A.3) as:

$$\begin{aligned}\mathrm{I}_3 = &\sum_{n=1}^{N}\sum_{m=1}^{M}\frac{\omega_n\sqrt{1+\varepsilon_n^2}\omega_m\sqrt{1+\varepsilon_m^2}}{\ln 2\lambda_{GF}R_L^2}\Omega_1\left(\varepsilon_n\right)\Omega_1\left(\varepsilon_m\right)\\ &\times\delta_1\left(\Omega_1\left(\varepsilon_n\right),\Omega_1\left(\varepsilon_m\right)\right)\Xi\left(\varepsilon_n,\varepsilon_m\right),\end{aligned} \tag{3.86}$$

$$\begin{aligned}\mathrm{I}_4 = &\sum_{n=1}^{N}\sum_{m=1}^{M}\frac{\omega_n\sqrt{1+\varepsilon_n^2}\omega_m\sqrt{1+\varepsilon_m^2}\Omega_1\left(\varepsilon_n\right)\Omega_1\left(\varepsilon_m\right)}{R_L^2\lambda_{GF}\Psi\left(\Omega_1\left(\varepsilon_n\right),\Omega_1\left(\varepsilon_m\right),1\right)}\\ &\times\exp\left(-\Psi\left(\Omega_1\left(\varepsilon_n\right),\Omega_1\left(\varepsilon_m\right),1\right)\frac{\sigma^2\Omega_1^{\beta}\left(\varepsilon_n\right)}{P_{GF}}\right),\end{aligned} \tag{3.87}$$

where $\Psi\left(y,z,t\right) = \left(\frac{P_{GF}y^{-\alpha}t}{\lambda_{GB}P_{GB}z^{-\alpha}} + \frac{1}{\lambda_{GF}}\right)$, $\Xi\left(\varepsilon_n,\varepsilon_m\right) = \Phi\left(1,\delta_2\left(\Omega_1\left(\varepsilon_m\right)\right)\right) - \delta_3\left(\Omega_1\left(\varepsilon_n\right)\right)\Phi\left(1,2\delta_2\left(\Omega_1\left(\varepsilon_m\right)\right)\right) - \Phi\left(\delta_4\left(\Omega_1\left(\varepsilon_n\right),\Omega_1\left(\varepsilon_m\right)\right),\delta_2\left(\Omega_1\left(\varepsilon_m\right)\right)\right) + \delta_3\left(\Omega_1\left(\varepsilon_n\right)\right)\Phi\left(\delta_4\left(\Omega_1\left(\varepsilon_n\right),\Omega_1\left(\varepsilon_m\right)\right),2\delta_2\left(\Omega_1\left(\varepsilon_m\right)\right)\right)$, $\delta_3\left(y\right) = \exp\left(-\frac{\sigma^2y^{\alpha}}{\lambda_{GF}P_{GF}}\right)$, $\delta_1\left(y,z\right) = \frac{\lambda_{GF}\lambda_{GB}P_{GB}z^{-\alpha}}{\left(\lambda_{GB}P_{GB}z^{-\alpha}-\lambda_{GF}P_{GF}y^{-\alpha}\right)}$, $\delta_2\left(z\right) = \sigma^2\Big/\left(\lambda_{GB}P_{GB}z^{-\alpha}\right)^{-1}$, $\delta_4\left(y,z\right) = \frac{\lambda_{GB}P_{GB}z^{-\alpha}}{\lambda_{GF}P_{GF}y^{-\alpha}}$, $\Phi\left(a,b\right) = \int_0^1\frac{\exp(-bt)}{t+a}dt = -\exp\left(ab\right)\mathrm{Ei}\left(-ab\right)$, and $\mathrm{Ei}\left(x\right) = \int_{-\infty}^{x}\frac{\exp(t)}{t}dt$ is the exponential integral in [127]. Other coefficients are defined in **Lemma 4**.

Proof. See Appendix A.2. □

Theorem 9. Combined the expressions of ergodic rate in two scenarios shown in **Lemma 4** and **Lemma 5**, the final ergodic rate expression for

the GB user $\left(\gamma_{GB}^{th} \in [0, \infty]\right)$ can be expressed as:

$$\mathbb{E}\left[R_{GB}\right] = \mathbb{E}\left[R_{GB}\right]_1 + \mathbb{E}\left[R_{GB}\right]_2 . \tag{3.88}$$

Remark 8. *It is observed that the ergodic rate of the GB user is proportional to the transmit power of the GB user P_{GB} but inversely proportional to the transmit power of GF users P_{GF} in the high SNR region.*

3.4.1.2 Ergodic Rates for the GF Users

The GF user should satisfy two conditions, denoted as 1) received power limit $P_{GF}|h_{GF}|^2 d_{GF}^{-\alpha} < P_{GB}|h_{GB}|^2 d_{GB}^{-\alpha}$ and 2) a success SIC procedure $\gamma_{GB} > \gamma_{GB}^{th}$. Based on those two conditions, the closed-form ergodic rate expressions for the GF user are derived in the following.

Theorem 10. The closed-form expressions of ergodic rates for the GF users can be derived as:

$$\begin{aligned} E\left[R_{GF}\right] = & \sum_{n=1}^{N}\sum_{m=1}^{M} \frac{-\omega_n\sqrt{1+\varepsilon_n^2}\omega_m\sqrt{1+\varepsilon_m^2}}{\ln 2 \lambda_{GF} R_L^2} \\ & \times \frac{\Omega_1\left(\varepsilon_n\right)\Omega_1\left(\varepsilon_m\right)\exp\left(-\frac{\sigma^2\gamma_{GB}^{th}\Omega_1^{\alpha}(\varepsilon_m)}{\lambda_{GB}P_{GB}}\right)}{\Psi\left(\Omega_1\left(\varepsilon_n\right),\Omega_1\left(\varepsilon_m\right),\gamma_{GB}^{th}\right)} \\ & \times \exp\left(\Psi\left(\Omega_1\left(\varepsilon_n\right),\Omega_1\left(\varepsilon_m\right),\gamma_{GB}^{th}\right)\frac{\sigma^2\Omega_1^{\alpha}\left(\varepsilon_n\right)}{P_{GF}}\right) \\ & \times \mathrm{Ei}\left(-\Psi\left(\Omega_1\left(\varepsilon_n\right),\Omega_1\left(\varepsilon_m\right),\gamma_{GB}^{th}\right)\frac{\sigma^2\Omega_1^{\alpha}\left(\varepsilon_n\right)}{P_{GF}}\right), \end{aligned} \tag{3.89}$$

where coefficients are defined in **Lemma 4** and **Lemma 5**.

Proof. See Appendix A.3. □

Remark 9. *Analytical results indicate the ergodic rate of the GF user is inversely proportional to P_{GB}. When P_{GF} enhances, although the SNR of GF users will increase, the probability of GF users joining into the occupied GB channel is reduced, thereby a maximum ergodic rate of GF users is obtained.*

3.4.2 Approximated Analysis on Ergodic Rates

This section investigates the approximated ergodic rate for GF users via **Corollary 24** in this subsection.

Corollary 24. It is assumed that the transmit power of the GF user to infinity, denoted as $\rho_{GF} = P_{GF}/\sigma^2 \to \infty$. With the aid of asymptotic expressions, the approximated expression of the ergodic rate for the GF user can be calculated as:

$$\begin{aligned} E\left[R_{GF}\right] = & \sum_{n=1}^{N}\sum_{m=1}^{M} \frac{-\omega_n\sqrt{1+\varepsilon_n^2}\omega_m\sqrt{1+\varepsilon_m^2}}{\ln 2\lambda_{GF}R_L^2} \\ & \times \frac{\Omega_1\left(\varepsilon_n\right)\Omega_1\left(\varepsilon_m\right)\exp\left(-\frac{\sigma^2\gamma_{GB}^{th}\Omega_1^{\alpha}(\varepsilon_m)}{\lambda_{GB}P_{GB}}\right)}{\Psi\left(\Omega_1\left(\varepsilon_n\right),\Omega_1\left(\varepsilon_m\right),\gamma_{GB}^{th}\right)} \\ & \times \left(\ln\left(\Psi\left(\Omega_1\left(\varepsilon_n\right),\Omega_1\left(\varepsilon_m\right),\gamma_{GB}^{th}\right)\frac{\sigma^2\Omega_1^{\alpha}\left(\varepsilon_n\right)}{P_{GF}}\right)+C\right) \\ & \times \left(1-\Psi\left(\Omega_1\left(\varepsilon_n\right),\Omega_1\left(\varepsilon_m\right),\gamma_{GB}^{th}\right)\frac{\sigma^2\Omega_1^{\alpha}\left(\varepsilon_n\right)}{P_{GF}}\right). \end{aligned} \tag{3.90}$$

Proof. When assumed $x \to 0$, asymptotic expressions such as $1 - e^{-x} = x$ and $\mathrm{Ei}(-\mathrm{x}) = \ln(\mathrm{x}) + \mathrm{C}$ can be utilized, where $C \approx 0.577215$ as a constant in [127]. □

Due to space limitations, the approximated ergodic rate expressions of the GB users are omitted. It is presented that the simulation results of approximated expressions via dashed lines in the next section.

3.5 Numerical Results

In this section, numerical results are indicated to validate analytical, approximated, and asymptotic expressions derived in the previous sections, and further facilitate the outage performance and ergodic rates.

Table 3-A: Diversity orders for the GB and GF users under two scenarios with different SIC orders.

Diversity orders	The GF Users	The GB users
Scenario I	0	1
Scenario II	1	0

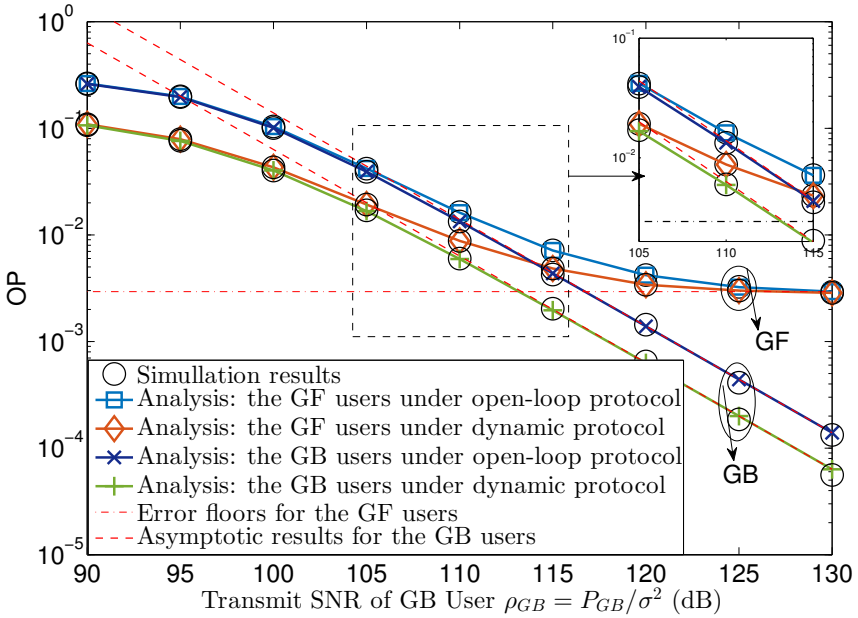

Figure 3.3: OP v.s. transmit SNR for the GB users with variations of protocols - Scenario I

3.5.1 Simulation Results on Outage Performance in Scenario I

3.5.1.1 Validation of Results - Scenario I

This part first validates the analytical results and investigate the impact of distances on OP. In this subsection, coefficients are fixed unless otherwise specified, including: the radium of the disc as $R_1 = 200$ m and the radius of the ring as $(R_1, R_2) = (200, 600)$ m. Other coefficients are set as follows: the channel gain for the GB and the GF users $|h_{GB}|^2$ and $|h_{GF}|^2$

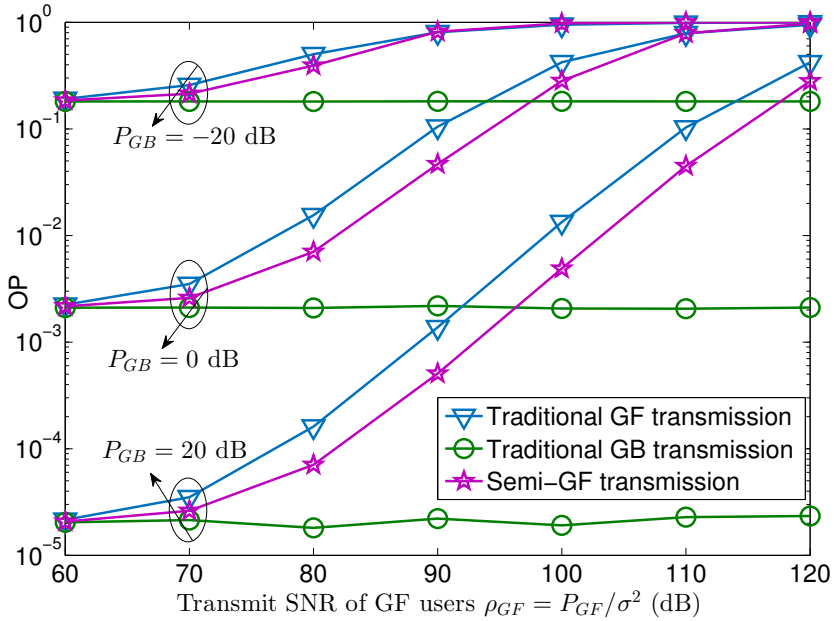

Figure 3.4: OP of the GB users v.s. transmit SNR of the GF users with variations of protocols - Scenario I

as 0 dB, pass-loss exponent α as 2.8, outage thresholds for the GB and GF users as $R_{GF} = 1$ BPCU and $R_{GB} = 1.5$ BPCU, where BPCU means bit per channel use, noise power σ^2 as -90 dBM, which is calculated as $\sigma^2 = 170 + 10\log_{10}(BW) + N_f$ with the carrier frequency BW as 10 MHz, the noise figure $N_f = 10$ dB. Additionally, channel quality thresholds of the open-loop protocol is denoted as τ_{th}, calculated as the mean of $P_{GB}P_{GF}^{-1}|h_{GB}|^2(d_{GB})^{-\alpha}$. In Scenario I, the transmit power of the GF users are fixed as 10 dBM and that of the GB users varies from $[0, 40]$ dBM. Comparing to the simulation and analytical results from Fig. 3.3 to Fig. 3.5, all curves are perfect matches, thereby validating the analysis of four theorems from **Theorem 1** to **Theorem 4**. It is also noted that asymptotic expressions match the analytical ones in high SNR region, which verifies the accuracy for asymptotic analysis.

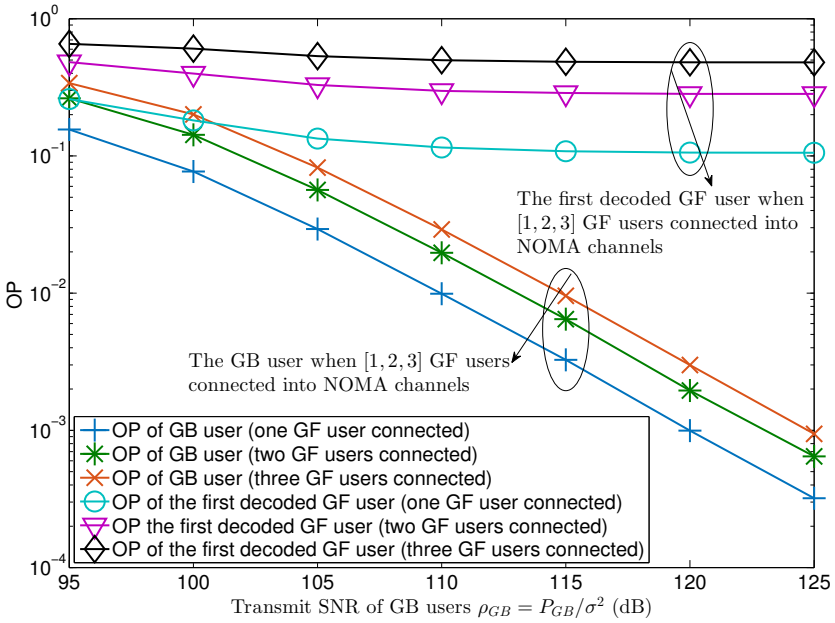

Figure 3.5: A comparison for GF and GB users with various number of connected GF users into NOMA channels - Scenario I.

3.5.1.2 Impact of Protocols on OP - Scenario I

In Scenario I, the outage performance of the GF and GB users is investigated under two protocols indicated in Fig. 3.3. One common observation on simulation results indicates that the dynamic protocol outperforms the open-loop protocol for all users. This is because under the dynamic protocol, frequent transmissions of the threshold by an added handshake can maintain the accuracy of access thresholds when the locations of the GB users are changed. However, under the open-loop protocol, the BS transmits an average threshold to all the GF users, which may cause more interference.

3.5.1.3 Comparison Among Various Transmission Schemes - Scenario I

The Fig. 3.4 compares the outage performance among traditional GB transmission, GF transmission, and Semi-GF transmission. It is observed that

the traditional GB transmission is the lower limit. Additionally, Semi-GF transmission performs better than traditional GF transmission. This is because Semi-GF protocols reduce the interference caused by GF users.

3.5.1.4 A Comparison With Various Connected GF Users - Scenario I

The Fig. 3.5 compares the performance of GF and GB users with various GF users joining into NOMA channels. In Fig. 3.5, it is concluded that GB users have better performance than GF users since in scenario I, the GF users will do the SIC procedure. If the SIC procedure fails, the outage situation will happen.

3.5.2 Simulation Results on Outage Performance in Scenario II

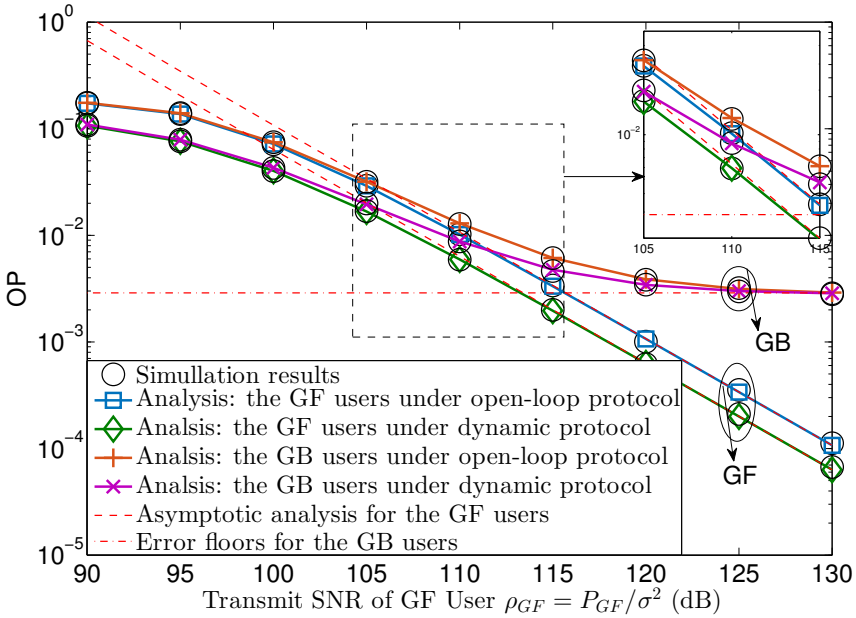

Figure 3.6: OP v.s. transmit SNR for the GF users with different protocols - Scenario II

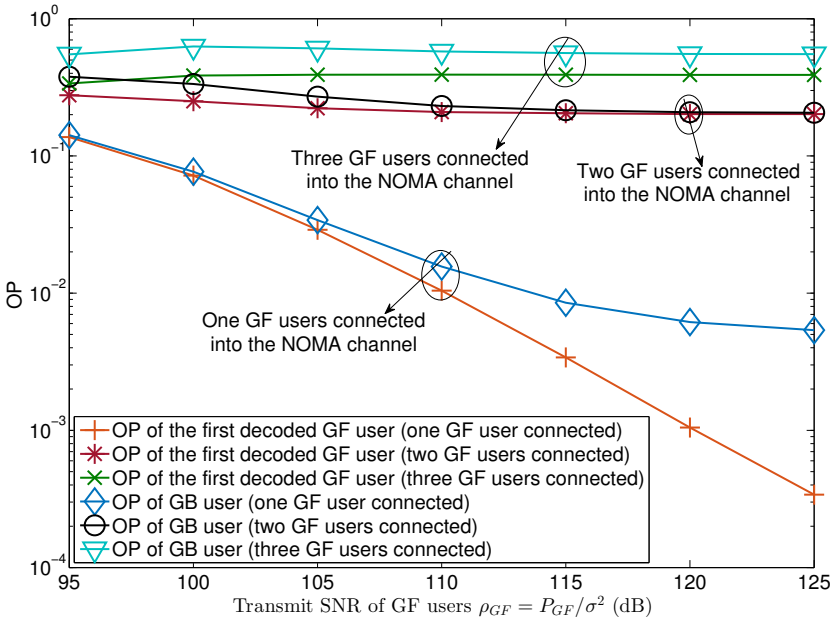

Figure 3.7: OP of the GB user with various number of connected GF users into NOMA channels - Scenario II

3.5.2.1 Validation of Results - Scenario II

Validation of analytical results on OP in Scenario II is demonstrated as a perfect match by Fig. 3.6 to Fig. 3.7, including four theorems from **Theorem 5** to **Theorem 8**. Additionally, curves for asymptotic expressions match simulation results in high SNR region to verify **Corollary 20** and **Corollary 23**. Without otherwise specification, numerical coefficients are the same as the Scenario-I except for the transmit power of the GF users as $[0, 40]$ dBM and the transmit power of the GB users as 10 dBM.

3.5.2.2 A Comparison With Various Connected GF Users - Scenario II

The Fig. 3.5 compares the performance of GF and GB users versus ρ_{GF} with different number of the connected GF users. One observation is that adding more GF users into NOMA channels have significant negative influence for

both of GF and GB users since the interference from the GF users increases.

3.5.3 Simulation Results on Ergodic Rates

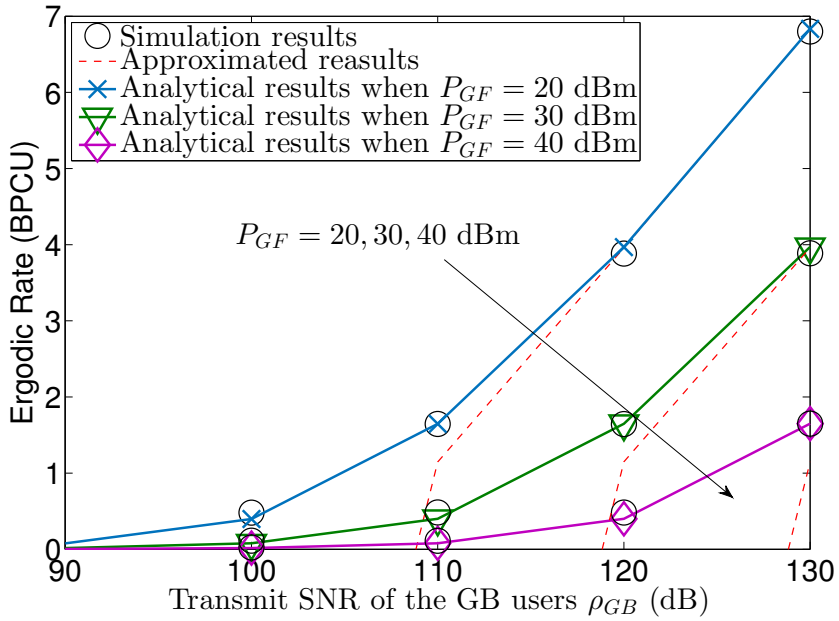

Figure 3.8: Ergodic rates (BPCU) of the GB user v.s. transmit SNR of GB users ρ_{GB} (dB)

In Fig. 3.8, it depicts the ergodic rates of the GB users versus $\rho_{GB} = P_{GB}/\sigma^2 \in [0, 40]$ dB with various transmit power of the GF user $P_{GF} = \{20, 40\}$ dBm. The dashed lines are the approximated ergodic rates, which match simulation results in high SNR regions. One observation is that the performance of the GB users has no error floors. Thus, allocating combinations of transmit powers for the GF and GB users can avoid performance deterioration. Another observation is that the ergodic rates are reduced when the transmit power P_{GF} increases since the GF users are considered as interference to the GB user.

In Fig. 3.9, this chapter investigates the ergodic rate performance corresponding to the GF users versus $\rho_{GF} = P_{GF}/\sigma^2 \in [0, 40]$ with transmit power of the GB user $P_{GB} = \{20, 40\}$ dBm. The dashed lines represent

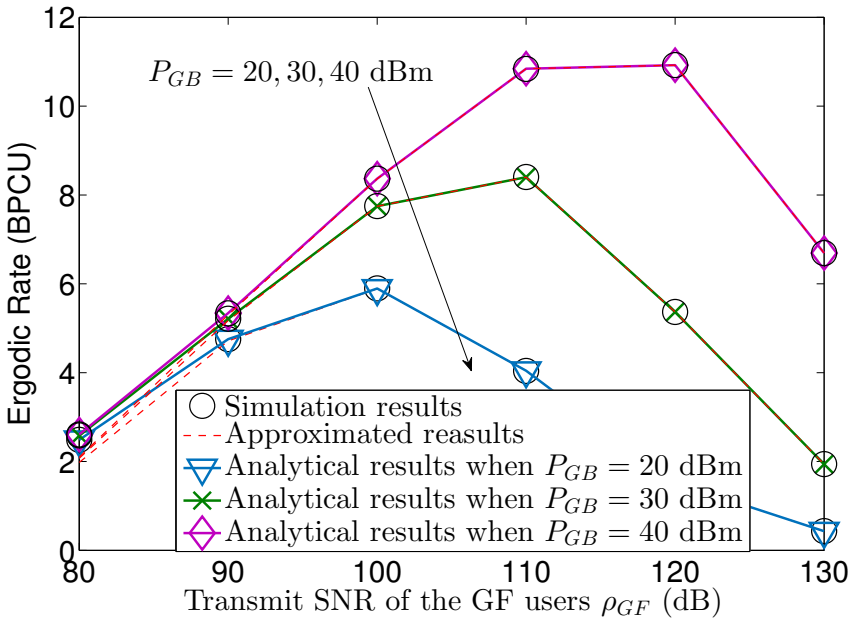

Figure 3.9: Ergodic rates (BPCU) of the GF user v.s. transmit SNR of GF user ρ_{GF} (dB)

approximated ergodic rate expressions. It is observed that the ergodic rate performance has the maximum value. After reaching the maximum value, the ergodic rates decrease when enhancing the GF users' transmit power. This is because when the transmit powers of GF users increase, the SIC procedure will have high outage situations, which causes the message of the GF users cannot be decoded.

The Fig. 3.10 compares the performance of NOMA and OMA in this Semi-GF transmission network. A GF user and a GB user are paired, and we separately exploit NOMA and OMA techniques to transmit the signals. The ergodic sum rates include the entire achievable rates of the two users. The transmit power of the GF user and the GB user is set as $[-20, 30]$ dB. This figure clearly reveals that the metric, ergodic sum rates, of NOMA performs better than that of OMA. Hence, for increasing the ergodic sum rates of the entire system, NOMA is a more promising technique than OMA.

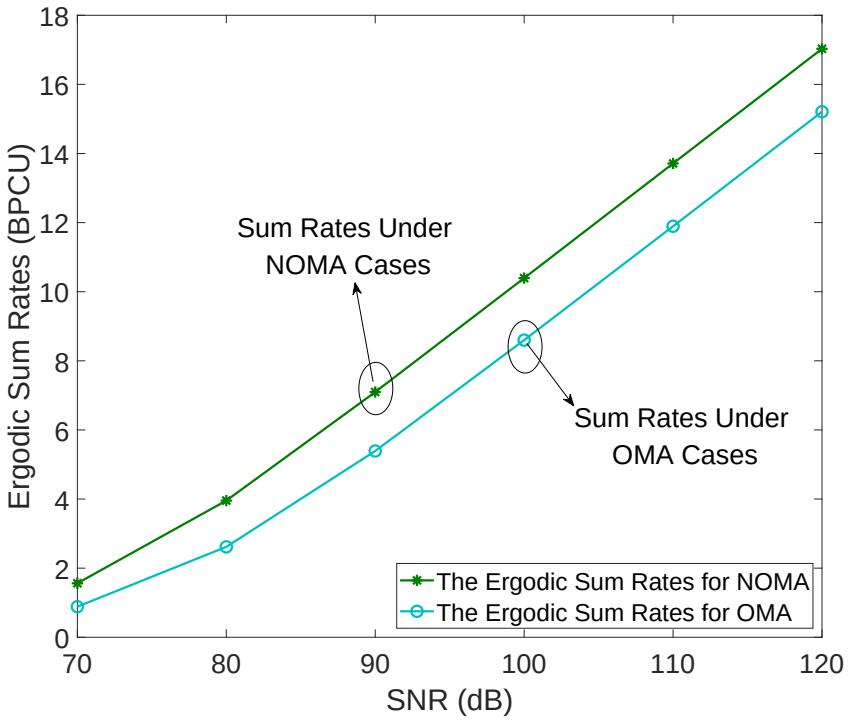

Figure 3.10: Ergodic sum rates (BPCU) v.s. transmit SNR of users (dB): A comparison between OMA and NOMA.

3.6 Conclusions

To reduce collision situations and enhanced spectrum efficiency, Semi-GF NOMA networks are investigated with the aid of stochastic geometry approaches. With the open-loop protocol as the benchmark, a novel dynamic protocol has been proposed to select GF users into NOMA channels. Compared with the open-loop protocol, the dynamic protocol provides more accurate channel quality thresholds, which enables to reduce the interference from the GF users. Based on the types of GB users (latency-sensitive users or latency-tolerant users), two potential scenarios with various SIC orders have been considered: 1) near GB users with far GF users in Scenario I and 2) far GB users and near GF users in Scenario II. Under the two scenarios, outage probabilities have been derived via analytical, asymptotic, and approximated expressions for the GB and GF users. Analytical results have

concluded that under two scenarios for both protocols, consistent diversity gains are determined by the SIC orders that equal to 1) one for near users and 2) zero for far users. Validated by numerical results, it is revealed that the dynamic protocol enhances the outage performance more than the open-loop protocol.

This chapter investigates NOMA-aided Semi-GF transmission which holds the potential to realize dual-functional massive connectivity in 6G mMTC systems. While NOMA-assisted Semi-GF transmission enhances connectivity in 6G mMTC systems, it cannot avoid the influence of channel environments. Users with significant blockages might be hard to decode information due to low received power and increased interference, typically experienced by cell-edge users in NOMA setups. As protocol design might not resolve environmental issues, this thesis shifts focus to exploring RISs in NOMA systems in the next chapter.

Chapter 4

Multi-Cell NOMA Networks With Linear RISs

This chapter investigates RIS-aided NOMA networks to cover the blind areas and thus to further enhance the connectivity. With the aid of stochastic geometry methods to capture the spatial effect of users and BSs, the RIS-aided NOMA networks are extended from single-cell scenarios to multi-cell scenarios to investigate the performance of practical cases. The main contributions of this chapter are summarized as follows:

- A general model of RIS reflecting links is characterized. Based on the general case of RIS reflecting links, the path loss model in long-distance regions is introduced. By modelling the multi-cell networks as a PCP model, the angle distributions are investigated, which verifies that the angles (formed by users, RISs, and BSs) are uniformly distributed in $[0, \pi]$.

- The closed-form analytical expressions for coverage probabilities of the paired NOMA users are derived to enhance the evaluation efficiency. To investigate the impact of RISs, the asymptotic expressions for the typical user in terms of the half-length of RISs L are calculated. The analytical results indicate that it is capable of improving the coverage probability by adding the length of RISs.

- The closed-form analytical expressions for ergodic rates of the paired NOMA users are derived. Additionally, the asymptotic ergodic rate

expressions for the typical user in terms of the half-length of RISs are calculated. The analytical results show that the achievable rates reach an upper limit when continuously enhancing the length of RISs. Additionally, enlarging the length of RISs can improve the path loss intercept, thereby enhancing the coverage performance.

- Numerical results illustrate the following conclusions. 1) For the connected user, RIS-aided NOMA channels have superior coverage performance than RIS-aided OMA channels while it is on the contrary for the typical user. Additionally, for both NOMA users, RIS-aided networks acquire significantly enhanced performance than conventional scenarios without RISs. 2) If near users are delay-sensitive users, the RISs can be exploited to avoid the SIC procedures at near users. This is because the RISs have the ability to enhance the channel quality effectively to alter the SIC orders.

4.1 System Model

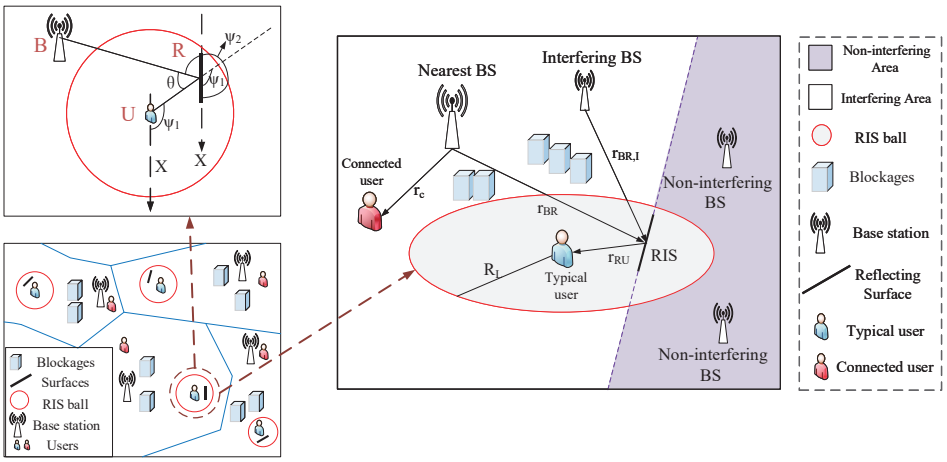

Figure 4.1: Illustration of the signal model: (a) Bottom-left: An illustration of RIS-aided multi-cell scenarios; (b) Top-left: A typical NOMA network with angle demonstrations; (c) Right: A typical NOMA network with two types of BSs, such as interfering BSs facing RISs and non-interfering BSs against RISs.

This chapter RIS-aided downlink NOMA networks, where BSs and users are modeled according to two independent homogeneous Poisson point processes (HPPPs), namely $\Phi_b \subset \mathbb{R}^2$ with density λ_b and $\Phi_u \subset \mathbb{R}^2$ with density λ_u, respectively. We consider RISs performing as linear materials, a sheet of electromagnetic material of negligible thickness. Additionally, we assume that two-user NOMA groups are served by orthogonal frequencies to cancel intra-cell interference. In each group, we assume that one of the paired users has already been connected to a BS in the previous user association process [33]. The other one, namely the typical user[1], joins this occupied resource block by applying power-domain NOMA techniques. To simplify the analysis, the connected user is not included in the user set Φ_u and the distance between this user to its BS is invariable as r_c. The typical user is randomly selected from Φ_u and its location is fixed at the origin $\mathbb{O}(0,0)$ [2] of the considered plane, namely $\mathbf{x}_U$.

4.1.1 LoS Ball Model

The blockage model is significant for RIS-aided networks as one promising application of RISs is to enhance the performance of blocked users by providing LoS transmission [23]. We consider an LoS ball model for the typical user in this work [35, 128]. For the typical user, its LoS ball has a radius R_L. The transmitters within this ball provide LoS transmission, while those outside this ball have NLoS links. The LoS ball region of the typical user is given by $\mathbb{O}(0, R_L) \subset \mathbb{R}^2$, where $\mathbb{O}(a, b)$ represents an annulus with the inner radius a and outer radius b. To ensure the RIS-to-User (RU) link is LoS, the RIS is uniformly distributed in the LoS ball area of the typical user. Due to considering a blocked typical user, the region of considered BSs is in the range $\mathbb{O}(R_L, \infty)$.

[1]We assume that the typical user is deployed in a cell with dense obstacles, i.e., tall buildings, thus the links from BSs to the user are blocked severely [35]. We additionally consider the RISs are deployed on tall buildings, hence the deployment of RISs is random.

[2]For BSs located in the RIS ball area $\mathbb{O}(0, R_L)$, RISs may weaken their direct LoS transmission due to phase difference [23]. Coherent transmission is desired for this case, which is beyond the scope of this paper.

4.1.2 RIS-aided Link Model

Before introducing the link modes, several assumptions are first listed here for the following use:

- Assume that only one RIS is employed for helping the typical user. As RISs have a significant influence on enhancing the performance of users, we consider one RIS is enough for the typical user on the performance enhancement. Hence, we can assume a few RISs are deployed in large areas, thus no more RIS in the same LoS ball. The cases with densely deployed RISs are left for future works. Hence, each LoS ball only has a piece of RISs assisting a typical user.

- Assume that the RISs near the typical user (in the LoS ball of the typical user) create the LoS link between the user and the RISs. We consider that the BS is located at a high altitude. Hence, the BS and the RISs can also build a LoS link although the BS is not in the LoS ball of the typical user.

- Assume that the distance between the BS and the typical user is much larger than the radius of the LoS ball. Hence, it is assumed that the distance between the BS and the RISs is approximately equal to the distance from the BS to the typical user[3].

Based on stochastic geometry principles and the randomness of the typical user, users and their serving RISs can be regarded as the Matern cluster process (MCP) pattern of PCP models with a fixed number of nodes in each cluster. More specifically, the possible typical users are the parent point process deployed by HPPPs, where we choose one of them as the considered typical user. The RISs are uniformly deployed in the clusters (LoS balls) as

[3]This assumption is exploited in the urban areas, such as the big cities like Sydney. Since tall buildings are distributed in the city, the height of a user (might be a person) is much lower than the buildings, hence the LoS ball radius is small. However, the BSs are placed at some tall buildings or use towers with high altitude. It is easy to make sure the links between the typical user and the BS are LoS links. Since the RISs only reflect the signals with limited angles or directions but do not transmit signals, the RISs should better be placed within the LoS ball to make sure of their effects.

the daughter point process. The channel conditions of the connected user have been known with a fixed distance. Based on the MCP model, there are three significant communication links in the considered NOMA group: 1) The BS-to-User (BU) link, the link between the typical user and its BS; 2) The BS-to-RIS (BR) link, the link between the BS and the employed RIS; and 3) The RU link, the link between the RIS and the typical user. This work focuses on analyzing a blocked typical user and the RIS is applied to establish LoS route between the typical user and BSs [23]. Therefore, the BU link is assumed to be NLoS and the BR and RU links are LoS. Moreover, all NLoS communications are ignored in this paper due to their negligible received power.

The association criterion (to connect a BS) for the typical user is to associate with the BS offering the highest received power, which means that the distance between the typical user and the associated BS is the nearest. We define the locations of the RIS and the associated BS are $\mathbf{x}_R$ and $\mathbf{x}_B$. Therefore, the distance between the associated BS and the RIS is correspondingly expressed as

$$\mathbf{x}_{BR} = \arg \min_{\mathbf{x}_B \in \Phi_B} \|\mathbf{x}_B - \mathbf{x}_R\|, \tag{4.1}$$

where $\mathbf{x}_R \in \mathbb{O}(0, R_L)$, $\Phi_B \subset \Phi_b$, $\Phi_B \subset \mathbb{O}(R_L, \infty)$ and the location of arbitrary interfering BS is denoted by $\mathbf{x}_I \in \Phi_r \setminus \mathbf{x}_B$.

4.1.3 Path Loss Model

This work considers a $2L$ linear RIS, whose central point is located at $\mathbf{X}_{R(0)} = \left(x_{R(0)}, y_{R(0)}\right) \subset \mathbb{O}(0, R_L)$. We define the associated BS and the typical user are distributed in the same side of the RIS to establish reflecting transmission [129]. In Fig. 4.2, we assume the x-axis is along the direction of RISs and the typical user is at the origin. Thus, the coordinate of each point on the RIS with a distance $l \in [-L, L]$ is expressed as $\mathbf{x}_R(l) = (x_R(0) + l\cos(\theta_R(l)), y_R(0) + l\sin(\theta_R(l))) \subset \mathbb{R}^2$, where $\theta_R(l)$ is the

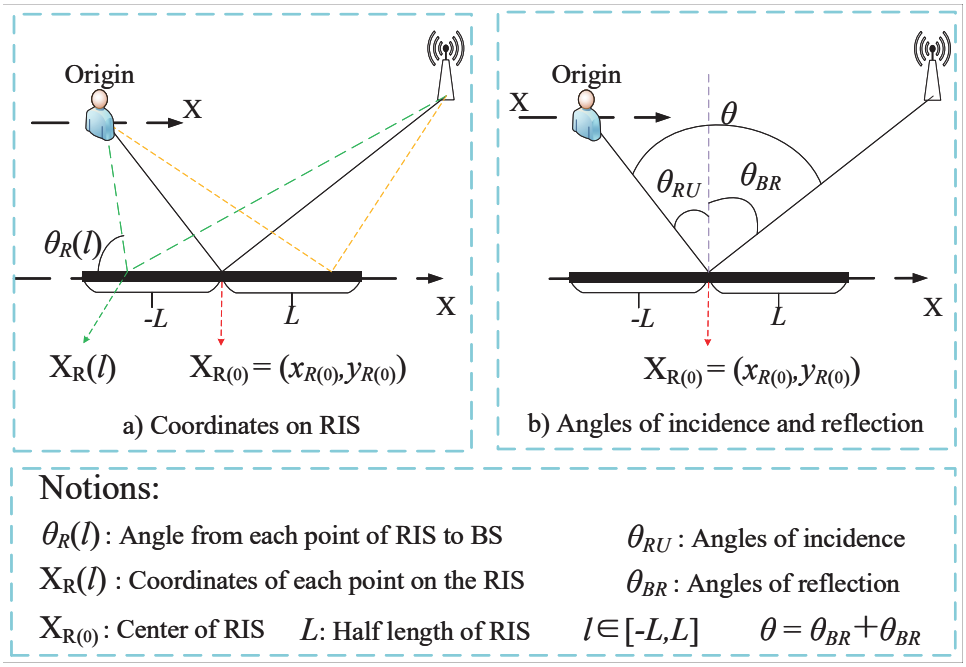

Figure 4.2: Coordinates and angles in LoS balls: a) Coordinates on RIS; b) Angles of incidence and reflection

angle to x-axis for each point on the RIS. We set $r_{Q(0)}$ and $\theta_{Q(0)}$ as the distance and angle through the center of RISs $\mathbf{X}_{R(0)}$, where $Q \in \{BR, RU\}$ represents the links from BSs to RISs and other links from RISs to the typical user. Additionally, we assume surfaces are deployed based on long-distance communication models, thereby the surfaces receive directional lights with approximations as $r_Q(x) \approx r_{Q(0)} + qx \sin\left(\theta_{Q(0)}\right)$ where $q = 1$ if $Q = BR$ and $q = -1$ if $Q = RU$ [27].

Influenced by devices' locations, the considered model suits for the communications with highly correlated channels, such as millimeter wave channels or THz channels. The channel correlation is provided in (4.3) and the description after (4.3). Hence, in Fig. 1, we exploit the physical angles, namely, angles of incident $\theta_{\mathrm{BR}}(l)$ and angles of reflection $\theta_{\mathrm{RU}}(l)$ instead of the angles of arrival (AoA) and the angles of departure (AoD). We express the AoA and AoD as $\angle AOA = \pi/2 - \theta_{\mathrm{BR}}(l)$ and $\angle AOD = \pi/2 + \theta_{\mathrm{RU}}(l)$. With the aid of AoA and AoD, our analysis is able to provide a general

guideline for designing RISs with MIMO systems. Under a high-frequency case with cylindrical electromagnetic (EM) waves [130], if one transmitting BS is located at $\mathbf{x}_b \in \{\mathbf{x}_B, \mathbf{x}_I\}$, the path loss model for the typical user is given by [27]

$$\mathcal{P}_t(\mathbf{x}_b, \mathbf{x}_R, \mathbf{x}_U) = \left| \int_{-L}^{+L} \Psi(l) \exp(-jk\Omega(l))\, dl \right|^2, \tag{4.2}$$

where

$$\Psi(l) = \frac{\cos(\theta_{\mathrm{BR}}(l)) + \cos(\theta_{\mathrm{RU}}(l))}{8\pi\sqrt{r_{\mathrm{BR}}(l) r_{\mathrm{RU}}(l)}}, \tag{4.3}$$

$$\Omega(l) = r_{\mathrm{BR}}(l) + r_{\mathrm{RU}}(l) - \Theta(l), \tag{4.4}$$

where $k = 2\pi/\lambda$ with wavelength λ and the communication distance for the BR and the RU links are $r_{\mathrm{BR}}(l) = \|\mathbf{x}_b - \mathbf{x}_R(l)\|$ and $r_{\mathrm{RU}}(l) = \|\mathbf{x}_R(l) - \mathbf{x}_U\| = \|\mathbf{x}_R(l)|$, respectively, with $\theta_{\mathrm{BR}}(l) = \arcsin\left(\frac{l}{\|\mathbf{x}_b - \mathbf{x}_R(l)\|}\right)$ and $\theta_{\mathrm{RU}}(l) = \arcsin\left(\frac{l}{\|\mathbf{x}_R(l)\|}\right)$. Considering the reflecting point is at $\mathbf{x}_R(l)$, the angle of incidence $\theta_{\mathrm{BR}}(l) \in \left(0, \frac{\pi}{2}\right]$ represents the angle between the corresponding BR link and the perpendicular bisector of the RIS, whilst the angle of reflection $\theta_{\mathrm{RU}}(l) \in \left(0, \frac{\pi}{2}\right]$ is the angle between the corresponding RU link and the perpendicular bisector of the RIS. The $\Theta(l)$ is the phase-shifting parameter of RISs which is decided by the desired transmitter and receiver.

For the connected user at $\mathbf{x}_c \subset \mathbb{R}^2$, we assume the transmission between this user and its BS follows conventional wireless communications. Therefore, the path loss expression of the connected user is as follows

$$\mathcal{P}_c(\mathbf{x}_b, \mathbf{x}_c) = C\|\mathbf{x}_b - \mathbf{x}_c\|^{-\alpha_c}, \tag{4.5}$$

where the C is intercept and α_c is the path loss exponent for the direct link. Note that the distance between the connected user and the associated BS is fixed. Therefore, $r_c = \|\mathbf{x}_B - \mathbf{x}_c\|$ is a constant.

4.1.4 Signal Model

We assume the BSs have known the demand of quality of service (QoS) of users to split delay-sensitive users and delay-tolerant users, thereby the QoS-based SIC is harnessed in this paper [131]. Additionally, knowing the channel state information at BSs is able to enhance the accuracy of beamforming designs. When we consider a special case where a delay-sensitive near user (the connected user) pairs with a delay-tolerant far user (the typical user), the far user with SIC process may experience outage frequently because of poor channel quality. By enhancing the channel quality of the far user, RISs are exploited to improve the SIC success rate. Based on QoS-based NOMA, the associated BS allocates more transmit power to the connected user than the typical user and SIC is processed at the typical user[4]. Therefore, the SINR for the SIC process at the typical user is given by

$$\gamma_{\mathrm{t,SIC}} = \frac{a_c P_b |h_{t_1,\mathbf{x}_B} h_{t_2,\mathbf{x}_B}|^2 \mathcal{P}_t(\mathbf{x}_b, \mathbf{x}_R, \mathbf{x}_U)}{a_t P_b |h_{t_1,\mathbf{x}_B} h_{t_2,\mathbf{x}_B}|^2 \mathcal{P}_t(\mathbf{x}_b, \mathbf{x}_R, \mathbf{x}_U) + I_{t,\rho_t} + \sigma^2}, \tag{4.6}$$

where

$$I_{t,\rho_t} = \rho_t \sum_{\mathbf{x}_I \in \Phi_b \setminus \mathbf{x}_B} P_b |h_{t_1,\mathbf{x}_I} h_{t_2,\mathbf{x}_I}|^2 \mathcal{P}_t(\mathbf{x}_I, \mathbf{x}_R, \mathbf{x}_U), \tag{4.7}$$

and P_b is the transmit power of BSs in each NOMA group and σ^2 is the variance of additive white Gaussian noise (AWGN). The a_t and a_c are the power allocation parameters for the typical user and the connected user, respectively. Moreover, $a_c > a_t$ and $a_c + a_t = 1$. When the transmitter is at $\mathbf{x}$, for the receiver κ, $h_{\kappa,\mathbf{x}}$ represents its Nakagami fading term with an integer parameter m_κ [132]. Additionally, $\kappa = c$ means the receiver is the connected user and $\kappa = \{t_1, t_2\}$ means the two channels from the RIS to the typical user. Additionally, we define the coefficients of Nakagami-m distributions as m_c for the connected user and $\{m_{t_1}, m_{t_2}\}$ for the typical

[4]In this paper, we exploit fixed power allocation coefficients. The optimized power allocation schemes will be considered in future works.

user. Regarding the interference I_{t,ρ_t}, since the signal from the back of RISs cannot pass through RISs, we assume $\rho_t \in [0,1]$ of the entire interference is able to reach the receiver κ. With the uniform deployment of BSs following the PPP, if we consider the RIS splits the area into two equal sub-areas, we have $\rho_t = 0.5$.

After the SIC process, the typical user decodes its data. The decoding SINR is expressed as

$$\gamma_t = \frac{a_t P_b |h_{t_1,\mathbf{x}_B} h_{t_2,\mathbf{x}_B}|^2 \mathcal{P}_t(\mathbf{x}_b, \mathbf{x}_R, \mathbf{x}_U)}{I_{t,\rho_t} + \sigma^2}. \tag{4.8}$$

For the connected user, it directly decodes its messages by regarding the partner's signal as interference. Therefore, the decoding SINR for the connected user is as follows

$$\gamma_c = \frac{a_c P_b |h_{c,\mathbf{x}_B}|^2 \mathcal{P}_c(\mathbf{x}_B, \mathbf{x}_c)}{a_t P_b |h_{c,\mathbf{x}_B}|^2 \mathcal{P}_c(\mathbf{x}_B, \mathbf{x}_c) + I_c + \sigma^2}, \tag{4.9}$$

where

$$I_c = \sum_{\mathbf{x}_I \in \Phi_b \setminus \mathbf{x}_B} P_b |h_{c,\mathbf{x}_I}|^2 \mathcal{P}_c(\mathbf{x}_I, \mathbf{x}_c). \tag{4.10}$$

It is worth noting that the connected user is interfered by all BSs excepting the associated BS.

4.2 Channel Model Approximation

In this section, we derive the expressions of the path loss model and angle distributions, which are fundamental for analyzing the performance of RIS-aided NOMA systems.

4.2.1 Small-scale Fading Approximation

First, we assume that the small-scale fading follows Nakagami-m fading channels. The Nakagami-m fading channels indicate the LoS or NLoS chan-

nels by adjusting the channel coefficient m. When we have $m = 2$, it reveals the Rayleigh fading channels with all NLoS links. When we increase the coefficient m, the LoS component gets stronger until $m = \infty$ as the ideal LoS case. As we consider the RIS as linear materials, we have two independent Nakagami-m fading channels for the RIS-aided link, i.e., $h_{t_1,\mathbf{x}_B}$ as the fading channel from the BS to the RIS, and $h_{t_2,\mathbf{x}_B}$ as the channel from the RIS to its aided user. Hence, the equivalent channel model is the product of these two variables, denoted as $h_{t,\mathbf{x}_B} = h_{t_1,\mathbf{x}_B} h_{t_2,\mathbf{x}_B}$. In power domain, the distribution of $|h_{t,\mathbf{x}_B}|^2$ is needed for the following derivations, thus we exploit the Matlab curve fitting tool to mimic the channel distribution [133]. We conclude that the distribution of $|h_{t,\mathbf{x}_B}|^2$ can be mimicked as a Gamma distribution with coefficient m_t and b_t. This approximated distribution is presented as

$$f_{|h_{t,\mathbf{x}_B}|^2}(x) = \frac{x^{m_t-1}}{\Gamma(m_t)\, b_t^{m_t}} \exp\left(-\frac{x}{b_t}\right), \tag{4.11}$$

$$F_{|h_{t,\mathbf{x}_B}|^2}(x) = \frac{\gamma(m_t, x/b_t)}{\Gamma(m_t)}, \tag{4.12}$$

where we obtained $m_t = 1$ and $b_t \approx 1$ when we set $m_{t_1} = m_{t_2} = 2$.

4.2.2 Path Loss Model

Since surfaces are always installed on the walls of buildings, adjusting angles of surface physically may have constraints based on the shapes or directions of the walls. In this scenario, we operate the surfaces as anomalous reflectors, which is configured for reflecting waves towards a distinct direction of users. Hence, the reflection angle of waves is able to be unequal to the incidence angle.

Lemma 6. We regard surfaces as RISs rather than mirrors, thereby the angle of incidence enables to be different from the angle of reflection. As we consider the RU link as a strong LoS link, we are interested in analyzing only reflections and thus ignore parasitic scattering [35]. Under this case, we are able to obtain the phase-shifting parameter as $\Theta(l) =$

$\left(\sin\left(\theta_{BR(0)}\right) - \sin\left(\theta_{RU(0)}\right)\right) l + \phi_0/k$, where $\phi_0 \in [0, 2\pi)$ is a fixed phase shift of the direction of a user and $k = 2\pi/\lambda$ is the wavenumber with the wavelengh λ [27]. Hence, the direction is altered to the typical user via the phase shifters. Considered on the long-distance regions with directional lights, the path loss model on RIS operations is expressed as

$$\mathcal{P}_t^{RIS} \approx C_{RIS}^2 \left(r_{BR(0)} r_{RU(0)}\right)^{-\alpha_t}, \tag{4.13}$$

where $C_{RIS}=\frac{L}{4\pi}\left(\cos\left(\theta_{BR(0)}\right) + \cos\left(\theta_{RU(0)}\right)\right)$, α_t is the path loss exponent of the typical user.

Proof. Substituting $\Theta(x)$ into $\Psi(x)$, it is simplified as $\Psi(x) = r_{BR(0)} + r_{RU(0)} - \frac{\phi_0}{k}$. Since the BSs are assumed to emit cylindrical waves, we assume that $r_Q(x) \approx r_{Q(0)} + qx \sin\left(\theta_{Q(0)}\right)$. Thus, the pass loss model is approximated as

$$\begin{aligned} \mathcal{P}_t^{RIS} \approx & \left| \frac{L}{4\pi} \left(r_{BR}(l)\, r_{RU}(l)\right)^{-\frac{\alpha_t}{2}} \right|^2 \\ & \times \left| \left(\cos\left(\theta_{BR(0)}\right) + \cos\left(\theta_{RU(0)}\right)\right) \right|^2 \\ & \times \left| \exp\left(-jk\left(r_{BR(0)} + r_{RU(0)} - \frac{\phi_0}{k}\right)\right) \right|^2, \end{aligned} \tag{4.14}$$

and we obtain (4.13) via algebraic manipulations. □

4.2.3 Distance Distributions

Note that the users and BSs are settled via two independent HPPPs and reflecting surfaces are uniformly deployed within the ball $\mathbb{O}(0, R_L)$ of the typical user. Based on the MCP pattern of PCP models, locations are defined that users are parent nodes obeying HPPP and surfaces are daughter nodes within the clusters of RIS balls. Based on the aforementioned settings, we derive the probability density functions (PDFs) of distances of the corresponding cluster and other clusters for a typical user.

4.2.3.1 The Corresponding Cluster of the Typical User

We focus on a typical user located at the center of the RIS ball area served by uniformly distributed intelligent surfaces [31]. Thus, we are capable of deriving the PDF of the distance from a surface to its targeted typical user, denoted as r_{RU}, as

$$f_{r_{RU}}(x) = \frac{2x}{R_L^2} U(R_L - x), \tag{4.15}$$

where $U(\cdot)$ is the unit step function.

4.2.3.2 Other Clusters of the Typical User

Since the LoS links from BSs to the typical user are blocked, we only investigate the reflecting links from the BSs to the surfaces. Thus, based on the null probability of a 2-D PPP within in the RIS ball area and order statistics [74, 134], the PDF of the distance between a RIS and its n^{th} nearest BS is derived as

$$f_{r_{BR}}(x, n) = \frac{2(\pi\lambda_b)^n}{(n-1)!} x^{2n-1} \exp\left(-\pi\lambda_b x^2\right). \tag{4.16}$$

4.2.4 Angle Distributions

Shown as Fig. 4.1, we denote a BS as node B, a RIS as node R, and a typical user as node U to clarify the angles. With the aid of a chosen positive X-axis that is parallel to the RIS, the angles are illustrated as $\psi_1 = \angle RUX$, $\psi_2 = \angle BRX$ and $\theta = |\pi - |\psi_2 - \psi_1||$. Notice that the angle of ψ_2 is uniformly distributed within $(0, 2\pi)$ based on the properties of HPPP. We additionally observe that the angle of ψ_1 obeys uniform distribution in $(0, 2\pi)$ since the RIS is uniformly distributed in the RIS ball. Based on ψ_1 and ψ_2 with the same distributions, the CDF of $|\psi_2 - \psi_1|$ is derived as

$$F_{|\psi_2 - \psi_1|}(z) = \frac{4\pi z - z^2}{4\pi^2}, \tag{4.17}$$

therefore, the PDF of the angle of $|\psi_2 - \psi_1|$ is derived as $f_{|\psi_2-\psi_1|}(z) = \frac{2\pi - z}{2\pi^2}$.

With the respect to $\theta = |\pi - |\psi_2 - \psi_1||$, the CDF of the angle θ is derived as

$$F_\theta(x) = F_{|\psi_2-\psi_1|}(x+\pi) - F_{|\psi_2-\psi_1|}(x-\pi) = \frac{x}{\pi}, \tag{4.18}$$

which is proved that the angle θ obeys uniform distribution within $(0, \pi)$ with the PDF as $f_\theta(x) = 1/\pi$.

Recall that we denote the angles of incidence as $\theta_{BR(0)}$ and the angles of reflection as $\theta_{RU(0)}$, thereby we are able to observe $\theta = \theta_{BR(0)} + \theta_{RU(0)}$ from Fig. 4.2. In the following, the angle analysis with respect to RISs is investigated.

When the surfaces are designed as RISs, the angles of incidence and reflection are unequal. We define the angles of incidence $\theta_{BR(0)} = \rho_a \theta$, where $\rho_a \in (0, 1)$, thereby the angles of reflection is $\theta_{RU(0)} = (1 - \rho_a)\theta$. Hence, the PDFs of the angles of incidence and reflection are derived as

$$f_{\theta_{BR(0)}}(x) = \frac{1}{\rho_a \pi}, x \in \left(0, \frac{\pi}{2}\right), \tag{4.19}$$

$$f_{\theta_{RU(0)}}(x) = \frac{1}{(1-\rho_a)\pi}, x \in \left(0, \frac{\pi}{2}\right). \tag{4.20}$$

Remark 10. *As shown in Fig. 4.2, we note that the angles ψ_1 and ψ_2 are uniform distributed in the range of $[0, 2\pi]$. Based on the derivations in this subsection, we conclude that the BS-RIS-User angle is uniformly distributed in $[0, \pi]$. Hence, we are able to extend the conclusion that any angle formed via three nodes of a PPP are uniformly distributed.*

Lemma 7. Considered on an average case with a 2-D HPPP, the angles are uniformly distributed. As communication distances are independent of incidence and reflection angles, after considering the random spatial effect, the path loss of RIS links in **Lemma 6** is rewritten as

$$\mathcal{P}_t^{RIS} = C_{RIS,E}^2 \left(r_{BR(0)} r_{R_i U(0)}\right)^{-\alpha_t}, \tag{4.21}$$

where $C_{RIS,E}^2 = \frac{L^2}{16\pi^3}\left(\pi + \frac{\sin(2\rho_a\pi)}{4\rho_a - 12\rho_a^2 + 8\rho_a^3}\right)$.

Proof. The average path loss with respect to angles is expressed as $\mathcal{P}_t^{RIS} = \mathbb{E}\left[C_{RIS}^2\right] \times \left(r_{BR(0)} r_{R_i U(0)}\right)^{-\alpha_t}$, where $\mathbb{E}[\cdot]$ is calculating the expectation. By plugging (4.19) and (4.20), this lemma is proved. □

Under a vacuum scenario with the best channel environment as mentioned in [27], the path loss exponent of reflecting links $\alpha_t = 1$. For practical scenarios, this path loss exponent α_t should be larger than one. Therefore, we consider $\alpha_t > 1$ in the rest of this work. The path loss exponent for conventional models are defined as $\alpha_{RF} > 2$.

Remark 11. *We assume the distance between the BS to the typical user as a fixed distance, denoted as r_{fix} with $r_{BR(0)} + r_{R_i U(0)} = \mathcal{D} r_{fix}$. We denote P_r^{RIS} and P_r^{RF} as the received power for RIS-aided channels and RF channels, respectively. When RF channels and RIS-aided channels follow the same kind of fading channels, we define the RIS gain as*

$$\beta_{RIS} = \frac{\mathbb{E}[P_r^{RIS}]}{\mathbb{E}[P_r^{RF}]} = \frac{C_{RIS,E}^2 \left(r_{BR(0)} r_{R_i U(0)}\right)^{-\alpha_t}}{C_{RF} r_{fix}^{-\alpha_t}} \geq \frac{4^{\alpha_t} C_{RIS,E}^2}{\mathcal{D}^2 C_{RF} r_{fix}^{\alpha_t}} = \frac{\beta_c L^2}{r_{fix}^{\alpha_t}}, \tag{4.22}$$

where $\beta_c = \frac{4^{\alpha_t}}{16\mathcal{D}^2 C_{RF}\pi^3}\left(\pi + \frac{\sin(2\rho_a\pi)}{4\rho_a - 12\rho_a^2 + \rho_a^3}\right)$, $\mathcal{D} \geq 1$ is an arbitrary positive number, $C_{RF} = \left(\frac{c}{4 f_c \pi}\right)^2 = \frac{1}{16\pi^2}\left(\frac{c}{f_c}\right)^2$ is the intercept, $c = 3 \times 10^8$ m/s is the speed of light, and f_c is the bandwidth of users. Hence, the minimum RIS gain is directly influenced by the length of RISs and the distance between the BS and the typical user. We conclude that deploying RISs at the perpendicular bisector of the BU link results in the minimum RIS gain.

Remark 12. *Compared to conventional far-field propagation model $\mathcal{P}_{\text{far-field}}^{RIS} = \left(r_{BR(0)} r_{R_i U(0)}\right)^{-\alpha_t} C_{RF}$, the path loss model for linear materials has several differences. 1) Different path loss intercept: With $\rho_a \in (0, 1]$, we have $C_{RIS,E}^2 = \frac{L^2}{16\pi^3}\left(\pi + \frac{\sin(2\rho_a\pi)}{4\rho_a - 12\rho_a^2 + 8\rho_a^3}\right) \in \left[\frac{3L^2}{32\pi^2}, \frac{L^2}{8\pi^2}\right]$, which is higher than $\frac{1}{16\pi^2}$ in far-field propagation model. 2) If RISs are near to the typical user, we*

approximately derive $\beta_{RIS} \approx \left(\frac{Lf_c}{c}\right)^2$*, thus we can enlarge the length of RISs to improve the path loss intercept. 3) As the channel model for linear materials is based on the Huygens-fresnel principle, it suits for both of near-field and far field scenarios with broad application scenarios.*

4.3 Coverage Performance Evaluation

When we pre-decide a fixed threshold rate, the communication performance is guaranteed when the transmit rates are higher than the threshold. By defining a fixed threshold to evaluate whether the QoS of a network is satisfied, we investigate the SINR coverage performance on our RIS-aided NOMA networks based on the derived path loss expressions.

Since we exploit the typical user with SIC procedures and the messages of the connected user are directly decoded, the coverage probability expressions for the connected user and the typical use are expressed respectively as

$$\mathbb{P}_t = \Pr\left\{\gamma_{\mathrm{t,SIC}} > \gamma_{SIC}^{th} | \gamma_t > \gamma_t^{th}\right\}, \tag{4.23}$$

$$\mathbb{P}_c = \Pr\left\{\gamma_{\mathrm{c}} > \gamma_c^{th}\right\}, \tag{4.24}$$

where $\Pr\{\cdot\}$ is the probability operation, γ_{SIC}^{th} is the threshold of SIC procedures, $\gamma_t^{th} = 2^{R_t/B_w} - 1$ is the coverage threshold of the typical user with threshold rate R_t and bandwidth B_w, $\gamma_c^{th} = 2^{R_c/B_w} - 1$ is the threshold of the connected user with threshold rate R_c.

4.3.1 Interference Analysis

Before evaluating the coverage performance of this network, we would first derive the Laplace transform of interference, I_{t,ρ_t} and I_c, under two scenarios.

4.3.1.1 Interference Analysis of the Connected User

Since the connected user is not served by reflecting surfaces, the Laplace transform of the interference for the connected user is expressed via conventional wireless communication analysis [31] as

$$\mathcal{L}_c(s)=\mathbb{E}\left[\exp\left(-\sum_{\mathbf{x}_I\in\Phi_r\setminus\mathbf{x}_B} P_b C|h_{t_1,\mathbf{x}_I}h_{t_2,\mathbf{x}_I}|^2 {r_{c,I}}^{-\alpha_c}\right)\right]. \tag{4.25}$$

Lemma 8. The Laplace transform of interference for the connected user is derived as

$$\mathcal{L}_c(s)=\exp\left(-\varsigma_1\left({}_2F_1\left(-\frac{2}{\alpha_c},m;1-\frac{2}{\alpha_c};-\varsigma_2 s\right)-1\right)\right), \tag{4.26}$$

where ${}_2F_1\left(\cdot,\cdot;\cdot;\cdot\right)$ is the hypergeometric function, $\varsigma_1=\pi\lambda_b r_c^2$ and $\varsigma_2=\frac{P_b C}{m r_c^{\alpha}}$.

Proof. See Appendix B.1. □

4.3.1.2 Interference Analysis of the Typical User in RIS Scenario

With the aid of **Lemma 7**, the Laplace transform of the interference under RIS scenarios is expressed as

$$\mathcal{L}_{t,RIS}(s)=\mathbb{E}\left[\exp\left(-\rho_t\sum_{\mathbf{x}_I\in\Phi_r\setminus\mathbf{x}_B}\frac{P_b C_{RIS,I}^2|h_{t_1,\mathbf{x}_I}h_{t_2,\mathbf{x}_I}|^2}{\left(r_{BR(I)}r_{RU(I)}\right)^{\alpha_t}}\right)\right]. \tag{4.27}$$

Lemma 9. With the aid of RISs, the Laplace transform of interference for the typical user is derived as

$$\mathcal{L}_{t,RIS}\left(s,r_{BR(0)},r_{RU(0)}\right)=\exp\left(-\varsigma_3\left({}_2F_1\left(-\frac{2}{\alpha_t},m;1-\frac{2}{\alpha_t};-s\varsigma_4\right)-1\right)\right), \tag{4.28}$$

where $\varsigma_3=\pi\lambda_b r_{BR(0)}^2$ and $\varsigma_4=\frac{P_b C_{RIS,E}^2}{m_t r_{RU(0)}{r_{BR(0)}}^{\alpha_t}}$.

Proof. See Appendix B.2. □

4.3.2 Coverage Analysis with RISs

In this subsection, the closed-form expressions of the coverage probabilities for the typical user and the connected users are derived via **Theorem 11-12** and **Corollary 25-26**.

4.3.2.1 Coverage Analysis of the Typical User with RISs

Note that the interference from the typical user is strived to be canceled with the aid of SIC procedures. When the surfaces perform as RISs, based on **Lemma 7** and (4.23), the coverage probability is rewritten as

$$\mathbb{P}_t = \Pr\left\{ |h_{t,\mathbf{x}_B}|^2 > \frac{\Upsilon\left(I_{t,\rho_t} + \sigma^2\right)}{P_b \mathcal{P}_t^{RIS}} \right\}, \tag{4.29}$$

where $\Upsilon = \max\left(\frac{\gamma_{SIC}^{th}}{a_c - \gamma_{SIC}^{th} a_t}, \frac{\gamma_t^{th}}{a_t}\right)$.

Theorem 11. We assume reflecting channels as Nakagami-m fading channels. With the aid of RISs, the approximated expression of coverage probability for the typical user is derived as

$$\begin{aligned}\mathbb{P}_t \approx & 2\pi\lambda_b \int_0^{R_L} \int_0^{\infty} \sum_{n=1}^{m_t} (-1)^{n+1} \binom{m_t}{n} x \exp\left(-\beta_0\left(y\right) x^{\alpha_t}\right) \\ & \times \exp\left(-\beta_2 x^2\right) dx f_{r_{RU}}\left(y\right) dy, \end{aligned} \tag{4.30}$$

where $\beta_0\left(x\right) = \beta_1 x_t^{\alpha}$, $\beta_1 = \frac{n\eta_t \Upsilon \sigma^2}{P_b C_{RIS,E}^2}$, $\beta_2 = \pi\lambda_b {}_2F_1\left(-\frac{2}{\alpha_t}, m; 1 - \frac{2}{\alpha_t}; -\frac{n\eta_t \Upsilon}{m_t}\right)$ and m_t is the coefficient in Nakagami-m fading channels with unit mean values.

Proof. See Appendix B.3. □

Remark 13. *When we analyze the performance with respect to the length of RISs L, we simplify the expression of coverage probability based on* ***Theorem 11*** *as*

$$\mathbb{P}_t \approx \exp\left(-\frac{A_1\left(x, y\right)}{L^2}\right) A_2\left(x, y\right). \tag{4.31}$$

where $A_1(x,y)$ and $A_2(x,y)$ are other items irrelevant to the length of RISs L. Thus, we conclude that when we improve the length of RISs, the coverage performance is enhanced. This is because the large RISs are able to absorb more incident waves and reflect them to the users.

Corollary 25. Conditioned on $\alpha_t = 2$, we are capable to derive the closed-form expression of the coverage probability for the typical user as

$$\mathbb{P}_t \approx \frac{\pi\lambda_b}{2}\sum_{n=1}^{m_t}(-1)^{n+1}\binom{m_t}{n}\left(\beta_1 R_L^2+2\beta_2\right). \tag{4.32}$$

Proof. When $\alpha_t = 2$, the coverage probability of the typical user is rewritten as

$$\begin{aligned}\mathbb{P}_c \approx & 2\pi\lambda_b\int_0^{R_L}\int_0^{\infty}\sum_{n=1}^{m_t}(-1)^{n+1}\binom{m_t}{n}x \\ & \times\exp\left(-\left(\beta_0(y)\ +\ \beta_2\right)x^2\right)dx f_{r_{RU(0)}}(y)\,dy.\end{aligned} \tag{4.33}$$

With the aid of Gamma functions $\Gamma(1) = 1$ and Eq. [2.3.18.2] in [127], (4.33) is derived as

$$\mathbb{P}_c \approx \pi\lambda_b\sum_{n=1}^{m_t}(-1)^{n+1}\binom{m_t}{n}\int_0^{R_L}\left(\beta_0(y)+\beta_2\right)f_{r_{RU(0)}}(y)\,dy, \tag{4.34}$$

and via several algebraic manipulations, the final expression is obtained. □

Corollary 26. Conditioned on $\alpha_t = 4$ in the derivation[5], the closed-form expression of the coverage probability for the typical user is derived via the error function as

$$\mathbb{P}_t \approx \sum_{n=1}^{m_t}(-1)^{n+1}\binom{m_t}{n}\sum_{i=1}^{K}\frac{\omega_i\pi^{\frac{3}{2}}\lambda_b\sqrt{1-\Xi_i^2}}{2R_L\sqrt{\beta_1}\Xi_i}\exp\left(\frac{\beta_2^2}{4\beta_1\Xi_i^4}\right)\mathrm{Erfc}\left(\frac{\beta_2}{2\sqrt{\beta_1}\Xi_i^2}\right), \tag{4.35}$$

[5]The scenario of $\alpha_t = 4$ means that the transmitting environment is complex, including severe obstacles, obstructions, and absorption.

where $\eta_t = m_t(m_t!)^{-\frac{1}{m_t}}$, $\varpi_i = \cos\left(\frac{2i-1}{2K}\pi\right)$, $\Xi_i = \frac{R_L}{2}(\varpi_i + 1)$, $\omega_i = \pi/K$ and $\mathrm{Erfc}(\cdot)$ is the error function.

Proof. Based on Appendix B.3 when $\alpha_t = 4$, this corollary is proved via substituting (4.15), Eq. [2.3.15.4] in [127] and Chebyshev-gauss quadrature into (4.30). □

4.3.2.2 Coverage Analysis of the Connected User

Based on (4.24), we are capable of rewriting the coverage probability expression as

$$\mathbb{P}_c = \Pr\left\{|h_{c,\mathbf{x}_B}|^2 < \frac{\gamma_c^{th}\left(I_c + \sigma^2\right)}{\left(a_c - a_t\gamma_c^{th}\right)P_b C {r_c}^{-\alpha_c}}\right\}. \tag{4.36}$$

Theorem 12. The closed-form expression of coverage probability for the connected users is derived as

$$\mathbb{P}_c \approx \sum_{n=1}^{m_c}(-1)^{n+1}\binom{m_c}{n}\exp\left(-\mu_1 r_c^2 - \mu_2 {r_c}^{\alpha_c}\right), \tag{4.37}$$

where $\mu_1 = \pi\lambda_b\left({}_2F_1\left(-\frac{2}{\alpha_c}, m; 1-\frac{2}{\alpha_c}; -\frac{n\eta_c\gamma_c^{th}}{m\left(a_c - a_t\gamma_c^{th}\right)}\right) - 1\right)$, $\mu_2 = \frac{n\eta_c\gamma_c^{th}\sigma^2}{\left(a_c - a_t\gamma_c^{th}\right)P_b C}$ and $\eta_c = m_c(m_c!)^{-\frac{1}{m_c}}$ with Nakagami-m fading coefficient m_c.

Proof. We exploit the Campbells theorem and **Theorem 11** to derive (4.37). □

Remark 14. *When we analyze the performance with respect to the density of BSs λ_b, we simplify the expression of coverage probability as*

$$\mathbb{P}_t \approx \exp\left(-\lambda_b B_1(x,y)\right) B_2(x,y), \tag{4.38}$$

where $B_1(x,y)$ and $B_2(x,y)$ are other items irrelevant to the density of BSs λ_b. Hence, the expression reveals that when we improve the density of BSs λ_b, the coverage probability is reduced. This is because the distance of

connected user has been fixed and the density of BSs λ_b only influence the strength of interference from other BSs.

4.3.3 Asymptotic Coverage Probability for the Typical user

In this subsection, we evaluate the coverage performance of the typical user when the half-length $L \to \infty$.

Corollary 27. Conditioned on $L \to \infty$, the asymptotic expression of coverage probability for the typical user is derived as

$$\begin{aligned}\mathbb{P}_c \approx & \sum_{n=1}^{m_t} (-1)^{n+1} \binom{m_t}{n} \frac{\pi\lambda_b}{\beta_2} - \frac{2\pi\lambda_b R_L^{\alpha_t}}{(2+\alpha_t)} \Gamma\left(\frac{\alpha_t+2}{2}\right) \\ & \times \sum_{n=1}^{m_t} (-1)^{n+1} \binom{m_t}{n} \frac{\beta_1}{\beta_2^{\frac{\alpha_t+2}{2}}}. \end{aligned} \tag{4.39}$$

Proof. After substituting the asymptotic expression $\exp(-x) = 1 - x$ into the coverage probability expression, we are able to rewrite (4.30) as

$$\begin{aligned}\mathbb{P}_c \approx & 2\pi\lambda_b \int_0^{R_L} \frac{2y}{R_L^2} dy \int_0^{\infty} \sum_{n=1}^{m_t} \binom{m_t}{n} \frac{x \exp\left(-\beta_2 x^2\right)}{(-1)^{-(n+1)}} dx \\ & - 2\pi\lambda_b\beta_1 \frac{2R_L^{\alpha_t}}{(2+\alpha_t)} \int_0^{\infty} \sum_{n=1}^{m_t} \binom{m_t}{n} \frac{x^{\alpha_t+1} \exp\left(-\beta_2 x^2\right)}{(-1)^{-(n+1)}}, \end{aligned} \tag{4.40}$$

and based on Eq. [2.3.18.2] in [127], we are able to obtain the final results. □

Corollary 28. *When the length of RISs are sufficiently large, we are capable to derive an upper limit from* ***Corollary 27*** *as*

$$\mathbb{P}_c \approx \sum_{n=1}^{m_t} (-1)^{n+1} \binom{m_t}{n} \frac{\pi\lambda_b}{\beta_2}, \tag{4.41}$$

which can increase the calculation efficiency to a large extent.

Remark 15. *Based on Huygens-Fresnel principle, this paper considers a one-dimensional (1-D) RIS [27] to evaluate the averaged performance. Con-*

sidering 1-D RISs instead of two-dimensional (2-D) RISs is to obtain tractable and clear derivations for further evaluation, while the properties may not be clearly reflected by exploiting the 2-D model as the complexity of derivations is high. The constraints will be released in future works.

Remark 16. *This paper considers the scenarios with fixed power allocation, which is to directly present the averaged long-term performance for the whole network. We also believe that well-designed plower allocation algorithms will improve the performance of RIS-aided systems. However, this will enhance the complexity of derivations, while we still leave the space for further investigation.*

4.4 Ergodic Rate Evaluation

Compared with the coverage probability with a fixed rate threshold, the achievable ergodic rate for the RIS-aided NOMA systems is opportunistically altered via the channel conditions of users. In this subsection, the closed-form expression of the ergodic rate for the typical user and the connected users are derived in the following theorems and corollaries.

4.4.1 Ergodic Rate for the Typical User

We consider the typical user to exploit the SIC procedure. The failure SIC procedure leads to the ergodic rate of the typical user always being zero. Thus, with the aid of the expression of the coverage probability, we express the ergodic rate expression of the typical user as

$$\mathbb{E}\left[R_t^{RIS}\right] = \mathbb{E}\left[\log_2\left(1+\gamma_t\right), \gamma_{\mathrm{SIC}} > \gamma_{SIC}^{th}\right] = \frac{1}{\ln 2}\int_0^{\infty} \frac{\mathbb{P}_t\left(\gamma_t^{th}\right)}{1+\gamma_t^{th}} d\gamma_t^{th}, \quad (4.42)$$

and the approximated and closed-form expressions are derived in the following.

Theorem 13. With the aid of the coverage probability expression in **Theorem 11**, the approximated expression of ergodic rates for the typical user

is derived as

$$\begin{aligned}\mathbb{E}\left[R_t^{RIS}\right] =& \frac{2\pi\lambda_b}{\ln 2R_L^2}\int_{a_t\Upsilon_1}^{\infty}\int_0^{R_L}\int_0^{\infty}\sum_{n=1}^{m_t}\frac{2yx(-1)^{n+1}}{1+z}\binom{m_t}{n}\\ &\times\exp\left(-\beta_1\left(\frac{z}{a_t}\right)(yx)^{\alpha_t}\right)\exp\left(-\beta_2\left(\frac{z}{a_t}\right)x^2\right)dxdydz\\ &+\frac{2\pi\lambda_b}{\ln 2R_L^2}\int_0^{a_t\Upsilon_1}\int_0^{R_L}\int_0^{\infty}\sum_{n=1}^{m_t}(-1)^{n+1}\binom{m_c}{n}\\ &\times\frac{2yx}{1+z}\exp\left(-\beta_1\left(\Upsilon_1\right)(yx)^{\alpha_t}\right)\exp\left(-\beta_2\left(\Upsilon_1\right)x^2\right)dxdydz, \quad (4.43)\end{aligned}$$

where $\beta_1\left(\Upsilon\left(z\right)\right) = \frac{n\eta_t\Upsilon(z)\sigma^2}{P_bC_{RIS,E}^2}$, $\Upsilon\left(z\right) = \max\left(\frac{\gamma_{SIC}^{th}}{a_c-\gamma_{SIC}^{th}a_t}, \frac{z}{a_t}\right)$, $\Upsilon_1 = \frac{\gamma_{SIC}^{th}}{a_c-a_t\gamma_{SIC}^{th}}$ and $\beta_2\left(z\right) = \pi\lambda_{b2}F_1\left(-\frac{2}{\alpha_t}, m; 1-\frac{2}{\alpha_t}; -\frac{n\eta_t\Upsilon(z)}{m_t}\right)$. This theorem is exploited to easily understand the following categories, includes **Corollary 29** and **Corollary 30** to make the derivations fluently.

Proof. When considering the threshold γ_t^{th} as a variable, the condition to maintain the SIC orders as $\Upsilon\left(z\right) = \max\left(\frac{\gamma_{SIC}^{th}}{a_c-\gamma_{SIC}^{th}a_t}, \frac{z}{a_t}\right)$ divides the expression into two items, such as $\gamma_t^{th} \in [0, a_t\Upsilon_1]$ and $\gamma_t^{th} \in [a_t\Upsilon_1, \infty]$. Thus, substituting the Laplace transform expressions of the interference caused by other *RU* links, this theorem is clarified. □

Remark 17. *As **Remark 13**, derivations in **Theorem 13** illustrate that the ergodic rate of the typical user increases if we enhance the half-length of RISs L.*

Corollary 29. When fixing the path loss exponent of the typical user $\alpha_t = 2$, the closed-form ergodic rate expression of the typical user is derived as

$$\begin{aligned}\mathbb{E}\left[R_t^{RIS}\right] =& \frac{\pi\lambda_b}{2\ln 2}\sum_{n=1}^{m_t}(-1)^{n+1}\binom{m_t}{n}\\ &\times\left(\sum_{j=1}^{J}\omega_j\sqrt{1-\Xi_j^2}\frac{a_t\Upsilon_1\left(\beta_1\left(\Upsilon_1\right)R_L^2 + 2\beta_2\left(\Upsilon_1\right)\right)}{2\left(1+\Xi_j\right)}\right.\\ &\left.+\sum_{v=1}^{V}\omega_v\sqrt{1-\Xi_v^2}\frac{2a_t\Upsilon_1\left(\beta_1\left(\frac{\Xi_v}{a_t}\right)R_L^2 + 2\beta_2\left(\frac{\Xi_v}{a_t}\right)\right)}{\left(\varpi_v+1\right)^2\left(1+\Xi_v\right)}\right), \quad (4.44)\end{aligned}$$

where $\Xi_j = \frac{a_t \Upsilon_1}{2}(\varpi_j + 1)$, $\varpi_j = \cos\left(\frac{2j-1}{2J}\pi\right)$, $\omega_j = \pi/J$, $\Xi_v = \frac{2a_t\Upsilon_1}{\varpi_v+1}$, $\varpi_v = \cos\left(\frac{2j-1}{2V}\pi\right)$ and $\omega_v = \pi/V$.

Proof. Based on the closed-form expression of the coverage probability for the typical user in **Corollary 25**, we are able to rewrite the ergodic rate expression as

$$\mathbb{E}\left[R_t^{RIS}\right] = \frac{\pi\lambda_b}{2\ln 2}\sum_{n=1}^{m_t}(-1)^{n+1}\binom{m_c}{n}\int_0^\infty \frac{\beta_1\left(\Upsilon\left(z\right)\right)R_L^2 + 2\beta_2\left(\Upsilon\left(z\right)\right)}{1+z}dz. \tag{4.45}$$

Based on the derivations in **Theorem 13** and harnessing the Chebyshev-Gauss quadrature, we are able to derive the closed-form ergodic rate expression for the typical user. □

Corollary 30. When targeting the typical user's path loss exponent $\alpha_t = 4$, we derive the closed-form ergodic rate expression of the typical user as

$$\begin{aligned}\mathbb{E}\left[R_t^{RIS}\right] =& \sum_{n=1}^{m_t}\frac{(-1)^{n+1}}{\ln 2}\binom{m_t}{n}\sum_{i=1}^{K}\sum_{j=1}^{J}\omega_i\omega_j\frac{a_t\Upsilon_1\pi^{\frac{3}{2}}\lambda_b\sqrt{1-\Xi_i^2}\sqrt{1-\Xi_j^2}}{4R_L\sqrt{\beta_1\left(\Upsilon_1\right)}\Xi_i\left(1+z\right)}\\ &\times\exp\left(\frac{\beta_2^2\left(\Upsilon_1\right)}{4\beta_1\left(\Upsilon_1\right)\Xi_i^4}\right)Erfc\left(\frac{\beta_2\left(\Upsilon_1\right)}{2\sqrt{\beta_1\left(\Upsilon_1\right)}\Xi_i^2}\right)\\ &+\sum_{n=1}^{m_t}\frac{(-1)^{n+1}}{\ln 2}\binom{m_c}{n}\sum_{i=1}^{K}\sum_{v=1}^{V}\omega_i\omega_v\frac{a_t\Upsilon_1\pi^{\frac{3}{2}}\lambda_b\sqrt{1-\Xi_i^2}\sqrt{1-\Xi_v^2}}{R_L\sqrt{\beta_1\left(\frac{\Xi_v}{a_t}\right)}\Xi_i(1+\Xi_v)^3}\\ &\times\exp\left(\frac{\beta_2^2\left(\frac{\Xi_v}{a_t}\right)}{4\beta_1\left(\frac{\Xi_v}{a_t}\right)\Xi_i^4}\right)Erfc\left(\frac{\beta_2\left(\frac{\Xi_v}{a_t}\right)}{2\sqrt{\beta_1\left(\frac{\Xi_v}{a_t}\right)}\Xi_i^2}\right),\end{aligned} \tag{4.46}$$

where the coefficients are the same as **Corollary 29**.

Proof. Substituting the closed-form coverage probability expression from

Corollary 26 into (4.42), the ergodic rate expression is calculated as

$$\mathbb{E}\left[R_t^{RIS}\right] = \frac{1}{\ln 2}\sum_{n=1}^{m_t}(-1)^{n+1}\binom{m_t}{n}\sum_{i=1}^{K}\int_0^{\infty}\frac{\omega_i \pi^{\frac{3}{2}}\lambda_b\sqrt{1-\Xi_i^2}}{2R_L\sqrt{\beta_1\left(\Upsilon\left(z\right)\right)}\Xi_i\left(1+z\right)} \times \exp\left(\frac{\beta_2^2\left(\Upsilon\left(z\right)\right)}{4\beta_1\left(\Upsilon\left(z\right)\right)\Xi_i^4}\right) Erfc\left(\frac{\beta_2\left(\Upsilon\left(z\right)\right)}{2\sqrt{\beta_1\left(\Upsilon\left(z\right)\right)}\Xi_i^2}\right) dz, \quad (4.47)$$

and with the aid of Chebyshev-Gauss quadrature, the final expression is derived. □

4.4.2 Ergodic Rate for the Connected User

Recall that the distance from the nearest BS to the connected user is fixed. We also express the expression of ergodic rate via the coverage probability expression as

$$\mathbb{E}\left[R_c^{RIS}\right] = \mathbb{E}\left[\log_2\left(1+\gamma_c\right)\right] = \frac{1}{\ln 2}\int_0^{\infty}\frac{\mathbb{P}_c\left(\gamma_c^{th}\right)}{1+\gamma_c^{th}}d\gamma_c^{th}, \quad (4.48)$$

and the approximated closed-form expression is derived via the following theorem.

Theorem 14. Since we consider the RISs to enhance the channel environments of the typical user, there is a high probability that the channel conditions of the typical user are better than the connected users. Thus, the connected user is allocated at the first stage of SIC orders to escape from the SIC procedure. In this scenario, the ergodic rate of the connected user is derived as

$$\mathbb{E}\left[R_c^{RIS}\right] = \frac{1}{\ln 2}\sum_{n=1}^{m_c}(-1)^{n+1}\binom{m_c}{n}\sum_{w=1}^{W}\omega_w\sqrt{1-\Xi_w^2} \times \frac{\Upsilon_2}{2\left(1+\Xi_w\right)}\exp\left(-\mu_1\left(\Xi_w\right)r_c^2 - \mu_2\left(\Xi_w\right){r_c}^{\alpha_c}\right), \quad (4.49)$$

where $\Upsilon_2 = \frac{a_c}{a_t}$, $\Xi_w = \frac{\Upsilon_2}{2}\left(\varpi_w + 1\right)$, $\varpi_w = \cos\left(\frac{2w-1}{2W}\pi\right)$ and $\omega_w = \pi/W$.

Proof. Based on the conditions when deriving the coverage probability, we

obtain that $\gamma_c^{th} < \frac{a_c}{a_t}$. Therefore, the range of γ_c^{th} is in $[0, \Upsilon_2]$. Based on the coverage probability expression of the connected user, we express the ergodic rate expression as

$$\mathbb{E}[R_c^{RIS}] = \frac{1}{\ln 2} \sum_{n=1}^{m_c} (-1)^{n+1} \binom{m_c}{n} \int_0^{\Upsilon_2} \frac{1}{1+z} \exp\left(-\mu_1(z) r_c^2 - \mu_2(z) {r_c}^{\alpha_c}\right) dz, \tag{4.50}$$

and utilizing Chebyshev-Gauss quadrature, the proof is accomplished. □

Remark 18. *Based on the analytical procedure in **Remark 14**, we are able to conclude that the ergodic rate of the connected user increases when the density of BSs λ_b is enhanced.*

4.4.3 Asymptotic Ergodic Rate for the Typical User

In this subsection, we evaluate the coverage performance of the typical user when $L \to \infty$ holds. With the aid of the asymptotic expression of the exponential functions, we derive the asymptotic coverage probability and diversity gains.

Corollary 31. We assume the half-length of the RIS to infinity, denoted as $L \to \infty$. With the aid of asymptotic expression, such as $\exp(-x) = 1 - x$ when $x \to 0$, we derive the approximated expression of the ergodic rate as

$$\begin{aligned} \mathrm{E}\left[R_t^{RIS}\right]|_{L\to\infty} &= \frac{2\pi\lambda_b}{\ln 2 R_L^2} \int_0^{\infty} \int_0^{R_L} \int_0^{\infty} \sum_{n=1}^{m_t} (-1)^{n+1} \binom{m_t}{n} \frac{2yx}{1+z} \\ &\quad \times \left(1 - \beta_1(\Upsilon(z))(yx)^{\alpha_t}\right) \exp\left(-\beta_2(\Upsilon(z)) x^2\right) dx dy dz \\ &= C_1 - C_2 f\left(\frac{1}{L^2}\right), \end{aligned} \tag{4.51}$$

where C_1 and C_2 are constants and $f\left(\frac{1}{L^2}\right)$ represents a function negatively correlated to L^2.

Proof. Substituting the asymptotic expression into the expression in **Theorem 13**, we achieve the asymptotic expression. □

Remark 19. When the condition $L \to \infty$ holds, which means we have a large RIS surface, we derive the slope to evaluate the performance as

$$S = \lim_{L\to\infty} \frac{\mathrm{E}\left[R_t^{RIS}\right]|_{L\to\infty}}{\log(L)} = 0. \tag{4.52}$$

Remark 20. *Since the slope versus L is zero, which represents that when we enhance the length of RISs, the performance would increase to an upper limit eventually shown as Fig. 4.3. This is because enhancing L is directly increases the path loss gain. Although the path loss gain of the typical user would increase when we continuously enlarge the RISs, the interference from other BSs would also be enhanced, which leads to an upper limit*[6].

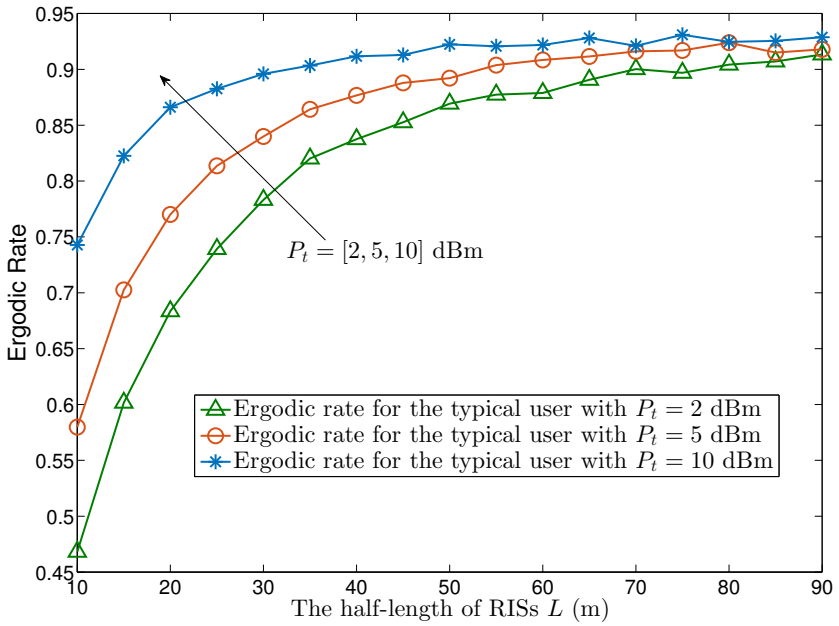

Figure 4.3: Simulation results sorely: The ergodic rate versus the half-length of the RIS L.

[6]We note that the path loss gain is in influenced by the distance between the BSs to the typical user as well, resulting in the path loss gain of the interference is lower than that of the associated BS. However, if we keep increasing the length of the RISs, there will be a point that the strength of the interference catches up to the strength of the signals, which causes an upper limit.

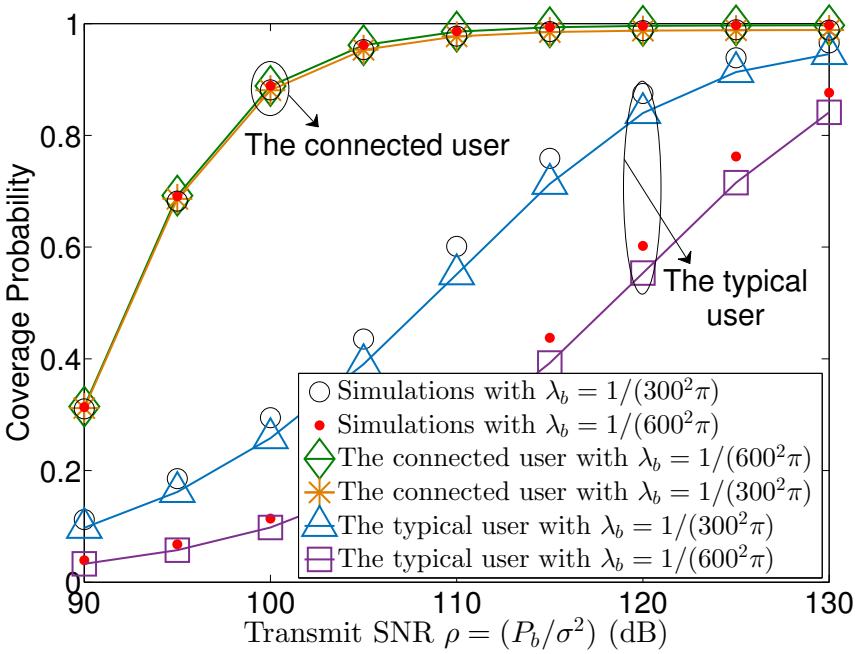

Figure 4.4: Coverage probability versus transmit SNR with various density of BSs $\lambda_b = [1/(300^2\pi), 1/(600^2\pi)]$: a verification of **Theorem 11** and **Theorem 12**. This figure includes simulation results and analytical results.

4.5 Numerical Results

In this section, numerical results are indicated to validate analytical and asymptotic expressions of coverage probability derived in the previous sections. We further accomplish the simulation results of the ergodic rate performance, including analytical and asymptotic expressions. Several comparisons are proposed to compare the performance under several cases, such as RIS-aided NOMA, RIS-aided OMA, and non-RIS-aided NOMA.

4.5.1 Simulation Results on Coverage Probability

In this subsection, numerical results validate analytical coverage probability for the typical user (**Theorem 11**) and the connected user (**Theorem 12**). Additionally, the asymptotic expressions via the length of RISs are validated to match the simulation results in high length region. Without otherwise

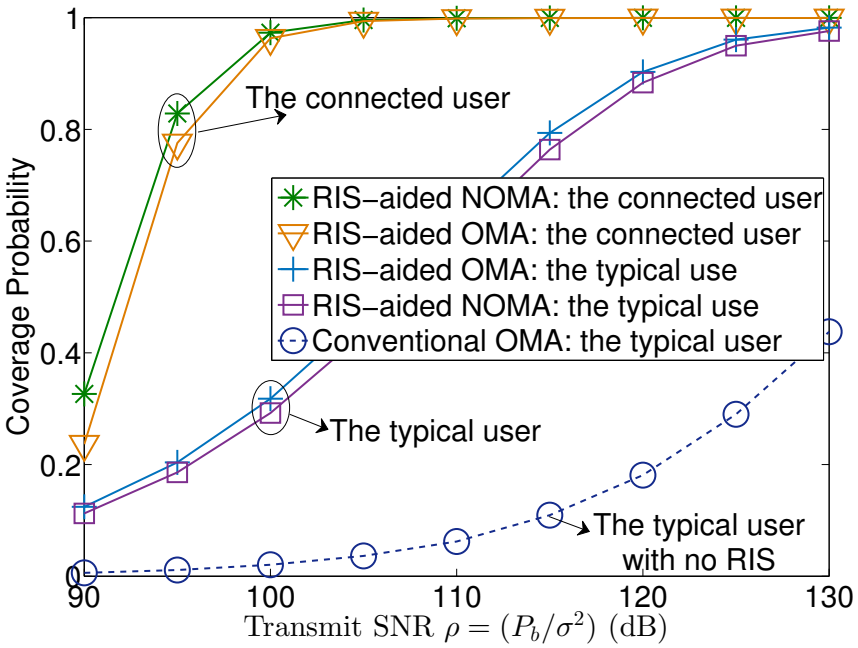

Figure 4.5: Coverage probability versus transmit SNR: a comparison among conventional OMA, RIS-aided OMA and RIS-aided NOMA scenarios. This figure only has simulation results to make this figure clear.

specification, we define the numerical settings as shown in the Table 6-A.

4.5.1.1 Validation of Results on Coverage Probability

The analytical coverage probability expressions of the typical user (**Theorem 11**) and the connected user (**Theorem 12**) are validated in Fig. 4.4. Additionally, we compare the performance of several scenarios with different density of BSs λ_b in Fig. 4.4. The observation is that the typical user is more sensitive than the connected user on coverage performance when the density of BSs is changed. The reason is clarified in the following. Based on the QoS-based SIC, the connected user considers the typical user's signals as interference. As the power level of the typical user's signals is higher than that of the interference from interfering BSs, the influence of enhancing the density of interfering BSs for the connected user is limited. For the typical user, the interference from interfering BSs is enhanced by the RIS and

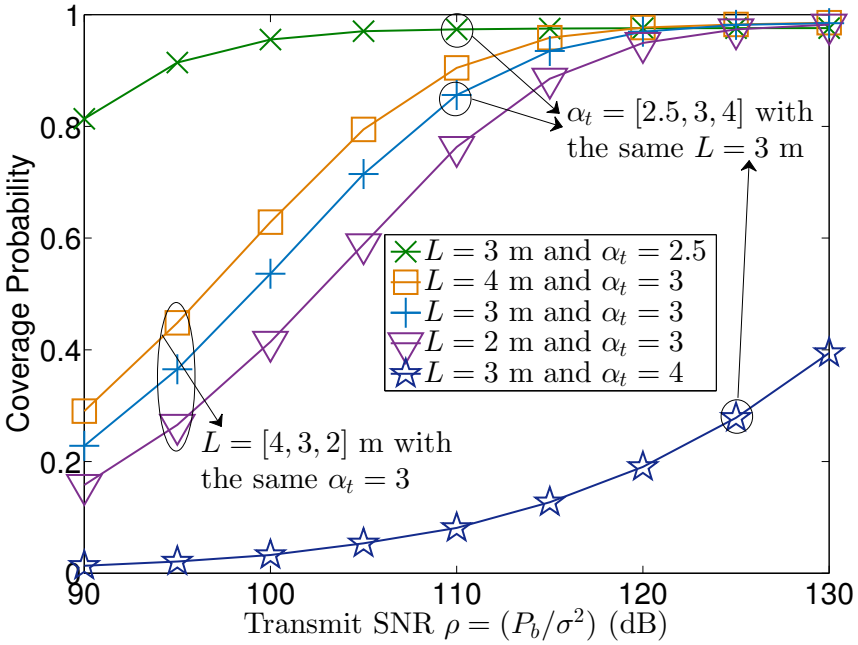

Figure 4.6: Coverage probability versus transmit SNR with various half-length of RISs $L = [2, 3, 4]$ m and path loss exponents $\alpha_t = [2.5, 3, 4]$. This figure shows simulation results.

the connected user's signals are removed by SIC. Thus, the density of BSs directly influences the strength of interference for the typical user.

4.5.1.2 Performance Comparison

The performance among conventional OMA, RIS-aided OMA, and RIS-aided OMA scenarios is compared in Fig. 4.5, which demonstrates that the performance of NOMA users boosts considerably with the aid of RISs, especially for the typical user. The enhancement of NOMA users are able to be explained that 1) when assisted with RISs, the connected users enable to avoid SIC procedures since the typical user with substantially improved channel gains takes over the SIC procedures, thereby the connected user would not experience outage scenarios caused by SIC failures; 2) with the aid of RISs, superior channel gains of the typical user increase coverage performance.

Table 4-A: Network Parameters

The length of RIS L	4 m
The noise power	$\sigma^2 = -170 + 10\log(f_c) + N_f = -90$ dB
The bandwidth of the carrier f_c	10 MHz
The noise figure from hardware N_f	10 dB
The transmit power of users P_t	$[0, 40]$ dBm
The path loss exponents α_c and α_t	3.3
The RIS ball radius R_L	20 m
The density of BSs λ_b	$\lambda_b = 1/(300^2\pi)$
The coverage and SIC thresholds	$\gamma_{SIC}^{th} = \gamma_t^{th} = \gamma_c^{th} = 10^{-2}$
The Gamma distribution coefficients	$m_c = m_{t_1} = m_{t_2} = 2$
The power allocation coefficients	$a_c = 0.6$ and $a_t = 0.4$
The distance between the connected user and BS	$r_C = 200$ m

4.5.1.3 Outage Performance on Path Loss Exponents

Considering the length of RISs, Fig. 4.6 investigates the performance varied by L and path loss exponents. Two observations are apparent to explain that: 1) long lengths of RISs cause high performance since more reconfigurable meta-material elements are involved and 2) enlarging path loss exponents results in reduced performance as the relationship between the path loss exponents and the coverage performance is a negative correlation.

4.5.1.4 Outage Performance on the Length of RIS

In Fig. 4.7, we investigate the outage performance versus the length of RIS. One observation is obtained that the coverage probability is enhanced when the length of RISs increases. This is because that larger RISs integrate more energy with the typical user. When we enlarge the radius of the RIS serving area, the performance of the typical user is reduced as the averaged distance from the typical user to its associated BS is enlarged, which leads to large path loss.

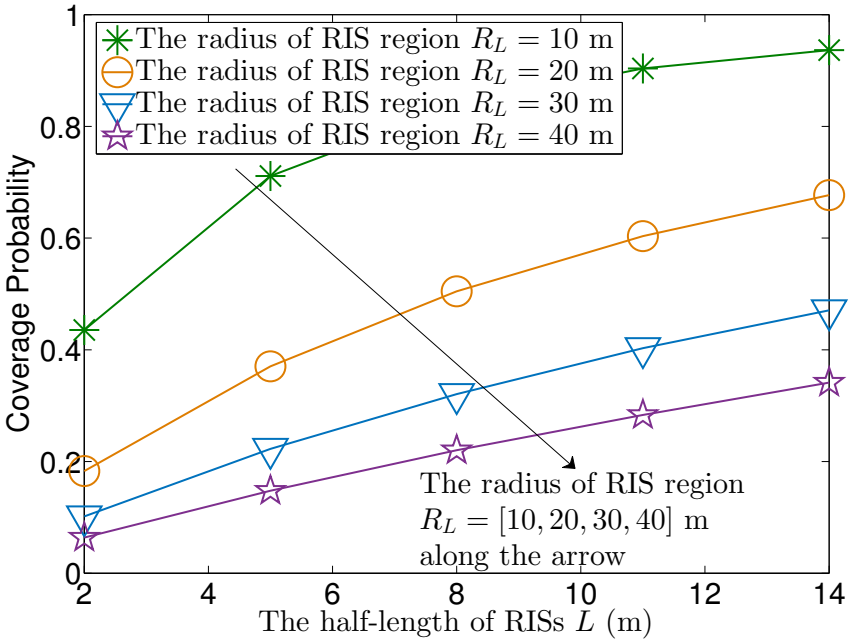

Figure 4.7: Coverage probability versus the half-length of RISs L m with various radii of RIS serving area as $R_L = [10, 15, 30]$ m. Simulation results are evaluated in this figure.

4.5.2 Simulation Results on Ergodic Rage

In this subsection, we validate analytical ergodic rate via numerical results for the typical user (**Theorem 13**) and connected users (**Theorem 14**). We note that the unit of ergodic rate is the bit per cell use (BPCU). We define the numerical settings as the same as the sections on coverage probability without otherwise specification.

4.5.2.1 Validation of Ergodic Rate for the Typical User

The ergodic rate performance with the unit BPCU versus the transmit SNR P_b/σ^2 is indicated in Fig. 4.8. We observe that when we have dense BSs, the performance of the typical user outperforms than users with small density. This is because a large density of BSs contributes to a short averaged distance between the nearest BS and the typical user, which leads to better

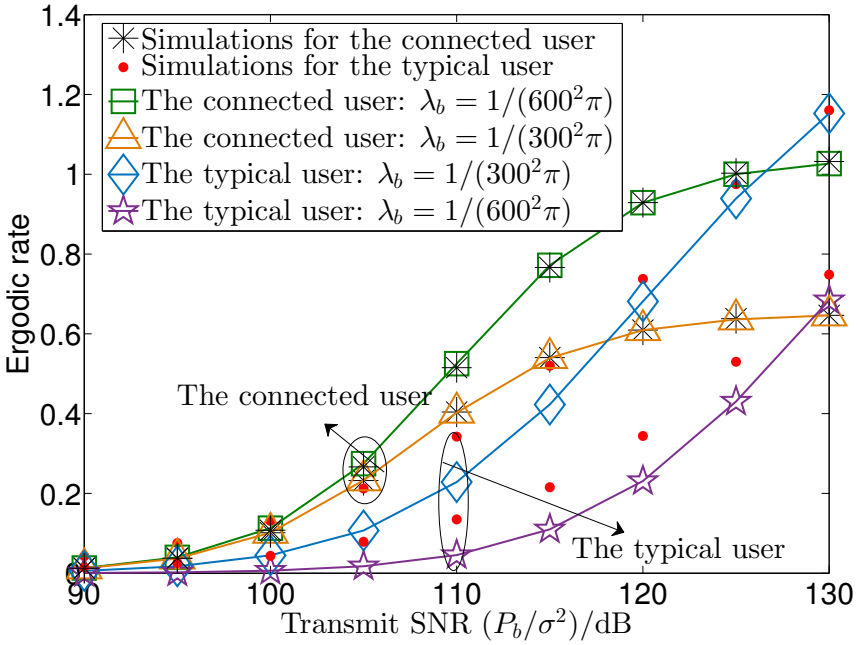

Figure 4.8: Ergodic rates (BPCU) versus transmit SNR with various density values of BSs $\lambda_b = [1/(200^2\pi), 1/(400^2\pi), 1/(600^2\pi)]$ for the typical user. The analytical results are proved to fit the simulation results.

performance than small density situations.

4.5.2.2 Validation of Ergodic Rate for the connected User

We validated the analytical results of the ergodic rate for the connected user via Fig. 4.9, which demonstrates the ergodic rate (BPCU) versus the transmit SNR. Observed by this figure, we conclude that when we increase the distance between the connected user and the nearest BS, the performance goes worse as the long-distance leads to heavy path loss.

4.6 Conclusion

This paper has investigated the coverage probability and ergodic rate of RIS-assisted NOMA frameworks, where the PCP principle has been invoked to capture the spatial effects of NOMA users. The path loss models of RIS

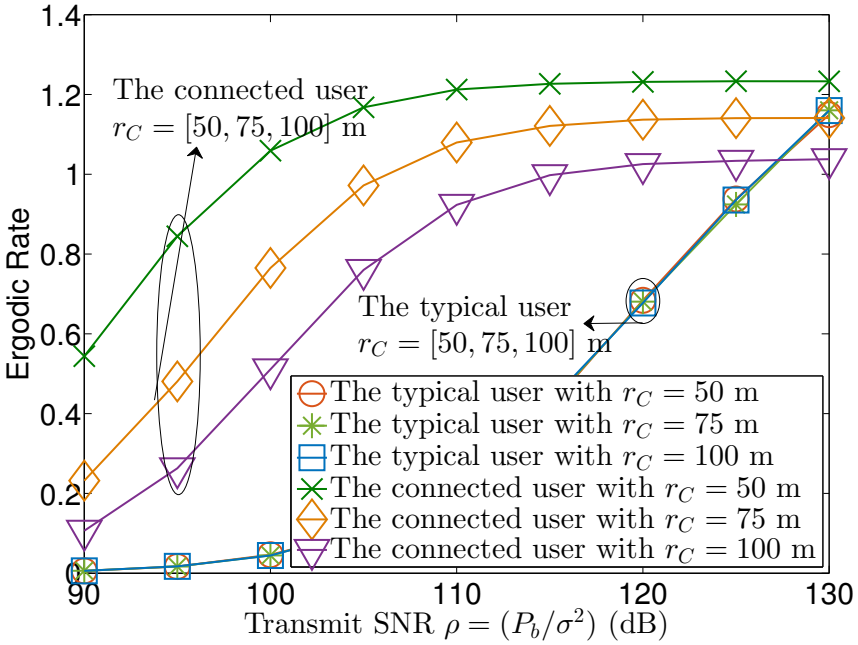

Figure 4.9: Ergodic rates (BPCU) versus transmit SNR with various distances between the connected user and the BS as $r_C = [50, 75, 100]$ m for the connected user. The simulation results are presented.

reflecting links has been derived, which is correlated with the "product of distances" model to conform with long-distance regions. The angle distributions have been presented with a conclusion that the BS-RIS-User angles obey uniform distributions in $[0.\pi]$. With the aid of the derived closed-form expressions of coverage probabilities and numerical results, the performance of conventional OMA, RIS-aided NOMA, and RIS-aided OMA scenarios has been compared, which has shown that RISs enhance the performance of users significantly. The asymptotic expressions of ergodic rates for the typical user have illustrated that the performance has upper limits when enhancing the length of the RIS. The analysis of this paper has verified that two applications of RISs in multi-cell NOMA networks are feasible, such that: 1) RISs are able to improve the channel conditions of blocked or far users; 2) RISs enable to alter the SIC order to maintain primary users avoiding SIC procedures. For future works, we will consider more practical scenar-

ios, i.e., the optimal power allocation methods, two dimensional RISs, other stochastic geometry models. Additionally, we will evaluate the performance of a user aided by more than two RISs.

Chapter 5

STAR-RIS-Aided NOMA Networks

Since the conventional RISs only reflect signals, new blind areas behind RISs may appear. Hence, this chapter investigates the performance of STAR-IOS-aided NOMA networks to achieve 360° connectivity. In this chapter, three different channel models are presented and the outage performance of STAR-IOS-aided NOMA systems is investigated. The main contributions are summarized as follows:

- Three physical-layer channel models for STAR-IOS-aided networks are proposed, including the CL model, the CF model, and the MFC model. More specifically, the CF and CL models are exploited to analyze the outage performance. It is concluded that the CL model is utilized in the case with a large number of independent STAR-IOS elements, while the CF model fits all conditions but needs different CF functions. As these two models cannot achieve accurate diversity orders, the MFC model is harnessed to evaluate asymptotic performance with diversity gains.
- The CF model and the CL model are exploited to derive the closed-form expressions of the outage probability for NOMA users under the ES protocol. The analytical results indicate that the CF model performs as a close lower bound of the simulation results while the CL model is an upper bound.

- With the aid of the ES, MS, and TS protocols, this chapter then derives the asymptotic outage probability expressions for NOMA users based on the MFC model. Then, the diversity orders for the three protocols are evaluated. The analytical results indicate that the diversity orders are equal to the active number of STAR-IOS elements.

- The analytical results by Monte Carlo simulations are verified. Numerical results demonstrate that: 1) STAR-IOSs enhance the outage performance of NOMA systems significantly and provide high flexibility for SIC orders; 2) the TS protocol has the best outage performance but it only serves one user in each time block; and 3) with two users served in the same resource block, the ES protocol outperforms the MS protocol as the diversity gains of the ES protocol is larger than that of the MS protocol.

5.1 System Model

A STAR-IOS-aided downlink NOMA network is considered, which includes a fixed BS, a fixed STAR-IOS, and randomly deployed users (reflecting users and transmitting users). It is considered that a reflecting user and a transmitting user are paired in the same resource block with different power levels. It is assumed that different NOMA pairs are allocated into orthogonal resource blocks, thereby inter-NOMA-cluster interference is ignored. Additionally, the direct links for the two NOMA users are assumed to be blocked. More specifically, for the reflecting user, the direct link is blocked by obstacles, such as trees or buildings. Thus, only the reflecting links via the STAR-IOS are considered for the reflecting user. For the transmitting user, its location is behind the STAR-IOS substrates. As the STAR-IOS is transparent for the signals of the transmitting user, the transmitting user still receives refracted signals with the aid of the STAR-IOS, which is the only approach for the transmitting user to receive signals. To sum up, the BS first transmits signals to the STAR-IOS, followed by the radiation signals

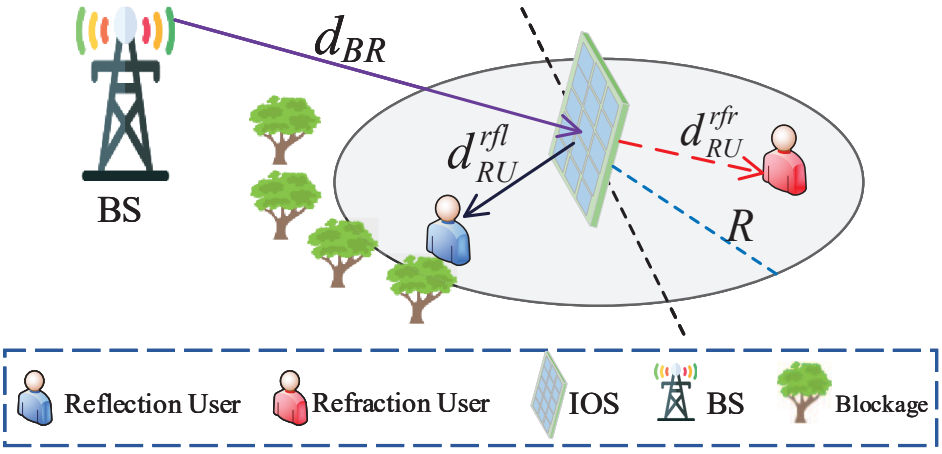

Figure 5.1: Illustration of the considered STAR-IOS-aided downlink NOMA networks.

to the reflecting user and the transmitting user.

5.1.1 Theoretic Foundation of STAR-IOSs

The main difference between STAR-IOSs and conventional RISs is that STAR-IOSs allow signals through themselves via refraction, which allows independent reflecting and refracting beamforming for the two half-spaces to achieve high flexibility [31, 42, 44]. Hence, the serving area of STAR-IOSs is enhanced from a half circle (for the conventional RISs) to a whole circle area with the aid of simultaneous reflection and refraction. Define the reflecting and refracting coefficients as R_m and T_m for the m^{th} STAR-IOS element, respectively. The phase shift coefficients are considered as two independent variables, denoted as ϕ_m^{rfl} for the reflecting user and ϕ_m^{rfr} for the transmitting user. Additionally, the STAR-IOS is assumed with M elements satisfying $1 \leq m \leq M$. Hence, the reflected and refracted signals of the m^{th} STAR-IOS element are expressed as $R_m = \sqrt{\beta_m^{rfl}} e^{j\phi_m^{rfl}}$ and $T_m = \sqrt{\beta_m^{rfr}} e^{j\phi_m^{rfr}}$, respectively, where $\phi_m^{rfl}, \phi_m^{rfr} \in [0, 2\pi)$. Additionally, the β_m^{rfl} is the energy coefficient for reflecting links and the β_m^{rfr} is the energy coefficient for transmitting links.

Based on the theories in [31, 42], it is noted that the STAR-IOS-aid

networks have three practical protocols to be exploited, namely the ES, MS, and TS protocols. The detailed description and constraints are presented in the following.

5.1.1.1 ES Protocol of STAR-IOSs

In terms of the ES protocol, all the STAR-IOS elements (M elements) simultaneously operate refraction and reflection modes, while the total radiation energy is split into two parts. When assuming the STAR-IOSs are passive with ignorable energy consumption, a constraint is presented based on the aforementioned coefficients as $|R_m|^2 + |T_m|^2 \leq 1$. Hence, this protocol is mathematically presented as $\beta_m^{rfl} + \beta_m^{rfr} \leq 1$ [44]. To achieve the best utilization rate of STAR-IOS elements, let us assume $\beta_m^{rfl} + \beta_m^{rfr} = 1$ in the following investigation [42].

5.1.1.2 MS Protocol of STAR-IOSs

For the MS protocol, no STAR-IOS element will simultaneously reflect and refract signals. Instead, the STAR-IOS elements are partitioned into two groups. More specifically, the first group of STAR-IOS elements is exploited to fully reflect signals for reflecting links, while the other group of the STAR-IOS elements performs in the full refraction mode to be utilized in transmitting links. It is assumed that M_{rfl} STAR-IOS elements are utilized for the reflecting links and M_{rfr} STAR-IOS elements are exploited for the transmitting links. Hence, with the best utilization of STAR-IOS elements, the constraint of the MS protocol is mathematically presented as $M_{rfl} + M_{rfr} = M$. For the M_{rfl} elements, the conditions hold, denoted as $\beta_m^{rfl} = 1$ and $\beta_m^{rfr} = 0$, while for the M_{rfr} elements, the mathematical expressions are denoted as $\beta_m^{rfl} = 0$ and $\beta_m^{rfr} = 1$.

5.1.1.3 TS Protocol of STAR-IOSs

When it comes to the TS protocol, the M elements are operated as the full refraction mode or the full reflection mode in different coherent time

slots. For time slots with refraction modes, the conditions are expressed as $\beta_m^{rfl} = 0$ and $\beta_m^{rfr} = 1$, which means that all the M STAR-IOS elements perform as full refraction mode. It is also noted as $\beta_m^{rfl} = 1$ and $\beta_m^{rfr} = 0$ for time slots with reflection modes where all the STAR-IOS elements fully reflect signals. Let us define two time variation coefficients, namely λ_{rfr} and λ_{rfl} for the transmitting and reflecting links, respectively. Hence, the constraint is mathematically expressed as $\lambda_{rfr} + \lambda_{rfl} = 1$ to present the percentage of time allocation.

5.1.2 Deployment of Devices

This chapter considers a single-cell STAR-IOS-aided NOMA network. In this case, the BS is deployed at the center of the cell. Since the STAR-IOSs are always deployed at building facades, the positions of STAR-IOSs are fixed and known by us. This chapter chooses one of them to investigate the performance with the position denoted as $\mathbf{x_R}$. Then, let us assume that the STAR-IOSs are deployed on tall buildings. Thus, the links between the BS and the STAR-IOS elements are LoS links. For the users, the positions of the reflecting user and the transmitting user are expressed as $\mathbf{x_{rfl}}$ and $\mathbf{x_{rfr}}$, respectively. Note that direct links from the BS to the reflecting users are blocked by obstacles. Hence, the channel links are defined as three types: 1) the link between the BS and the STAR-IOS as the BR link with the distance $d_{BR} = \|\mathbf{x_R}\|$, 2) the link between the STAR-IOS and the reflecting user as the RU_{rfl} link with the distance $d_{RU}^{rfl} = \|\mathbf{x_R} - \mathbf{x_{rfl}}\|$, and 3) the link from the STAR-IOS to the transmitting user as the RU_{rfr} link with the distance $d_{RU}^{rfr} = \|\mathbf{x_R} - \mathbf{x_{rfr}}\|$.

It is assumed that users are uniformly distributed within the serving area of the STAR-IOS. Without loss of generality, this chapter considers that the serving area of the STAR-IOS is a circle with the radius R, denoted as $\mathbb{O}(0, R)$, where $\mathbb{O}(a, b)$ is an annulus with the inner radius a and outer radius b. Additionally, this area is split into two parts: 1) the half ball facing the STAR-IOS as the reflecting area, namely $\mathbb{B}_{rfl}$, and 2) the rest half ball

behind the STAR-IOS as the refracting area, namely $\mathbb{B}_{rfr}$. Let us randomly choose a user from $\mathbb{B}_{rfl}$ and a user from $\mathbb{B}_{rfr}$ as the NOMA pair. Hence, the spatial effect of the chosen NOMA users is evaluated. In this case, the PDFs of d_{RU}^{rfl} and d_{RU}^{rfr} are expressed as:

$$f_{d_{RU}^{rfl}}(x) = \frac{\partial}{\partial x}\int_0^{\pi}\int_0^{x}\frac{2r}{\pi R^2}drd\theta = \frac{2x}{R^2} \tag{5.1}$$

and

$$f_{d_{RU}^{rfl}}(x) = \frac{\partial}{\partial x}\int_{\pi}^{2\pi}\int_0^{x}\frac{2r}{\pi R^2}drd\theta = \frac{2x}{R^2}. \tag{5.2}$$

5.1.3 Signal Model

Based on the NOMA technique, the strong NOMA user in the NOMA pair accomplishes the SIC procedure. As the STAR-IOS is able to adjust the energy allocation coefficients β_m^{rfl} and β_m^{rfr} via the ES protocol, more energy is allocated for reflecting links. In practical application scenarios, to ensure the links between the STAR-IOS and the users are LoS links, it is assumed that the radius of STAR-IOS serving area R is not large. Thus, the influence of path loss is not severe. Under this situation, let us find a pair of energy allocation coefficients (β_m^{rfl} and β_m^{rfr}) satisfying that the reflecting user is always kept as the strong user. Therefore, the reflecting user operates the SIC process. For the MS and TS protocol, this assumption is further extended by allocating different numbers of active STAR-IOS elements or time slots. Based on this assumption, the channel models are designed in the following.

5.1.3.1 Small-Scale Fading Model

It is assumed that all the links in this model follow the Rician distribution. The small-scale fading coefficients of the three types of links are denoted as $h_{BR,m}$ for BR links, $h_{RU,m}^{rfl}$ for RU_{rfl} links, and $h_{RU,m}^{rfr}$ for RU_{rfr} links for $\forall m \in \{1, 2, \cdots, M\}$. Hence, the PDF for the Rician distribution is expressed

as:

$$f_{h_{BR,m}}(x) = f_{h_{RU,m}^{rfl}}(x) = f_{h_{RU,m}^{rfr}}(x) = \frac{2(1+k)}{\exp(k)} x \exp\left[-(1+k)x^2\right] I_0\left[2\sqrt{k(1+k)}x\right], \tag{5.3}$$

where k is the coefficient of the Rician distribution and $I_0(x)$ is the Bessel function. In this case, assume that the mean values and variances of all the Rician channels are expressed as $\bar{h} = \sqrt{\frac{\pi}{4(1+k)}}{}_1F_1\left(-\frac{1}{2}, 1; -k\right)$ and $\eta = 1 - \frac{\pi}{4(1+k)}\left[{}_1F_1\left(-\frac{1}{2}, 1; -k\right)\right]^2$, where ${}_1F_1(\cdot,\cdot;\cdot)$ is the confluent hypergeometric function of the first kind.

The BR and RU_{rfl} links are combined as the reflecting link, namely g_m^{rfl} for the m^{th} STAR-IOS element. Additionally, the BR and RU_{rfr} links are combined as the transmitting link, namely g_m^{rfr} for the m^{th} STAR-IOS element. Based on the theoretic fundamental constraint of STAR-IOSs, the small-scale fading model of the reflecting and transmitting links is expressed as:

$$\left|g_m^{rfl}\right| = \left|\mathbf{G_{RU}^{rfl}}\mathbf{\Theta_{rfl}}\mathbf{G_{BR}}\right|, \tag{5.4}$$

$$\left|g_m^{rfr}\right| = \left|\mathbf{G_{RU}^{rfr}}\mathbf{\Theta_{rfr}}\mathbf{G_{BR}}\right|, \tag{5.5}$$

where we have a diagonal matrix for reflecting links, denoted as $\mathbf{\Theta_{rfl}} = \text{diag}\left[\sqrt{\beta_1^{\text{rfl}}}\text{e}^{\text{j}\phi_1^{\text{rfl}}}, \sqrt{\beta_2^{\text{rfl}}}\text{e}^{\text{j}\phi_2^{\text{rfl}}}, \cdots, \sqrt{\beta_{\text{M}}^{\text{rfl}}}\text{e}^{\text{j}\phi_{\text{M}}^{\text{rfl}}}\right]$ with diag $[\cdot]$ as a diagonal matrix with its principal diagonal elements. The RIS matrix for transmitting links is denoted as $\mathbf{\Theta_{rfr}} = \text{diag}\left[\sqrt{\beta_1^{\text{rfr}}}\text{e}^{\text{j}\phi_1^{\text{rfr}}}, \sqrt{\beta_2^{\text{rfr}}}\text{e}^{\text{j}\phi_2^{\text{rfr}}}, \cdots, \sqrt{\beta_{\text{M}}^{\text{rfl}}}\text{e}^{\text{j}\phi_{\text{M}}^{\text{rfl}}}\right]$ as a diagonal matrix. It is defined that the channel gain for the reflecting links is expressed as a column vector, denoted as $\mathbf{G_{RU}^{rfl}} = \left[h_{RU,1}^{rfl}, h_{RU,2}^{rfl}, \cdots, h_{RU,M}^{rfl}\right]^T$ and the channel gain for the transmitting links is expressed as a column vector, denoted as $\mathbf{G_{RU}^{rfr}} = \left[h_{RU,1}^{rfr}, h_{RU,2}^{rfr}, \cdots, h_{RU,M}^{rfr}\right]^T$, where $[\cdot]^T$ is the matrix transpose. Additionally, the channel gain from the BSs to the RISs is expressed as a row vector, denoted as $\mathbf{G_{BR}} = [h_{BR,1}, h_{BR,2}, \cdots, h_{BR,M}]$.

5.1.3.2 STAR-IOS-Aided Path Loss Model

Define the path loss model of the three links via conventional wireless communication models. Hence, the path loss expressions for BR, RU_{rfl}, and RU_{rfr} links are respectively expressed as:

$$\mathcal{P}_{BR}(\mathbf{x}_R) = C_{BR}\|\mathbf{x_R}\|^{-\alpha_t} = C_{BR}d_{BR}^{-\alpha_t}, \tag{5.6}$$

$$\mathcal{P}_{RU}^{rfl}(\mathbf{x}_R, \mathbf{x_{RU}^{rfl}}) = C_{RU}^{rfl}\left\|\mathbf{x}_R - \mathbf{x_{RU}^{rfl}}\right\|^{-\alpha_t} = C_{RU}^{rfl}\left(d_{RU}^{rfl}\right)^{-\alpha_t}, \tag{5.7}$$

$$\mathcal{P}_{RU}^{rfr}(\mathbf{x_R}, \mathbf{x_{RU}^{rfr}}) = C_{RU}^{rfr}\left\|\mathbf{x}_R - \mathbf{x_{RU}^{rfr}}\right\|^{-\alpha_t} = C_{RU}^{rfr}\left(d_{RU}^{rfr}\right)^{-\alpha_t}, \tag{5.8}$$

where the $\mathcal{P}$ expresses the path loss, $\{C_{BR}, C_{RU}^{rfl}, C_{RU}^{rfr}\} = \left(\frac{c}{4\pi f_c}\right)^2$ are reference-distance based intercepts for different links and the reference distance $d_0 = 1$ m in this work, in which $c = 3 \times 10^8$ m/s is the speed of light and f_c is the used carrier frequency. Additionally, the α_t is the path loss exponent for users.

5.1.3.3 SINR Expressions

To ensure that the strong user (the reflecting user) has the SIC process, more transmit power is allocated to the weak user (the transmitting user) by the BS compared to the strong user. Hence, the SINR of the SIC process for the reflecting user is given by

$$\gamma_{\text{SIC}} = \frac{a_{rfr}P_t\mathcal{P}_{BR}(\mathbf{x}_R)\mathcal{P}_{RU}^{rfl}(\mathbf{x}_R, \mathbf{x}_{RU}^{rfl})\left|g_m^{rfl}\right|^2}{a_{rfl}P_t\mathcal{P}_{BR}(\mathbf{x}_R)\mathcal{P}_{RU}^{rfl}(\mathbf{x}_R, \mathbf{x}_{RU}^{rfl})\left|g_m^{rfl}\right|^2 + \sigma^2}, \tag{5.9}$$

where P_t is the transmit power of the BS, σ^2 is the variance of AWGN, and a_{rfr} and a_{rfl} are transmit power allocation coefficient satisfying $a_{rfr}+a_{rfl} = 1$ and $a_{rfl} < a_{rfr}$.

With the aid of SIC, the reflecting user removes the messages of the transmitting user. Then, the reflecting user decodes its required messages.

Hence, the SNR of the reflecting user is presented as:

$$\gamma_{\text{rfl}} = \frac{a_{rfl} P_t \mathcal{P}_{BR}(\mathbf{x}_R) \mathcal{P}_{RU}^{rfl}(\mathbf{x}_R, \mathbf{x}_{RU}^{rfl}) \left| g_m^{rfl} \right|^2}{\sigma^2}. \tag{5.10}$$

When the other NOMA users' messages are considered interference, the transmitting user directly decodes its signal. Hence, the SINR of the transmitting user is expressed as:

$$\gamma_{\text{rfr}} = \frac{a_{rfr} P_t \mathcal{P}_{BR}(\mathbf{x}_R) \mathcal{P}_{RU}^{rfr}(\mathbf{x}_R, \mathbf{x}_{RU}^{rfr}) \left| g_m^{rfr} \right|^2}{a_{rfl} P_t \mathcal{P}_{BR}(\mathbf{x}_R) \mathcal{P}_{RU}^{rfr}(\mathbf{x}_R, \mathbf{x}_{RU}^{rfr}) \left| g_m^{rfr} \right|^2 + \sigma^2}. \tag{5.11}$$

Based on the aforementioned SINR expressions, the first target is to derive the STAR-IOS-aided channel models in the following section.

5.2 STAR-IOS-aided Channel Model Approximation

As the exact channel models of STAR-IOS-aided networks are complex, it is important to derive approximated mathematical channel models that are tractable for performance analysis. Hence, three approximated models for different using conditions are presented, namely the CL model, the MFC model, and the CF model. More specifically, the MFC model is used to derive diversity orders. The CL model is suitable for large STAR-IOSs with a large number of elements. For the CF model, it fits all using conditions by adjusting the CF functions and parameters but exploring a suitable CF function is a challenge. Detailed derivations and discussions are expressed in the following subsections.

5.2.1 CL Model

When the channel gains of all the elements of STAR-IOSs are irrelevant, the channel model of STAR-IOS-aided networks is expressed as the sum-

mation of different variables. Hence, the CL theorem is an appropriate mathematical tool to derive the approximated channel model. Although it has the constraint that the STAR-IOS elements are large enough, the CL model is one of the most popular models in recent works because of its great tractability on derivations. Hence, in the case where quantities of uncorrelated channels are generated by different STAR-IOS elements, the CL model is exploited to investigate the channel performance.

Lemma 10. *Assume that the quantity of STAR-IOS elements M is large and the channels for different STAR-IOS elements are independent. For the ES protocol and with the aid of the CL theorem, the PDF and CDF of the CL model are derived as:*

$$f_{\left|g_m^{rf}\right|^2}(y) = \frac{1}{2\sqrt{2\pi\eta_{eq}^{rf}}}\frac{1}{\sqrt{y}} \times \left(\exp\left(-\frac{\left(\sqrt{y}-\bar{h}_{eq}^{rf}\right)^2}{2\eta_{eq}^{rf}}\right) + \exp\left(-\frac{\left(\sqrt{y}+\bar{h}_{eq}^{rf}\right)^2}{2\eta_{eq}^{rf}}\right)\right) \quad (5.12)$$

and

$$F_{\left|g_m^{rf}\right|^2}(y) = \frac{1}{2}\left(\operatorname{erf}\left(\frac{\bar{h}_{eq}^{rf}+\sqrt{x}}{\sqrt{2\eta_{eq}^{rf}}}\right) - \operatorname{erf}\left(\frac{\bar{h}_{eq}^{rf}-\sqrt{x}}{\sqrt{2\eta_{eq}^{rf}}}\right)\right), \quad (5.13)$$

where $\bar{h}_{eq}^{rf}$ is the mean value of $|g_m^{rf}|$ with $rf \in \{rfr, rfl\}$ representing the transmitting links and the reflecting links, respectively. The η_{eq}^{rf} is the variance of $|g_m^{rf}|$. Based on the properties of the expectation and the variance for independent variables, the following derivations are presented as $\bar{h}_{eq}^{rf} = \sqrt{\beta_{rf}}M\bar{h}^2$ and $\eta_{eq}^{rf} = \beta_{rf}M\left(2\bar{h}^2\eta + \eta^2\right)$. Additionally, the function $\operatorname{erf}(\cdot)$ *is the error function.*

Proof. See Appendix C.1. □

Remark 21. *For the MS and TS protocols, the CL channel model expressions are the same but the coefficients are different. More specifically, for*

the MS protocol, the following equations hold, denoted as $\bar{h}^{rf}_{eq,MS} = M_{rf}\bar{h}^2$ *and* $\eta^{rf}_{eq,MS} = M_{rf}\left(2\bar{h}^2\eta + \eta^2\right)$ *with* $rf \in \{rfr, rfl\}$ *for transmitting links and reflecting links, respectively. For the TS model, the channel model coefficients are expressed as* $\bar{h}^{rf}_{eq,TS} = M\bar{h}^2$ *and* $\eta^{rf}_{eq,TS} = M\left(2\bar{h}^2\eta + \eta^2\right)$.

5.2.2 MFC Model

When analyzing the performance of a system, this chapter always considers the diversity orders to evaluate the performance in high SNR regions. Although the CL model provides a well-matched channel model with closed-form expressions, accurate diversity orders are not obtained since the high SNR region is not a perfect match. Hence, exploiting the Laplace transform, the accurate diversity orders are achieved by the MFC model.

Lemma 11. *To investigate the diversity orders, the MFC method is utilized to derive the STAR-IOS-aided channel model. Denote the Rician coefficient of the BR links as* k_1 *and that of the RU links as* k_2. *Additionally, the ES protocol is utilized in this theorem. In high SNR regions, the approximated PDF and CDF expressions are derived as:*

$$f^{0+}_{\left|g^{rf}_m\right|^2,ES}(x) = \frac{\left[\sigma\left(0,0\right)\right]^M x^{M-1}}{2(\beta_{rf})^M\left(2M-1\right)!} \tag{5.14}$$

and

$$F^{0+}_{\left|g^{rf}_m\right|^2,ES}(x) = \frac{\left[\sigma\left(0,0\right)\right]^M}{2(\beta_{rf})^M M\left(2M-1\right)!}x^M, \tag{5.15}$$

where

$$\begin{aligned}\sigma\left(t,n\right) = &\frac{4^{t-n+1}\sqrt{\pi}k_1^t k_2^t[\left(1+k_1\right)\left(1+k_2\right)]^{t+1}}{\left(t!\right)^2\left(n!\right)^2\exp\left(k_1+k_2\right)}\\ &\times\Gamma\begin{pmatrix}2n+2, 2t+2\\ t+n+\dfrac{5}{2}\end{pmatrix}{}_2F_1\left(2t+2, t-n+\frac{1}{2}; t+n+\frac{5}{2}; 1\right),\end{aligned} \tag{5.16}$$

and ${}_2F_1\left(\cdot,\cdot;\cdot;\cdot\right)$ *is the ordinary hypergeometric function. If consider all*

the channel links with the same Rician distribution with parameter k, the parameter is further derived as $\sigma(t,n) = \frac{4^{t-n+1}\sqrt{\pi}k^{2t}(1+k)^{2(t+1)}}{(t!)^2(n!)^2\exp(2k)}\Gamma\binom{2n+2,2t+2}{t+n+\frac{5}{2}}$ $\times_2 F_1\left(2t+2, t-n+\frac{1}{2}; t+n+\frac{5}{2}; 1\right)$.

Proof. See Appendix C.2. □

Corollary 32. *For the MS protocol, the PDF and CDF of the MFC channel model are expressed as:*

$$f^{0+}_{\left|g_m^{rf}\right|^2,MS}(x) = \frac{[\sigma(0,0)]^{M_{rf}} x^{M_{rf}-1}}{2(2M_{rf}-1)!} \tag{5.17}$$

and

$$F^{0+}_{\left|g_m^{rf}\right|^2,MS}(x) = \frac{[\sigma(0,0)]^{M_{rf}}}{2M_{rf}(2M_{rf}-1)!} x^{M_{rf}}, \tag{5.18}$$

where $M_{rfr} + M_{rfl} = M$ to fully utilize the STAR-IOS elements.

Additionally, for the TS protocol, the PDF and CDF of the MFC channel model are derived as:

$$f^{0+}_{\left|g_m^{rf}\right|^2,TS}(x) = \frac{[\sigma(0,0)]^{M} x^{M-1}}{2(2M-1)!} \tag{5.19}$$

and

$$F^{0+}_{\left|g_m^{rf}\right|^2,TS}(x) = \frac{[\sigma(0,0)]^{M}}{2M(2M-1)!} x^{M}. \tag{5.20}$$

Proof. The proof is similar to **Lemma 11**. □

5.2.3 CF Model

The third approximated channel model is denoted as the CF model. The Matlab CF tool is exploited to mimic the channel model as an extant distribution. More specifically, independent channels of different STAR-IOS elements are considered. Thus, the CF model approximately mimics the channel model as a Gamma distribution. In a word, the CF model has

wider using conditions compared to the aforementioned two channel models, while it has new challenges.

Compared to the MFC, accurate diversity gains cannot be obtained by the CF model as the CF model does not match the high SNR regions well. Hence, the MFC is still irreplaceable for diversity analysis.

Compared to the CL model, the CF model has pros and cons as follows. The advantage of the CF model is that it suits using consitions and it is tractable for further derivation, i.e., the STAR-IOS-aided networks with few elements and multi-cell networks[1]. Additionally, it even fits the condition when the STAR-IOS elements are influenced by each other with different CF functions. However, the disadvantage is that the CF model does not include detailed mathematical derivations, and exploring an accurate distribution may be challenging in some specific cases. Moreover, it is hard to ensure the possibility of finding the best CF function to make it more accurate than the CL model. Hence, the solution may select different channel models based on specific conditions but not advocate exploiting anyone.

Remark 22. *Compared to the using conditions of three channel models, including the CL, CF, and MFC models, the CL model fits the condition with large-sized STAR-IOSs while the CF model is extended to all the using conditions with different curve fitting functions. However, these two models cannot obtain accurate diversity orders. Hence, we figure out the MFC model to derive accurate diversity orders.*

Lemma 12. *Utilizing the CF tool, it indicates that the combined channel* $\left|g_m^{rf}\right|^2$ *is able to be simulated as the Gamma distribution with the coefficients* α *and* β*. Under the ES protocol, the PDF and CDF for the CF model are*

[1]The CL model cannot match STAR-IOS-aided networks with few elements. Hence, a channel model needs to be exploited with few STAR-IOS elements. Additionally, the channel models are expected to have exponential functions, which are tractable for multi-cell networks as the Laplace transform is always utilized to calculate the interference.

expressed as:

$$f_{\left|g_m^{rf}\right|^2}(x) = \frac{x^{\alpha-1}}{\Gamma(\alpha)(\beta_{rf}\beta)^{\alpha}} \exp\left(-\frac{x}{\beta_{rf}\beta}\right) \tag{5.21}$$

and

$$F_{\left|g_m^{rf}\right|^2}(x) = \frac{\gamma\left(\alpha, \frac{x}{\beta_{rf}\beta}\right)}{\Gamma(\alpha)}, \tag{5.22}$$

where $\gamma(\cdot,\cdot)$ is the incomplete Gamma function and $\Gamma(\cdot)$ is the Gamma function. Based on the mathematical tool, it is observed with $\alpha = M$ and $\beta < M$, e.g., $\alpha = 30$ and $\beta = 22.46$ with the number of STAR-IOS elements $M = 30$. The detailed values of the coefficient β should be further calculated by the Matlab CF tools.

Proof. Because of $\left|g_m^{rf}\right|^2 = \beta_{rf}\left(\sum_{m=1}^{M} h_{RU,m}^{rf} h_{BR,m}\right)^2$ with $rf \in \{rfl, rfr\}$ representing the reflecting and transmitting links, the CF tool is first utilized to mimic the variable of $\frac{|g_m^{rf}|^2}{\beta_{rf}}$ as a Gamma distribution. Hence, the PDF of $\frac{|g_m^{rf}|^2}{\beta_{rf}}$ is expressed as:

$$f_{\left|g_m^{rf}\right|^2 / \beta_{rf}}(x) = \frac{x^{\alpha-1}}{\Gamma(\alpha)\beta^{\alpha}} \exp\left(-\frac{x}{\beta}\right). \tag{5.23}$$

Based on (5.23), the final PDF and CDF of $\left|g_m^{rf}\right|^2$ are then derived as (5.21) and (5.22) in this theorem and this proof ends. □

Remark 23. *For the MS and TS protocols, the CF model expressions are the same as the expressions for the ES model, while the coefficients should be changed. In detail, the MS protocol has the conditions, denoted as $\alpha = M_{rfr}$ and $\alpha = M_{rfl}$ for the transmitting links and reflecting links, respectively. Additionally, we have the coefficient $\beta_{rf} = 1$ as no energy allocation is included. For the TS model, the channel model coefficients are expressed as $\alpha = M$ and $\beta_{rf} = 1$. The coefficient β under the MS and TS protocols should be further determined by the Matlab CF tools.*

5.2.4 Comparison

In this section, let us compare the accuracy and complexity of the three channel models. For diversity analysis, since the CF model and the CL model have changed the channel distributions and do not match the high SNR regions well [135], the MFC model has more accurate diversity orders[2]. Additionally, as the MFC model exploits the Taylor series to derive the asymptotic expressions, the complexity of the MFC model is the lowest among the three models.

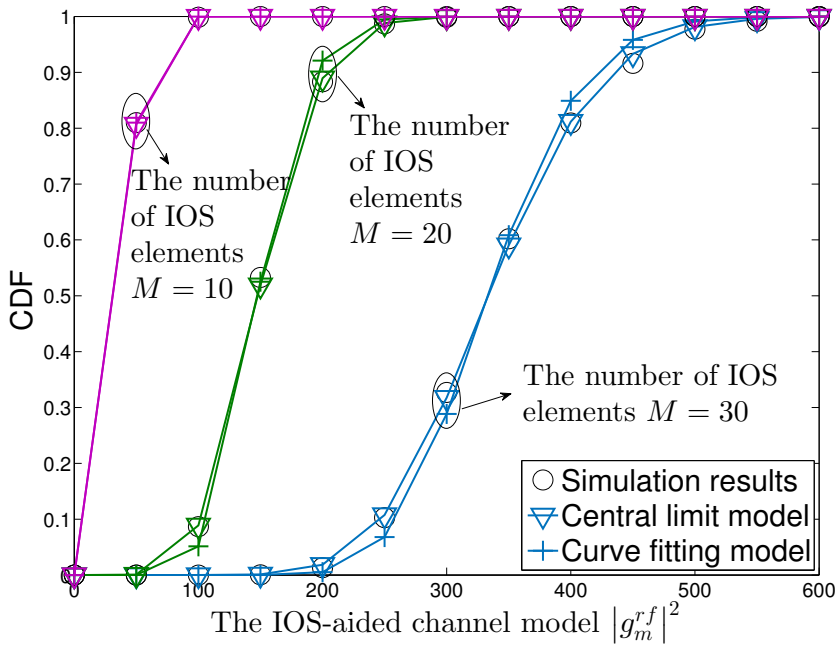

Figure 5.2: A CDF comparison between the CF model and the CL model with various numbers of STAR-IOS elements.

Then, the CDFs of the CL model and the CF model are compared. For accuracy, Fig. 5.2 demonstrates that the CL model is more accurate than the CF model. Thus, the CL model has more accurate outage performance than the CF model. For the complexity, as the CF model mimics the STAR-IOS

[2]As the CL model and the CF model have changed the distributions for the STAR-IOS channels, they cannot fit the high SNR regions well. The MFC derives the original distribution of the IOS channels, thus it has accurate diversity orders.

channel as a Gamma distribution, the current methods can be exploited to evaluate the outage performance, especially for multi-cell networks. Hence, the complexity of the CF model on performance analysis is lower than the CL model.

To sum up, the CL model is exploited to obtain the best accuracy of outage performance. Additionally, the CF model is harnessed to obtain tractable derivations (especially for multi-cell networks). Moreover, the M-FC model is utilized to obtain accurate diversity gains.

5.3 Outage Performance Analysis

In this section, the outage performance of the STAR-IOS-aided downlink NOMA network is investigated. More specifically, let us exploit the CL model and the CF model to calculate the approximated expressions of the OP for the reflecting and transmitting users.

In the following, the ES protocol is utilized to calculate the approximated OP via the CL model and the CF model. The outage performance of the MS protocol and the TS protocol is investigated with the same approaches of **Theorem 15** to **Theorem 18**, while the details are omitted due to space limitations.

Based on the NOMA technique, the definition expressions of the outage probabilities of the reflecting and transmitting users are first expressed as:

$$\mathbb{P}_{out,rfl}(x) = 1 - \Pr\left\{\gamma_{\text{SIC}} > \gamma_{th}^{SIC}, \gamma_{rfl} > \gamma_{th}^{out}\right\} \tag{5.24}$$

and

$$\mathbb{P}_{out,rfr}(x) = \Pr\left\{\gamma_{rfr} < \gamma_{th}^{out}\right\}, \tag{5.25}$$

where γ_{th}^{SIC} is the threshold for the SIC process, γ_{th}^{out} is the outage threshold. The closed-form OP expressions are then calculated based on the three aforementioned models as follows.

5.3.1 CL Model

As the channel model has been calculated in **Lemma 10**, the CL model is first utilized to calculate the approximated OP expressions of the reflecting and transmitting users. Recall that the power allocation coefficients as a_{rfr} and a_{rfl} for the transmitting user and reflecting user, respectively. Based on the OP definitions, the following expressions are obtained, denoted as $\mathbb{P}_{out,rfl}(x) = 1$ when $a_{rfr} < \gamma_{th}^{SIC} a_{rfl}$ and $\mathbb{P}_{out,rfr}(x) = 1$ when $a_{rfr} < \gamma_{th} a_{rfl}$.

Recall that more energy is allocated to the reflecting user by the STAR-IOS elements than the transmitting user. Hence, the reflecting user performs as the strong user. With the SIC process, the OP of the reflecting user is evaluated in **Theorem 15**. Without the SIC process, the OP expression of the transmitting user is derived in **Theorem 16**.

Theorem 15. *Note that the OP expression is expressed as* $\mathbb{P}_{out,rfl}(x) = 1$ *in the case of* $a_{rfr} < \gamma_{th}^{SIC} a_{rfl}$. *In the case of* $a_{rfr} > \gamma_{th}^{SIC} a_{rfl}$, *the closed-form OP expression of the reflecting user is derived for the ES protocol as:*

$$\mathbb{P}_{out,rfl}^{cl} = \sum_{n=0}^{\infty} \frac{4(-1)^n}{n!\sqrt{\pi}\,(2n+1)\left(2\eta_{eq}^{rfl}\right)^{\frac{2n+1}{2}}} \times \sum_{r=\{1,3,\cdots,2n+1\}}^{2n+1} \binom{2n+1}{r} \frac{R^{\frac{\alpha_t r}{2}} \left(\bar{h}_{eq}^{rfl}\right)^{2n+1-r}}{\frac{\alpha_t r}{2}+2} \left(\frac{\Upsilon_{\max} d_{BR}^{\alpha_t}}{P_t C_{BR} C_{RU}^{rfl}}\right)^{\frac{r}{2}}, \tag{5.26}$$

where $\Upsilon_{\max} = \max\left\{\frac{\gamma_{th}^{SIC}\sigma^2}{a_{rfr}-\gamma_{th}^{SIC}a_{rfl}}, \frac{\gamma_{th}^{out}\sigma^2}{a_{rfl}}\right\}$, γ_{th}^{out} *is the outage threshold and* $\binom{n}{r} = \frac{n!}{r!(n-r)!}$.

Proof. See Appendix C.3. □

Theorem 16. *Note that the OP is evaluated as* $\mathbb{P}_{out,rfr}(x) = 1$ *with the case of* $a_{rfr} < \gamma_{th} a_{rfl}$. *Under the condition with* $a_{rfr} > \gamma_{th} a_{rfl}$ *and with the aid of the ES protocol, the closed-form OP expression of the transmitting*

user is derived as:

$$\mathbb{P}^{cl}_{out,rfr} = \sum_{n=0}^{\infty} \frac{4(-1)^n}{n!\sqrt{\pi}\,(2n+1)\left(2\eta^{rfr}_{eq}\right)^{\frac{2n+1}{2}}} \sum_{r=\{1,3,\cdots,2n+1\}}^{2n+1} \binom{2n+1}{r} \times \frac{R^{\frac{\alpha_t r}{2}}\left(\bar{h}^{rfr}_{eq}\right)^{2n+1-r}}{\frac{\alpha_t r}{2}+2} \left(\frac{\Upsilon_2 d^{\alpha_t}_{BR}}{P_t C_{BR} C^{rfr}_{RU}}\right)^{\frac{r}{2}}, \tag{5.27}$$

where $\Upsilon_2 = \frac{\gamma^{out}_{th}\sigma^2}{a_{rfr}-\gamma^{out}_{th}a_{rfl}}$.

Proof. With the aid of (5.1) and the Taylor series of the error function, following the process of **Theorem 15**, this OP of the transmitting user is derived as:

$$\mathbb{P}^{cl}_{out,rfr}(x) = \frac{2}{\sqrt{\pi}R^2}\int_0^R x\left(\sum_{n=0}^{\infty}\frac{(-1)^n}{n!\,(2n+1)}\left(\frac{\bar{h}^{rfr}_{eq}+\sqrt{\frac{\Upsilon_2 d^{\alpha_t}_{BR}x^{\alpha_t}}{P_t C_{BR}C^{rfr}_{RU}}}}{\sqrt{2\eta^{rfr}_{eq}}}\right)^{2n+1} - \frac{2}{\sqrt{\pi}}\sum_{n=0}^{\infty}\frac{(-1)^n}{n!\,(2n+1)}\left(\frac{\bar{h}^{rfr}_{eq}-\sqrt{\frac{\Upsilon_2 d^{\alpha_t}_{BR}x^{\alpha_t}}{P_t C_{BR}C^{rfr}_{RU}}}}{\sqrt{2\eta^{rfr}_{eq}}}\right)^{2n+1}\right)dx. \tag{5.28}$$

and this theorem is proved based on the binomial theorem. □

5.3.2 CF Model

As the CL theorem only fits the condition when the STAR-IOS is large with plenty of STAR-IOS elements. For those with few STAR-IOS elements, the CL model is not accurate. Hence, let us consider the CF model to cope with this problem. Additionally, the CF model can be exploited in multi-cell networks since it is able to mimic the multi-cell networks as distributions with an exponential function to calculate the Laplace transform of interference.

Note that $\mathbb{P}_{out,rfl}(x) = 1$ when $a_{rfr} < \gamma^{SIC}_{th}a_{rfl}$ and $\mathbb{P}_{out,rfr}(x) = 1$ when $a_{rfr} < \gamma_{th}a_{rfl}$. Hence, in the following theorems, the OP expressions

of the reflecting and transmitting users are calculated, respectively, when the OP is not constantly equal to one. The OP of the reflecting user is evaluated in **Theorem 17**. Then, the same channel model is utilized to investigate the outage performance of the transmitting user in **Theorem 18**.

Theorem 17. *Consider the condition that all the channels through different STAR-IOS elements are independent. Based on the CF model with the ES protocol, the STAR-IOS channel is modelled as a Gamma distribution. In the case of* $a_{rfr} > \gamma_{th}^{SIC} a_{rfl}$*, the closed-form OP expression of the reflecting user is derived as:*

$$\mathbb{P}_{out,rfl}^{cf} = \frac{2}{\Gamma(\alpha)} \sum_{n=0}^{\infty} \frac{(-1)^n R^{\alpha_t(\alpha+n)}}{n!\,(\alpha+n)\,[\alpha_t(\alpha+n)+2]} \left(\frac{\Upsilon_{\max} d_{BR}^{\alpha_t}}{P_t C_{BR} C_{RU}^{rfl} \beta_{rfl} \beta} \right)^{\alpha+n}. \tag{5.29}$$

Proof. See Appendix C.4. □

Theorem 18. *Consider the same condition in* ***Theorem 17*** *with independent channels generated by the STAR-IOS elements. In the case of* $a_{rfr} > \gamma_{th} a_{rfl}$ *and with the aid of the ES protocol, the closed-form OP expression of the transmitting user is derived as:*

$$\mathbb{P}_{out,rfr}^{cf} = \frac{2}{\Gamma(\alpha) R^2} \sum_{n=0}^{\infty} \frac{(-1)^n}{n!\,(\alpha+n)} \left(\frac{\Upsilon_2 d_{BR}^{\alpha_t}}{P_t C_{BR} C_{RU}^{rfr} \beta_{rfr} \beta} \right)^{\alpha+n} \frac{R^{\alpha_t(\alpha+n)+2}}{\alpha_t(\alpha+n)+2}. \tag{5.30}$$

Proof. The proof is similar to the Appendix C.4. □

5.4 Asymptotic Outage Performance and Diversity Analysis

Based on the analysis, it is noted that the two models, namely the CL model and the CF model, match the OP perfectly when the transmit power is not

too large, while the performance in high SNR regions is not matched well. When the aforementioned two models are verified, it is found that the two channel models perform as upper or lower limits when the transmit SNR is high enough. This is because both the CL theorem and the CF tool have changed the distribution of the STAR-IOS channels. Hence, accurate diversity orders cannot be obtained. Instead, the upper or lower boundaries of the accurate diversity orders are received. To obtain the accurate ones, the MFC model is exploited to calculate the asymptotic expressions of the OP for the NOMA users under three protocols, i.e., the ES, MS, and TS protocols. Then, the asymptotic expressions are harnessed to derive and compare the accurate diversity orders among the three protocols.

In the following, the asymptotic expressions are derived by the MFC model based on the ES, MS and TS protocols, respectively, which are shown in the theorems from **Theorem 19** to **Theorem 20** and the corollaries from **Corollary 33** to **Corollary 36**. The diversity orders of three protocols are then compared by the corollaries from **Corollary 37** to **Corollary 40** and the remarks from **Remark 24** to **Remark 26**.

5.4.1 Asymptotic Analysis on the MFC Model

Based on the ES protocol, the closed-form asymptotic OP expressions for the reflecting user and the transmitting user are derived in **Theorem 19** and **Theorem 20**, respectively. Then, the asymptotic outage expressions are derived based on the MS and TS protocols by **Corollary 33** and **Corollary 36** in the following.

5.4.1.1 The Reflecting User

With the consideration of the ES, MS, and TS protocols, the asymptotic expressions of the OP for the reflecting users are first derived in the following.

Theorem 19. *Note that all the channels for different STAR-IOS elements are independent. Additionally, it is tractable to calculate that the outage situation always happens for the case as* $a_{rfr} < \gamma_{th}^{SIC} a_{rfl}$. *Under the ES*

protocol and considering $a_{rfr} > \gamma_{th}^{SIC} a_{rfl}$*, the closed-form asymptotic OP expression for the transmitting user is derived as:*

$$\mathbb{P}_{out,rfl}^{mf,ES}(x) = \frac{[\sigma(0,0)]^M R^{\alpha_t M}}{M(\alpha_t M+2)(2M-1)!(\beta_{rfl})^M}\left(\frac{\Upsilon_{\max} d_{BR}^{\alpha_t}}{P_t C_{BR} C_{RU}^{rfl}}\right)^M. \quad (5.31)$$

Proof. Since the CDF of the STAR-IOS channel model has been derived via the MFC method in **Lemma 11**, by substituting the CDF of the MFC model into the equation (5.24), the integration is obtained as:

$$\begin{aligned}\mathbb{P}_{out,rfl}^{mf,ES}(x) =& \int_0^R F_{\left|g_m^{rfl}\right|^2}\left(\frac{\Upsilon_{\max} d_{BR}^{\alpha_t} x^{\alpha_t}}{P_t C_{BR} C_{RU}^{rfl}}\right) f_{d_{RU}^{rfl}}(x)\, dx \\ =& \frac{[\sigma(0,0)]^M}{M(2M-1)!(\beta_{rfl})^M}\left(\frac{\Upsilon_{\max} d_{BR}^{\alpha_t}}{P_t C_{BR} C_{RU}^{rfl}}\right)^M \int_0^R \frac{x^{\alpha_t M+1}}{R^2} dx. \quad (5.32)\end{aligned}$$

By calculating the integration $\int_0^R \frac{x^{\alpha_t M+1}}{R^2} dx = \frac{R^{\alpha_t M}}{\alpha_t M+2}$, the final expression is obtained. □

Corollary 33. *For the MS protocol, the asymptotic OP expression is derived as:*

$$\mathbb{P}_{out,rfl}^{mf,MS}(x) = \frac{[\sigma(0,0)]^{M_{rfl}} R^{\alpha_t M_{rfl}}}{M_{rfl}(\alpha_t M_{rfl}+2)(2M_{rfl}-1)!}\left(\frac{\Upsilon_{\max} d_{BR}^{\alpha_t}}{P_t C_{BR} C_{RU}^{rfl}}\right)^{M_{rfl}}. \quad (5.33)$$

Proof. The proof is similar to **Theorem 19**. □

Corollary 34. *For the TS protocol, the closed-form asymptotic OP expression is derived as:*

$$\mathbb{P}_{out,rfl}^{mf,TS}(x) = \frac{[\sigma(0,0)]^M R^{\alpha_t M}}{M(\alpha_t M+2)(2M-1)!}\left(\frac{\Upsilon_{\max} d_{BR}^{\alpha_t}}{P_t C_{BR} C_{RU}^{rfl}}\right)^M. \quad (5.34)$$

Proof. The proof is similar to **Theorem 19**. □

5.4.1.2 The Transmitting User

Then, the asymptotic OP expressions of the transmitting user are derived based on the ES, MS, and TS protocols in the following.

Theorem 20. *Note that the OP for the transmitting user is constantly equal to one when $a_{rfr} < \gamma_{th} a_{rfl}$. Hence, consider $a_{rfr} > \gamma_{th} a_{rfl}$ and derive the closed-form asymptotic OP expression for the transmitting user as:*

$$\mathbb{P}_{out,rfr}^{mf,ES}(x) = \frac{[\sigma(0,0)]^M R^{\alpha_t M}}{M(\alpha_t M+2)(2M-1)!(\beta_{rfr})^M}\left(\frac{\Upsilon_2 d_{BR}^{\alpha_t}}{P_t C_{BR} C_{RU}^{rfr}}\right)^M. \quad (5.35)$$

Proof. By substituting the CDF of the MFC model in **Lemma 11** into (5.25), the OP of the transmitting user is expressed as:

$$\mathbb{P}_{out,rfr}^{mf,ES} = \frac{[\sigma(0,0)]^M}{(\beta_{rfr})^M M(2M-1)!}\left(\frac{\Upsilon_2 d_{BR}^{\alpha_t}}{P_t C_{BR} C_{RU}^{rfr}}\right)^M \int_0^R \frac{x^{\alpha_t M+1}}{R^2} dx, \quad (5.36)$$

and this integration can be easily calculated to obtain the final expression. □

Corollary 35. *For the MS protocol, the asymptotic OP expression for the transmitting user is derived as:*

$$P_{out,rfr}^{mf,MS}(x) = \frac{[\sigma(0,0)]^{M_{rfr}} R^{\alpha_t M_{rfr}}}{M_{rfr}(\alpha_t M_{rfr}+2)(2M_{rfr}-1)!}\left(\frac{\Upsilon_2 d_{BR}^{\alpha_t}}{P_t C_{BR} C_{RU}^{rfr}}\right)^{M_{rfr}}. \quad (5.37)$$

Proof. The proof is similar to **Theorem 20**. □

Corollary 36. *For the TS protocol, the asymptotic OP expression for the transmitting user is derived as:*

$$\mathbb{P}_{out,rfr}^{mf,TS}(x) = \frac{[\sigma(0,0)]^M R^{\alpha_t M}}{M(\alpha_t M+2)(2M-1)!}\left(\frac{\Upsilon_2 d_{BR}^{\alpha_t}}{P_t C_{BR} C_{RU}^{rfr}}\right)^M. \quad (5.38)$$

Proof. As the proof has been provided in **Theorem 20**, the proof is omitted. □

5.4.2 Diversity Analysis

After deriving the asymptotic expressions for the ES, MS, and TS protocols, the diversity orders for the reflecting user and the transmitting user are then derived by the following remarks and corollaries.

5.4.2.1 The ES Protocol

The diversity orders of the reflecting and transmitting users are first expressed based on the ES protocol as follows.

Corollary 37. *Denote the transmit SNR as $\rho_t \to \infty$. For the ES protocol, the accurate diversity order of the reflecting user is derived as:*

$$d_{rfl}^{ES} = -\lim_{\rho_t \to \infty} \frac{\log\left[\mathbb{P}_{out,rfl}^{mf,ES}(\rho_t)\right]}{\log(\rho_t)} = M. \tag{5.39}$$

where $\rho_t = P_t/\sigma^2$

Proof. As $\mathbb{P}_{out,rfl}^{mf}(\rho_t)$ is expressed as $\mathbb{P}_{out,rfl}^{mf,ES}(\rho_t) = A\rho_t^{-M}$, where A is the constant without ρ_t. Hence, the limit is calculated as $d_{rfl} = -\lim_{\rho_t \to \infty} \frac{\log\left[A\rho_t^{-M}\right]}{\log(\rho_t)}$ $= M$ and this proof ends. □

Corollary 38. *Let us assume the transmit SNR as $\rho_t \to \infty$. For the ES protocol, the accurate diversity order of the reflecting user is derived as:*

$$d_{rfr}^{ES} = -\lim_{\rho_t \to \infty} \frac{\log\left[\mathbb{P}_{out,rfr}^{mf,ES}(\rho_t)\right]}{\log(\rho_t)} = M. \tag{5.40}$$

Proof. The proof is similar to **Corollary 37**. □

Remark 24. *As for the ES protocol, the diversity orders for the reflecting and transmitting user are equal to M, which is the total number of the STAR-IOS elements.*

5.4.2.2 The MS Protocol

The diversity orders of the reflecting and transmitting users based on the MS protocol are then derived by the following remarks.

Corollary 39. *Consider the transmit SNR as $\rho_t \to \infty$. For the MS protocol, the accurate diversity orders of the NOMA users are derived as:*

$$d_{rfl}^{MS} = -\lim_{\rho_t \to \infty} \frac{\log\left[\mathbb{P}_{out,rfl}^{mf,MS}(\rho_t)\right]}{\log(\rho_t)} = M_{rfl} \tag{5.41}$$

and

$$d_{rfr}^{MS} = -\lim_{\rho_t \to \infty} \frac{\log\left[\mathbb{P}_{out,rfr}^{mf,MS}(\rho_t)\right]}{\log(\rho_t)} = M_{rfr}. \tag{5.42}$$

Proof. The proof is similar to **Corollary 37**. □

Remark 25. *As for the MS protocol, the diversity orders for the reflecting and transmitting user are equal to M_{rf}, where $rf \in \{rfl, rfr\}$ for the reflecting links and transmitting links, respectively. This value is the active number of the STAR-IOS elements.*

5.4.2.3 The TS Protocol

Additionally, the diversity orders of the reflecting and transmitting users according to the TS protocol are derived.

Corollary 40. *With the assumption of the transmit SNR, denoted as $\rho_t \to \infty$, the diversity order for the TS protocol is calculated as:*

$$d_{rfl}^{TS} = d_{rfr}^{TS} = M. \tag{5.43}$$

which is the number of the total STAR-IOS elements.

Remark 26. *When the diversity orders of the three protocols are compared in Table 5-A, it is concluded that the diversity order of users is equal to the number of active STAR-IOS elements. For the ES and TS protocols,*

Table 5-A: Diversity orders for different STAR-IOS protocols.

Protocol	The TS Protocol	The ES Protocol	The MS Protocol
Diversity Orders	M	M	M_{rf}

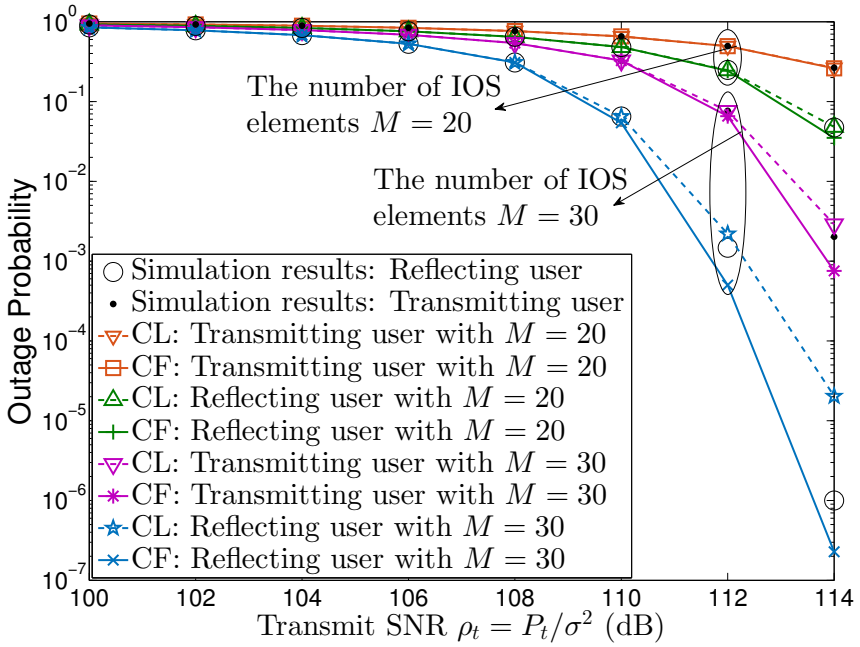

Figure 5.3: Comparisons between the CF model and the CL model based on the ES protocol.

all the STAR-IOS elements are fully activated, thereby the diversity order is high. However, for the MS protocol, the active STAR-IOS elements are split into two portions to be exploited to reflect or refract signals. Hence, the diversity orders of the MS protocol generally cannot match the transmitting and reflecting gain of the ES or TS protocol.

5.5 Numerical Results

This section presents the numerical results for the outage performance of users. More specifically, the Monte Carlo simulations validate: 1) the analytical closed-form expressions based on the CL model and the CF model,

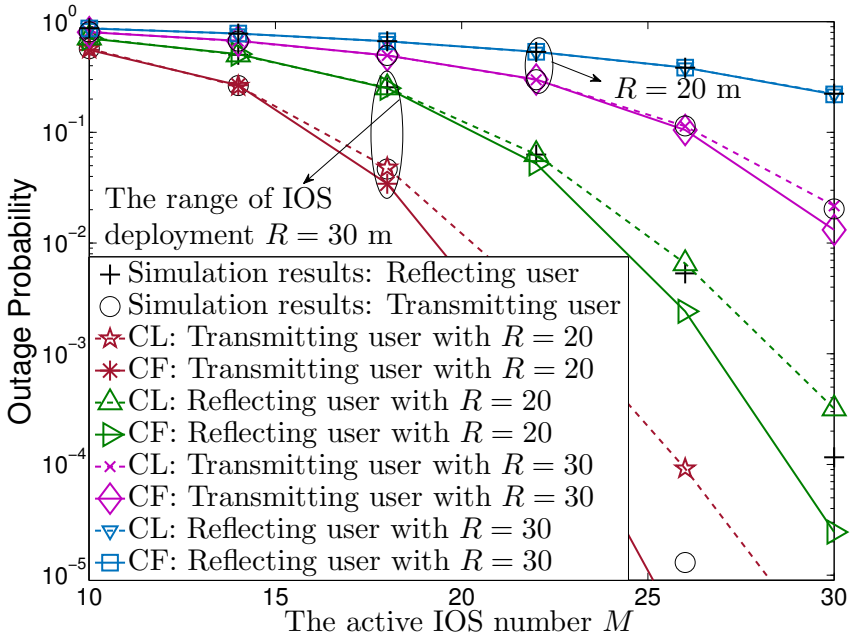

Figure 5.4: OP v.s. the number of STAR-IOS elements with various STAR-IOS deployment radii.

and 2) the diversity orders based on the MFC model with three protocols, namely the ES, MS, and TS protocols. Unless otherwise stated, the numerical coefficient settings are defined as follows. The noise power is $\sigma^2 = -170 + 10\log(f_c) + N_f = -90$ dB, where N_f is 10 dB and the carrier bandwidth f_c is 10 MHz. The transmit power P_t varies in $[10, 24]$ dBm. The path loss exponent is $\alpha_t = 2.4$. The outage threshold and the SIC threshold are equal as $\gamma_{th}^{SIC} = \gamma_{th}^{out} = 2^{0.1} - 1$. The power allocation coefficients of the BS are $a_{rfr} = 0.6$ and $a_{rfl} = 0.4$. The ES coefficients for the ES protocol are $\beta_{rfr} = 0.3$ and $\beta_{rfl} = 0.7$. The distance from the BS to STAR-IOS is $d_{BR} = 100$ m. The other coefficients are varied and specifically defined in the following paragraph.

In Fig. 5.3, let us further define the number of STAR-IOS elements as $M = \{20, 30\}$ and the radius of STAR-IOS deployment area as $R = 20$ m. Then, the outage performance versus the transmit SNR $\rho_t = P_t/\sigma^2$ is investigated. One observation is that increasing the number of STAR-

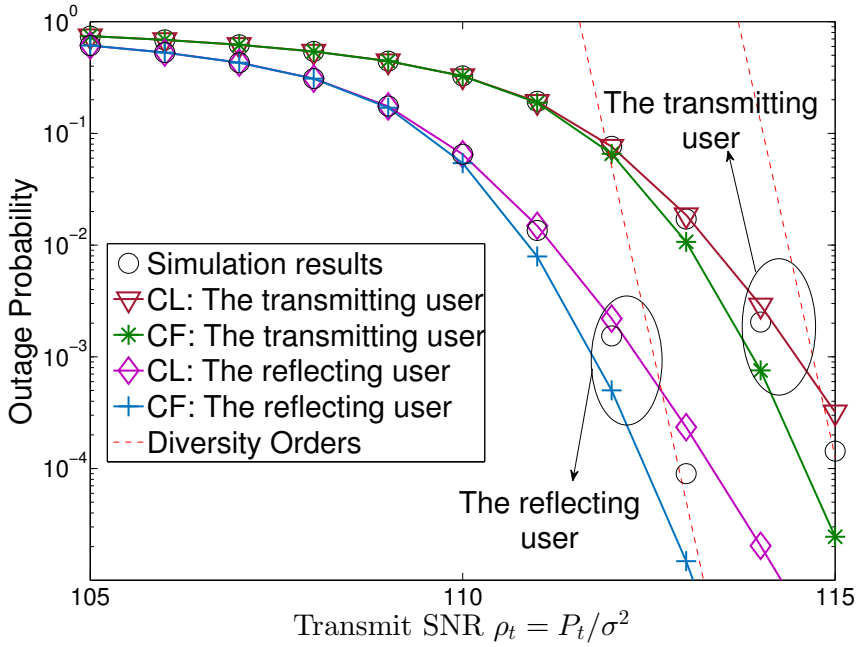

Figure 5.5: OP v.s. the transmit SNR for different channel models, including the CF, CL, and MFC models.

IOS elements is able to significantly increase the performance of NOMA users, which is because a large number of STAR-IOS elements provide well-integrated signals to enhance the channel quality.

In Fig. 5.4, the coefficients are defined that the number of STAR-IOS elements varies in $M = [10, 30]$ and the radius of STAR-IOS deployment area is chosen from $R = \{20, 30\}$ m. Hence, the outage performance versus the number of STAR-IOS elements is evaluated. It is observed that reducing the STAR-IOS deployment range enhances the performance as it reduces the influence of path loss. Comparing Fig. 5.3 and Fig. 5.4, it is concluded that the two channel models match the low SNR regions better than the high SNR regions. Specifically, the CF model performs as a lower bound of the simulation results while the CL model is an upper bound.

With the same settings of Fig. 5.5, let us compare the outage performance of the ES, TS, and MS protocols versus the transmit SNR in Fig. 5.6. Additionally, the outage performance of the NOMA and OMA techniques

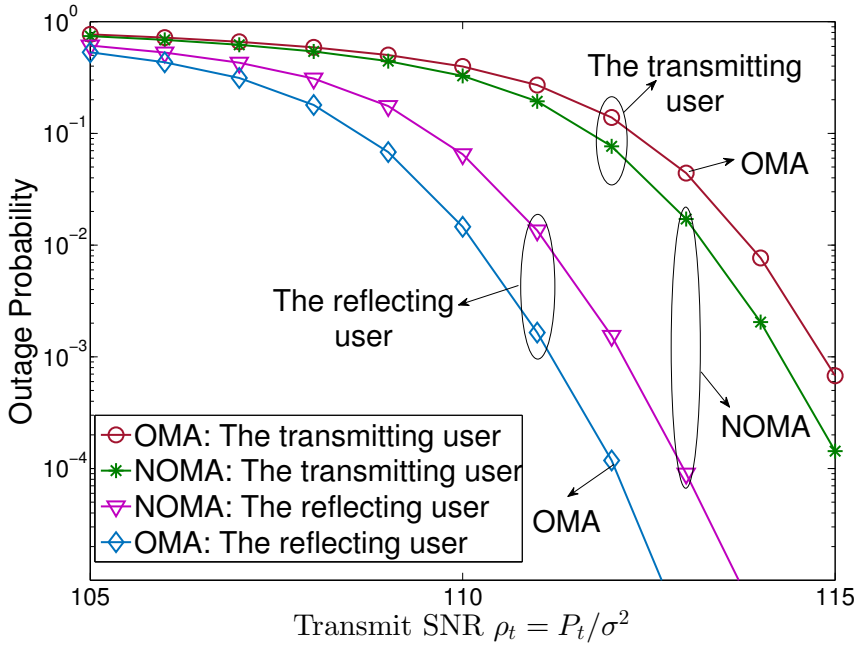

Figure 5.6: OP versus the transmit SNR to compare the NOMA technique and the OMA technique.

is compared in Fig. 5.6. One observation is that the TS protocol performs the best but it cannot serve two users in the same resource block. To serve two users in the same resource block, the ES protocol outperforms the MS protocol as the ES protocol integrates more STAR-IOS elements for each user to achieve higher diversity gains than the MS protocol.

5.6 Conclusions

This chapter has proposed three channel models of STAR-IOS channels and evaluated the outage performance of a STAR-IOS-aided downlink NOMA framework with randomly deployed users. More specifically, the CL model and the CF model have been exploited to derive the closed-form OP expressions and exploited the MFC model to derive the diversity gains under the ES, MS, and TS protocols, respectively. The analytical results have revealed that 1) the CL model has the closed-form expression as the manipulation

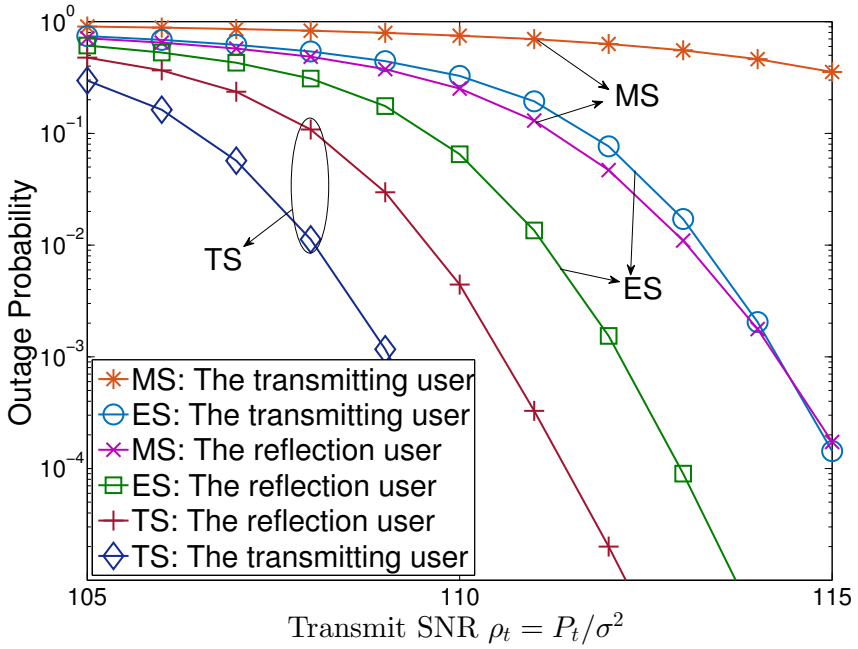

Figure 5.7: OP versus the transmit SNR to compare different protocols, including the ES, TS, and MS protocols.

of error functions; 2) the coefficients of the CF model have the relationship with the number of STAR-IOS elements as $\alpha = M$ and $\beta < M$; and 3) the diversity gains under three protocols are equal to the active number of STAR-IOS elements. Numerical results have shown that: 1) STAR-IOSs enhance the channel quality of its aided user; 2) the CL model and the CF model perform as boundaries of the simulation results in high SNR regions; 3) the TS protocol has the best performance but it cannot serve two users in the same resource block; and 4) the ES protocol outperforms the MS protocols in the same resource block.

Chapter 6

Semi-Integrated Sensing and Communication: From OMA to NOMA

To consider a practical scenario having high BE, Semi-ISaC networks are advocated, where the bandwidth is split into three portions, namely the communication-only bandwidth, the radar-echo-only bandwidth, and the ISaC bandwidth. Since the NOMA and ISaC concepts match each other harmoniously, this chapter commences by investigating an OMA-based Semi-ISaC network first and then evolves it to a NOMA-based scenario. The main contributions are summarized as follows:

- The novel philosophy of Semi-ISaC networks is proposed, where the total bandwidth is split into three portions: the communication-only bandwidth, the radar-echo-only bandwidth, and the ISaC bandwidth. Both the OMA-based and the NOMA-based Semi-ISaC scenarios are defined. Additionally, three parameters (α_{semi}, β_{semi}, and ϵ_{semi}) are exploited for controlling the bandwidth of different scenarios.

- The performance of the OMA-based Semi-ISaC networks is evaluated. As for communication signals, the closed-form expressions of the OP and the ergodic rate are derived. As for radar echoes, the ergodic REIR is characterized.

- The performance of NOMA-based Semi-ISaC networks is also investi-

gated. This chapter considers two scenarios to clarify the deployment of a pair of users. For each scenario, the closed-form expressions of the OP for the communication signals (for both the communication transmitter and the radar target) are first derived. Then, the ergodic rate expressions of the communication signals are derived. The closed-form analytical expressions of the ergodic REIR for the radar echo are also calculated.

- The asymptotic performance of the NOMA-based Semi-ISaC networks is evaluated. Based on the asymptotic expressions, this chapter gleans some further insights. First, the asymptotic expressions of both the OP and of the ergodic REIR are derived, followed by deriving both the diversity orders of communication signals and the high-SNR slopes for characterizing the radar echoes. As for the diversity orders, analytical results indicate that the near user's diversity order is m, which is the parameter of Nakagami-m fading channels, while the far user's diversity gain is zero. As for the high-SNR slopes of the ergodic REIR, it is observed that the high-SNR slope is related both to the radar's duty cycle and to the pulse duration during its transmission from the BS to the radar target.

- Numerical results illustrate the following conclusions. 1) For the communication signals, increasing the line-of-sight (LoS) component's power enhances the outage performance. 2) For the radar echo, dense pulses emerging from the BS enhance the performance of radars. 3) The high-SNR slopes of the radar echo are also related to the radar's duty cycle and pulse duration, separately.

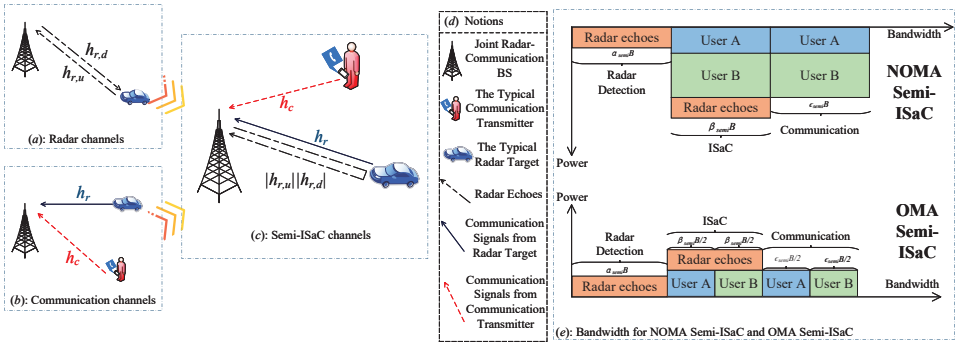

Figure 6.1: Illustration of the NOMA-based Semi-ISaC system.

6.1 System Model

This chapter focuses the attention on an uplink (UL) Semi-ISaC system[1], which includes a BS, a communication transmitter, and a radar target[2]. The BS is equipped with an active, mono-static, pulsed radar that exploits the intervals of pulses to detect the radar targets. A single-input-single-output (SISO) model is considered. It is assumed that the radar target also has communication functions, as exemplified by cars or UAVs. To design the Semi-ISaC system, the total bandwidth B is split into three portions, including the bandwidth for wireless communication (denoted as B_W), the bandwidth for ISaC (denoted as B_I), and the bandwidth for radar detection (denoted as B_R). Three coefficients, denoted as (α_{semi}, β_{semi}, and ϵ_{semi}), are defined for controlling the bandwidth of different scenarios as:

$$B = \underbrace{\alpha_{semi}B}_{B_R} + \underbrace{\beta_{semi}B}_{B_I} + \underbrace{\epsilon_{semi}B}_{B_W}. \tag{6.1}$$

where $\alpha_{semi} \in [0,1]$, $\beta_{semi} \in [0,1]$, $\epsilon_{semi} \in [0,1]$, and $\alpha_{semi} + \beta_{semi} + \epsilon_{semi} = 1$.

[1]The "uplink" means that the wireless communication users send signals to the BS. The radar sensing pulses will still be sent by the BS, reflected by the radar target, and finally received by the BS.

[2]This chapter assumes that the radar target passively reflects the pulses sent by the BS to indicate the parameters of the radar target, such as range, cross-section, etc. For further information, the radar targets will use the communication function to send signals to the BS in the uplink channels.

Before introducing the Semi-ISaC channel model, let us highlight the assumptions as follows:

- 1) There is only one radar target located in the serving area of the BS. Other radar targets are served by the BSs of other cells, and hence are ignored in the analysis.
- 2) Based on prior observations, the BS is capable of accurately predicting and estimating the time delay of radar echoes to avoid synchronization errors.
- 3) The range resolution of the radar system is sufficiently accurate for avoiding the interference between two radar targets[3].
- 4) The range fluctuation is interpreted as a time-delay fluctuation modeled by the Gaussian distribution [54].
- 5) The cross-section of the radar target is represented by a constant parameter, denoted as σ_{RCS}. The Doppler shift estimation is perfect for the radar target in order to predict and correct the waveforms.

6.1.1 Frequency-Division (FD) ISaC, OMA-Based Semi-ISaC, and NOMA-Based Semi-ISaC

This subsection presents the fundamental concepts and definitions of the conventional (FD) ISaC, OMA-based Semi-ISaC, and NOMA-based Semi-ISaC.

6.1.1.1 FD ISaC

The benchmark is the FD ISaC having the coefficients of α_{semi}=0, β_{semi}=1, and ϵ_{semi}=0. The total bandwidth B is exploited for the ISaC scenario. The users are assigned to orthogonal resource blocks.

[3]This assumption is only used for the case when there are more than two radar targets in the serving area of the BS. If there is only a single radar target in the serving area, this assumption can be neglected.

6.1.1.2 OMA-Based Semi-ISaC

The total bandwidth B is split into three portions with the constraints in Eq. (6.1) as $\alpha_{semi} \in [0, 1]$, $\beta_{semi} \in (0, 1]$, $\epsilon_{semi} \in [0, 1]$, and $\alpha_{semi}+\beta_{semi}+\epsilon_{semi} = 1$ (which means $\beta_{semi} \neq 0$). In the ISaC bandwidth, SIC is utilized for extracting the radar echo and communication signals from the superimposed signals, while SIC is not utilized to support detecting multiple users with same function. The following part of this chapter considers a two-user case, namely the user A and B. As the radar-echo-only bandwidth (B_R) has no communication signal, OMA is used both in the ISaC bandwidth (B_I) and in the communication-only bandwidth (B_W). Hence, B_I and B_W are further divided into two OMA sub-bands for the two users, respectively. As shown in Fig. 6.1. (e), the total bandwidth is finally divided into five parts, including the radar-echo-only bandwidth B_R, the ISaC bandwidth for user A ($B_I/2$), the ISaC bandwidth for user B ($B_I/2$), the communication-only bandwidth for user A ($B_W/2$), and the communication-only bandwidth for user B ($B_W/2$).

6.1.1.3 NOMA-Based Semi-ISaC

As indicated at the top of Fig. 6.1. (e), the total bandwidth is split into three portions (B_W, B_I, and B_R) subject to the same coefficient constraints as the OMA-based Semi-ISaC. However, the wireless communication in the bandwidth B_W and B_I relies on NOMA instead of OMA. As exemplified by a two-user case, the communication signals of the two users share the same bandwidth instead of being split into two OMA sub-bands. Additionally, the NOMA-based Semi-ISaC system has to activate SIC in the ISaC bandwidth twice to obtain the radar detection information, while the OMA-based Semi-ISaC scenario only once.

Since the deployment of users directly influence the SIC-based detection orders, two specific deployment scenarios are considered: i) A near communication transmitter is paired with a far radar target, termed as *Scenario-I*; and ii) A far communication transmitter is paired with a near radar target,

referred to *Scenario-II*. In the following sections, the system performance based on these two scenarios is evaluated.

6.1.2 Channel Model

This section provides the signal models of the radar target and the communication transmitter in terms of the small-scale fading, the large-scale fading, and the SIC orders.

6.1.2.1 Small-Scale Fading

The path loss model and small-scale fading model are defined in this subsection for both the radar and communication links. As the ISaC channels are hosted in the mm-wave band, it is assumed that Nakagami-m fading is encountered both by the radar and communication channels [123]. The probability density function (PDF) can be expressed as $f_{|h_i|^2}(x) = \frac{m^m}{\Gamma(m)} x^{m-1} \exp(-mx)$, with m being the Nakagami-m shape parameter and its mean value being one. As seen in Fig. 6.1. (a)-(c), the subscript $i = \{(r,d),(r,u),r,c\}$ represents different small-scale channel gains, where $|h_{r,d}|^2$ and $|h_{r,u}|^2$ are those of the downlink (DL) transmission and the UL echo of the radar target, $|h_c|^2$ is that of the transmitter's UL communication signal, and $|h_r|^2$ is that of the radar target's UL communication signal.

6.1.2.2 Large-Scale Fading

The path loss models of radar echoes are different from that of communication signals. Assume that the distance between the BS and the communication transmitter is d_c and the distance between the BS and the radar target is d_r. For the communication channels, the path loss model follows the conventional model of

$$\mathcal{P}_c(d_c) = G_c C_c (d_c)^{-\alpha_c}, \tag{6.2}$$

where α_c is the path loss exponent of communication links, $C_c = \left(\frac{c}{4\pi f_c}\right)^2$ is associated with the reference distance of $d_0 = 1$ m, the speed of light is $c = 3 \times 10^8$ m/s, and the carrier frequency is f_c. The antenna gain is valued as $G_c = 1$ for single-antenna systems.

This chapter uses different coefficients but presents the path loss function of the radar echoes in the same form as in Eq. (6.2):

$$\mathcal{P}_r\left(d_r\right) = G_r C_r (d_r)^{-\alpha_r}, \tag{6.3}$$

where α_r is the path loss exponent of the radar echoes with $\alpha_r = 4$ representing the free-space scenario [123]. The parameter $C_r = \frac{\sigma_{RCS}\lambda^2}{(4\pi)^3}$ is the reference-distance-based intercept, λ is the wavelength of the carrier, and $\sigma_{RCS} = \frac{4\pi S_r}{S_t}$ is associated with the target radar cross section, where S_r is the power density that is intercepted by the target and S_t is the scattered power density at the reference distance of $d_0 = 1$ m [123]. The antenna gain, denoted as $G_r = 1$, is also obtained for single-antenna scenarios.

6.1.3 SIC-Based Detection Orders for NOMA

The SIC processes of the conventional NOMA system and the NOMA-based Semi-ISaC system are different. For the conventional NOMA system, the BS only receives signals at two different power levels, when a two-user case is considered, where the near user receives more power and is detected first compared to the far user[4]. For the Semi-ISaC NOMA-based system under a two-user case, the BS receives a superposition of various signal components, including the communication signal from the radar target, the communication signal from the communication transmitter, and the radar echo reflected by the radar target. As the BS is capable of estimating the radar echo, the estimated radar echo can be subtracted from the superimposed signals to reduce its interference inflicted upon other communication signals. Hence,

[4] As fixed power allocation, the path loss has more dominant effects than the small-scale fading, as the average performance is considered. Thus, this paper consider the near user to be the strong user [126].

the communication signals detected from the two users have higher power levels and thus higher priority than the radar echo. As a consequence, it is better to fix the SIC-based detection order of the radar echo to be the last. For the two communication signals, the near user's signal is detected first and the far user's signal is detected at the middle stage [54].

6.1.4 Signal Model

This chapter aim to support the communication function, but to also add the sensing function into the ISaC system. Since communication signals convey more data than radar pulses over a long period, the communication signals will have high-priority SIC detection orders than the radar echoes. In this case, let us fix the radar echo as the last stage of the SIC detection. If the radar echo has a higher power level than those of the communication signals, they will inflict excessive interference. Hence, a predicted radar echo from the integrated signals is subtracted to ensure the radar echo's power level as the lowest [54]. In this model, both OMA and NOMA cases need SIC to split the communication signals and radar pulses. Hence, for both OMA and NOMA cases, subtracting the predicted radar echo may enhance the SIC success rate and then enhance the performance.

Assume that the BS has known the pulse type that was sent to the radar target and acquired prior observations to evaluate the predicted range of the radar target's position. If the radar pulses are regularly sent to the radar target but broadcasting as a fixed frequency, the BS is able to calculate the predicted radar echo based on the prior observations. Naturally, the uncertainty in the positioning directly corresponds to time delay fluctuations in radar systems [54]. As stated in the assumptions, the time delay fluctuation τ obeys a Gaussian distribution with the variance of $\sigma_\tau^2 = \mathbb{E}\left[|\tau - \tau_{pre}|^2\right]$, where $\mathbb{E}[\cdot]$ is the expectation. Based on [54], the average power level of the radar echo is derived by considering the uncertainty in the positioning

decision as:

$$\mathbb{E}\left[|x(t-\tau)-x(t-\tau_{pre})|^2\right] \approx \gamma^2 \beta_{semi}^2 B^2 \sigma_\tau^2, \tag{6.4}$$

where the radar has the pulse for a flat spectral shape, denoted as $\gamma^2 = (2\pi)^2/12$. The variance τ is the observation of the time delay for the radar target and τ_{pre} is the predicted value of τ.

Since the SIC-based detection order of the radar echo is fixed to be the last, a drawback has to be tolerated, namely that when the radar echo has a high received power level, the ISaC system may face eroded performance, since the radar echo is regarded as interference for the communication signals in the SIC step. To mitigate this, the predicted target range is exploited to generate a predicted radar return and subtract it from the superimposed signals [54]. Assume that the predicted radar echo is accurate enough for the SIC process. By harnessing this approach, the performance of the communication system is improved. Hence, the received superimposed aggregate signal $v(t)$ is expressed as:

$$\begin{aligned} v\left(t\right) = & \underbrace{h_c\sqrt{P_c\mathcal{P}_c\left(d_c\right)}z\left(t\right)}_{s_c} + \underbrace{h_r\sqrt{P_r\mathcal{P}_c\left(d_r\right)}y\left(t\right)}_{s_r} \\ & + \underbrace{h_{r,d}h_{r,u}\sqrt{P_{BS}\mathcal{P}_r\left(d_r\right)}\left[x\left(t-\tau\right)-x\left(t-\tau_{pre}\right)\right]}_{e_r} + n\left(t\right), \end{aligned} \tag{6.5}$$

where s_c is the communication signal received from the UL communication transmitter at the BS, s_r represents the communication signal received from the radar target at the BS, and e_r is the radar echo reflected from the radar target impinging at the BS. Additionally, P_c and P_r are the UL transmit power of the communication transmitter and the radar target, respectively. Moreover, P_{BS} is the DL transmit power of the BS used for radar detection. Finally, $n\left(t\right)$ represents the noise having a variance of $\sigma^2 = k_B T_{temp} \beta_{semi} B$, where k_B is the Boltzmann constant and T_{temp} is the absolute temperature.

Based on the assumptions and derivations above, the signal models of the OMA-based Semi-ISaC and NOMA-based Semi-ISaC are presented in

Table 6-A: Notation of Parameters

$\mathcal{P}_c\left(d_c\right)=C_c(d_c)^{-\alpha_c}$	$\mathcal{P}_r\left(d_r\right)=C_r(d_r)^{-\alpha_r}$
$C_c=\left(\frac{c}{4\pi f_c}\right)^2$	$C_r=\frac{\sigma_{RCS}\lambda^2}{(4\pi)^3}$
$\Omega=\frac{m\left(P_{BS}\mathcal{P}_r(d_r)\gamma^2\beta_{semi}^2B^2\sigma_\tau^2+\sigma^2\right)}{P_j\mathcal{P}_c(d_j)}$	$\Xi_{r,1}=2T\beta_{semi}B\gamma_r^{echo}$
$Q\left(x\right)=\frac{1}{\sqrt{2}}\int_x^\infty\exp\left(-\frac{y^2}{2}\right)dy$	$C_n^m=n!/(m!(n-m)!)$
$a_1=\frac{P_{BS}G_rC_r(d_r)^{-\alpha_r}\gamma^2\beta_{semi}^2B^2\sigma_\tau^2}{G_cC_c(d_c)^{-\alpha_c}}$	$a_2=\frac{\sigma^2}{G_cC_c(d_c)^{-\alpha_c}}$
$a_4=\frac{P_{BS}G_rC_r\gamma^2\beta_{semi}^2B^2\sigma_\tau^2}{G_cC_c(d_r)^{-\alpha_c}(d_r)^{\alpha_r}}$	$a_3=\frac{(d_r)^{-\alpha_c}}{(d_c)^{-\alpha_c}}$
$b_1=\frac{P_{BS}G_rC_r\gamma^2\beta_{semi}^2B^2\sigma_\tau^2}{G_cC_c(d_r)^{\alpha_r-\alpha_c}}$	$a_5=\frac{\sigma^2}{G_cC_c(d_r)^{-\alpha_c}}$
$b_2=\frac{\sigma^2}{G_cC_c(d_r)^{-\alpha_c}}$	$b_3=\frac{(d_c)^{-\alpha_c}}{(d_r)^{-\alpha_c}}$
$\Lambda_1=\frac{m(a_1+a_2)}{P_c}$	$\Lambda_3=\frac{m(b_1+b_2)}{P_r}$
$\Lambda_2=\frac{m(a_4+a_5)}{P_r}\left(\frac{\gamma_{SIC}a_3P_r}{P_c}+1\right)$	$\Lambda_5=\frac{m\gamma_{SIC}(b_1+b_2)}{P_r}$
$\Lambda_4=\frac{m}{P_c}\left(a_1+a_2\right)\left(\frac{\gamma_{SIC}}{P_r}P_cb_3+1\right)$	

the following part. Additionally, the notations of parameters are also summarized in TABLE I.

6.1.4.1 Communication Signals for OMA-Based Semi-ISaC

The SINR expression of the communication transmitter and the radar target is expressed as:

$$\gamma_j^{OMA}=\frac{P_j\mathcal{P}_c\left(d_j\right)\left|h_j\right|^2}{P_{BS}\mathcal{P}_r\left(d_r\right)\left|g_r\right|^2+\sigma^2}, \tag{6.6}$$

where $j\in\{c,r\}$ represents for the communication transmitter and the radar target, respectively. The channel fading parameter is denoted as:

$$|g_r|^2=|h_{r,d}|^2|h_{r,u}|^2\gamma^2\beta_{semi}^2B^2\sigma_\tau^2. \tag{6.7}$$

6.1.4.2 Communication Signals for NOMA-Based Semi-ISaC in Scenario-I

For Scenario-I, the communication transmitter is the near user, whose signals is detected first. Given the different power levels, the BS directly detects the UL signal received from the communication transmitter by considering both the communication signals and the radar echo of the radar target as interference. Hence, the SINR of the communication transmitter is formulated as:

$$\gamma_c^I = \frac{\overbrace{P_c \mathcal{P}_c\left(d_c\right)\left|h_c\right|^2}^{\text{Transmitter's Communication Signals}}}{\underbrace{P_r \mathcal{P}_c\left(d_r\right)\left|h_r\right|^2}_{\substack{\text{Radar Target's} \\ \text{Communication Signals}}} + \underbrace{P_{BS} \mathcal{P}_r\left(d_r\right)\left|g_r\right|^2}_{\text{Radar Echoes}} + \underbrace{\sigma^2}_{\text{Noise}}}. \tag{6.8}$$

By subtracting the signal of the communication transmitter from the composite signal by the SIC remodulated process, the SINR of the communication signals for the radar target becomes:

$$\gamma_r^I = \frac{\overbrace{P_r \mathcal{P}_c\left(d_r\right)\left|h_r\right|^2}^{\text{Radar Target's Communication Signals}}}{\underbrace{\varsigma_c P_c \mathcal{P}_c\left(d_c\right)\left|h_c\right|^2}_{\substack{\text{SIC of Transmitter's} \\ \text{Communication Signals}}} + \underbrace{P_{BS} \mathcal{P}_r\left(d_r\right)\left|g_r\right|^2}_{\text{Radar Echoes}} + \underbrace{\sigma^2}_{\text{Noise}}}, \tag{6.9}$$

where $0 < \varsigma_c < 1$ represents the imperfect SIC while $\varsigma_c = 0$ corresponds to the perfect SIC.

6.1.4.3 Communication Signals for NOMA-Based Semi-ISaC in Scenario-II

For Scenario-II, the near user is the radar target. Thus, the BS firstly detects the communication signals of the radar target, yielding an SINR of

$$\gamma_r^{II} = \frac{\overbrace{P_r \mathcal{P}_c\left(d_r\right)\left|h_r\right|^2}^{\text{Radar Targets's Communication Signals}}}{\underbrace{P_c \mathcal{P}_c\left(d_c\right)\left|h_c\right|^2}_{\substack{\text{Transmitter's} \\ \text{Communication Signals}}} + \underbrace{P_{BS} \mathcal{P}_r\left(d_r\right)\left|g_r\right|^2}_{\text{Radar Echoes}} + \underbrace{\sigma^2}_{\text{Noise}}}. \tag{6.10}$$

Following the (perfect/imperfect) SIC process, the SINR of communication signals for the communication transmitter becomes:

$$\gamma_c^{II} = \frac{\overbrace{P_c \mathcal{P}_c\left(d_c\right)\left|h_c\right|^2}^{\text{Transmitter's Communication Signals}}}{\underbrace{\varsigma_r P_r \mathcal{P}_c\left(d_r\right)\left|h_r\right|^2}_{\substack{\text{SIC of Radar Targets's} \\ \text{Communication Signals}}} + \underbrace{P_{BS} \mathcal{P}_r\left(d_r\right)\left|g_r\right|^2}_{\text{Radar Echoes}} + \underbrace{\sigma^2}_{\text{Noise}}}, \tag{6.11}$$

where $0 < \varsigma_r < 1$ represents the imperfect SIC while $\varsigma_r = 0$ corresponds to the perfect SIC.

6.1.4.4 Radar Echoes for OMA and NOMA

Since this chapter aims to ensure the priority of communication signals, the radar echo is simply left behind after the last SIC stage. With the aid of SIC, the SNR is expressed as:

$$\gamma_r^{echo} = \frac{\overbrace{P_{BS} \mathcal{P}_r\left(d_r\right)\left|g_r\right|^2}^{\text{Radar Echoes}}}{\underbrace{\varsigma_c P_c \mathcal{P}_c\left(d_c\right)\left|h_c\right|^2 + \varsigma_r P_r \mathcal{P}_c\left(d_r\right)\left|h_r\right|^2}_{\text{SIC of Communication Signals}} + \sigma^2}. \tag{6.12}$$

For the equation above, both the NOMA and OMA cases associated with perfect SIC have $\varsigma_c = 0$ and $\varsigma_r = 0$. The NOMA case with imperfect SIC has $0 < \varsigma_c < 1$ and $0 < \varsigma_r < 1$. The OMA case with imperfect SIC has two

combinations: 1) $0 < \varsigma_c < 1$ and $\varsigma_r = 0$ for the communication transmitter's subchannel and 2) $\varsigma_c = 0$ and $0 < \varsigma_r < 1$ for the radar target's subchannel.

Sections III to V will consider the ergodic REIR as the metric for characterizing the performance of the radar detection system. This metric is directly related to γ_r^{echo} derived above.

6.1.4.5 Perfect or Imperfect SIC

This chapter aims to first propose the Semi-ISaC network to enhance the multi-functional connectivity, hence perfect SIC schemes are exploited to investigate the performance of upper bounds ($\varsigma_c = 0$ and $\varsigma_r = 0$). Based on the derivations in Sections III to V, some insights are obtained to indicate the properties of the Semi-ISaC network. As for the imperfect SIC scenarios, a figure will be drawn in the simulation part to compare the performance between the upper bounds and practical scenarios. The analytical derivation and investigation of imperfect SIC cases can be extended by this model and will be left for the future work due to the strict limitation of space.

6.2 Performance Evaluation for OMA-Based Semi-ISaC

This section evaluates the OMA-based Semi-ISaC networks. Again, two performance metrics are adopted, namely the OP and the ergodic rate, for communication signals. Likewise, the ergodic REIR is adopted as the performance metric for the radar echoes.

6.2.1 Performance Evaluation for Communication Signals

This subsection aims to investigate the performance of communication signals. Before that, the average interference strength is first evaluated.

Lemma 13. To simplify the expression of interference (radar echoes), let us introduce the shorthand of $I_R = P_{BS}\mathcal{P}_r\left(d_r\right)|h_{r,d}|^2|h_{r,u}|^2\gamma^2B^2\sigma_\tau^2$. The

expectation of interference is expressed as:

$$\mathbb{E}\left[I_R\right](d_r) = P_{BS}\mathcal{P}_r\left(d_r\right)\gamma^2\beta_{semi}^2 B^2\sigma_\tau^2. \tag{6.13}$$

Proof. Given the definition of expectation and the distribution of Nakagami-m fading channels, the expression of interference is presented as:

$$\begin{aligned}\mathbb{E}\left[I_R\right](d_r) =& P_{BS}\mathcal{P}_r\left(d_r\right)\gamma^2\beta_{semi}^2 B^2\sigma_\tau^2\left(\frac{m^m}{\Gamma\left(m\right)}\right)^2 \\ &\times\int_0^\infty x^m\exp\left(-mx\right)dx\int_0^\infty y^m\exp\left(-my\right)dy,\end{aligned} \tag{6.14}$$

and with the aid of Eq. [2.3.3.1] in [127], this lemma is proved. The detailed proof is expressed in Section I of [136]. □

In the OMA-based Semi-ISaC network, the OP of the communication signals is defined as $\mathbb{P}_j^{OMA} = \Pr\left\{\gamma_j^{OMA} < \gamma_{th}^{OMA}\right\}$, given the threshold γ_{th}^{OMA}. The achieved rate is defined as $R_j^{OMA} = \frac{1}{2}\log_2\left(1+\gamma_j^{OMA}\right)$. **Theorem 21** provides the closed-form expressions of both the OP and the ergodic rate for communication signals in the OMA-based Semi-ISaC network.

Theorem 21. Upon introducing the subscript of $j \in \{c, r\}$ for representing the communication transmitter and the radar target, the expression of the OP and that of the ergodic rate are derived respectively as:

$$\mathbb{P}_j^{OMA} = \frac{\gamma\left(m, \Omega\gamma_{th}^{OMA}\right)}{\Gamma\left(m\right)} \tag{6.15}$$

and

$$R_j^{OMA} = \frac{1}{2\ln 2}\sum_{k=0}^{m-1}\exp\left(\Omega\right)E_{1+k}\left(\Omega\right), \tag{6.16}$$

where $\Omega = \frac{m\left(P_{BS}\mathcal{P}_r(d_r)\gamma^2\beta_{semi}^2 B^2\sigma_\tau^2+\sigma^2\right)}{P_j\mathcal{P}_c(d_j)}$, $\Gamma(x)$ is the Gamma function, $\gamma(a,b)$ is the incomplete Gamma function, and $E_n\left(\cdot\right)$ is the generalized exponential integral.

Proof. The OP is derived by exploiting the CDF of the Gamma distribution, denoted as $F_{|h_j|^2}(x) = \frac{\gamma(m,mx)}{\Gamma(m)}$. Additionally, the ergodic rate is derived by exploiting $\gamma(m,t) = (m-1)! - \exp(-t)\sum_{k=0}^{m-1}\frac{(m-1)!}{k!}t^k$, $\Gamma(-k,\Omega) = \frac{E_{1+k}(\Omega)}{\Omega^k}$, and $\int_0^\infty \frac{x^a}{1+x}\exp(-bx) = \exp(b) \times\Gamma(a+1)\Gamma(-a,b)$, where $\Gamma(a,b)$ is the incomplete Gamma function. The detailed proof is presented in Section II of [136]. □

6.2.2 Performance Evaluation for Radar Echoes

Again for radar echoes, the authors of [54] have proposed the REIR metric to evaluate the performance of radar targets. The REIR is analogous to the data information rate of the communications system. This is the calculated estimation rate of the parameters (range, cross-section, etc.). A higher REIR means better performance for radar detection. Let us represent a clear relationship between the REIR and the SNR γ_r^{echo}, presented as:

$$R_{est} \leqslant \frac{\delta}{2T}\log_2\left(1 + 2T\beta_{semi}B\gamma_r^{echo}\right), \tag{6.17}$$

where $\gamma_r^{echo} = \frac{P_{BS}\mathcal{P}_r(d_r)\left|h_{r,d}\right|^2|h_{r,u}|^2\gamma^2\beta_{semi}^2B^2\sigma_\tau^2}{\sigma^2}$ is the SNR for the radar echoes of the radar target, T is the radar pulse duration, and δ is the radar's duty cycle. The ergodic REIR is then used for quantifying the average radar estimation rate, which may be viewed as the dual counterpart of the data information rate, presented as:

$$R_{est} \leqslant \mathbb{E}\left[\frac{\delta}{2T}\log_2\left(1 + 2T\beta_{semi}B\gamma_r^{echo}\right)\right]. \tag{6.18}$$

The following expression shows the relationship between the REIR and radar estimation. Note that the time-delay estimation is a basic range measurement, denoted as $\sigma_{\tau,est}^2$. The REIR metric is characterized by the Cramér-Rao lower bound (CRLB) of the radar estimation (range measurement) [137, 138], denoted as $\sigma_{\tau,est}^2 = \frac{\sigma_\tau^2}{2T\beta_{semi}B\gamma_r^{echo}}$. First, the definition of the REIR is $R_{est} \leq \frac{H_{\tau_{\rm rr}} - H_{\tau_{\rm est}}}{T_{\rm bit}}$, where $H_{\tau_{\rm rr}}$ is the entropy of received signal,

denoted as $H_{\tau_{\rm rr}} = \frac{1}{2}\log_2\left[2\pi e\left(\sigma_\tau^2 + \sigma_{\tau,est}^2\right)\right]$, $H_{\tau_{\rm est}}$ is the entropy of errors, denoted as $H_{\tau_{\rm est}} = \frac{1}{2}\log_2\left[2\pi e\sigma_{\tau,est}^2\right]$, and $T_{\rm bit} = T/\delta$ represents the bits per pulse repetition interval. Hence, the REIR can be derived by substituting the CRLB into the definition equation. It is also concluded that the REIR is strongly influenced by the radar's time-delay estimation.

6.2.2.1 Equivalent Radar Channels

The radar channel may be considered as a pair of independent serially concatenated links, constituted by the DL channel spanning from the BS to the radar target and the UL channel reflected from the radar target back to the BS. Thus, the equivalent small-scale channel gain may be expressed by $|h_{r,eq}|^2 = |h_{r,d}|^2|h_{r,u}|^2$. The distribution of $|h_{r,eq}|^2$ is first derived in **Lemma 14** and the ergodic REIR is then given in **Theorem 22**.

Lemma 14. If the UL and DL channels are Nakagami-m fading channels, the PDF and CDF of the equivalent channel gain is expressed as:

$$f_{|h_{r,eq}|^2}(z) = \frac{2m^{2m}}{\left(\Gamma(m)\right)^2} z^{m-1} K_0\left(2m\sqrt{z}\right) \tag{6.19}$$

and

$$F_{|h_{r,eq}|^2}(z) = \frac{G_{13}^{21}\left(m^2 x\,\middle|_{m,m,0}^{1}\right)}{\left(\Gamma(m)\right)^2}, \tag{6.20}$$

where $K_0(\cdot)$ is the modified Bessel function of the third kind and $G_{p\ q}^{mn}\left(\cdot\,\middle|\begin{smallmatrix}(a_p)\\(b_q)\end{smallmatrix}\right)$ is the Meijer G function.

Proof. The above PDF and CDF are derived by the following equations as $K_v(x) = \frac{1}{2}G_{02}^{20}\left(\frac{x^2}{4}\,\middle|\begin{smallmatrix}\cdot\ \cdot\\ \frac{v}{2}\ \frac{-v}{2}\end{smallmatrix}\right)$, $z^p G_{p\ q}^{mn}\left(z\,\middle|\begin{smallmatrix}(a_p)\\(b_q)\end{smallmatrix}\right) = G_{p\ q}^{mn}\left(z\,\middle|\begin{smallmatrix}(a_p)+p\\(b_q)+p\end{smallmatrix}\right)$, $\int_0^x z^{m-1}$ $\times G_{02}^{20}\left(m^2 z\,\middle|_{00}^{\cdot\ \cdot}\right)dz = x^m G_{13}^{21}\left(m^2 y\,\middle|_{0,0\ -m}^{1-m\ \cdot}\right)$, and Eq.[2.3.6.7] in [127]. The comprehensive proof is presented in Section III of [136]. □

6.2.2.2 Ergodic REIR

Based on the equivalent channel distribution, the ergodic REIR of the radar echoes will be derived in **Theorem 22**. This subsection will also exploit **Corollary 41** to evaluate the performance under the Rayleigh fading channels.

Theorem 22. For the analytical results of the radar echoes, the expressions of the ergodic REIR are formulated as:

$$R_{est}^{low}=\frac{\delta}{2T\ln\left(2\right)}\int_{0}^{\infty}\frac{1}{z+1}\left(1-\frac{G_{13}^{21}\left(\frac{m^{2}d_{t}^{\alpha_{r}}}{\Xi_{r,1}}z\,\middle|_{m,m,0}^{1}\right)}{\left(\Gamma\left(m\right)\right)^{2}}\right)dz, \tag{6.21}$$

where $\Xi_{r,1}=2T\beta_{semi}B\gamma_{r}^{echo}$.

Proof. With the aid of **Lemma 14**, this theorem is proved. The comprehensive proof is presented in Section IV of [136]. □

Corollary 41. Assuming that the radar channel experiences Raleigh fading, the ergodic rate in Eq. (6.21) is simplified as:

$$R_{est}^{low}=\frac{\delta}{2T\ln\left(2\right)}G_{13}^{31}\left(d_{t}^{\alpha_{r}}\Xi_{r,1}^{-1}\,\middle|_{0,0,1}^{0}\right). \tag{6.22}$$

Proof. This corollary is proved by exploiting Eq.[2.3.4.4] in [127] and the Meijer G function. Detailed derivations are similar to those of **Lemma 14**. The comprehensive proof is jointly presented in Section IV of [136] with **Theorem 22**. □

6.3 Analytical Performance Evaluation for NOMA-Based Semi-ISaC

In this section, the performance metrics are analyzed for NOMA-based Semi-ISaC networks. The analytical results in this section will be useful for the asymptotic analysis to obtain deep insights.

6.3.1 Performance Analysis for Communication Signals in Scenario-I

Recall that the communication transmitter is the near user and the radar target is the far user in Scenario-I. The OP expressions for the NOMA users in Scenario-I are given by:

$$\mathbb{P}_c^I = \Pr\left\{\gamma_c^I < \gamma_{th}\right\} \tag{6.23}$$

and

$$\mathbb{P}_r^I = 1 - \Pr\left\{\gamma_c^I > \gamma_{SIC}, \gamma_r^I > \gamma_{th}\right\}, \tag{6.24}$$

where $\Pr\{\mathcal{A}, \mathcal{B}\}$ is the probability that both $\mathcal{A}$ and $\mathcal{B}$ are true, γ_{SIC} is the threshold of the SIC process, and γ_{th} is the threshold of communication signal transmission in the NOMA-based Semi-ISaC scenario. If the OP is lower than the threshold, the communication fails and vise versa.

In the following, the closed-form expressions of the OP and the ergodic rate for a pair of NOMA users are given in **Theorem 23-24** and **Corollary 42-43**.

Theorem 23. In Scenario-I of the NOMA-based Semi-ISaC scenario, the OP expression of the communication transmitter is

$$\begin{aligned}\mathbb{P}_c^I =& 1 - \exp\left(-\frac{m\gamma_{th}}{P_c}\left(a_1 + a_2\right)\right) \sum_{p=0}^{m-1} \frac{m^r \gamma_{th}^p}{(m-1)!p!} \\ &\times \sum_{r=0}^{p} C_p^r \Gamma\left(m + p - r\right) \frac{\left(a_1 + a_2\right)^r \left(P_r a_3\right)^{p-r}}{P_c^p \left(\frac{\gamma_{th} a_3 P_r}{P_c} + 1\right)^{m+p-r}},\end{aligned} \tag{6.25}$$

where $a_1 = \frac{P_{BS} G_r C_r (d_r)^{-\alpha_r} \gamma^2 \beta_{semi}^2 B^2 \sigma_\tau^2}{G_c C_c (d_c)^{-\alpha_c}}$, $a_2 = \frac{\sigma^2}{G_c C_c (d_c)^{-\alpha_c}}$, $a_3 = \frac{(d_r)^{-\alpha_c}}{(d_c)^{-\alpha_c}}$, and $C_n^m = n!/(m!(n-m)!)$.

Proof. See Appendix D.1. □

Corollary 42. In Scenario-I, the ergodic rate of the communication transmitter in the NOMA-based Semi-ISAC scenario is formulated as:

$$\begin{aligned} R_c^{er,I} =& \frac{1}{\ln 2} \sum_{p=0}^{m-1} \sum_{r=0}^{p} C_p^r \frac{\Lambda_1^{r-(1+p+k)} (P_r a_3)^{p-r}}{(m-1)! p! P_c^{p-r}} \\ & \times \Gamma(m+p-r) \sum_{k=0}^{\infty} \binom{m+p-r+k-1}{k} \\ & \times \left(-\frac{a_3 P_r}{P_c}\right)^k \exp(\Lambda_1) \Gamma(p+k+1) E_{1+p+k}(\Lambda_1), \end{aligned} \tag{6.26}$$

where $\Lambda_1 = \frac{m(a_1+a_2)}{P_c}$.

Proof. By substituting the equation in **Theorem 23** into the definition of the ergodic rate, which is expressed as $R_c^{er,I} = \frac{1}{\ln 2} \int_0^{\infty} \frac{1-\mathbb{P}_c^I(\gamma_{th})}{1+\gamma_{th}} d\gamma_{th}$, the ergodic rate expression is given by

$$\begin{aligned} R_c^{er,I} =& \frac{1}{\ln 2} \sum_{p=0}^{m-1} \frac{m^r}{(m-1)! p!} \sum_{r=0}^{p} C_p^r \frac{(a_1+a_2)^r (P_r a_3)^{p-r}}{P_c^p} \\ & \times \Gamma(m+p-r) \int_0^{\infty} \frac{x^p}{1+x} \left(\frac{x a_3 P_r}{P_c} + 1\right)^{-(m+p-r)} \\ & \times \exp\left(-\frac{mx}{P_c}(a_1+a_2)\right) dx. \end{aligned} \tag{6.27}$$

The corollary can be proved by noting $(1+x)^{-n} = \sum_{k=0}^{\infty} \binom{n+k-1}{k} (-x)^k$, $\Gamma(a,b) = \sum_{p=0}^{a-1} \frac{(a-1)!}{p!} b^p \times \exp(-b)$, $E_n(x) = x^n \Gamma(1-n, x)$, and $\int_0^{\infty} \frac{x^a}{1+x} \exp(-bx) = \exp(b) \Gamma(a+1) \Gamma(-a, b)$. The detailed proof is given in Section V of [136]. □

Theorem 24. In Scenario-I of NOMA-based Semi-ISaC, the OP of the

radar target is given by

$$\begin{aligned}\mathbb{P}_r^I =& 1-\sum_{p=0}^{m-1}\sum_{r=0}^{p} C_p^r \frac{(a_1+a_2)^{p-r}(a_3P_r)^r}{\Gamma(m)\,m^r p!}\left(\frac{m\gamma_{SIC}}{P_c}\right)^p \\ &\times \exp\left(-\frac{m\gamma_{SIC}(a_1+a_2)}{P_c}\right)\left(\frac{\gamma_{SIC}a_3P_r}{P_c}+1\right)^{-(r+m)} \\ &\times \Gamma\left(r+m, \frac{\gamma_{th}m(a_4+a_5)}{P_r}\left(\frac{\gamma_{SIC}a_3P_r}{P_c}+1\right)\right), \end{aligned} \tag{6.28}$$

where $a_4 = \frac{P_{BS}G_rC_r(d_r)^{-\alpha_r}\gamma^2\beta_{semi}^2B^2\sigma_\tau^2}{G_cC_c(d_r)^{-\alpha_c}}$ and $a_5 = \frac{\sigma^2}{G_cC_c(d_r)^{-\alpha_c}}$.

Proof. See Appendix D.2. □

Corollary 43. In Scenario-I, the ergodic rate expression for the communication signal of the radar target is derived as:

$$\begin{aligned}R_r^{er,I} =& \frac{1}{\ln 2}\sum_{p=0}^{m-1}\sum_{r=0}^{p} C_p^r \frac{(a_1+a_2)^{p-r}(a_3P_r)^r}{\Gamma(m)\,m^r p!}\left(\frac{m\gamma_{SIC}}{P_c}\right)^p \\ &\times \exp\left(-\Lambda_1\gamma_{SIC}\right)\left(\frac{\gamma_{SIC}a_3P_r}{P_c}+1\right)^{-(r+m)}\sum_{k=0}^{r+m-1}\frac{\Lambda_2}{k!} \\ &\times (r+m-1)!\exp(\Lambda_2)\,\Gamma(k+1)\,E_{1+k}(\Lambda_2), \end{aligned} \tag{6.29}$$

where $\Lambda_2 = \frac{m(a_4+a_5)}{P_r}\left(\frac{\gamma_{SIC}a_3P_r}{P_c}+1\right)$.

Proof. The proof is similar to that of **Theorem 21**. □

6.3.2 Performance Analysis for Communication Signals in Scenario-II

This subsection evaluates both the OP and the ergodic rate of NOMA-based Semi-ISaC in Scenario-II. Compared to Scenario-I, the SIC detection orders are the opposite way round. Thus, the OP expressions become:

$$\mathbb{P}_r^{II} = \Pr\left\{\gamma_r^{II} < \gamma_{th}\right\} \tag{6.30}$$

and

$$\mathbb{P}_c^{II} = 1 - \Pr\left\{\gamma_r^{II} > \gamma_{SIC}, \gamma_c^{II} > \gamma_{th}\right\}, \tag{6.31}$$

and the expressions of the OP and those of the ergodic rate are presented by **Theorem 25-26** and **Corollary 44-45**.

Theorem 25. For NOMA-based Semi-ISaC in Scenario-II, the OP for the communication signal of the radar target is formulated as:

$$\begin{aligned}\mathbb{P}_r^{II} =& 1 - \sum_{p=0}^{m-1}\sum_{r=0}^{p} \frac{C_p^r \Gamma(m+r)}{\Gamma(m)\, m^r p!}\left(\frac{m\gamma_{th}}{P_r}\right)^p \\ &\times \exp\left(-\frac{m\gamma_{th}(b_1 + b_2)}{P_r}\right) \\ &\times (b_1 + b_2)^{p-r}(P_c b_3)^r \left(\frac{\gamma_{th} P_c b_3}{P_r} + 1\right)^{-(m+r)},\end{aligned} \tag{6.32}$$

where $b_1 = \frac{P_{BS} G_r C_r \gamma^2 \beta_{semi}^2 B^2 \sigma_\tau^2}{G_c C_c (d_r)^{\alpha_r - \alpha_c}}$, $b_2 = \frac{\sigma^2}{G_c C_c (d_r)^{-\alpha_c}}$, and $b_3 = \frac{(d_c)^{-\alpha_c}}{(d_r)^{-\alpha_c}}$.

Proof. By the accurate series expansion for the lower incomplete Gamma function and the binomial theorem, the OP expression is formulated as:

$$\begin{aligned}\mathbb{P}_r^{II} =& 1 - \sum_{p=0}^{m-1} \frac{1}{p!}\left(\frac{m\gamma_{th}}{P_r}\right)^p \exp\left(-\frac{m\gamma_{th}(b_1 + b_2)}{P_r}\right) \\ &\times \sum_{r=0}^{p} C_p^r (b_1 + b_2)^{p-r}(P_c b_3)^r \\ &\times \underbrace{\int_0^\infty x^r \exp\left(-\frac{m\gamma_{th} P_c b_3}{P_r} x\right) f_{|h_c|^2}(x)\, dx}_{I_2}.\end{aligned} \tag{6.33}$$

Furthermore, according to Eq. [2.3.3.1] in [127], the final analytical results are obtained. Additionally, the detailed proof is similar to that of **Theorem 23**. □

Corollary 44. Let us define a parameter of $\Lambda_3 = \frac{m(b_1 + b_2)}{P_r}$. When the NOMA-based Semi-ISaC network is considered in Scenario-II, the ergodic

rate of the communication signal for the radar target is derived as:

$$\begin{aligned} R_r^{er,II} =& \frac{1}{\ln 2} \sum_{p=0}^{m-1} \sum_{r=0}^{p} \sum_{k=0}^{\infty} \binom{m+r+k-1}{k} \\ & \times \frac{C_p^r \Gamma(m+r)\,\Gamma(p+k+1)}{\Gamma(m)\, m^r p! (b_1 + b_2)^r \Lambda_3^{k+1}} \\ & \times (P_c b_3)^r \left(-\frac{P_c b_3}{P_r}\right)^k \exp(\Lambda_3)\, E_{p+k+1}(\Lambda_3). \end{aligned} \tag{6.34}$$

Sketch of Proof: The proof is similar to that of ***Corollary 42****.*

Theorem 26. Recall that the NOMA-based Semi-ISaC network in Scenario-II. For the communication signal of the communication transmitter, the OP expression is formulated as:

$$\begin{aligned} \mathbb{P}_c^{II} =& 1 - \sum_{p=0}^{m-1} \frac{1}{p!} \left(\frac{m\gamma_{SIC}}{P_r}\right)^p \exp\left(-\frac{m\gamma_{SIC}(b_1 + b_2)}{P_r}\right) \\ & \times \sum_{r=0}^{p} C_p^r (b_1 + b_2)^{p-r} (P_c b_3)^r I_3, \end{aligned} \tag{6.35}$$

where I_3 is given by

$$\begin{aligned} I_3 =& \frac{1}{\Gamma(m)\, m^r} \left(\frac{\gamma_{SIC}}{P_r} P_c b_3 + 1\right)^{-(m+r)} \\ & \times \Gamma\left(m + r, \frac{\gamma_{th} m}{P_c}(a_1 + a_2)\left(\frac{\gamma_{SIC}}{P_r} P_c b_3 + 1\right)\right). \end{aligned} \tag{6.36}$$

Sketch of Proof: By exploiting the series expansion of the incomplete Gamma function, the binomial theorem, and some equation manipulations,

the OP of the communication transmitter in Scenario-II is

$$\begin{aligned}\mathbb{P}_c^{II} =& 1-\sum_{p=0}^{m-1}\frac{1}{p!}\left(\frac{m\gamma_{SIC}}{P_r}\right)^p \exp\left(-\frac{m\gamma_{SIC}\left(b_1+b_2\right)}{P_r}\right)\\ &\times\sum_{r=0}^{p} C_p^r (b_1+b_2)^{p-r}(P_c b_3)^r\\ &\times\underbrace{\int_{\frac{\gamma_{th}}{P_c}(a_1+a_2)}^{\infty} x^r \exp\left(-\frac{m\gamma_{SIC}}{P_r}P_c b_3 x\right) f_{|h_c|^2}(x)\,dx}_{I_3}. \end{aligned} \tag{6.37}$$

Then, the final OP expression is derived by substituting Eq. [2.3.6.6] from [127] into the expression as Eq. (6.37)*. The detailed proof is similar to that of* ***Theorem 24****.*

Corollary 45. For Scenario-II, the ergodic rate expression of the communication signal for the communication transmitter is formulated as:

$$\begin{aligned}R_c^{er,II} =& \frac{1}{\ln 2}\sum_{p=0}^{m-1}\sum_{r=0}^{p}\frac{C_p^r (P_c b_3)^r \Lambda_5^p \exp\left(-\Lambda_5\right)}{p!\Gamma\left(m\right) m^r \left(b_1+b_2\right)^r}\\ &\times\left(\frac{\gamma_{SIC}}{P_r}P_c b_3+1\right)^{-(m+r)}\sum_{k=0}^{m+r-1}\frac{(m+r-1)!}{k!\Lambda_4}\\ &\times\exp\left(\Lambda_4\right)\Gamma\left(k+1\right)E_{k+1}\left(\Lambda_4\right), \end{aligned} \tag{6.38}$$

where $\Lambda_4 = \frac{m}{P_c}\left(a_1+a_2\right)\left(\frac{\gamma_{SIC}}{P_r}P_c b_3+1\right)$ and $\Lambda_5 = \frac{m\gamma_{SIC}(b_1+b_2)}{P_r}$.

Sketch of Proof: The proof is similar to that of ***Corollary 42****.*

6.3.3 Analytical Performance Evaluation for Radar Echoes

As the radar echoes are simply left behind after the last SIC process, the definition of ergodic REIR is the same as the OMA-based Semi-ISaC scenario when the SIC processes are successful. That is, under a perfect SIC case, the derivations of the ergodic REIR in the NOMA-based Semi-ISaC scenario are the same as those in the OMA-based Semi-ISaC scenario in **Theorem 21**. Hence, the derivations are omitted here. To gain further insights, the

closed-form asymptotic expressions of the ergodic REIR are derived and evaluated in the next section.

6.4 Asymptotic Performance Evaluation for NOMA-Based Semi-ISaC

This section investigates the asymptotic OP and the asymptotic ergodic REIR for further evaluating the performance of the NOMA-based Semi-ISaC system in the high-SNR region. The diversity orders of the OP (for the communication signals) are presented as the insights in **Remark 27-31**. This section additionally evaluates the high-SNR slopes of the ergodic REIR (for the radar echoes) and summarizes them in **Remark 32-33**.

6.4.1 Asymptotic Outage Performance and Diversity Gains for Communication Signals

Recall that two scenarios are considered, namely Scenario-I having a near communication transmitter and a far radar target and Scenario-II associated with a far communication transmitter and a near radar target.

6.4.1.1 Diversity Evaluation in Scenario-I

Based on **Theorem 23** and **Theorem 24**, the performance in the high-SNR region is evaluated. Explicitly, the asymptotic series of the lower incomplete Gamma function are exploited and only a single term is retained as the following form of

$$\gamma\left(a,b\right)\approx\sum_{n=0}^{\infty}\frac{\left(-1\right)b^{a+n}}{n!\left(a+n\right)}\approx\frac{b^{a}}{a}. \tag{6.39}$$

Then, by substituting Eq. (6.39) into the results of **Theorem 23** and **Theorem 24**, and following some further manipulations, the asymptotic OP expressions are presented in **Corollary 46** and **Corollary 47**.

Corollary 46. For the communication signal of the communication transmitter in Scenario-I, the asymptotic OP expression is

$$\mathbb{P}_{c,\infty}^{I} = \left(\frac{m\gamma_{th}}{P_c}\right)^{m} \sum_{r=0}^{m} C_m^r (a_1 + a_2)^{m-r} \frac{(P_r a_3)^r \Gamma(m+r)}{\Gamma(m+1)\Gamma(m) m^r}. \tag{6.40}$$

Sketch of Proof: Upon Substituting Eq. (6.39) *into the OP expression of* ***Theorem 23****, the derivation is calculated as:*

$$\mathbb{P}_{c,\infty}^{I} = \left(\frac{m\gamma_{th}}{P_c}\right)^{m} \sum_{r=0}^{m} C_m^r (a_1 + a_2)^{m-r} \frac{(P_r a_3)^r}{\Gamma(m+1)} \int_0^{\infty} x^r f_{|h_r|^2}(x)\, dx. \tag{6.41}$$

With the aid of the PDF of the Gamma distribution, the integral is derived as $\int_0^{\infty} x^r f_{|h_r|^2}(x)\, dx = \frac{m^m}{\Gamma(m)} \int_0^{\infty} x^{m+r-1} \exp(-mx)\, dx = \frac{\Gamma(m+r)}{\Gamma(m) m^r}$. *Then, after substituting the integral into the OP expression, this proof is completed.*

Remark 27. To evaluate the outage performance in the high-SNR region, the diversity order of the communication transmitter in Scenario-I is expressed as:

$$D_c^I = -\lim_{P_c \to \infty} \frac{\log\left(\mathbb{P}_{c,\infty}^{I}\right)}{\log(P_c)} = m, \tag{6.42}$$

which is proved by $\lim_{x\to\infty} \frac{\log[(A/x)^m]}{\log(x)} = m$ for a constant A independent of the variable x. In the high-SNR region, the slope of the OP of the communication transmitter is m

Corollary 47. For the communication signal of the radar target in Scenario-I, the asymptotic OP is formulated as:

$$\begin{aligned} \mathbb{P}_{r,\infty}^{I} = {} & F_{|h_r|^2}\left(\frac{\gamma_{th}(a_4 + a_5)}{P_r}\right) + \left(\frac{m\gamma_{SIC}}{P_c}\right)^{m} \\ & \times \sum_{r=0}^{m} C_m^r \frac{(a_3 P_r)^r \Gamma\left(m+r, \frac{m\gamma_{th}(a_4+a_5)}{P_r}\right)}{(a_1 + a_2)^{r-m} \Gamma(m+1)\Gamma(m) m^r}. \end{aligned} \tag{6.43}$$

Sketch of Proof: With the aid of ***Theorem 24****, the OP expression is formulated as:*

$$\mathbb{P}^{I}_{r,\infty} = F_{|h_r|^2}\left(\frac{\gamma_{th}\left(a_4+a_5\right)}{P_r}\right) + \left(\frac{m\gamma_{SIC}}{P_c}\right)^m \times \sum_{r=0}^{m} C_m^r \frac{\left(a_3 P_r\right)^r \int_{\frac{\gamma_{th}(a_4+a_5)}{P_r}}^{\infty} x^r f_{|h_r|^2}\left(x\right) dx}{\left(a_1+a_2\right)^{r-m}\Gamma\left(m+1\right)}, \tag{6.44}$$

and based on the PDF of the Gamma distribution and the integral $\frac{m^m}{\Gamma(m)} \times \int_{\frac{\gamma_{th}(a_4+a_5)}{P_r}}^{\infty} x^{m+r-1}\exp\left(-mx\right)dx = \frac{1}{\Gamma(m)m^r}\Gamma\left(m+r, \frac{m\gamma_{th}(a_4+a_5)}{P_r}\right)$*, the final OP expression is derived.*

Remark 28. For the high-SNR region in Scenario-I, based on the asymptotic expression of the radar target's communication signal, the diversity order for the radar target is derived as:

$$D_r^I = -\lim_{P_c\to\infty} \frac{\log\left(\mathbb{P}^{I}_{r,\infty}\right)}{\log\left(P_c\right)} = 0, \tag{6.45}$$

which is proved by $\lim\limits_{x\to\infty} \frac{\log[(A/x)^m+B]}{\log(x)} = 0$ with the constants A and B that are independent of the variable x. The OP of the radar target catches the lower limit in the high-SNR region of Scenario-I.

6.4.1.2 Diversity Evaluation in Scenario-II

For Scenario-II of the NOMA-based Semi-ISaC network, based on the results of **Theorem 25** and **Theorem 26**, the asymptotic series expansion of Eq. (6.39) is exploited for deriving the asymptotic OP. Thus, the asymptotic OP of the communication transmitter and radar target are given by **Corollary 48** and **Corollary 49**, respectively.

Corollary 48. In Scenario-II, the asymptotic OP expression of the com-

munication transmitter is

$$\mathbb{P}_{c,\infty}^{II} = F_{|h_c|^2}\left(\frac{\gamma_{th}}{P_c}\left(a_1+a_2\right)\right) + \left(\frac{m\gamma_{SIC}}{P_r}\right)^m \times \sum_{r=0}^{m} C_m^r \frac{\left(P_c b_3\right)^r \Gamma\left(m+r, \frac{m\gamma_{th}}{P_c}\left(a_1+a_2\right)\right)}{\left(b_1+b_2\right)^{r-m}\Gamma\left(m+1\right)\Gamma\left(m\right)m^r}. \tag{6.46}$$

Sketch of Proof: The proof is similar to that of ***Corollary 47****.*

Remark 29. In Scenario-II, the outage performance is evaluated in the high-SNR region by assuming that the transmit power of the radar target is infinity. Based on the **Corollary 48**, the diversity order of the communication transmitter is expressed as:

$$D_c^{II} = -\lim_{P_r\to\infty} \frac{\log\left(\mathbb{P}_{c,\infty}^{II}\right)}{\log\left(P_r\right)} = 0, \tag{6.47}$$

indicating that the OP of the communication transmitter in Scneario-II has a lower bound.

Corollary 49. In Scenario-II, the asymptotic OP expression of the radar target is derived as:

$$\mathbb{P}_{r,\infty}^{II} = \left(\frac{m\gamma_{th}}{P_r}\right)^m \sum_{r=0}^{m} C_m^r \left(b_1+b_2\right)^{m-r} \frac{\left(P_c b_3\right)^r \Gamma\left(m+r\right)}{\Gamma\left(m+1\right)\Gamma\left(m\right)m^r}. \tag{6.48}$$

Sketch of Proof: The proof is similar to that of ***Corollary 46****.*

Remark 30. Under the same assumptions as in **Remark 29**, the asymptotic expressions is exploited, yielding the diversity order of the communication signal of the radar target in Scenario-II as:

$$D_r^{II} = -\lim_{P_r\to\infty} \frac{\log\left(\mathbb{P}_{r,\infty}^{II}\right)}{\log\left(P_r\right)} = m, \tag{6.49}$$

showing that the communication signal is directly influenced by the LoS component m.

Remark 31. *For Nakagami-m fading channels, it is concluded that with a strong LoS component (large m), large diversity gains are obtained, yielding a Neal-Gaussian performance reminiscent of an asymptotically infinite diversity order.*

6.4.2 Asymptotic Ergodic REIR and High-SNR Slopes

By exploiting the asymptotic expansions of the lower incomplete Gamma function and the generalized exponential integral, the asymptotic ergodic REIR is derived for the radar target as $\gamma(m,t) = (m-1)! - \exp(-t) \times \sum_{k=0}^{m-1} \frac{(m-1)!}{k!} t^k$, $E_n(z) \approx \frac{(-z)^{n-1}}{(n-1)!}(\psi(n) - \ln(z)) - \sum_{k=0\&\ k\neq n-1} \frac{(-z)^k}{k!(1-n+k)}$ for $n > 1$, and $E_1(z) \approx -C_\gamma - \ln(z) + z$, where C_γ is the Euler constant and $\psi(n)$ is the Psi function. The asymptotic expression of the ergodic REIR for radar target is given in **Corollary 50**. The high-SNR slopes are further evaluated in **Remark 32**.

Corollary 50. Upon assuming that m is an integer denoted as $m \in \mathbb{Z}$, the closed-form asymptotic expression of the ergodic REIR is derived as:

$$R_{est}^{\infty} = \frac{\delta m^m}{2T\ln(2)\Gamma(m)} I_4 + \sum_{k=1}^{m-1} \frac{\delta m^m}{2T\ln(2)\Gamma(m)} I_5, \tag{6.50}$$

where I_4 and I_5 are formulated as:

$$\begin{aligned} I_4 =& \frac{d_t^{\alpha_r}\Gamma(m-1)}{\Xi_{r,1} m^{m-2}} - \frac{\Gamma(m)}{m^m}\left(\log\left(\frac{m^2 d_t^{\alpha_r}}{\Xi_{r,1}}\right) - \psi^{(0)}(m) - C_\gamma\right) \\ &+ \left(\frac{m d_t^{\alpha_r}}{\Xi_{r,1}}\right)^2 \frac{\Gamma(m-2)}{m^{m-2}} - \frac{m d_t^{\alpha_r}}{\Xi_{r,1}} \frac{\Gamma(m-1)}{m^{m-1}} \\ &\times \left(\log\left(\frac{m^2 d_t^{\alpha_r}}{\Xi_{r,1}}\right) - \psi^{(0)}(m-1) - C_\gamma\right) \end{aligned} \tag{6.51}$$

and

$$I_5 = \left(-\frac{d_t^{\alpha_r}}{\Xi_{r,1}}\right)^k \frac{\psi\left(k+1\right)\Gamma\left(m-k\right)}{k!m^m} + \sum_{q=0\&q\neq k}^{m-1} \frac{\Gamma\left(m-q\right)\left(-\frac{md_t^{\alpha_r}}{\Xi_{r,1}}\right)^q}{q!\left(q-k\right)m^{m-q}} - \frac{\Gamma\left(m-k\right)}{m^{m-k}k!}\left(-\frac{md_t^{\alpha_r}}{\Xi_{r,1}}\right)^k \times \left(\ln\left(\frac{m^2 d_t^{\alpha_r}}{\Xi_{r,1}}\right) - \psi^{(0)}\left(m-k\right)\right). \tag{6.52}$$

Proof. See Appendix D.3. □

With the aid of the derived asymptotic expressions, the high-SNR slope of the radar target is evaluated. Conditioned on $P_{BS} \to \infty$, the high-SNR slope is defined as $S = \lim_{P_{BS}\to\infty} \frac{R_{est,\infty}^{low}(P_{BS})}{\ln(P_{BS})}$.

Remark 32. *Upon substituting the expression in* ***Corollary 50*** *into the high-SNR slope definition, the high-SNR slope is formulated as:*

$$S = \lim_{P_{BS}\to\infty} \frac{\frac{\delta m^m}{2T\ln(2)\Gamma(m)} I_7}{\ln\left(P_{BS}\right)} + \lim_{P_{BS}\to\infty} \frac{\frac{\delta m^m}{2T\ln(2)\Gamma(m)} I_8}{\ln\left(P_{BS}\right)} = \frac{\delta}{2T\ln\left(2\right)}, \tag{6.53}$$

which is proved by exploiting equations $\lim_{P_{BS}\to\infty} \frac{\left(\frac{A}{P_{BS}}\right)^k - B\ln\left(\frac{C}{P_{BS}}\right) + D}{\ln(P_{BS})} = B$ *and* $\lim_{P_{BS}\to\infty} \frac{\left(\frac{A}{P_{BS}}\right)^k}{\ln(P_{BS})} - \frac{\left(\frac{B}{P_{BS}}\right)^k \ln\left(\frac{C}{P_{BS}}\right)}{\ln(P_{BS})} + \frac{D}{\ln(P_{BS})} = 0$*, where* A*,* B*,* C*, and* D *are constants that are independent of the variable* P_{BS}*.*

Remark 33. *The high-SNR slope is only influenced by the radar's duty cycle* δ *and the pulse duration* T*. Additionally, the high-SNR slope is proportional to* δ/T*.*

6.5 Numerical Results

Numerical analysis is presented in this section, where the parameters are set as: the distance of the near user is 800 meters and that of the far user is 1300 meters, the bandwidth is $B = 10$ MHz, the noise power is

$\sigma^2 = k_b \beta_{semi} B T_{temp}$ with $T_{temp} = 724$ K [5], the target rates of the wireless communications are $\hat{R}_{OMA} = \hat{R}_{NOMA} = 1$ given the thresholds $\gamma_{th} = 2^{\hat{R}_{NOMA}} - 1$ for NOMA and $\gamma_{th}^{OMA} = 2^{\hat{R}_{OMA}} - 1$ for OMA, the threshold for SIC is $\gamma_{SIC} = 0.4$, the carrier frequency is $f_c = 10^9$ Hz, the speed of light is $c = 3 \times 10^8$ m/s, the radar target's cross section is $\sigma_{RCS} = 0.1$, the pulse duration is $T = 1$ μs, the path loss exponents are $\alpha_r = 4.5$ and $\alpha_c = 2.5$, the radar's duty cycle is $\delta = 0.01$, and the Nagakami coefficient is $m = 3$. Define the average received SINR as $\mathbb{E}\left[P_j |h_j|^2 C_j d_j^{-\alpha_j} / \sigma^2\right]$ (dB) where the subscript of $j \in \{c, r\}$ represents the communication channels or the radar detection channels. For the SIC settings, the perfect SIC is associated with the parameters $\varsigma_c = 0$ and $\varsigma_r = 0$. The realistic imperfect SIC cases will be investigated in future work.

6.5.1 From OMA-Based Semi-ISaC to NOMA-Based Semi-ISaC

In Fig. 6.2, this section validates the OP and the ergodic rate (with the unit as BPCU) expressions of the communication signals versus the received power level ($d = 800$ meters) under the OMA-based Semi-ISaC scenario ($P_t = 20$ dBm and $P_{BS} = [5, 30]$ dBm). It can be seen that the analytical results are closely matched by the simulation results and there is no lower or higher limit of the metrics. This is because the interference arising from the radar signals is fixed and it is not increased when the OMA user's transmit power is increased. Fig. 6.3 investigates the performance interplay between the radar detection and wireless communications for $\beta_{semi} \in [0, 1]$ when the conditions, including $\alpha_{semi} = 0$ and $\epsilon_{semi} = 1 - \beta_{semi}$, hold. The transmit power is set as 10 dBm for both the users and the BS. By comparing the performance among conventional (FD) ISaC, OMA-based Semi-ISaC, and NOMA-based Semi-ISaC networks, it is observed that Semi-ISaC has better channel capacity than the conventional FD ISaC. The reason is that for

[5] The T_{temp} includes the environment temperature ($T_e = 290$ K) and antenna temperature (T_a). By considering the noise factor (F) as 2.495 dB, we can calculate $T_a = (F - 1)T_e \approx 434$ K. Hence, the effective noise temperature is 724 K.

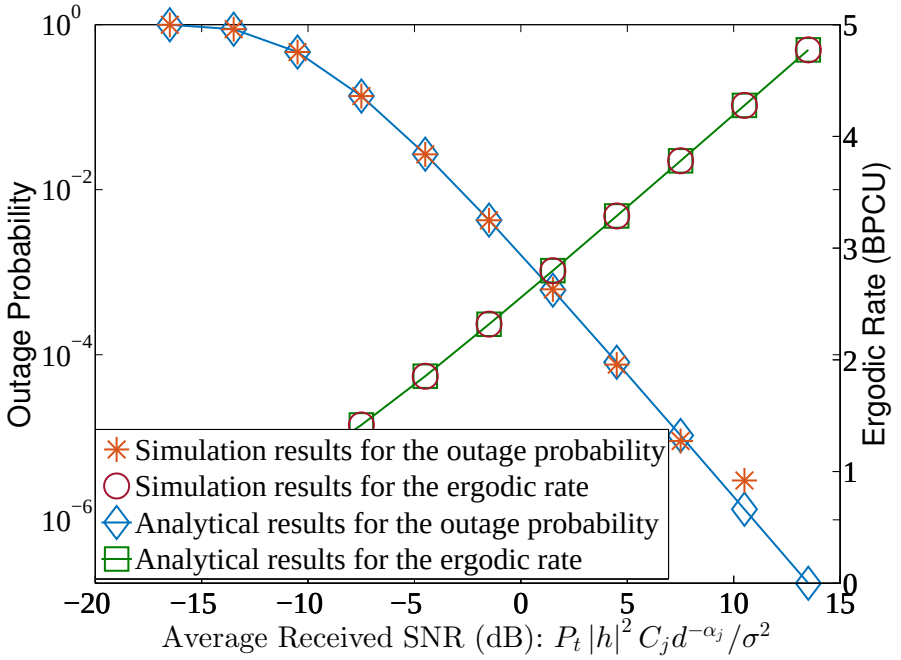

Figure 6.2: The verification of the OP and the ergodic rate for the OMA-based Semi-ISaC system.

Semi-ISaC, the radar and communication signals share the same resource blocks in ISaC bandwidth with the aid of the SIC to obtain better BE than that of the conventional FD ISaC. it is concluded that the NOMA-based Semi-ISaC scenario has a higher capacity than the OMA-based Semi-ISaC because the BE is further enhanced by the NOMA technique to share the resources by multiple communication users. Additionally, the ergodic REIR (for radar echoes) is zero with $\beta_{semi} = 0$ because all the bandwidth is used for wireless communication and no bandwidth is set aside for radar detection. Thus, non-zero ergodic rates with zero ergodic RIER are obtained. Upon considering $\beta_{semi} = 1$, the ergodic REIR reaches the highest, while the ergodic rate (for communication signals) cannot be reduced to zero. This represents the ISaC scenario (not Semi-ISaC), where the total bandwidth is utilized both for radar detection and for wireless communication.

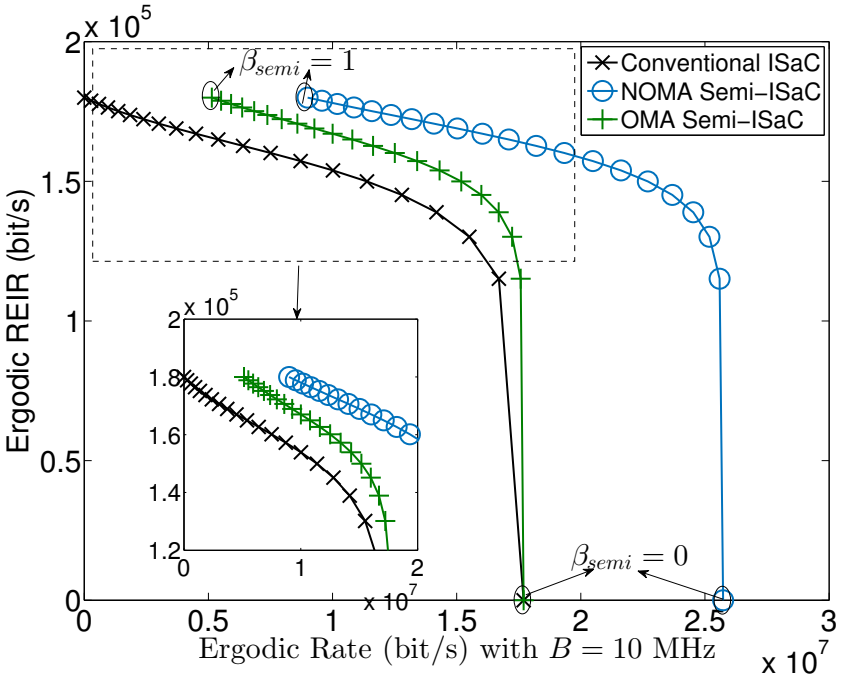

Figure 6.3: A comparison among the conventional (FD) ISaC, OMA-based Semi-ISaC, and NOMA-based Semi-ISaC.

6.5.2 OP for Communication Signals in NOMA-Based Semi-ISaC

This part validates the analytical and asymptotic OP expressions of NOMA users in Fig. 6.4 and Fig. 6.5 under $P_{BS} = 10$ dBm. Explicitly, in Fig. 6.4, a close communication transmitter ($d_c = \{500, 800\}$ meters) and a distant radar target ($d_r = \{800, 1000\}$ meters) are considered as Scenario-I ($P_c = [5, 35]$ dBm and $P_r = 20$ dBm). By contrast, in Fig. 6.5, the Scenario-II of a distant communication transmitter ($d_c = \{800, 1000\}$ meters) and a close radar target ($d_r = \{500, 800\}$ meters) is considered ($P_r = [5, 35]$ dBm and $P_c = 20$ dBm). An observation is that the simulation results closely match the analytical results and the diversity analysis matches the OP performance in the high-SNR region. Additionally, a conclusion for both scenarios is that upon increasing the near user's received SNR, the OP of both users will be reduced while the far user has an OP floor. The reason is

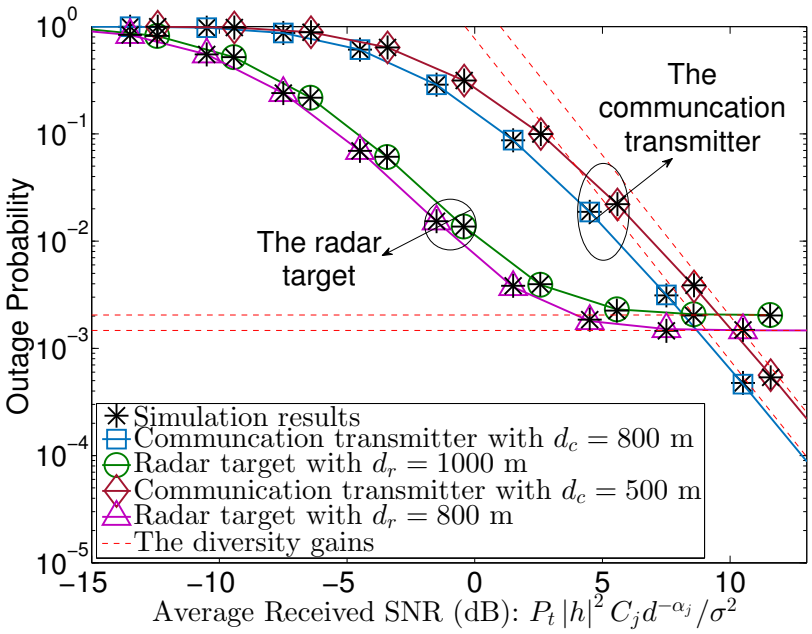

Figure 6.4: Outage performance v.s. the received SNR of the communication transmitter in Scenario-I.

that increasing the near user's signal strength can enhance its received SNR directly. Additionally, the interference of the near user is not increased, hence resulting in the reduced OP. By contrast, it beneficially improves the far user's error rate of SIC by enhancing the near user's received SNR, which only improves the OP of the distant user to a lower limit. But once the SIC process becomes perfect, the lower OP limit is reached.

6.5.3 Ergodic REIR for Radar Echoes in NOMA-Based Semi-ISaC

In Fig. 6.6, the ergodic REIR of NOMA users is quantified. The analytical results fit the simulation results well and the asymptotic results represent the upper bound of the simulation results. Based on **Remark 32**, the high-SNR slope is influenced by the ratio of the radar's duty cycle to pulse duration (δ/T). With the same settings of Fig. 6.3, Fig. 6.7 compares the performance of NOMA-based Semi-ISaC networks both with and without

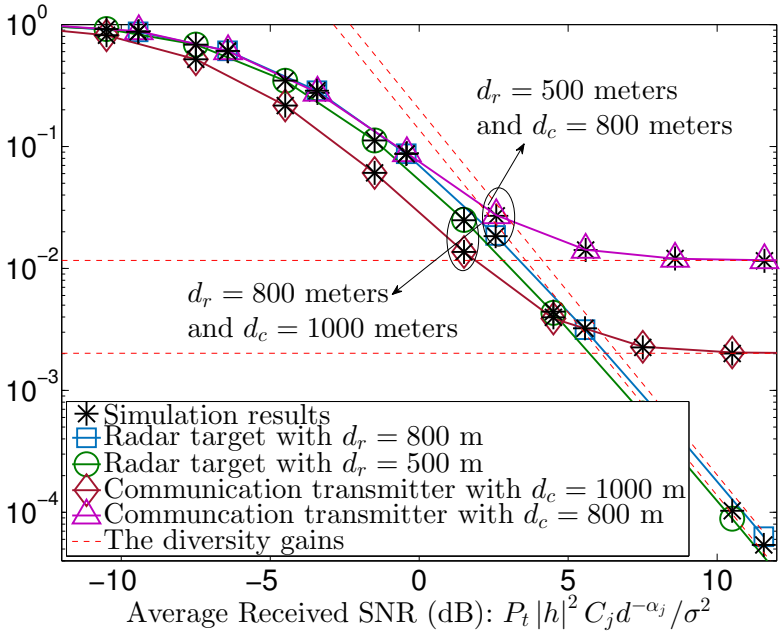

Figure 6.5: Outage performance v.s. the received SNR of the radar target in Scenario-II.

perfect SIC. The figure indicates that the perfect SIC scenario represents the upper bounds compared to the imperfect SIC scenarios. With the interference left from the SIC process, both the ergodic rate of communication signals and the ergodic REIR of radar sensing are lower than those metrics with perfect SIC. This is because the SIC process will have errors in practical scenarios, hence the signals might become erroneously detected.

6.6 Conclusions

This chapter has proposed the Semi-ISAC concept, where the total bandwidth is split as the radar-echo-only bandwidth, the communication-only bandwidth, and the ISaC bandwidth. A novel Semi-ISaC concept has been evolved from OMA to NOMA. Then, the novel ergodic REIR metric have been characterized for quantifying the average radar estimation rate. The performance metrics have been derived, including the OP and the ergodic

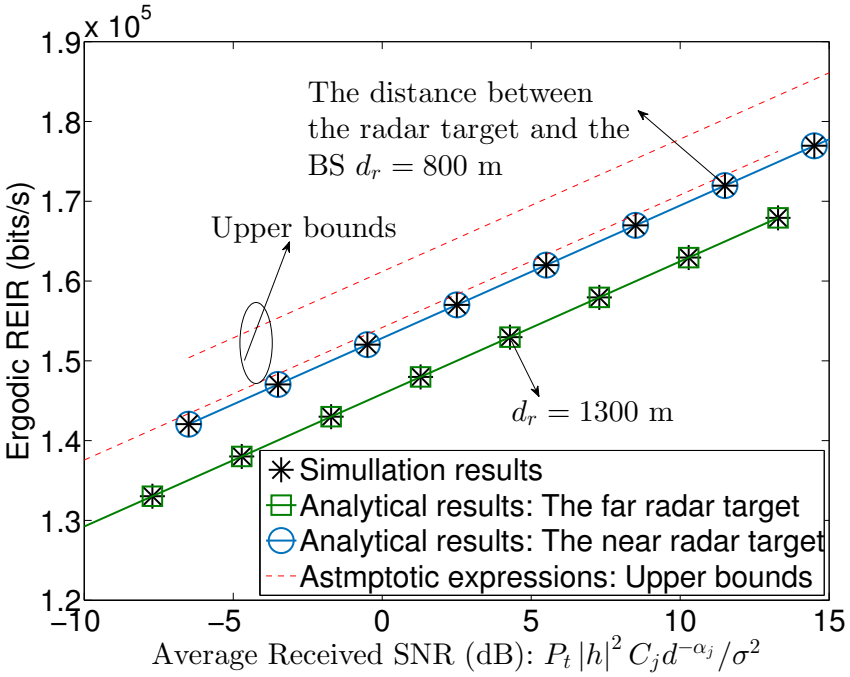

Figure 6.6: The ergodic REIR v.s. the received SNR of the BS with various distance d_r.

rate for the communication signals and the ergodic REIR for the radar echo in the OMA-based Semi-ISaC scenario. In the NOMA-based Semi-ISaC scenario, the analytical expressions of the OP and the ergodic rate for communication signals have been derived. This chapter has also derived the asymptotic OP along with the diversity gains attained for communication signals and the analytical expressions of the ergodic REIR for the radar echo, followed by the asymptotic ergodic REIR along with the high-SNR slopes. The analysis has confirmed that: 1) The channel capacity of the conventional ISaC is lower than that of Semi-ISaC. 2) NOMA-based Semi-ISaC has better capacity than OMA-based Semi-ISsC; 3) The diversity gain of the communication signal is determined by the power of the line-of-sight component m; and 4) We can strike a flexible trad-off by balancing the radar and communication signals upon jointly controlling the transmit power of the BS, the radar's duty cycle, and the pulse duration.

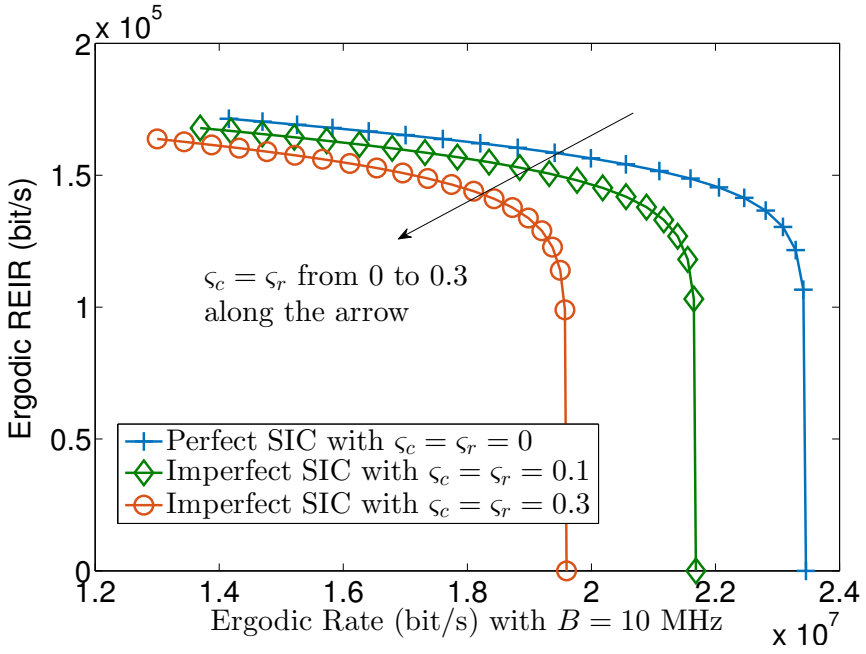

Figure 6.7: The comparison between NOMA-based Semi-ISaC networks with perfect SIC and imperfect SIC.

Chapter 7

Conclusions

This thesis investigates emerging technologies within NOMA networks for 6G wireless communications. Leveraging stochastic geometry models, it comprehensively evaluates the average performance of systems by considering spatial effects. Starting from the main property of NOMA to improve the connectivity of the system, this thesis has first investigated massive connectivity for 6G mMTC networks. Instead of solely exploiting GF or GB transmission, Semi-GF transmission has been examined in Chapter 3 to allow both GF and GB users in the same resource blocks to enhance connectivity with low latency and high reliability. Particularly for latency-sensitive and latency-tolerant user scenarios, respectively, to meet different requirements in application scenarios, a dynamic protocol for Semi-GF transmission is proposed, enhancing the outage performance of the entire system. Acquiring further connection, the ideal objective is to obtain full coverage connectivity with no blind areas. Hence, this thesis has evaluated the performance of RISs-aided NOMA networks in Chapter 4. A promising conclusion has been highlighted that it is capable of adjusting the SIC orders of NOMA networks without sacrificing the other users' performance by exploiting RISs to enhance the target user's channel condition or not. This significantly enhances the application scope of NOMA and fulfills the weakness in the NOMA concept, that is, NOMA has to sacrifice some users' performance to achieve the enhancement of the sum rates. Instead of conventional RISs with constraints on reflecting regions, STAR-IOSs allowed to

simultaneously transmit and reflect signals truly achieve full coverage of the physical space. With the investigation of STAR-IOS-aided NOMA networks in Chapter 5, the massive connectivity based on spatial distinction, such as LoS or NLoS, has expanded considerably as a 360° full coverage. To explore further increase of connectivity, we note that the incessant escalation of wireless tele-traffic pushes the impending spectrum-crunch to be circumvented by the migration to mm-wave. Given the inevitable overlap between sensing and wireless communications, this thesis has covered dual-functional connectivity by investigating Semi-ISaC systems in Chapter 6. It is revealed that the capacity region of Semi-ISaC is larger than both the conventional ISaC and the OMA case.

From voice talk to mMTC networks, from user selection to 360° full coverage, and from sorely functional system to multi-functional transmission, this thesis have covered plenties of contents to achieve massive connectivity. However, more efforts are required to the next generation multiple access for further enhancement of connectivity. The directions may includes jumping over the power-domain with other possible multiple access schemes, while let us leave some space for future work.

Appendix A

Appendixes for Chapter 3

Appendix A.1

When $\gamma_{GB}^{th} \in [1, \infty]$, the ergodic rate expression can be rewritten via integrations as:

$$\mathbb{E}\left[R_{GB}\right] = \frac{1}{\ln 2}\int_1^{\infty}\frac{1}{1+t}\int_0^{R_L}\int_0^{R_L} \underbrace{\times \int_0^{\infty}\left(1 - F_{|h_{GB}|^2}\left(\frac{P_{GF}txy^{-\alpha}+\sigma^2 t}{P_{GB}z^{-\alpha}}\right)\right) f_{|h_{GF}|^2}(x)\,dx}_{\mathrm{I}_1} \times f_{d_{GF}}(y)\,dy f_{d_{GB}}(z)\,dzdt, \tag{A.1}$$

where all the channels obey Rayleigh fading channels and $f_{d_{GF}}(x) = f_{d_{GB}}(x) = 2x/\left(R_L^2\right)$.

With the aid of Eq. [3.194.1] in [127] and hypergeometric functions, I_2 can be expressed and derived as:

$$\mathrm{I}_2 = \int_0^{R_L}\frac{2y\mathrm{I}_1}{R_L^2}dy = \frac{R_L^{\alpha}\exp\left(-\Theta_2 tz^{\alpha}\right)}{\left(1+\frac{1}{\alpha}\right)\Theta_1 tz^{\alpha}\left(1+t\right)}{}_2F_1\left(1, \frac{2+\alpha}{\alpha}; 2+\frac{2}{\alpha}; -\frac{R_L^{\alpha}}{\Theta_1 tz^{\alpha}}\right). \tag{A.2}$$

The Chebyshev-Gauss quadrature can be defined as $\int_{-1}^{1}\frac{f(x)}{\sqrt{1-x^2}}dx \approx \sum_{i=1}^{N}\omega_i f\left(x_i\right)$, where $x_i = \cos\left(\frac{2i-1}{2I}\pi\right)$ and $\omega_i = \pi/I$. Substituting I_2 into (A.1) and harnessing the Chebyshev-Gauss quadrature, the final expressions

of the ergodic rate are obtained for the GB user with $\gamma_{GB}^{th} \in [1, \infty]$.

Appendix A.2

When $\gamma_{GB}^{th} < 1$, the integration expressions of ergodic rates can be expressed as:

$$\begin{aligned}\mathbb{E}[R_{GB}]_2 =& \frac{1}{\ln 2}\int_0^1\int_0^{R_L}\int_0^{R_L}\frac{\exp\left(-\frac{t\sigma^2}{\lambda_{GB}P_{GB}z^{-\alpha}}\right)}{1+t}\\ &\times\int_0^{\frac{\sigma^2 y^\alpha}{P_{GF}}}\exp\left(-\Psi\left(y,z,t\right)x\right)dxf_{d_{GF}^{-\alpha}}\left(y\right)dyf_{d_{GB}^{-\alpha}}\left(z\right)dzdt\\ &+\int_0^{R_L}\int_0^{R_L}\int_{\frac{\sigma^2 y^\alpha}{P_{GF}}}^{\infty}\exp\left(-\frac{P_{GF}xy^{-\alpha}}{\lambda_{GB}P_{GB}z^{-\alpha}}\right)f_{|h_{GF}|^2}\left(x\right)dx\\ &\times f_{d_{GF}^{-\alpha}}\left(y\right)dyf_{d_{GB}^{-\alpha}}\left(z\right)dz. \end{aligned} \tag{A.3}$$

Denoted the first item of (A.3) as I_3. For the first item, based on Eq. [1.3.2.22] and Eq. [2.3.4.3] in [127], the ergodic rate expressions can be derived as:

$$\begin{aligned}\mathrm{I}_3 =& \frac{4}{\ln 2\lambda_{GF}R_L^4}\int_0^{R_L}\int_0^{R_L}yz\delta_1\left(y,z\right)\left\{\Phi\left(1,\delta_2\left(z\right)\right)\right.\\ &-\delta_3\left(y\right)\Phi\left(1,2\delta_2\left(z\right)\right)-\Phi\left(\delta_4\left(y,z\right),\delta_2\left(z\right)\right)\\ &\left.+\delta_3\left(y\right)\Phi\left(\delta_4\left(y,z\right),2\delta_2\left(z\right)\right)\right\}dydz. \end{aligned} \tag{A.4}$$

Denote the second item of (A.3) as I_4. The equation I_4 is derived as:

$$\mathrm{I}_4 = \frac{4}{R_L^4}\int_0^{R_L}\int_0^{R_L}\frac{yz\exp\left(-\Psi\left(y,z,t\right)\frac{\sigma^2 y^\alpha}{P_{GF}}\right)}{\lambda_{GF}\Psi\left(y,z,t\right)}dydz. \tag{A.5}$$

Substituting (A.4) and (A.5) into (A.3) and utilizing the Chebyshev-Gauss quadrature, the final closed-form expressions can be achieved.

Appendix A.3

With the consideration of the SIC condition and the dynamic protocol, the ergodic rate for the GF user can be expressed as:

$$\mathbb{E}\left[R_{GF}\right] = \int_0^{\infty}\int_0^{R_L}\int_0^{R_L}\int_{\frac{\sigma^2 t y^{\alpha}}{P_{GF}}}^{\infty} \frac{f_{d_{GF}}\left(y\right) f_{d_{GB}}\left(z\right)}{\ln 2(1+t)} \times \exp\left(-\frac{P_{GF}\gamma_{GB}^{th} x y^{-\alpha} + \sigma^2 \gamma_{GB}^{th}}{\lambda_{GB} P_{GB} z^{-\alpha}}\right) f_{|h_{GF}|^2}\left(x\right) dx dy dz dt. \quad \text{(A.6)}$$

Based on Eq. [1.3.2.22] and Eq. [2.3.4.3] in [127], two integrals of (A.6) can be derived. Then, utilizing the Chebyshev-Gauss quadratures in (A.6), the final expressions can be derived. Hence, the expressions of the ergodic rate for GF users are proved.

Appendix B

Appendixes for Chapter 4

Appendix B.1

With the aid of the expansions of exponential functions and based on (4.25), the Laplace transform of the interference for the connected user is expressed as:

$$\begin{aligned}\mathcal{L}_c(s)=&\mathbb{E}\left[\exp\left(-\sum_{\mathbf{x}_I\in\Phi_r\setminus\mathbf{x}_B} sP_bC|h_{c,\mathbf{x}_I}|^2{r_{c,I}}^{-\alpha_c}\right)\right]\\ =&\mathbb{E}\left[\prod_{\mathbf{x}_I\in\Phi_r\setminus\mathbf{x}_B}\exp\left(-sP_bC|h_{c,\mathbf{x}_I}|^2{r_{c,I}}^{-\alpha_c}\right)\right].\end{aligned} \tag{B.1}$$

Based on the binomial expansion, we obtain a tight upper bound for the normalized Gamma variables $|h|^2$, denoted as $\mathbb{P}\left\{|h|^2<x\right\}=(1-\exp(-x\eta))^m$, where m is the coefficient of Gamma distribution and $\eta=m(m!)^{-\frac{1}{m}}$. Thus, the equation (D.2) is approximately expressed as

$$\mathcal{L}_c(s)=\mathbb{E}\left[\prod_{\mathbf{x}_I\in\Phi_r\setminus\mathbf{x}_B}\left(1+\frac{sP_bC{r_{c,I}}^{-\alpha_c}}{m}\right)^{-m}\right]. \tag{B.2}$$

For some stochastic processes, the probability generating functional (PGFL) are useful tools for dealing with sums and limits of random variables, which

is expressed as

$$\mathbb{E}\left[\prod_{x\in\Phi} f\left(x\right)\right] = \exp\left(-\lambda \int_{\mathbb{R}^2} \left(1 - f\left(x\right)\right) dx\right), \tag{B.3}$$

where Φ is a PPP with density λ and $f\left(x\right) : \mathbb{R}^2 \to [0,1]$ is a real value function. Then, we utilize PGFL to derive the Laplace transform as

$$L_c(s) = \exp\left(-2\pi\lambda_b \int_{r_c}^{\infty} \left(1 - \left(1 + \frac{sP_bCr^{-\alpha_c}}{m}\right)^{-m}\right) r dr\right), \tag{B.4}$$

and via the integration

$$\int_A^{\infty} \left(1 - \left(1 + sy^{-\alpha}\right)^{-N}\right) y dy = \frac{A^2}{2}\left({}_2F_1\left(-\frac{2}{\alpha}, N; 1 - \frac{2}{\alpha}; -\frac{s}{A^{\alpha}}\right) - 1\right), \tag{B.5}$$

this lemma is proved.

Appendix B.2

With the aid of the properties of exponential functions such as $\exp\left(ab\right) = \exp\left(a\right)\exp\left(b\right)$, the Laplace transform expressions of the interference from other cells for the typical user can be expressed as:

$$\begin{aligned}\mathcal{L}_{t,RIS}(s) =& \mathbb{E}\left[\exp\left(\sum_{\substack{\mathbf{x}_I\in\Phi_r \\ \mathbf{x}_I\neq\mathbf{x}_B}} \frac{-\rho_t s P_b |h_{t_1,\mathbf{x}_I} h_{t_2,\mathbf{x}_I}|^{-2}}{C_{RIS,I}^{-2}\left(r_{BR(I)} r_{RU(I)}\right)^{\alpha_t}}\right)\right] \\ =& \mathbb{E}\left[\prod_{\mathbf{x}_I\in\Phi_r\setminus\mathbf{x}_B} \left(1 + \frac{sP_bC_{RIS,I}^2}{2m\left(r_{BR(I)} r_{RU(I)}\right)^{\alpha_t}}\right)^{-m}\right].\end{aligned} \tag{B.6}$$

Based on the PGFL theorem, the Laplace transform (B.6) can be derived

as:

$$\mathcal{L}_{t,RIS}(s) = \exp\left(-2\pi\lambda_b \int_{r_{BR(0)}}^{\infty} \left(1 - \left(1 + \frac{sP_b C_{RIS,E}^2}{m\left(x r_{RU(0)}\right)^{\alpha_t}}\right)^{-m}\right) x dx\right). \tag{B.7}$$

Exploiting the integration expressions in Appendix B.1, the Laplace transform of the interference can be derived.

Appendix B.3

The Campbell's theorem is expressed as $\mathbb{E}\left[\sum_{x\in\Phi} f(x)\right] = \lambda \int_{\mathbb{R}^2} f(x)\, dx$, where Φ is a PPP with density λ. Based on the Campbell's theorem, the expressions of the average interference for the connected user is derived as

$$\mathbb{E}[I_c] = 2\pi\lambda_b \int_{r_c}^{\infty} P_b C r^{1-\alpha_c} dr = \frac{2\pi\lambda_b P_b C r_c^{2-\alpha_c}}{\alpha_c - 2}. \tag{B.8}$$

Note that the normalized Gamma variables have a tight upper bound, denoted as $\mathbb{P}\left[\left|h^2\right| < x\right] < (1 - e^{-x\eta_t})^{m_t}$. Utilizing binomial expansions, the expressions of coverage probability for the typical user can be expressed as:

$$\mathbb{P}_t \approx \sum_{n=1}^{m_t} (-1)^{n+1} \binom{m_t}{n} \mathcal{L}_{t,RIS}\left[\frac{n\eta_t \Upsilon I_{t,\rho_t}}{P_b \mathcal{P}_t^{RIS}}\right] \mathbb{E}\left[e^{-\frac{n\eta_t \Upsilon \sigma^2}{P_b \mathcal{P}_t^{RIS}}}\right], \tag{B.9}$$

and via substituting **Lemma 7** and **Lemma 9** into the equation above, the theorem can be verified.

Appendix C

Appendixes for Chapter 5

Appendix C.1

As $\left|g_m^{rf}\right|^2 = \beta_{rf}\left(\sum_{m=1}^{M} h_{RU,m}^{rf} h_{BR,m}\right)^2$ for $rf \in \{rfl, rfr\}$, we exploit the central limit theorem to derive the variable $\left|g_m^{rf}\right| = \sqrt{\beta_{rf}} \sum_{m=1}^{M} h_{RU,m}^{rf} h_{BR,m}$. As we assume that independent Rician variables have the same mean and variance, denoted as $\bar{h}$ and η, we derive the mean and variance of $\left|g_m^{rf}\right|$ as:

$$\bar{h}_{eq}^{rf} = \mathbb{E}\left(\left|g_m^{rf}\right|\right) = \mathbb{E}\left(\sqrt{\beta_{rf}} \sum_{m=1}^{M} h_{RU,m}^{rf} h_{BR,m}\right) = \sqrt{\beta_{rf}} M \bar{h}^2 \tag{C.1}$$

and

$$\eta_{eq}^{rf} = \mathrm{Var}\left(\left|\mathrm{g_m^{rf}}\right|\right) = \mathrm{Var}\left(\sqrt{\beta_{\mathrm{rf}}} \sum_{\mathrm{m=1}}^{\mathrm{M}} \mathrm{h_{RU,m}^{rf} h_{BR,m}}\right) = \beta_{\mathrm{rf}} \mathrm{M}\left(2\bar{\mathrm{h}}^2 \eta + \eta^2\right), \tag{C.2}$$

where $E(\cdot)$ and $\mathrm{Var}(\cdot)$ are the expectation and variance of a certain variable.

Hence, the PDF of $\left|g_m^{rf}\right|$ is expressed as:

$$f_{\left|g_m^{rf}\right|}(x) = \frac{1}{\sqrt{2\pi\eta_{eq}^{rf}}} \exp\left(-\frac{\left(x - \bar{h}_{eq}^{rf}\right)^2}{2\eta_{eq}^{rf}}\right). \tag{C.3}$$

The PDF of $\left|g_m^{rf}\right|^2$ is then derived as:

$$f_{\left|g_m^{rf}\right|^2}(y) = \frac{1}{2\sqrt{2\pi\eta_{eq}^{rf} y}}\left(\exp\left(-\frac{\left(\sqrt{y}-\bar{h}_{eq}^{rf}\right)^2}{2\eta_{eq}^{rf}}\right)+\exp\left(-\frac{\left(\sqrt{y}+\bar{h}_{eq}^{rf}\right)^2}{2\eta_{eq}^{rf}}\right)\right). \tag{C.4}$$

Finally, the CDF of the channel model is derived in **Lemma 10** according to the equation as:

$$\int_0^x \frac{1}{\sqrt{y}}\left(\exp\left(-\frac{\left(\sqrt{y}-a\right)^2}{b}\right)+\exp\left(-\frac{\left(\sqrt{y}+a\right)^2}{b}\right)\right)dy = \sqrt{\pi b}\left(\operatorname{erf}\left(\frac{a+\sqrt{x}}{\sqrt{b}}\right)-\operatorname{erf}\left(\frac{a-\sqrt{x}}{\sqrt{b}}\right)\right). \tag{C.5}$$

Appendix C.2

With the assumption that k_1 and k_2 represent the Rician coefficients for the BR links and RU links, respectively, the PDF expression of $|h_{RU,m}^{rf} h_{BR,m}|$ is expressed as:

$$f_{|h_{RU,m}^{rf} h_{BR,m}|}(z) = \int_0^\infty \frac{1}{w} f_{|h_{RU,m}^{rf}|}(w)\, f_{|h_{BR,m}|}\left(\frac{z}{w}\right)dw. \tag{C.6}$$

Exploiting the series of the Bessel function as $I_v[p] = \sum_{s=0}^{\infty} \frac{1}{s!\Gamma(s+v+1)}\left(\frac{p}{2}\right)^{2s+v}$, the function of $f_{|h_{RU,m}^{rf} h_{BR,m}|}$ is derived as:

$$\begin{aligned} f_{\left|h_{RU,m}^{rf} h_{BR,m}\right|}(z) &= \frac{4(1+k_1)(1+k_2)z^{2n+1}}{\exp(k_1)\exp(k_2)} \\ &\times \sum_{t=0}^{\infty}\frac{(k_1(1+k_1))^t}{t!\Gamma(t+1)}\sum_{n=0}^{\infty}\frac{(k_2(1+k_2))^n}{n!\Gamma(n+1)} \\ &\times \int_0^\infty \frac{x^{t-n-1}}{2}\exp\left[-(1+k_1)x\right]\exp\left[-(1+k_2)\frac{z^2}{x}\right]dw. \end{aligned} \tag{C.7}$$

Based on Eq. [2.3.16.1] in [127] and the formula calculation, the PDF is

further derived as:

$$f_{\left|h_{RU,m}^{rf}h_{BR,m}\right|}(z) = 4z^{t+n+1}\sum_{t=0}^{\infty}\sum_{n=0}^{\infty}\frac{k_1^t k_2^t[(1+k_1)(1+k_2)]^{\frac{t+n}{2}+1}}{(t!)^2(n!)^2\exp(k_1+k_2)} \times K_{t-n}\left(2z\sqrt{(1+k_1)(1+k_2)}\right), \tag{C.8}$$

where $K_v(\cdot)$ is the modified Bessel function of the second kind.

Based on (C.8), the Laplace transform expression of the above equation is expressed as:

$$\mathcal{L}\left[f_{\left|h_{RU,m}^{rf}h_{BR,m}\right|}(x)\right] = 4\sum_{t=0}^{\infty}\sum_{n=0}^{\infty}\frac{k_1^t k_2^t[(1+k_1)(1+k_2)]^{\frac{t+n}{2}+1}}{(t!)^2(n!)^2\exp(k_1+k_2)} \times \int_0^{\infty} x^{t+n+1}\exp(-sx)K_{t-n}\left(2x\sqrt{(1+k_1)(1+k_2)}\right). \tag{C.9}$$

Based on the M-fold convolution, let us express the Laplace transform expression of the sum of combined channels of different STAR-IOS elements $\sum_{m=1}^{M}|h_{RU,m}^{rf}h_{BR,m}|$ as:

$$\mathcal{L}\left[\left|\sum_{m=1}^{M}h_{RU,m}^{rf}h_{BR,m}\right|\right](s) = \left\{\mathcal{L}\left[f_{\left|h_{RU,m}^{rf}h_{BR,m}\right|}(x)\right]\right\}^{M}. \tag{C.10}$$

Using Eq. [2.16.6.3] in [127], the Laplace transform of $f_{\left|h_{RU,m}^{rf}h_{BR,m}\right|}(x)$ is derived as:

$$\mathcal{L}\left[f_{\left|h_{RU,m}^{rf}h_{BR,m}\right|}(x)\right](s) = 4\sum_{t=0}^{\infty}\sum_{n=0}^{\infty}\frac{k_1^t k_2^t[(1+k_1)(1+k_2)]^{\frac{t+n}{2}+1}}{(t!)^2(n!)^2\exp(k_1+k_2)} \times \frac{\left(4\sqrt{(1+k_1)(1+k_2)}\right)^{t-n}\sqrt{\pi}}{\left(s+2\sqrt{(1+k_1)(1+k_2)}\right)^{2t+2}}\Gamma\binom{2n+2,2t+2}{t+n+\frac{5}{2}} \times {}_2F_1\left(2t+2, t-n+\frac{1}{2}; t+n+\frac{5}{2}; \frac{s-2\sqrt{(1+k_1)(1+k_2)}}{s+2\sqrt{(1+k_1)(1+k_2)}}\right). \tag{C.11}$$

With the assumption of $s \to \infty$, the following equation holds as:

$$ {}_2F_1\left(2t+2, t-n+\frac{1}{2}; t+n+\frac{5}{2}; \frac{s-2\sqrt{(1+k_1)(1+k_2)}}{s+2\sqrt{(1+k_1)(1+k_2)}}\right) = {}_2F_1\left(2t+2, t-n+\frac{1}{2}; t+n+\frac{5}{2}; 1\right). \quad \text{(C.12)} $$

Hence, the Laplace transform is finally derived as:

$$ \begin{aligned} \mathcal{L}\left[f_{\left|h_{RU,m}^{rf} h_{BR,m}\right|}(x)\right](s) &= \sum_{t=0}^{\infty}\sum_{n=0}^{\infty} \frac{4^{t-n+1}\sqrt{\pi}k_1^t k_2^t[(1+k_1)(1+k_2)]^{t+1}}{(t!)^2(n!)^2\exp(k_1+k_2)} \\ &\times \Gamma\binom{2n+2, 2t+2}{t+n+\frac{5}{2}} {}_2F_1\left(2t+2, t-n+\frac{1}{2}; t+n+\frac{5}{2}; 1\right) s^{-(2t+2)} \\ &= \sum_{t=0}^{\infty}\sum_{n=0}^{\infty} \sigma(t,n) s^{-(2t+2)}. \end{aligned} \quad \text{(C.13)} $$

Substituting (C.13) into (C.10), the Laplace transform expression of $\sum_{m=1}^{M} |h_{RU,m}^{rf} h_{BR,m}|$ is derived as:

$$ \begin{aligned} \mathcal{L}\left[\left|\sum_{m=1}^{M} h_{RU,m}^{rf} h_{BR,m}\right|\right](s) &= \left\{\mathcal{L}\left[f_{\left|h_{RU,m}^{rf} h_{BR,m}\right|}(x)\right]\right\}^M \\ &= \left(\sum_{t=0}^{\infty}\sum_{n=0}^{\infty} \sigma(t,n) s^{-(2t+2)}\right)^M. \end{aligned} \quad \text{(C.14)} $$

We only keep the first item of the two Taylor series of the Bessel function in (C.14), which means that two conditions, denoted as $n = 0$ and $t = 0$, are considered in (C.14). The inverse Laplace transform is utilized to obtain the PDF of $\sum_{m=1}^{M} |h_{RU,m}^{rf} h_{BR,m}|$ as:

$$ \begin{aligned} f^{0+}_{\left|\sum_{m=1}^{M} h_{RU,m}^{rf} h_{BR,m}\right|}(x) &= \mathcal{L}^{-1}\left[\left(\sum_{t=0}^{\infty}\sum_{n=0}^{\infty} \sigma(t,n) s^{-(2t+2)}\right)^M\right](x) \\ &= \mathcal{L}^{-1}\left[\left(\sigma(0,0) s^{-2}\right)^M\right](x) \\ &= \frac{[\sigma(0,0)]^M}{(2M-1)!} x^{2M-1}. \end{aligned} \quad \text{(C.15)} $$

Additionally, we note the equation $f_{X^2}(x) = \frac{1}{2\sqrt{x}}\left[f_X(\sqrt{x}) + f_X(-\sqrt{x})\right]$. We ignore the negative part of the aforementioned equation because of $\left|\sum_{m=1}^{M} h_{RU,m}^{rf} h_{BR,m}\right| > 0$. And then, the PDF of $\left|\sum_{m=1}^{M} h_{RU,m}^{rf} h_{BR,m}\right|^2$ is derived as:

$$f^{0+}_{\left|\sum_{m=1}^{M} h_{RU,m}^{rf} h_{BR,m}\right|^2}(x) = \frac{\left[\sigma(0,0)\right]^M x^{M-1}}{2(2M-1)!}. \tag{C.16}$$

Denote $\left|g_m^{rf}\right|^2 = \beta_{rf}\left|\sum_{m=1}^{M} h_{RU,m}^{rf} h_{BR,m}\right|^2, rf \in \{rfl, rfr\}$. Hence, based on the equation $f_{aX}(x) = \frac{1}{|a|} f_X\left(\frac{x}{a}\right)$, the PDF and CDF of $\left|g_m^{rf}\right|^2$ are derived as the final expressions.

Appendix C.3

With the aid of the outage probability definition, the outage probability of the reflecting user is expressed as

$$\mathbb{P}_{out,rfl}(x) = \int_0^R F_{\left|g_m^{rfl}\right|^2}\left(\frac{\Upsilon_{\max} d_{BR}^{\alpha_t} x^{\alpha_t}}{P_t C_{BR} C_{RU}^{rfl}}\right) f_{d_{RU}^{rfl}}(x)\, dx. \tag{C.17}$$

Substituting the CDF of the central limit model and (5.1) into (C.17), we further derive the outage probability expression above as

$$\begin{aligned}\mathbb{P}_{out,rfl}(x) =& \frac{1}{R^2}\int_0^R x\left(\operatorname{erf}\left(\frac{\bar{h}_{eq}^{rfl} + \sqrt{\frac{\Upsilon_{\max} d_{BR}^{\alpha_t} x^{\alpha_t}}{P_t C_{BR} C_{RU}^{rfl}}}}{\sqrt{2\eta_{eq}^{rf}}}\right)\right. \\ &\left.\times \operatorname{erf}\left(\frac{\bar{h}_{eq}^{rfl} - \sqrt{\frac{\Upsilon_{\max} d_{BR}^{\alpha_t} x^{\alpha_t}}{P_t C_{BR} C_{RU}^{rfl}}}}{\sqrt{2\eta_{eq}^{rf}}}\right)\right)\end{aligned} \tag{C.18}$$

As the integration above cannot be derived, we utilize the Taylor series of the error function $\operatorname{erf}(z) = \frac{2}{\sqrt{\pi}} \sum_{n=0}^{\infty} \frac{(-1)^n}{n!(2n+1)} z^{2n+1}$ to approximately calculate

the outage probability. Hence, we derive the equation (C.19) as

$$\mathbb{P}_{out,rfl}\left(x\right)=\sum_{n=0}^{\infty}\frac{4(-1)^{n}}{n!\sqrt{\pi}\left(2n+1\right)\left(2\eta_{eq}^{rf}\right)^{\frac{2n+1}{2}}}\sum_{r=\{1,3,\cdots,2n+1\}}^{2n+1}\binom{2n+1}{r}$$
$$\times\left(\bar{h}_{eq}^{rfl}\right)^{2n+1-r}\left(\frac{\Upsilon_{\max}d_{BR}^{\alpha_t}}{P_tC_{BR}C_{RU}^{rfl}}\right)^{\frac{r}{2}}\int_{0}^{R}\frac{x^{\frac{\alpha_t r}{2}+1}}{R^2}dx, \tag{C.19}$$

and after calculating the integration $\int_0^R \frac{x^{\frac{\alpha_t r}{2}+1}}{R^2}dx = \frac{R^{\frac{\alpha_t r}{2}}}{\frac{\alpha_t r}{2}+2}$, we obtain the final expressions.

Appendix C.4

Firstly, we substitute the CDF of the Gamma distribution, (5.22), into the definition of the outage probability of the reflecting user, (5.24). Hence, we obtain the integration as

$$\mathbb{P}_{out,rfl}\left(x\right)=\frac{2}{\Gamma\left(\alpha\right)R^2}\int_{0}^{R}x\gamma\left(\alpha,\frac{\Upsilon_{\max}d_{BR}^{\alpha_t}x^{\alpha_t}}{P_tC_{BR}C_{RU}^{rfl}\beta_{rfl}\beta}\right)dx. \tag{C.20}$$

We then exploit the Taylor series the expand the incomplete Gamma function as $\gamma\left(\alpha,\beta\right)=\sum\limits_{n=0}^{\infty}\frac{(-1)^n\beta^{\alpha+n}}{n!(\alpha+n)}$. In this way, we further calculate the equation above as the following

$$\mathbb{P}_{out,rfl}\left(x\right)=\frac{2}{\Gamma\left(\alpha\right)R^2}\sum_{n=0}^{\infty}\frac{(-1)^n}{n!\left(\alpha+n\right)}\left(\frac{\Upsilon_{\max}d_{BR}^{\alpha_t}}{P_tC_{BR}C_{RU}^{rfl}\beta_{rfl}\beta}\right)^{\alpha+n}$$
$$\times\int_{0}^{R}x^{\alpha_t(\alpha+n)+1}dx. \tag{C.21}$$

Finally, we derive the integration $\int_0^R x^{\alpha_t(\alpha+n)+1}dx=\frac{R^{\alpha_t(\alpha+n)+2}}{[\alpha_t(\alpha+n)+2]}$ and obtain the final answers.

Appendix D

Appendixes for Chapter 6

Appendix D.1

For deriving the closed-form OP expressions for the communication transmitter, the probability expression should be manipulated as follows:

$$\begin{aligned}\mathbb{P}_c^I &= \Pr\left\{\gamma_c^I < \gamma_{th}\right\} \\ &= \Pr\left\{|h_c|^2 < \frac{\gamma_{th}P_r|h_r|^2(d_r)^{-\alpha_c}}{P_c(d_c)^{-\alpha_c}} + \frac{\gamma_{th}\mathbb{E}\left[I_R\right](d_r) + \gamma_{th}\sigma^2}{P_cG_cC_c(d_c)^{-\alpha_c}}\right\}. \end{aligned} \tag{D.1}$$

Upon substituting the expectation of interference in **Lemma 13** and rewriting the probability equation in form of integrals, the OP expression is presented by exploiting the PDF and CDF of the Nakagami-m fading channel as:

$$\begin{aligned}\mathbb{P}_c^I = \int_0^\infty \frac{1}{\Gamma(m)}\gamma\left(m, m\left(\frac{\gamma_{th}P_r x(d_r)^{-\alpha_c}}{P_c(d_c)^{-\alpha_c}} + \frac{\gamma_{th}\mathbb{E}\left[I_R\right](d_r) + \gamma_{th}\sigma^2}{P_cG_cC_c(d_c)^{-\alpha_c}}\right)\right) \\ \times f_{|h_r|^2}(x)\,dx. \end{aligned} \tag{D.2}$$

Since the CDF of the Nakagami-m fading channel (in power domain) is a lower incomplete Gamma function, the accurate series expansion of the incomplete Gamma function is exploited for reducing the complexity of

derivation, which is expressed as:

$$\gamma\left(a,b\right)=\Gamma\left(a\right)-\Gamma\left(a,b\right)=\Gamma\left(a\right)-\sum_{p=0}^{a-1}\frac{(a-1)!}{p!}\exp\left(-b\right)b^{p}, \tag{D.3}$$

where $\Gamma\left(a,b\right)$ is the upper incomplete Gamma function.

By substituting the above equation into Eq. (D.2), we obtain the further streamlined expressions of

$$\begin{aligned}\mathbb{P}_{c}^{I}=&1-\exp\left(-\frac{m\gamma_{th}}{P_{c}}\left(a_{1}+a_{2}\right)\right)\sum_{p=0}^{m-1}\int_{0}^{\infty}f_{|h_{r}|^{2}}\left(x\right)\\&\times\frac{(m\gamma_{th})^{p}}{p!}\exp\left(-\frac{m\gamma_{th}P_{r}a_{3}}{P_{c}}x\right)\left(\frac{P_{r}a_{3}x}{P_{c}}+\frac{a_{1}+a_{2}}{P_{c}}\right)^{p}dx.\end{aligned} \tag{D.4}$$

The former expression Eq. (D.4) is then formulated with the aid of the Binomial theorem as:

$$\begin{aligned}\mathbb{P}_{c}^{I}=&1-\exp\left(-\frac{m\gamma_{th}}{P_{c}}\left(a_{1}+a_{2}\right)\right)\\&\times\sum_{p=0}^{m-1}\frac{(m\gamma_{th})^{p}}{p!}\sum_{r=0}^{p}C_{p}^{r}\frac{(a_{1}+a_{2})^{r}(P_{r}a_{3})^{p-r}}{P_{c}^{p}}\\&\times\int_{0}^{\infty}\exp\left(-\frac{m\gamma_{th}a_{3}P_{r}}{P_{c}}x\right)x^{p-r}f_{|h_{r}|^{2}}\left(x\right)dx.\end{aligned} \tag{D.5}$$

We now exploit Eq. [2.3.3.1] of [127] to obtain Eq. (6.25). Then, the proof is completed.

Appendix D.2

The OP for the radar target under the NOMA-based Semi-ISaC scenario is expressed as the top of the next page, denoted as

$$\mathbb{P}_{r}^{I}=1-\Pr\left\{|h_{c}|^{2}>\gamma_{SIC}\frac{a_{3}P_{r}|h_{r}|^{2}+a_{1}+a_{2}}{P_{c}},|h_{r}|^{2}>\frac{\gamma_{th}\left(a_{4}+a_{5}\right)}{P_{r}}\right\}. \tag{D.6}$$

Substituting the CDF of the Nakagami-m fading channels into Eq. D.6, the resultant probability expression can be further transformed as:

$$\begin{aligned}\mathbb{P}_r^I =& 1 - \int_{\frac{\gamma_{th}(a_4+a_5)}{P_r}}^{\infty} \left(1 - \frac{1}{\Gamma(m)}\gamma\left(m, \frac{m\gamma_{SIC}}{P_c}\left(a_3 P_r |h_r|^2 + a_1 + a_2\right)\right)\right) \\ & \times f_{|h_r|^2}(x)\, dx. \end{aligned} \tag{D.7}$$

By exploiting an accurate series expansion of the lower incomplete Gamma function, and then further manipulating the equations, the OP expression is derived as:

$$\begin{aligned}\mathbb{P}_r^I =& 1 - \sum_{p=0}^{m-1} \frac{1}{p!}\left(\frac{m\gamma_{SIC}}{P_c}\right)^p \exp\left(-\frac{m\gamma_{SIC}(a_1+a_2)}{P_c}\right) \\ & \times \sum_{r=0}^{p} C_p^r (a_1+a_2)^{p-r} (a_3 P_r)^r \\ & \times \underbrace{\int_{\frac{\gamma_{th}(a_4+a_5)}{P_r}}^{\infty} \exp\left(-\frac{m\gamma_{SIC} a_3 P_r x}{P_c}\right) x^r f_{|h_r|^2}(x)\, dx}_{I_1}. \end{aligned} \tag{D.8}$$

Then we can derive I_1 based on Eq. [2.3.6.6] of [127], yielding:

$$\begin{aligned} I_1 =& \frac{1}{\Gamma(m)\, m^r}\left(\frac{\gamma_{SIC} a_3 P_r}{P_c} + 1\right)^{-(r+m)} \\ & \times \Gamma\left(r+m, \frac{\gamma_{th} m (a_4+a_5)}{P_r}\left(\frac{\gamma_{SIC} a_3 P_r}{P_c} + 1\right)\right). \end{aligned} \tag{D.9}$$

Finally, upon substituting I_1 from Eq. (D.9) into the OP expression of Eq. (D.8), we can obtain the closed-form expression Eq. (6.28). This completes the proof.

Appendix D.3

We first express the ergodic REIR with the aid of the following integrals as:

$$R_{est} \approx \sum_{k=0}^{m-1} \frac{\delta}{2T\ln(2)} \int_0^{\infty} \left(\frac{md_t^{\alpha_r}}{\Xi_{r,1}x}\right)^k \times \int_0^{\infty} \frac{1}{z+1} \exp\left(-\frac{md_t^{\alpha_r}}{\Xi_{r,1}x} z\right) \frac{z^k}{k!} dz f_{|h_{r,u}|^2}(x)\, dx. \tag{D.10}$$

With the aid of Eq. [2.3.6.9] of [127], we have

$$R_{est} \approx \sum_{k=0}^{m-1} \frac{\delta}{2T\ln(2)} \int_0^{\infty} \left(\frac{md_t^{\alpha_r}}{\Xi_{r,1}x}\right)^k \times \Psi\left(k+1, k+1, \frac{md_t^{\alpha_r}}{\Xi_{r,1}x}\right) f_{|h_{r,u}|^2}(x)\, dx, \tag{D.11}$$

and based on $\Psi(a,a,z) = z^{1-a}\exp(z)\,E_a(z)$, the expression above is further formulated as

$$R_{est}^{\infty} \approx \frac{\delta m^m}{2T\ln(2)\,\Gamma(m)} \underbrace{\int_0^{\infty} \left(1 + \frac{md_t^{\alpha_r}}{\Xi_{r,1}x}\right) x^{m-1} \exp(-mx)\, E_1\left(\frac{md_t^{\alpha_r}}{\Xi_{r,1}x}\right) dx}_{I_4} + \sum_{k=1}^{m-1} \frac{\delta m^m}{2T\ln(2)\,\Gamma(m)} \underbrace{\int_0^{\infty} x^{m-1} \exp(-mx) \underset{P_{BS}\to\infty}{E_{k+1}}\left(\frac{md_t^{\alpha_r}}{\Xi_{r,1}x}\right) dx}_{I_5}, \tag{D.12}$$

Since we have $\underset{P_{BS}\to\infty}{E_{k+1}}\left(\frac{md_t^{\alpha_r}}{\Xi_{r,1}x}\right) \approx \frac{\left(-\frac{md_t^{\alpha_r}}{\Xi_{r,1}x}\right)^k}{k!}\left(\psi(k+1) - \ln\left(\frac{md_t^{\alpha_r}}{\Xi_{r,1}x}\right)\right) -$

$\sum_{q=0\&q\neq k}^{m-1} \frac{\left(-\frac{md_t^{\alpha_r}}{\Xi_{r,1}x}\right)^q}{q!(q-k)}$ for $k>0$. The equation I_4 is further formulated as:

$$I_4 = \underbrace{\int_0^\infty x^{m-1}\exp\left(-mx\right)E_1\left(\frac{md_t^{\alpha_r}}{\Xi_{r,1}x}\right)dx}_{I_6} + \underbrace{\frac{md_t^{\alpha_r}}{\Xi_{r,1}}\int_0^\infty x^{m-2}\exp\left(-mx\right)E_1\left(\frac{md_t^{\alpha_r}}{\Xi_{r,1}x}\right)dx}_{I_7}. \tag{D.13}$$

Based on the asymptotic expressions, respectively expressed as $\gamma\left(m,t\right) = (m-1)!-\exp\left(-t\right)\sum_{k=0}^{m-1}\frac{(m-1)!}{k!}t^k$, $E_n\left(z\right)\approx\frac{(-z)^{n-1}}{(n-1)!}\left(\psi\left(n\right)-\ln\left(z\right)\right)-\sum_{k=0\&\ k\neq n-1}$ $\times\frac{(-z)^k}{k!(1-n+k)}$ for $n>1$, and $E_1\left(z\right)\approx -C_\gamma-\ln\left(z\right)+z$, I_6 and I_7 are derived as:

$$I_6 = \frac{d_t^{\alpha_r}\Gamma\left(m-1\right)}{\Xi_{r,1}m^{m-2}} - \frac{\Gamma\left(m\right)}{m^m}\left(\log\left(\frac{m^2d_t^{\alpha_r}}{\Xi_{r,1}}\right)-\psi^{(0)}\left(m\right)-C_\gamma\right) \tag{D.14}$$

and

$$I_7 = \left(\frac{md_t^{\alpha_r}}{\Xi_{r,1}}\right)^2\frac{\Gamma\left(m-2\right)}{m^{m-2}} - \frac{md_t^{\alpha_r}}{\Xi_{r,1}}\frac{\Gamma\left(m-1\right)}{m^{m-1}} \times\left(\log\left(\frac{m^2d_t^{\alpha_r}}{\Xi_{r,1}}\right)-\psi^{(0)}\left(m-1\right)-C_\gamma\right). \tag{D.15}$$

Then, we can derive I_5 of Eq. (D.12) by substituting the asymptotic expressions of $\underset{P_{BS}\to\infty}{E_{k+1}}\left(\frac{md_t^{\alpha_r}}{\Xi_{r,1}x}\right)$, Finally, we can substitute I_4 and I_5 into (D.12) to obtain the final answer as Eq. (6.50).

Bibliography

[1] Y. Liu, Z. Qin, M. Elkashlan, Z. Ding, A. Nallanathan, and L. Hanzo, "Nonorthogonal multiple access for 5G and beyond," *Proc. IEEE*, vol. 105, no. 12, pp. 2347–2381, 2017.

[2] Y. Yuan, S. Wang, Y. Wu, H. V. Poor, Z. Ding, X. You, and L. Hanzo, "NOMA for next-generation massive IoT: Performance potential and technology directions," *IEEE Commun. Mag.*, vol. 59, no. 7, pp. 115–121, 2021.

[3] C. Zhang, W. Yi, Y. Liu, K. Yang, and Z. Ding, "Reconfigurable intelligent surfaces aided multi-cell NOMA networks: A stochastic geometry model," *IEEE Trans. Commun.*, vol. 70, no. 2, pp. 951–966, Feb. 2022.

[4] J. G. Andrews, S. Buzzi, W. Choi, S. V. Hanly, A. Lozano, A. C. K. Soong, and J. C. Zhang, "What will 5G be?" *IEEE J. Sel. Areas Commun.*, vol. 32, no. 6, pp. 1065–1082, 2014.

[5] F. Boccardi, R. W. Heath, A. Lozano, T. L. Marzetta, and P. Popovski, "Five disruptive technology directions for 5G," *IEEE Commun. Mag.*, vol. 52, no. 2, pp. 74–80, 2014.

[6] A. Kamilaris and A. Pitsillides, "Mobile phone computing and the internet of things: A survey," *IEEE Internet Things J.*, vol. 3, no. 6, pp. 885–898, 2016.

[7] M. A. Razzaque, M. Milojevic-Jevric, A. Palade, and S. Clarke, "Middleware for internet of things: A survey," *IEEE Internet Things J.*, vol. 3, no. 1, pp. 70–95, 2016.

[8] L. Zhang, Y. Liang, and M. Xiao, "Spectrum sharing for internet of things: A survey," *IEEE Wireless Commun.*, vol. 26, no. 3, pp. 132–139, 2019.

[9] S. Ali, N. Rajatheva, and W. Saad, "Fast uplink grant for machine type communications: Challenges and opportunities," *IEEE Commun. Mag.*, vol. 57, no. 3, pp. 97–103, 2019.

[10] K. Yang, N. Yang, N. Ye, M. Jia, Z. Gao, and R. Fan, "Non-orthogonal multiple access: Achieving sustainable future radio access," *IEEE Commun. Mag.*, vol. 57, no. 2, pp. 116–121, 2019.

[11] L. Liu, E. G. Larsson, W. Yu, P. Popovski, C. Stefanovic, and E. de Carvalho, "Sparse signal processing for grant-free massive connectivity: A future paradigm for random access protocols in the internet of things," *IEEE Signal Process. Mag.*, vol. 35, no. 5, pp. 88–99, 2018.

[12] A. Azari, P. Popovski, G. Miao, and C. Stefanovic, "Grant-free radio access for short-packet communications over 5G networks," in *IEEE Global Commun. Conf.*, 2017, pp. 1–7.

[13] L. Dai, B. Wang, Y. Yuan, S. Han, I. Chih-lin, and Z. Wang, "Non-orthogonal multiple access for 5G: solutions, challenges, opportunities, and future research trends," *IEEE Commun. Mag.*, vol. 53, no. 9, pp. 74–81, 2015.

[14] G. Wunder, P. Jung, M. Kasparick, T. Wild, F. Schaich, Y. Chen, S. T. Brink, I. Gaspar, N. Michailow, A. Festag, L. Mendes, N. Cassiau, D. Ktenas, M. Dryjanski, S. Pietrzyk, B. Eged, P. Vago, and F. Wiedmann, "5GNOW: non-orthogonal, asynchronous waveforms for future mobile applications," *IEEE Commun. Mag.*, vol. 52, no. 2, pp. 97–105, 2014.

[15] Y. Huang, C. Zhang, J. Wang, Y. Jing, L. Yang, and X. You, "Signal processing for MIMO-NOMA: Present and future challenges," *IEEE Wireless Commun.*, vol. 25, no. 2, pp. 32–38, 2018.

[16] S. M. R. Islam, N. Avazov, O. A. Dobre, and K. Kwak, "Power-domain non-orthogonal multiple access (NOMA) in 5G systems: Potentials and challenges," *IEEE Commun. Surveys Tuts.*, vol. 19, no. 2, pp. 721–742, 2017.

[17] Y. Saito, Y. Kishiyama, A. Benjebbour, T. Nakamura, A. Li, and K. Higuchi, "Non-orthogonal multiple access (NOMA) for cellular future radio access," *IEEE Veh. Tech. Conf.*, pp. 1–5, 2013.

[18] Q. Wang, R. Zhang, L. Yang, and L. Hanzo, "Non-orthogonal multiple access: A unified perspective," *IEEE Wireless Commun.*, vol. 25, no. 2, pp. 10–16, 2018.

[19] Y. Zhang, K. Peng, Z. Chen, and J. Song, "SIC vs. JD: Uplink NOMA techniques for M2M random access," *Proc. IEEE Int. Conf. Commun. (ICC)*, pp. 1–6, 2017.

[20] Z. Ding, X. Lei, G. K. Karagiannidis, R. Schober, J. Yuan, and V. K. Bhargava, "A survey on non-orthogonal multiple access for 5G networks: Research challenges and future trends," *IEEE J. Sel. Areas Commun.*, vol. 35, no. 10, pp. 2181–2195, 2017.

[21] W. Yi, Y. Liu, A. Nallanathan, and M. Elkashlan, "Clustered millimeter-wave networks with non-orthogonal multiple access," *IEEE Trans. Commun.*, vol. 67, no. 6, pp. 4350–4364, 2019.

[22] M. A. ElMossallamy, H. Zhang, L. Song, K. G. Seddik, Z. Han, and G. Y. Li, "Reconfigurable intelligent surfaces for wireless communications: Principles, challenges, and opportunities," *IEEE Trans. Cogn. Commun. Netw.*, vol. 6, no. 3, pp. 990–1002, Sep. 2020.

[23] Q. Wu and R. Zhang, "Towards smart and reconfigurable environment: Intelligent reflecting surface aided wireless network," *IEEE Commun. Mag.*, vol. 58, no. 1, pp. 106–112, Jan. 2020.

[24] C. Huang, S. Hu, G. C. Alexandropoulos, A. Zappone, C. Yuen, R. Zhang, M. D. Renzo, and M. Debbah, "Holographic MIMO surfaces for 6G wireless networks: Opportunities, challenges, and trends," *IEEE Wireless Commun.*, vol. 27, no. 5, pp. 118–125, 2020.

[25] H. Wymeersch, J. He, B. Denis, A. Clemente, and M. Juntti, "Radio localization and mapping with reconfigurable intelligent surfaces: Challenges, opportunities, and research directions," *IEEE Veh. Technol. Mag.*, vol. 15, no. 4, pp. 52–61, Dec. 2020.

[26] Z. Zhang, L. Dai, X. Chen, C. Liu, F. Yang, R. Schober, and H. V. Poor, "Active RIS vs. passive RIS: Which will prevail in 6G?" *IEEE Trans. Commun.*, vol. 71, no. 3, pp. 1707–1725, Mar. 2023.

[27] M. Di Renzo, F. Habibi Danufane, X. Xi, J. de Rosny, and S. Tretyakov, "Analytical modeling of the path-loss for reconfigurable intelligent surfaces−anomalous mirror or scatterer?" *Proc. IEEE 21th Int. Workshop Signal Process. Adv. Wireless Commun. (SPAWC)*, pp. 1–5, 2020.

[28] W. Tang, M. Z. Chen, X. Chen, J. Y. Dai, Y. Han, M. Di Renzo, Y. Zeng, S. Jin, Q. Cheng, and T. J. Cui, "Wireless communications with reconfigurable intelligent surface: Path loss modeling and experimental measurement," *IEEE Trans. Wireless Commun.*, vol. 20, no. 1, pp. 421–439, Jan. 2021.

[29] E. Basar, M. Di Renzo, J. De Rosny, M. Debbah, M. Alouini, and R. Zhang, "Wireless communications through reconfigurable intelligent surfaces," *IEEE Access*, vol. 7, pp. 116 753–116 773, 2019.

[30] G. Pan, J. Ye, J. An, and M.-S. Alouini, "Full-duplex enabled intelligent reflecting surface systems: Opportunities and challenges," *IEEE Wireless Commun.*, vol. 28, no. 3, pp. 122–129, Jun. 2021.

[31] Y. Liu, X. Mu, J. Xu, R. Schober, Y. Hao, H. V. Poor, and L. Hanzo, "STAR: Simultaneous transmission and reflection for 360° coverage by intelligent surfaces," *IEEE Wireless Commun.*, vol. 28, no. 6, pp. 102–109, Dec. 2021.

[32] M. Di Renzo, A. Zappone, M. Debbah, M.-S. Alouini, C. Yuen, J. de Rosny, and S. Tretyakov, "Smart radio environments empowered by reconfigurable intelligent surfaces: How it works, state of research, and the road ahead," *IEEE J. Sel. Areas Commun.*, vol. 38, no. 11, pp. 2450–2525, Nov. 2020.

[33] Y. Liu, Z. Qin, M. Elkashlan, A. Nallanathan, and J. A. McCann, "Non-orthogonal multiple access in large-scale heterogeneous networks," *IEEE J. Sel. Areas Commun.*, vol. 35, no. 12, pp. 2667–2680, Dec. 2017.

[34] W. Yi, Y. Liu, E. Bodanese, A. Nallanathan, and G. K. Karagiannidis, "A unified spatial framework for UAV-aided mmwave networks," *IEEE Trans. Commun.*, vol. 67, no. 12, pp. 8801–8817, 2019.

[35] T. Bai and R. W. Heath, "Coverage and rate analysis for millimeter-wave cellular networks," *IEEE Trans. Wireless Commun.*, vol. 14, no. 2, pp. 1100–1114, 2015.

[36] M. Haenggi, "On distances in uniformly random networks," *IEEE Trans. Inf. Theory*, vol. 51, no. 10, pp. 3584–3586, 2005.

[37] E. Rousseau and D. Felbacq, "Concept of a generalized law of refraction: A phenomenological model," *ACS Photonics*, vol. 7, no. 7, pp. 1649–1654, 2020. [Online]. Available: https://doi.org/10.1021/acsphotonics.0c00639

[38] A. Díaz-Rubio and S. A. Tretyakov, "Acoustic metasurfaces for scattering-free anomalous reflection and refraction," *Phys. Rev. B*, vol. 96, p. 125409, Sep. 2017. [Online]. Available: https://link.aps.org/doi/10.1103/PhysRevB.96.125409

[39] Y. Nakata, Y. Urade, K. Okimura, T. Nakanishi, F. Miyamaru, M. W. Takeda, and M. Kitano, "Anisotropic babinet-invertible metasurfaces to realize transmission-reflection switching for orthogonal polarizations of light," *Phys. Rev. Applied*, vol. 6, p. 044022, Oct. 2016. [Online]. Available: https://link.aps.org/doi/10.1103/PhysRevApplied.6.044022

[40] V. Asadchy, M. Albooyeh, S. Tcvetkova, Y. Ra'di, and S. A. Tretyakov, "Metasurfaces for perfect and full control of refraction and reflection," in *Proc. 10th Int. Congr. Adv. Electromagn. Mater. Microw. Opt.*, Sep. 2016, pp. 364–366.

[41] A. Patri, G. Lavigne, and C. Caloz, "Metasurface particle with independent transmission and reflection full phase coverage," in *Proc. 2018 IEEE Int. Symp. Antennas Propag.*, Jul. 2018, pp. 995–996.

[42] X. Mu, Y. Liu, L. Guo, J. Lin, and R. Schober, "Simultaneously transmitting and reflecting (STAR) RIS aided wireless communications," *IEEE Trans. Wireless Commun.*, vol. 21, no. 5, pp. 3083–3098, May 2022.

[43] C. Pérez-Arancibia, R. Pestourie, and S. G. Johnson, "Sideways adiabaticity: beyond ray optics for slowly varying metasurfaces," *Opt. Express*, vol. 26, no. 23, pp. 30 202–30 230, Nov. 2018. [Online]. Available: http://www.opticsexpress.org/abstract.cfm?URI=oe-26-23-30202

[44] J. Xu, Y. Liu, X. Mu, and O. A. Dobre, "STAR-RISs: Simultaneous transmitting and reflecting reconfigurable intelligent surfaces," *IEEE Commun. Lett.*, vol. 25, no. 9, pp. 3134–3138, Sep. 2021.

[45] C. L. Holloway, E. F. Kuester, and A. H. Haddab, "Retrieval approach for determining surface susceptibilities and surface porosities of a symmetric metascreen from reflection and transmission coefficients," Feb. 2019, arXiv preprint arXiv:1902.08703. [Online]. Available: https://arxiv.org/abs/1902.08703

[46] S. Zhang, H. Zhang, B. Di, Y. Tan, Z. Han, and L. Song, "Beyond intelligent reflecting surfaces: Reflective-transmissive metasurface aided communications for full-dimensional coverage extension," *IEEE Trans. Veh. Technol.*, vol. 69, no. 11, pp. 13 905–13 909, Nov. 2020.

[47] L. Bariah, L. Mohjazi, S. Muhaidat, P. C. Sofotasios, G. K. Kurt, H. Yanikomeroglu, and O. A. Dobre, "A prospective look: Key enabling technologies, applications and open research topics in 6G networks," *IEEE Access*, vol. 8, pp. 174 792–174 820, 2020.

[48] G. C. Alexandropoulos, N. Shlezinger, I. Alamzadeh, M. F. Imani, H. Zhang, and Y. C. Eldar, "Hybrid reconfigurable intelligent metasurfaces: Enabling simultaneous tunable reflections and sensing for 6G wireless communications," Apr. 2021, arXiv preprint arXiv:2104.04690. [Online]. Available: https://arxiv.org/abs/2104.04690

[49] T. Wild, V. Braun, and H. Viswanathan, "Joint design of communication and sensing for beyond 5G and 6G systems," *IEEE Access*, vol. 9, pp. 30 845–30 857, 2021.

[50] C. Sturm and W. Wiesbeck, "Waveform design and signal processing aspects for fusion of wireless communications and radar sensing," *Proc. IEEE*, vol. 99, no. 7, pp. 1236–1259, Jul. 2011.

[51] J. A. Zhang, F. Liu, C. Masouros, R. W. Heath, Z. Feng, L. Zheng, and A. Petropulu, "An overview of signal processing techniques for joint communication and radar sensing," *IEEE J. Sel. Topics Signal Process.*, vol. 15, no. 6, pp. 1295–1315, Nov. 2021.

[52] A. Liu, Z. Huang, M. Li, Y. Wan, W. Li, T. X. Han, C. Liu, R. Du, D. K. P. Tan, J. Lu, Y. Shen, F. Colone, and K. Chetty, "A survey on fundamental limits of integrated sensing and communication," *IEEE Commun. Surveys Tuts.*, vol. 24, no. 2, pp. 994–1034, 2nd Quart. 2022.

[53] H. Griffiths, L. Cohen, S. Watts, E. Mokole, C. Baker, M. Wicks, and S. Blunt, "Radar spectrum engineering and management: Technical and regulatory issues," *Proc. IEEE*, vol. 103, no. 1, pp. 85–102, Jan. 2015.

[54] A. R. Chiriyath, B. Paul, G. M. Jacyna, and D. W. Bliss, "Inner bounds on performance of radar and communications co-existence," *IEEE Trans. Signal Process.*, vol. 64, no. 2, pp. 464–474, Jan. 2016.

[55] T. M. Cover, "Broadcast channels," *IEEE Trans. Inf. Theory*, vol. 18, pp. 2–14, 1972.

[56] P. Bergmans, "A simple converse for broadcast channels with additive white gaussian noise (corresp.)," *IEEE Trans. Inf. Theory*, vol. 20, no. 2, pp. 279–280, 1974.

[57] P. Xu, Z. Ding, X. Dai, and H. V. Poor, "A new evaluation criterion for non-orthogonal multiple access in 5G software defined networks," *IEEE Access*, vol. 3, pp. 1633–1639, 2015.

[58] P. Xu, Y. Yuan, Z. Ding, X. Dai, and R. Schober, "On the outage performance of non-orthogonal multiple access with 1-bit feedback," *IEEE Trans. Wireless Commun.*, vol. 15, no. 10, pp. 6716–6730, Oct. 2016.

[59] P. D. Diamantoulakis and G. K. Karagiannidis, "Performance analysis of distributed uplink NOMA," *IEEE Commun. Lett.*, vol. 25, no. 3, pp. 788–792, Mar. 2021.

[60] F. Tabee Miandoab, M. S. Fazel, and M. Mahdavi, "Outage analysis of multiuser MIMO-NOMA transmissions in uplink full-duplex coop-

erative system," *IEEE Wireless Commun. Lett.*, vol. 11, no. 10, pp. 2076–2079, Oct. 2022.

[61] W. Yu, C. H. Foh, A. U. Quddus, Y. Liu, and R. Tafazolli, "Throughput analysis and user barring design for uplink NOMA-enabled random access," *IEEE Trans. Wireless Commun.*, vol. 20, no. 10, pp. 6298–6314, Oct. 2021.

[62] L. Liu, M. Sheng, J. Liu, Y. Dai, and J. Li, "Stable throughput region and average delay analysis of uplink NOMA systems with unsaturated traffic," *IEEE Trans. Commun.*, vol. 67, no. 12, pp. 8475–8488, Dec. 2019.

[63] N. Zhang, J. Wang, G. Kang, and Y. Liu, "Uplink nonorthogonal multiple access in 5G systems," *IEEE Commun. Lett.*, vol. 20, no. 3, pp. 458–461, Mar. 2016.

[64] Z. Ding, X. Lei, G. K. Karagiannidis, R. Schober, J. Yuan, and V. K. Bhargava, "A survey on non-orthogonal multiple access for 5G networks: Research challenges and future trends," *IEEE J. Sel. Areas Commun.*, vol. 35, no. 10, pp. 2181–2195, Oct. 2017.

[65] H. Nikopour and H. Baligh, "Sparse code multiple access," in *IEEE PIMRC 2013*, Sep. 2013, pp. 332–336.

[66] X. Li, Q. Zhu, and X. Wang, "Privacy-aware crowdsourced spectrum sensing and multi-user sharing mechanism in dynamic spectrum access networks," *IEEE Access*, vol. 7, pp. 32 971–32 988, 2019.

[67] L. Dai, B. Wang, Y. Yuan, S. Han, I. Chih-lin, and Z. Wang, "Non-orthogonal multiple access for 5G: solutions, challenges, opportunities, and future research trends," *IEEE Commun. Mag.*, vol. 53, no. 9, pp. 74–81, Sep. 2015.

[68] Z. Ding, F. Adachi, and H. V. Poor, "The application of MIMO to non-orthogonal multiple access," *IEEE Trans. Wireless Commun.*, vol. 15, no. 1, pp. 537–552, Jan. 2016.

[69] Z. Ding, R. Schober, and H. V. Poor, "A general MIMO framework for noma downlink and uplink transmission based on signal alignment," *IEEE Trans. Wireless Commun.*, vol. 15, no. 6, pp. 4438–4454, Jun. 2016.

[70] L. Dai, B. Wang, M. Peng, and S. Chen, "Hybrid precoding-based millimeter-wave massive MIMO-NOMA with simultaneous wireless information and power transfer," *IEEE J. Sel. Areas Commun.*, vol. 37, no. 1, pp. 131–141, Jan. 2019.

[71] X. Dai, S. Chen, S. Sun, S. Kang, Y. Wang, Z. Shen, and J. Xu, "Successive interference cancelation amenable multiple access (SAMA) for future wireless communications," in *IEEE International Commun. System (ICCS)*, 2014, pp. 222–226.

[72] B. Clerckx, Y. Mao, E. A. Jorswieck, J. Yuan, D. J. Love, E. Erkip, and D. Niyato, "A primer on rate-splitting multiple access: Tutorial, myths, and frequently asked questions," *IEEE J. Sel. Areas Commun.*, vol. 41, no. 5, pp. 1265–1308, May 2023.

[73] M. Haenggi, J. G. Andrews, F. Baccelli, O. Dousse, and M. Franceschetti, "Stochastic geometry and random graphs for the analysis and design of wireless networks," *IEEE J. Sel. Areas Commun.*, vol. 27, no. 7, pp. 1029–1046, 2009.

[74] J. G. Andrews, F. Baccelli, and R. K. Ganti, "A tractable approach to coverage and rate in cellular networks," *IEEE Trans. Commun.*, vol. 59, no. 11, pp. 3122–3134, 2011.

[75] H. ElSawy, E. Hossain, and M. Haenggi, "Stochastic geometry for modeling, analysis, and design of multi-tier and cognitive cellular wire-

less networks: A survey," *IEEE Commun. Surveys Tuts.*, vol. 15, no. 3, pp. 996–1019, 2013.

[76] R. Abbas, M. Shirvanimoghaddam, Y. Li, and B. Vucetic, "A novel analytical framework for massive grant-free NOMA," *IEEE Trans. Commun.*, vol. 67, no. 3, pp. 2436–2449, 2019.

[77] W. Yi, Y. Liu, and A. Nallanathan, "Cache-enabled HetNets with millimeter wave small cells," *IEEE Trans. Commun.*, vol. 66, no. 11, pp. 5497–5511, 2018.

[78] Y. Sun, Z. Ding, X. Dai, and O. A. Dobre, "On the performance of network NOMA in uplink CoMP systems: A stochastic geometry approach," *IEEE Trans. Commun.*, vol. 67, no. 7, pp. 5084–5098, 2019.

[79] E. Turgut and M. C. Gursoy, "Downlink analysis in unmanned aerial vehicle (UAV) assisted cellular networks with clustered users," *IEEE Access*, vol. 6, pp. 36 313–36 324, 2018.

[80] T. Hou, Y. Liu, Z. Song, X. Sun, and Y. Chen, "Multiple antenna aided NOMA in UAV networks: A stochastic geometry approach," *IEEE Trans. Commun.*, vol. 67, no. 2, pp. 1031–1044, 2019.

[81] Y. Liu, Z. Ding, M. Elkashlan, and H. V. Poor, "Cooperative non-orthogonal multiple access with simultaneous wireless information and power transfer," *IEEE J. Sel. Areas Commun.*, vol. 34, no. 4, pp. 938–953, 2016.

[82] B. Makki, K. Chitti, A. Behravan, and M. Alouini, "A survey of NOMA: Current status and open research challenges," *IEEE Open J. Commun. Soc.*, vol. 1, pp. 179–189, 2020.

[83] L. Dai, B. Wang, Z. Ding, Z. Wang, S. Chen, and L. Hanzo, "A survey of non-orthogonal multiple access for 5G," *IEEE Commun. Surveys Tut.*, vol. 20, no. 3, pp. 2294–2323, 2018.

[84] N. Zhang, J. Wang, G. Kang, and Y. Liu, "Uplink non-orthogonal multiple access in 5G systems," *IEEE Wireless Commun. Lett.*, vol. 20, no. 3, pp. 458–461, 2016.

[85] M. Al-Imari, P. Xiao, M. A. Imran, and R. Tafazolli, "Uplink non-orthogonal multiple access for 5G wireless networks," *Proc. 11th Int. Symp. Wireless Commun. Syst. (ISWCS)*, pp. 781–785, 2014.

[86] K. Higuchi and A. Benjebbour, "Non-orthogonal multiple access (NOMA) with successive interference cancellation for future radio access," *IEICE Trans. Commun.*, vol. 98, no. 3, pp. 403–414, 2015.

[87] M. A. Sedaghat and R. R. Mller, "On user pairing in uplink NOMA," *IEEE Trans. Wireless Commun.*, vol. 17, no. 5, pp. 3474–3486, 2018.

[88] Z. Yang, Z. Ding, P. Fan, and N. Al-Dhahir, "A general power allocation scheme to guarantee quality of service in downlink and uplink NOMA systems," *IEEE Trans. Wireless Commun.*, vol. 15, no. 11, pp. 7244–7257, 2016.

[89] P. D. Diamantoulakis, K. N. Pappi, Z. Ding, and G. K. Karagiannidis, "Wireless-powered communications with non-orthogonal multiple access," *IEEE Trans. Wireless Commun.*, vol. 15, no. 12, pp. 8422–8436, 2016.

[90] J. Ye, Z. Liu, H. Zhao, G. Pan, Q. Ni, and M. Alouini, "Relay selections for cooperative underlay CR systems with energy harvesting," *IEEE Trans. Cogn. Commun. Netw.*, vol. 5, no. 2, pp. 358–369, 2019.

[91] B. Wang, L. Dai, Y. Zhang, T. Mir, and J. Li, "Dynamic compressive sensing-based multi-user detection for uplink grant-free NOMA," *IEEE Commun. Lett.*, vol. 20, no. 11, pp. 2320–2323, 2016.

[92] Y. Du, B. Dong, Z. Chen, X. Wang, Z. Liu, P. Gao, and S. Li, "Efficient multi-user detection for uplink grant-free NOMA: Prior-information

aided adaptive compressive sensing perspective," *IEEE J. Sel. Areas Commun.*, vol. 35, no. 12, pp. 2812–2828, 2017.

[93] J. Xu and Y. Liu, "A novel physics-based channel model for reconfigurable intelligent surface-assisted multi-user communication systems," *IEEE Trans. Commun.*, vol. 21, no. 2, pp. 1183–1196, Feb. 2022.

[94] V. S. Asadchy, W. Wickberg, A. Diaz-Rubio, and M. Wegener, "Eliminating scattering loss in anomalously reflecting optical metasurfaces," *ACS Photonics*, vol. 4, no. 5, pp. 1264–1270, Apr. 2017.

[95] N. Shlezinger, G. C. Alexandropoulos, M. F. Imani, Y. C. Eldar, and D. R. Smith, "Dynamic metasurface antennas for 6G extreme massive MIMO communications," *IEEE Wireless Commun.*, pp. 1–8, 2021.

[96] E. Björnson, L. Sanguinetti, H. Wymeersch, J. Hoydis, and T. L. Marzetta, "Massive MIMO is a reality - What is next?: Five promising research directions for antenna arrays," *Digital Signal Processing*, vol. 94, pp. 3–20, 2019.

[97] W. Yan, X. Yuan, Z. He, and X. Kuai, "Passive beamforming and information transfer design for reconfigurable intelligent surfaces aided multiuser MIMO systems," *IEEE J. Sel. Areas Commun.*, doi: 10.1109/JSAC.2020.3000811, 2020.

[98] M. Jung, W. Saad, M. Debbah, and C. S. Hong, "On the optimality of reconfigurable intelligent surfaces (RISs): Passive beamforming, modulation, and resource allocation," 2019, arXiv preprint, arXiv:1910.00968. [Online]. Available: https://doi.org/10.48550/arXiv.1910.00968

[99] B. Di, H. Zhang, L. Song, Y. Li, Z. Han, and H. V. Poor, "Hybrid beamforming for reconfigurable intelligent surface based multi-user communications: Achievable rates with limited discrete phase shifts," *IEEE J. Sel. Areas Commun.*, vol. 38, no. 8, pp. 1809–1822, 2020.

[100] R. Karasik, O. Simeone, M. D. Renzo, and S. Shamai Shitz, "Adaptive coding and channel shaping through reconfigurable intelligent surfaces: An information-theoretic analysis," *IEEE Transa. Commun.*, vol. 69, no. 11, pp. 7320–7334, Nov. 2021.

[101] C. Huang, R. Mo, and C. Yuen, "Reconfigurable intelligent surface assisted multiuser MISO systems exploiting deep reinforcement learning," *IEEE J. Sel. Areas Commun.*, vol. 38, no. 8, pp. 1839–1850, 2020.

[102] S. Khan and S. Y. Shin, "Deep-learning-aided detection for reconfigurable intelligent surfaces," 2019, arXiv preprint arXiv:1910.09136. [Online]. Available: https://doi.org/10.48550/arXiv.1910.09136

[103] X. Yang, C. Wen, and S. Jin, "MIMO detection for reconfigurable intelligent surface-assisted millimeter wave systems," *IEEE J. Sel. Areas Commun.*, doi: 10.1109/JSAC.2020.3000822, 2020.

[104] M. Nemati, B. Maham, S. R. Pokhrel, and J. Choi, "Modeling RIS empowered outdoor-to-indoor communication in mmWave cellular networks," *IEEE Trans. Commun.*, vol. 69, no. 11, pp. 7837–7850, Nov. 2021.

[105] A. U. Makarfi, K. M. Rabie, O. Kaiwartya, O. S. Badarneh, X. Li, and R. Kharel, "Reconfigurable intelligent surface enabled IoT networks in generalized fading channels," *Proc. IEEE Int. Conf. Commun. (ICC)*, pp. 1–6, 2020.

[106] S. Zhang, H. Zhang, B. Di, Y. Tan, Z. Han, and L. Song, "Beyond intelligent reflecting surfaces: Reflective-transmissive metasurface aided communications for full-dimensional coverage extension," *IEEE Trans. Veh. Technol.*, vol. 69, no. 11, pp. 13 905–13 909, Nov. 2020.

[107] S. Zhang, H. Zhang, B. Di, Y. Tan, M. Di Renzo, Z. Han, H. Vincent Poor, and L. Song, "Intelligent omni-surface: Ubiquitous wireless transmission by reflective-transmissive metasurface,"

Nov. 2020, arXiv preprint arXiv:2011.00765. [Online]. Available: https://arxiv.org/abs/2011.00765

[108] C. Wu, Y. Liu, X. Mu, X. Gu, and O. A. Dobre, "Coverage characterization of STAR-RIS networks: NOMA and OMA," *IEEE Commun. Lett.*, vol. 25, no. 9, pp. 3036–3040, Sep. 2021.

[109] T. Hou, Y. Liu, Z. Song, X. Sun, Y. Chen, and L. Hanzo, "MIMO assisted networks relying on intelligent reflective surfaces: A stochastic geometry based analysis," *IEEE Trans. Veh. Technol.*, vol. 71, no. 1, pp. 571–582, Jan. 2022.

[110] J. A. Mahal, A. Khawar, A. Abdelhadi, and T. C. Clancy, "Spectral coexistence of MIMO radar and MIMO cellular system," *IEEE Trans. Aerosp. Electron. Syst.*, vol. 53, no. 2, pp. 655–668, Apr. 2017.

[111] B. Kang, O. Aldayel, V. Monga, and M. Rangaswamy, "Spatio-spectral radar beampattern design for coexistence with wireless communication systems," *IEEE Trans. Aerosp. Electron. Syst.*, vol. 55, no. 2, pp. 644–657, Apr. 2019.

[112] F. Liu, L. Zhou, C. Masouros, A. Li, W. Luo, and A. Petropulu, "Toward dual-functional radar-communication systems: Optimal waveform design," *IEEE Trans. Signal Process.*, vol. 66, no. 16, pp. 4264–4279, Aug. 2018.

[113] F. Wang and H. Li, "Power allocation for coexisting multicarrier radar and communication systems in cluttered environments," *IEEE Trans. Signal Process.*, vol. 69, pp. 1603–1613, 2021.

[114] J. Qian, M. Lops, L. Zheng, X. Wang, and Z. He, "Joint system design for coexistence of MIMO radar and MIMO communication," *IEEE Trans. Signal Process.*, vol. 66, no. 13, pp. 3504–3519, Jul. 2018.

[115] N. Cao, Y. Chen, X. Gu, and W. Feng, "Joint radar-communication waveform designs using signals from multiplexed users," *IEEE Trans. Commun.*, vol. 68, no. 8, pp. 5216–5227, Aug. 2020.

[116] K. Wu, J. A. Zhang, X. Huang, Y. J. Guo, and R. W. Heath, "Waveform design and accurate channel estimation for frequency-hopping MIMO radar-based communications," *IEEE Trans. Commun.*, vol. 69, no. 2, pp. 1244–1258, Feb. 2021.

[117] M. Temiz, E. Alsusa, and M. W. Baidas, "Optimized precoders for massive MIMO OFDM dual radar-communication systems," *IEEE Trans. Commun.*, vol. 69, no. 7, pp. 4781–4794, Jul. 2021.

[118] K. Wu, J. A. Zhang, X. Huang, Y. J. Guo, and J. Yuan, "Reliable frequency-hopping MIMO radar-based communications with multi-antenna receiver," *IEEE Trans. Commun.*, vol. 69, no. 8, pp. 5502–5513, Aug. 2021.

[119] F. Liu, C. Masouros, A. Li, T. Ratnarajah, and J. Zhou, "MIMO radar and cellular coexistence: A power-efficient approach enabled by interference exploitation," *IEEE Trans. Signal Process.*, vol. 66, no. 14, pp. 3681–3695, Jul. 2018.

[120] L. Zheng, M. Lops, and X. Wang, "Adaptive interference removal for uncoordinated radar/communication coexistence," *IEEE J. Sel. Topics Signal Process.*, vol. 12, no. 1, pp. 45–60, Feb. 2018.

[121] N. Nartasilpa, A. Salim, D. Tuninetti, and N. Devroye, "Communications system performance and design in the presence of radar interference," *IEEE Trans. Commun.*, vol. 66, no. 9, pp. 4170–4185, Sep. 2018.

[122] F. Liu, C. Masouros, A. Li, H. Sun, and L. Hanzo, "MU-MIMO communications with MIMO radar: From co-existence to joint transmission," *IEEE Trans. Wireless Commun.*, vol. 17, no. 4, pp. 2755–2770, Apr. 2018.

[123] P. Kumari, S. A. Vorobyov, and R. W. Heath, "Adaptive virtual waveform design for millimeter-wave joint communication-radar," *IEEE Trans. Signal Process.*, vol. 68, pp. 715–730, 2020.

[124] Z. Ding, R. Schober, P. Fan, and H. V. Poor, "Simple semi-grant-free transmission strategies assisted by non-orthogonal multiple access," *IEEE Trans. Commun.*, vol. 67, no. 6, pp. 4464–4478, 2019.

[125] K. Alam and K. T. Wallenius, "Mobile radio communications: Second and third generation cellular and watm systems," *Scandinavian J. Statistics*, 1999.

[126] R. Steele and L. Hanzo, "Mobile radio communications: Second and third generation cellular and watm systems," *Scandinavian J. Statistics*, vol. 6, no. 3, pp. 123–126, 1979.

[127] A. P. Prudnikov, Y. A. Brychkov, and O. I. Marichev, "*Integrals and series, vol. 1 & vol. 2, elementary functions and special functions*," 1986.

[128] W. Yi, Y. Liu, and A. Nallanathan, "Cache-enabled HetNets with millimeter wave small cells," *IEEE Trans. Commun.*, vol. 66, no. 11, pp. 5497–5511, Nov. 2018.

[129] M. D. Renzo and J. Song, "Reflection probability in wireless networks with metasurface-coated environmental objects: an approach based on random spatial processes," *EURASIP J. on Wireless Commun. and Netw.*, vol. 2019, no. 1, p. 99, Apr. 2019.

[130] M. Di Renzo, K. Ntontin, J. Song, F. H. Danufane, X. Qian, F. Lazarakis, J. De Rosny, D. Phan-Huy, O. Simeone, R. Zhang, M. Debbah, G. Lerosey, M. Fink, S. Tretyakov, and S. Shamai, "Reconfigurable intelligent surfaces vs. relaying: Differences, similarities, and performance comparison," *IEEE Open J. Commun. Soc.*, vol. 1, pp. 798–807, 2020.

[131] Z. Ding, R. Schober, and H. V. Poor, "Unveiling the importance of SIC in NOMA systems-part 1: State of the art and recent findings," *IEEE Commun. Lett.*, vol. 24, no. 11, pp. 2373–2377, Nov. 2020.

[132] W. Yi, Y. Liu, Y. Deng, A. Nallanathan, and R. W. Heath, "Modeling and analysis of mmwave V2X networks with vehicular platoon systems," *IEEE J. Sel. Areas Commun.*, vol. 37, no. 12, pp. 2851–2866, 2019.

[133] C. Zhang, W. Yi, Y. Liu, Z. Ding, and L. Song, "STAR-IOS aided NOMA networks: Channel model approximation and performance analysis," *IEEE Trans. Wireless Commun.*, vol. 21, no. 9, pp. 6861–6876, Sep. 2022.

[134] D. Moltchanov, "Distance distributions in random networks," *Ad Hoc Networks*, vol. 10, no. 6, pp. 1146–1166, 2012.

[135] T. Hou, Y. Liu, Z. Song, X. Sun, and Y. Chen, "MIMO-NOMA networks relying on reconfigurable intelligent surface: A signal cancellation-based design," *IEEE Trans. Commun.*, vol. 68, no. 11, pp. 6932–6944, Nov. 2020.

[136] C. Zhang, W. Yi, Y. Liu, and L. Hanzo, "The proofs in the paper titled by 'Semi-Integrated-Sensing-and-Communication (Semi-ISaC): From OMA to NOMA'," Apr. 2022, arXiv preprint arXiv:2204.11245. [Online]. Available: https://arxiv.org/abs/2204.11245

[137] Z. Ni, J. A. Zhang, K. Yang, X. Huang, and T. A. Tsiftsis, "Multi-metric waveform optimization for multiple-input single-output joint communication and radar sensing," *IEEE Trans. Commun.*, vol. 70, no. 2, pp. 1276–1289, Feb. 2022.

[138] C. Li, N. Raymondi, B. Xia, and A. Sabharwal, "Outer bounds for a joint communicating radar (comm-radar): The uplink case," *IEEE Trans. Commun.*, vol. 70, no. 2, pp. 1197–1213, Feb. 2022.